ABSTRACT

Title of Dissertation: MICROSTRUCTURAL EVOLUTION AND THE RESULTANT MECHANICAL BEHAVIOR OF DUPLEX STAINLESS STEELS

Samuel Christian Schwarm, Doctor of Philosophy, 2018
University of Maryland, College Park

Dissertation directed by: Professor Sreeramamurthy Ankem
Department of Materials Science and Engineering,
University of Maryland, College Park

As the current generation of commercial light water nuclear reactors approach initial design life specifications (40-50 years), the plausibility of extending the operational life of duplex stainless steel piping to 80 years has become an important research focus. Successful evaluation of this potential requires an improved understanding of microstructural evolution and corresponding changes in mechanical behavior that occur during continuous operation at temperatures up to 320 °C, which notably results in aging embrittlement in these systems. This investigation characterizes the effects of thermal aging on the mechanical properties of cast CF–3 and CF–8 stainless steels at operational (280 °C, 320 °C) and accelerated temperatures (360 °C, 400 °C) by a variety of test methods.

Bulk mechanical tests have been performed to measure changes in properties such as tensile strength, impact energy, and ductility during aging embrittlement. The results show an increase in strength and decrease in ductility and impact energy after aging to 17,200 h.

The phase structure is investigated by electron microscopy and correlated to the mechanical properties and aging conditions in order to form a comprehensive understanding of the progression of embrittlement and elucidate trends. Smaller length scale tests, such as instrumented nanoindentation, reveal the effects of aging on local properties of the constituent ferrite and austenite phases. The resulting data are utilized to evaluate the influence of local microstructural changes, such as spinodal decomposition, on thermal aging embrittlement of the steels. Finite element method (FEM) models have been developed based on the real microstructure and local properties of the steels in order to analyze the micromechanical relationships between phases at different stages in the aging process. This research combines mechanical, microstructural, and computational characterization methods to build a comprehensive evaluation of the effects of thermal aging on structure-property relationships of these important structural stainless steels.

MICROSTRUCTURAL EVOLUTION AND THE RESULTANT MECHANICAL BEHAVIOR OF DUPLEX STAINLESS STEELS

by

Samuel C. Schwarm

Dissertation submitted to the Faculty of the Graduate School of the
University of Maryland, College Park in partial fulfillment
of the requirements for the degree of
Doctor of Philosophy

2018

Advisory Committee:

Professor Sreeramamurthy Ankem, Chair; University of Maryland
Professor Mohamad Al-Sheikhly; University of Maryland
Professor Aris Christou; University of Maryland
Professor Abhijit Dasgupta; University of Maryland
Dr. Stuart Maloy; Los Alamos National Laboratory

© Copyright by
Samuel C. Schwarm
2018

ACKNOWLEDGEMENTS

First and foremost, I would like to thank the members of my wonderful support system. Without the love and support of my fiancée Sawyer, I could not dream of reaching the levels of drive and success that have allowed me to reach these goals. I would also like to thank my parents, who have done nothing but support me and set me up to succeed. They have never failed to encourage me to pursue my goals.

I would like to thank my esteemed advisor, Dr. S. Ankem, for his guidance, support, and commitment to my success. And I thank my colleagues, especially Sarah Mburu and Matt Draper, for their assistance and commitment to our independent and shared research. I am pleased to count them among my friends as well as my coworkers.

I would very much like to thank all of the committee members for their insight and guidance, and for taking the time to review this work.

This dissertation would not have been possible without the help of Dr. Prakash Kolli for his help with experiments and analysis; Dr. Robert Bonenberger and Dr. Aldo Ponce for their help in the Modern Engineering Materials Instructional Laboratory (MEMIL); Dr. Sz-Chian Liou and Dr. Wen-An Chiou for their support in the Advanced Imaging and Microscopy Laboratory (AIMLab); Dr. Stuart Maloy, Dr. Carl Cady, Dr. Nan Li, and Dr. Eda Aydogan at Los Alamos National Laboratory for their assistance during my internship; Dr. Daniel Perea at Pacific Northwest National Laboratory for his help with the APT work on this project; and Mr. Mike Perna at the UMD Aerospace machine shop for his help with machining of test specimens.

I would also like to sincerely thank the U.S. Department of Energy: Office of Nuclear Energy (DOE-NE) Integrated University Program (IUP) fellowship program for

support for the last three years, without which attending graduate school would have been a much larger burden. This research project was funded by the U.S. Department of Energy Nuclear Energy University Program (DOE-NEUP); technical monitor Dr. Jeremy T. Busby, Oak Ridge National Laboratory; contract number DOE-NE0000724.

Portions of this research were performed using EMSL (Ringgold ID 130367) – a DOE Office of Science User Facility sponsored by the Office of Biological and Environmental Research – at PNNL, the Modern Engineering Materials Instructional Laboratory (MEMIL) at UMD, the Advanced Imaging and Microscopy Laboratory (AIMLab) at UMD, and the Center for Integrated Nanotechnologies (CINT) at LANL.

TABLE OF CONTENTS

LIST OF TABLES vi
LIST OF FIGURES vii

I. INTRODUCTION 1
A. GENERAL INTRODUCTION AND MOTIVATION 1
B. MATERIALS STRUCTURE AND EFFECTS OF THERMAL AGING 4
i. *Duplex Stainless Steels* 4
ii. *Fundamentals of Ferrite Decomposition* 5
iii. *Spinodal Domains* 8
iv. *G-phase Precipitation* 9
v. *$M_{23}C_6$ Carbides* 11
C. MECHANICAL SYSTEMS OVERVIEW 13
i. *Previous Studies on CDSS* 13
ii. *Composites, Micromechanics, and Mechanisms* 17
D. NANOINDENTATION 21
E. FINITE ELEMENT METHODS 24

II. MATERIALS AND THERMAL AGING PARAMETERS 27

III. MECHANICAL TESTING 32
A. MECHANICAL PROPERTIES AND AGING TRENDS 32
i. EXPERIMENTAL METHODS 33
ii. RESULTS 38
B. NANOINDENTATION INVESTIGATION AND METHOD COMPARISON 61
i. EXPERIMENTAL METHODS 62
ii. RESULTS 65

IV. MICROSCOPY AND MICROSTRUCTURE 71
A. INTRODUCTION 71
B. SPECIMEN PREPARATION AND EXPERIMENTAL METHODS 72
i. *Optical Microscopy* 72
ii. *Scanning Electron Microscopy – Fractography* 73
iii. *Electron Backscatter Diffraction* 74
iv. *Transmission Electron Microscopy* 77
v. *Atom Probe Tomography* 79

C. RESULTS 80
i. *Optical Microscopy* 80
ii. *Scanning Electron Microscopy – Fractography* 82
iii. *Electron Backscatter Diffraction* 87
iv. *Transmission Electron Microscopy* 93
v. *Atom Probe Tomography* 107

V. FINITE ELEMENT METHOD MODELING 111
A. INTRODUCTION 111
B. COMPUTATIONAL METHODS 113
i. *General Modeling Details* 113
ii. *Individual Model Specifics* 117
C. RESULTS 131
i. *Unaged Isotropic Model (2-D)* 131
ii. *Unaged Anisotropic Model (3D)* 134
iii. *Aged Isotropic – Elastic/Plastic Near Yield* 138
iv. 2-D Isotropic – Carbides and Phase Boundaries 143
v. 2-D Isotropic – Decomposed Ferrite 146

VI. DISCUSSION 150
A. INTRODUCTION 150
B. BULK MECHANICAL PROPERTIES AND EMBRITTLEMENT 151
C. YIELD BEHAVIOR 158
D. EFFECTS OF FERRITE DECOMPOSITION ON MECHANICAL BEHAVIOR 162
E. VALIDITY OF THE ACCELERATED AGING TEMPERATURES 168
F. FINITE ELEMENT MODELING AND COMPOSITE BEHAVIOR 171

VII. CONCLUSIONS 179
A. SUMMARY 179
B. CONCLUSIONS 180
C. FUTURE WORK 182

VIII. References 185

LIST OF TABLES

Table 1. Nominal composition (wt.%) of the CF–3 and CF–8 steels used in this study. 28
Table 2. Thermal aging conditions and associated nomenclature. 28
Table 3. Measured tensile properties for the CF–3 and CF–8 steels at each aging condition tested at room temperature. 41
Table 4. 300 °C tensile properties for the DSS at following aging at selected conditions. 51
Table 5. Mean values of the elastic parameters in the ferrite and austenite phases of the CF–3 and CF–8 CDSS derived from the individual load-displacement curves and by the Oliver and Pharr (O&P) and Dao methods. 64
Table 6. Ferrite volume percentage in the unaged CF–3 and CF–8 duplex stainless steels as determined by three different methods. 81
Table 7. Input properties for 2-D isotropic CF–3 and CF–8 duplex microstructure models. 117
Table 8. Compliance constants for both phases applied to the 3-D anisotropic model. 120
Table 9. Input properties for the bilinear models of the unaged and aged steels. 124
Table 10. Elastic input properties for the ferrite, austenite, $M_{23}C_6$, α, and α' phases..... 128

LIST OF FIGURES

Fig. 1. Contribution of major power generation sources in the United States to total electricity production from 1949 to 2011. Figure courtesy of the U.S. Energy Information Administration (EIA). 2

Fig. 2. Fe-Cr phase diagram based on experiment and CALPHAD calculation after Martinez, et al. [28] and Bonny, et al. [27]. Blue dotted lines indicate the four aging temperatures used in this study and the approximate Cr composition of the ferrite... 6

Fig. 3. A schematic shear stress vs. shear strain diagram showing the effect of interaction stresses ($\Delta\tau$) between two phases of a different stiffness. In this case, the plastic properties (yield strength and strain hardening) are assumed to be identical, thus resulting in yielding of the stiffer (δ) phase prior to yielding of the less stiff (γ) phase. Figure after Ankem, et al. [40]. 19

Fig. 4. Optical micrograph of the CF–3 microstructure showing the networked ferrite islands in the austenite matrix. 29

Fig. 5. Schematic of the thermal aging heat treatment process following solution treatment at 1065 °C for 2 h. 29

Fig. 6. Schematic diagram of the cylindrical tensile specimen used for this study. The gauge length, G, is 1 in. and the gauge diameter, D, is 0.25 in. 33

Fig. 7. Schematic diagram of a typical DSS stress-strain curve with the tensile properties labeled. 34

Fig. 8. Schematic diagram of the S1 tensile geometry. 35

Fig. 9. Schematic diagram of the Charpy V-notch specimens with a notch angle of 45 ° used in this study. 37

Fig. 10. (a) A representative nanoindentation load-displacement curve (unaged CF–3 austenite) obtained using **(b)** the indentation load function. 38

Fig. 11. Tensile stress-strain curves of **(a)** the unaged CF–3 and CF–8 steels and **(b)** a representative set of curves demonstrating the effect of aging on the tensile behavior. 40

Fig. 12. Representative schematic of the elastic/near yield bulk behavior of a CF–3 stress-strain curve. 42

Fig. 13. Bulk tensile test results for ultimate tensile strength and 0.2% offset yield stress as a function of time and temperature for **(a)** CF–3 and **(b)** CF–8. 44
Fig. 14. Bulk tensile test results for proportional limit as a function of time and temperature for **(a)** CF–3 and **(b)** CF–8. 46
Fig. 15. Bulk tensile test results for ductility as a function of time and temperature for **(a)** CF–3 and **(b)** CF–8. 50
Fig. 16. Tensile stress-strain curves of **(a)** the unaged CF–3 and CF–8 steels and **(b)** a subset of CF–8 curves demonstrating the effect of aging on the tensile behavior at 300 °C. 52
Fig. 17. Bulk tensile test results tested at 300 °C for ultimate tensile strength and 0.2% offset yield stress as a function of time for **(a)** CF–3 and CF–8 aged at 400 °C and as a function of temperature for **(b)** CF–8 aged for 4300 h. 53
Fig. 18. Charpy V-notch impact testing results as a function of time and temperature for **(a)** CF–3 and **(b)** CF–8. 57
Fig. 19. Evolution of elastic modulus of the ferrite and austenite phases with aging temperature for each of the four aging times for **(a)** CF–3 and **(b)** CF–8 DSS. 59
Fig. 20. Evolution of nanoindentation hardness of the ferrite and austenite phases with aging temperature for each of the four aging times for **(a)** CF–3 and **(b)** CF–8. 60
Fig. 21. Results for local elastic modulus and nanohardness for the unaged ferrite and austenite phases using both the Oliver and Pharr and Dao methods for **(a)** CF–3 and **(b)** CF–8. 66
Fig. 22. The number of valid calculated strain-hardening exponent, n, values that are between 0 and 1 for both the ferrite and austenite phases in CF–3 and CF–8 using the Dao and Ogasawara methods. The maximum number of successfully calculated n values is 36 in each phase. 69
Fig. 23. SEM fractographs of tensile specimens at 2 kx magnification comparing the fracture behavior in CF–3 in the **(a)** unaged condition and **(b)** aged at 400 °C for 17,200 h; and CF–8 **(c)** unaged and **(d)** aged at 400 °C for 17,200 h. 83
Fig, 24. SEM fractographs of CVN specimens at 2 kx magnification comparing the impact fracture behavior in CF–3 in the **(a)** unaged condition and **(b)** aged at 400 °C for

17,200 h; and CF–8 **(c)** unaged and **(d)** aged at 400 °C for 17,200 h. Following aging, exposed ferrite facets are visible. 84
Fig. 25. SEM fractographs of CVN specimens at 500x magnification comparing the impact fracture behavior in CF–3 in the **(a)** unaged condition and **(b)** aged at 400 °C for 17,200 h; and CF–8 **(c)** unaged and **(d)** aged at 400 °C for 17,200 h. 85
Fig. 26. IPF EBSD maps of unaged CF–3 microstructure showing **(a)** full orientation map, **(b)** map of just the austenite phase, and **(c)** map of just the ferrite phase for clarity. 88
Fig. 27. IPF EBSD maps of unaged CF–8 microstructure showing **(a)** full orientation map, **(b)** map of just the austenite phase, and **(c)** map of just the ferrite phase for clarity. 88
Fig. 28. KAM EBSD maps of **(a)**,**(b)** CF–3 and **(c)**,**(d)** CF–8 DSS in the **(a)**,**(c)** undeformed state and in the **(b)**,**(d)** failed tensile specimens. 90
Fig. 29. GOS EBSD maps of unaged **(a),(b)** CF–3 and **(c),(d)** CF–8 tensile specimens deformed **(a),(c)** uniformly and **(b),(d)** non-uniformly to failure within the gauge length. 92
Fig. 30. Conventional TEM images of the δ–ferrite/γ–austenite heterophase interface in **(a)** CF–3 and **(b)** CF–8 duplex stainless steels with (insets) SAED patterns along the γ–austenite [001] zone axis. 94
Fig. 31. (a)–(b) Conventional TEM images of an $M_{23}C_6$ carbide observed at the heterophase interface in CF–8 duplex stainless steel with **(c)** associated SAED pattern of the f.c.c. carbide along the γ–austenite/$M_{23}C_6$ [301] zone axis and **(d)** TEM-EDS scan results of element concentrations taken along a 430 nm line across the $M_{23}C_6$ carbide from the δ–ferrite phase to the γ–austenite phase along the dashed arrow. . 95
Fig. 32. Conventional TEM images of ferrite/austenite phase boundaries for CF–3 steels at **(a)** 280 °C, **(b)** 360 °C, and **(c)** 400 °C for 17,200 h. 98
Fig. 33. Conventional TEM images ferrite/austenite phase boundaries for CF–8 steels at **(a)** 280 °C, **(b)** 360 °C, and **(c)** 400 °C for 17,200 h. 99
Fig. 34. General changes in carbide size and distribution in CF–8 prior to aging and after aging at 400 °C for 17,200 h. 100
Fig. 35. Dark field TEM images of ferrite/austenite phase boundaries for CF–8 showing the altered morphology and distribution of boundary carbides following thermal aging at 400 °C for 17,200 h. 101

Fig. 36. (a) Dark field TEM image of ferrite/austenite phase boundaries for CF–8 D4 showing the presence of carbides and G-phase. **(b)** SAED image showing diffraction spots corresponding to all four phases. 103
Fig. 37. Bright field TEM image of ferrite/austenite phase boundaries for CF–3 D4 showing contrast appearing to correspond to the G-phase and (inset) SAED pattern along a ferrite zone axis within the ferrite phase. 105
Fig. 38. Conventional TEM images of ferrite phase in **(a)** CF–3 B4 and **(b)** CF–8 B4 showing contrast appearing to correspond to the G-phase. 106
Fig. 39. Bright field TEM images of ferrite phase in **(a)** CF–3 D1 and **(b)** CF–8 D1 showing no significant contrast indicative of G-phase..... 107
Fig. 40. Fluctuations of iron (Fe, blue) and chromium (Cr, magenta) concentrations along an **(a)** ROI taken in the ferrite of an unaged CF-3 APT tip. **(b)** Corresponding Fe and Cr concentration profiles illustrate the deviation of the Fe-rich α and Cr-rich α' domains from the mean elemental concentrations. [50], [125] 108
Fig. 41. Effects of aging temperature on the decomposition of the ferrite phase measured by APT on **(a)** spinodal amplitude of CF–3, **(b)** spinodal amplitude of CF–8, **(c)** spinodal wavelength of CF–3, and **(d)** spinodal wavelength of CF–8 DSS. 109
Fig. 42. Schematic diagram of the standard constraints applied to the 2-D FEM models.... 115
Fig. **43.** 2-D isotropic duplex microstructure model including mesh and phases of CF–3... 118
Fig. 44. Meshed CF–8 microstructure **(a)** elements and constraints and **(b)** corresponding nodes with an added-thickness third dimension to accommodate anisotropy. 121
Fig. 45. (a) TEM micrograph of a representative CF–8 microstructure phase boundary and **(b)** corresponding meshed FEM model of the boundary area with carbides. 127
Fig. 46. (a) APT reconstruction of the decomposed CF–3 microstructure and corresponding FEM models of the spinodal area **(b)** without and **(c)** with G-phase..... 130
Fig. 47. Von Mises **(a)**,**(b)** stress and **(c)**,**(d)** distributions for the **(a)**,**(c)** CF–3 and **(b)**,**(d)** CF–8 duplex microstructure models. 132
Fig. 48. Von Mises **(a)** stress and **(b)** strain distributions for the CF–8 3-D anisotropic duplex microstructure model. 134
Fig. 49. Von Mises stress distributions for the CF–8 3-D anisotropic duplex microstructure model at **(a)** 0.075% and **(b)** 0.100% applied strain. 136

Fig. 50. (a) x elastic strain and **(b)** z elastic strain distributions for the CF–8 3-D anisotropic duplex microstructure model. 136
Fig. 51. Progression of von Mises plastic strain distribution in the unaged microstructure of CF–3 unaged DSS under applied load over progressive substeps from **(a)** 0.0719 % applied strain – **(f)** 0.0854 % applied strain. 140
Fig. 52. Progression of von Mises plastic strain distribution in the aged microstructure of CF–3 unaged DSS under applied load over progressive substeps from **(a)** 0.0765 % applied strain – **(f)** 0.0873 % applied strain. 142
Fig. 53. Von Mises **(a)**,**(b)** stress and **(c)**,**(d)** strain distributions for the **(a)**,**(c)** CF–8 phase boundaries not containing carbides and **(b)**,**(d)** CF–8 boundaries containing carbides. 144
Fig. 54. Von Mises **(a)**,**(b)** stress and **(c)**,**(d)** strain distributions for the **(a)**,**(c)** CF–3 decomposed ferrite not containing G-phase and **(b)**,**(d)** CF–3 decomposed ferrite containing G-phase. 148
Fig. 55. Bilinear loading schematic based on Figure 3 showing the effects of raising the yield strength of the elastically stiffer phase (in this case, ferrite). 160
Fig. 56. Nanoindentation hardness values of the ferrite phase plotted as a function of the Cr concentration amplitude of the decomposed ferrite domains for both CF–3 (closed shapes) and CF–8 (open shapes) steels. Dependence on aging temperature is highlighted by different shapes/colors. 164
Fig. 57. Schematic diagram of possible hardening and softening mechanisms acting during decomposition of the ferrite phase. 164

I. INTRODUCTION

A. GENERAL INTRODUCTION AND MOTIVATION

As the U.S. reaches a turning point in power generation, the importance of the integrity of commercial nuclear power plants cannot be understated. Reliance on fossil fuels as the traditional source of electricity is becoming unfavorable from both an environmental and economic standpoint. The transition to fully renewable energy is progressing, but is not yet fully viable with respect to economics, infrastructure, or efficiency [1]. Conversely, nuclear power maintains a stable position providing ~20% of electric power in the U.S., Figure 1, at high efficiency, with an excellent safety record, and without the negative environmental impacts of carbon emissions [2]. As a result, the current generation of nuclear power reactors (Gen. III) stands to contribute significantly to the transition from fossil fuels to the next generation of power sources: solar, wind, and nuclear (Gen. IV) power production. In order to continue to take advantage of this readily available clean energy source, the viability of extending their operation to as long as 80 years must be thoroughly studied. This is an extensive task, covering many fields and areas of expertise. One of the most prominent of these challenges regards the longevity and integrity of the metallic structural materials used in the cooling pipes, valve bodies, pressure vessels and other similar components [3].

Austenitic-ferritic “duplex” stainless steels are commonly used in commercial nuclear power plants as structural components such as cooling water pipes, pump casings, and valve bodies. These cast duplex stainless steels (DSS) are a critical part of light water reactor-based nuclear infrastructure in the United States due to their high corrosion resistance, good strength, and ductility [2]–[4]. Currently, many nuclear plants are

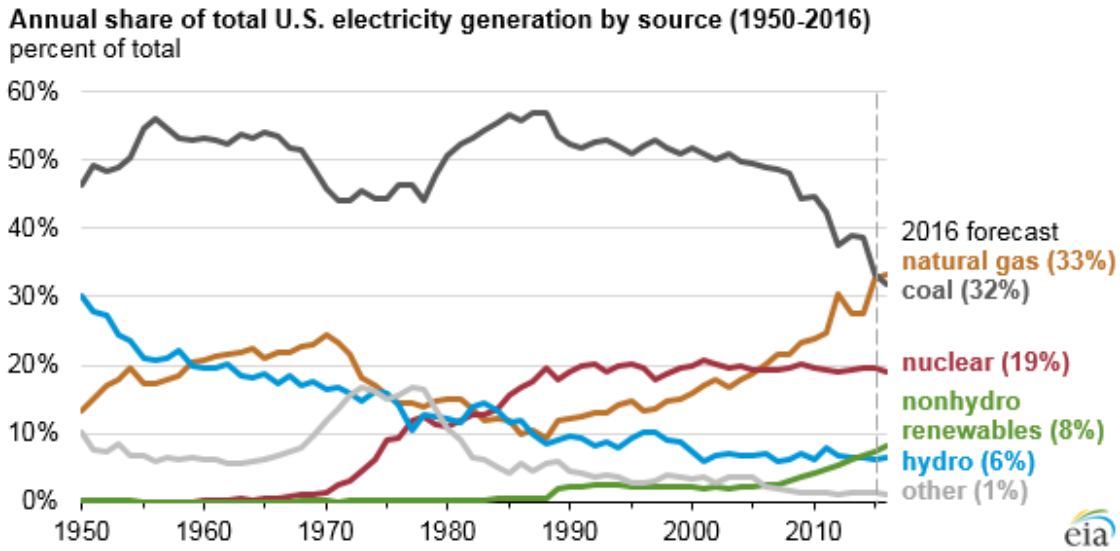

Fig. 1. Contribution of major power generation sources in the United States to total electricity production from 1949 to 2011. Figure courtesy of the U.S. Energy Information Administration (EIA).

approaching their initial design life of ~40-50 years and must be re-evaluated for life extensions of up to 80 years in continuous operation. Common DSS grades, such as CF–3 and CF–8, are utilized in multiple nuclear applications and their operating conditions include continuous elevated temperatures for decades at a time. Since these elevated temperatures, generally ~275 °C – 325 °C in light water reactors (LWRs), provide sufficient energy for thermal aging to occur, it is not enough to simply evaluate the materials systems in their initial "unaged" condition. In fact, cast DSS are known to exhibit significant structural and mechanical changes during the course of operational aging resulting in a decrease in ductility and impact toughness, i.e. embrittlement [4]–[9]. Thus, the thermal aging evolution of these systems must be thoroughly evaluated before extension of the service life can be safely considered.

In order to better understand these important materials systems, it is crucial to study the effects that thermal aging has on each constituent phase of the microstructure, and the associated structure-property relationships that occur on the microstructural and bulk scale. In multiphase (i.e. composite) systems such as duplex stainless steels, the bulk mechanical behavior is governed by the micromechanics, including mechanical interactions between the constituent phases, and changes in the individual phases during aging can significantly influence the mechanical behavior [10]–[12]. In the case of the CF–3 and CF–8 steels relevant to this research, the embrittlement of the steels during thermal aging can be traced back to the nanostructural evolution of the ferrite phase in the microstructure [5], [13], [14]. Furthermore, the presence of additional precipitate phases, such as chromium carbides, can significantly influence the behavior and changes in behavior observed in these systems [4], [15], [16].

In this work, the thermal aging evolution of CF–3 and CF–8 DSS is evaluated on multiple length scales. Bulk and local mechanical properties are measured and analyzed to obtain a comprehensive picture of the effects of thermal aging on the deformation behavior of these steels. Additionally, microscopy is performed using different techniques such as optical microscopy, transmission electron microscopy (TEM), electron backscatter diffraction (EBSD), and atom probe tomography (APT) to observe the changes in structure occurring during the corresponding aging steps and establish a clear picture of structure-property relationships in the steels. Finally, state-of-the-art modeling using finite element methods (FEM) to reconstruct the micro- and nano-structures of the materials have been utilized and new techniques have been developed to analyze local deformation behavior on multiple length scales. These techniques, taken together, help to form a clearer picture of

the effects of aging on the microstructure, micromechanics, and aging embrittlement of duplex stainless steels. The overall goal of this dissertation is to combine experimental characterization with FEM computation to increase the mechanistic understanding of thermal aging embrittlement of cast duplex stainless steels.

NOTE: This dissertation work has been performed as part of a larger project focusing on aging evolution of CF–3 and CF–8 stainless steels. The work presented here in detail is the author's own, but some additional results that add to the discussion are incorporated, notably regarding the atom probe tomography (APT) results, which strongly complement the structural data obtained by TEM. All outside work is cited and acknowledged as such.

B. Materials Structure and Effects of Thermal Aging

i. Duplex Stainless Steels

A typical duplex stainless steel is composed of a face-centered cubic (f.c.c.) austenite matrix phase containing an interconnected network of body-centered cubic (b.c.c.) ferrite phase islands. Depending on the steel composition and processing parameters, the volume percentage of the ferrite can range from as little as 5 vol.% to greater than 50 vol.% [17], [18]. These DSS are alloy systems containing multiple elements, including Fe, Cr, Ni, Si, Mn, Mo, and C [19]. Though both constituent phases are cubic in nature, the various alloying elements are more soluble in one phase or the other and as a result contribute to thermodynamic stabilization of their preferred phase. Typically, but not exclusively, elements are stabilizers of their preferred pure elemental crystal structures. In DSS systems Cr, Mo, and Si are known ferrite stabilizers and Ni, Mn, and C are known austenite stabilizers [17]. Fe, which can be stable in a b.c.c. ferrite or f.c.c austenite configuration is not included as a stabilizer of either phase, though EDS measurements have shown that Fe

is slightly enhanced in the austenite phase of CF–3 and CF–8 DSS [20]. Hence the compositions of individual DSS designated steels are designed with particular compositions (along with processing steps) intended to result in a particular duplex volume percentage and morphology.

In general, austenitic stainless steels possess moderate strength, high ductility, and high corrosion resistance, but lose their strength at relatively low temperatures (~500-550 °C) and suffer from significant void swelling under irradiation [2], [3], [21]. This class of stainless steels includes the ubiquitous 304 and 316 grades, which have a similar composition to the austenite matrix phase in CF–3 and CF–8 DSS. In comparison, ferritic stainless steels tend to be considerably less ductile, but possess greater strength and much improved resistance to irradiation (note that due to the significant nickel content of the DSS in this study, there are not single-phase ferritic stainless steels of high compositional comparability to the ferrite phase in these duplex systems) [22], [23]. As a result, the duplex systems investigated here are essentially designed metal-matrix composite materials, traditionally chosen because they can exhibit the benefits of both constituent phases, such as good strength and high ductility.

ii. Fundamentals of Ferrite Decomposition

During thermal aging of DSS, it is well-established that embrittlement occurs at temperatures up to ~475 °C, hence it is known as 475° Embrittlement [24]. Many previous studies concur that the primary cause of 475° Embrittlement is the embrittlement of the ferrite phase, and that there is little change in the properties of the austenite matrix [5], [6], [9], [14], [25], [26]. This is supported by the known effects of aging in this temperature range on ferritic steels, which are largely driven by the phase transformations approximated

by the binary iron-chromium (Fe-Cr) phase diagram, Figure 2. It can be seen that the Fe-Cr system contains a miscibility gap up to approximately 475 °C, consistent with the observed embrittlement range of the duplex (and ferritic) systems [27]–[29]. The miscibility gap indicates a thermodynamic driving force in the direction of un-mixing of Fe and Cr atoms in this region. In the immiscible region of the phase diagram, the enthalpy of mixing is positive, $\Delta H_{mix} > 0$, due to the Fe-Fe bonds and Cr-Cr bonds having a lower bond energy than Fe-Cr bonds under these temperature, pressure, and compositional conditions [30]. This dictates the separation of the δ-ferrite phase into distinct Fe-rich and Cr-rich phases, α and α', respectively (δ → α + α′) [25], [31], [32]. While this occurs in the b.c.c. Fe-Cr system, the f.c.c. austenite phase matrix in the DSS is stabilized by the crystal structure and inclusion of significant nickel (Ni) composition in the steel and thus does not undergo a transformation at these temperatures [4].

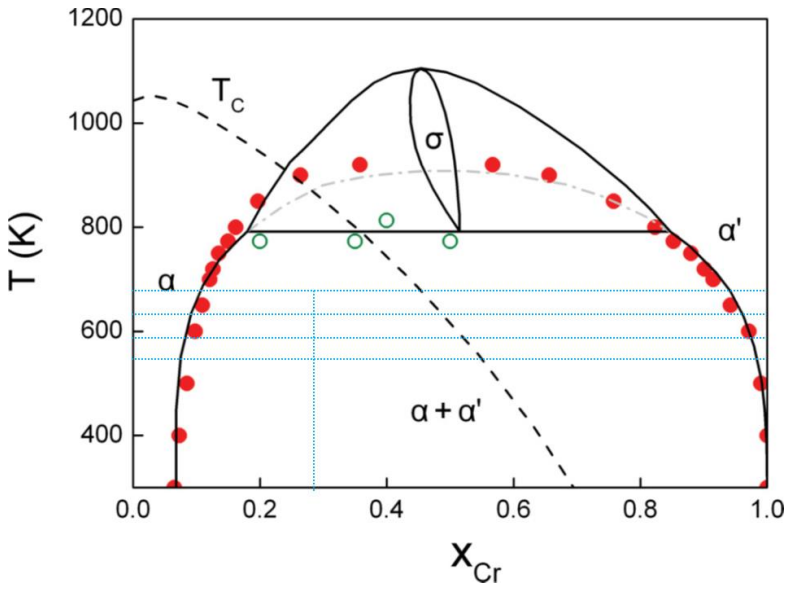

Fig. 2. Fe-Cr phase diagram based on experiment and CALPHAD calculation after Martinez, et al. *[28]* and Bonny, et al. *[27]*. Blue dotted lines indicate the four aging temperatures used in this study and the approximate Cr composition of the ferrite.

The un-mixing of the Fe and Cr atoms in the ferrite phase can manifest by two different modes – nucleation and growth or spinodal decomposition. The spinodal decomposition of the Fe-Cr system is a well-known phenomenon and results from a miscibility gap in the Fe-Cr phase diagram from approximately 9-95 % Cr and below a peak temperature of ~750 °C [27], [33]. The miscibility gap, as can be seen in the Fe-Cr phase diagram shown in Figure 2, is the result of the presence of two local minima in the free energy of mixing curve between Fe and Cr. In this spinodal compositional region, the separation of the Fe and Cr atoms occurs solely by diffusion and without the need for nucleus formation, thus limiting the activation energy of the process of forming α and α' domains to the activation energies of the diffusing atoms in the ferrite lattice [30]. This results in two stable b.c.c. phases: one with an Fe-rich composition (α) and one with a Cr-rich composition (α'). Furthermore, the inflection points of the curvature of the free energy curves form the boundaries of the spinodal region where the formation of α and α' from the original mixed b.c.c. phase is not only favorable, but has no energy barrier except for the diffusion of the Fe and Cr atoms [30], [34]. Thus, the decomposition of the ferrite differs from a nucleation and growth process and occurs spontaneously, limited only by the kinetics of diffusion.

It has been shown that changes in the concentration of elements other than Fe and Cr in the alloy, particularly Ni, can shift the free energy curve and alter the region of the phase diagram in which spinodal decomposition occurs [35], [36]. In the ferrite system undergoing decomposition here, the composition may actually be quite close to the left inflection point (Cr concentration lower bound), but the system still is found to undergo segregation under a spinodal decomposition rather than a nucleation and growth process

[37]–[40]. It is noted that the final resulting domain structure at equilibrium in the Fe-Cr system is the same regardless of the initial separation mechanism, but the composition and morphology during the early stages of segregation would differ depending on the process.

iii. Spinodal Domains

The decomposition of the Fe-Cr system depends on the composition of the ferrite phase. Following decomposition, both Fe-rich and Cr-rich domains form continuous, interconnected networks provided that the Cr composition in the ferrite is more than ~15-20%, which is the case for the alloys in this study [20], [34], [38]. These networks are typically defined as a wavelength (~ domain size) and amplitude (compositional variation) due to their periodic form [31]. The presence of decomposed ferrite can result in major changes in the mechanical properties of the phase and several factors must be taken into account, though the significance of each factor – including domain size, domain amplitude, G-phase precipitation, presence of carbides, etc. – in the real system remains unclear.

The end result of the Fe-Cr segregation in the ferrite phase is an intertwined network of Fe-rich and Cr-rich domains (α and α', respectively), both of which are continuous within the compositional bounds of the specific CF–3 and CF–8 ferrite systems. Both domains possess a b.c.c. structure, have very similar lattice parameters, and are coherent at the interfaces, leading to primarily compositional differences (and, hence, not fully physically distinct phases) [41]–[43]. There is, however, likely additional segregation of elements between the phases, such as the segregation of Ni atoms to the α phase from the α' phase [42]. Additionally, due to the (albeit small) difference in atomic radii of Fe and Cr atoms, the lattice mismatch at the domain interfaces should predictably increase during aging, resulting in more physically formed boundaries, geometrically necessary dislocations, and

a strain field [44], [45]. As a result, there is the possibility of additional elemental segregation to these boundaries and the formation of potential nucleation sites at the domain interfaces. There are three primary takeaways from decomposition of the ferrite during thermal aging: (1) the decomposed ferrite is structurally similar to that of a two-phase composite, with the potential for complex stress-strain interactions; (2) the ferrite is a compositionally complex region containing the potential for additional phase formation during thermal aging; and (3) the segregation of the elements, introduction of new boundaries and lattice structure, and potential for new phase formation lead to the possibility of different mechanical behaviors.

iv. G-phase Precipitation

One additional phase commonly shown to form by nucleation and growth within the ferrite during thermal aging (and more quickly under irradiation [46]) is the nickel silicide G-phase. This f.c.c. phase has been shown to form at the α/α' domain boundaries as these boundaries increase in distinction during thermal aging and provide viable nucleation sites. Due to this relationship to the decomposition of the ferrite and the additional activation barrier for nucleation, the G-phase tends to form later in the thermal aging process than the spinodal domains. The G-phase, as originally defined in the literature, is composed of $Ni_{16}Si_7Ti_6$, in a complex f.c.c. structure with a lattice parameter of 1.09 nm – 1.16 nm [47], [48]. However, in the absence of sufficient quantities of Ti, the commonly ascribed composition in CDSS consists of substitutions for Ti of predominantly Mn, but also Fe, Mo, and Cu [37], [49]. Henceforth, in general the G-phase composition here can be referred to as simply $Ni_{16}Si_7M_6$, where designates the possibility of several different metal substitutions.

Mburu, et al., have shown by atom probe tomography (APT) that for the CF–3 and CF–8 DSS in this study, the early formation stages of G-phase are characterized by segregation of Ni, Si, Mn, and Cu to the α/α' domain boundaries within the ferrite [37], [50], [51]. Furthermore, the APT results demonstrate that this elemental segregation is occurring primarily at accelerated temperatures of 360 °C and 400 °C at the early stages of thermal aging. These results, along with others, suggest that the G-phase formation is closely intertwined with the progression of spinodal decomposition. Pareige, et al. and Mburu, et al. found that the volume fraction of G-phase within the decomposed ferrite correlates to a larger degree of spinodal decomposition, i.e. higher domain wavelength and amplitude [37], [52]. This corresponds to enhanced nucleation sites at the domain boundaries as the phase separation leads to a decrease in coherency, as well as the possibility of ejection of G-phase forming elements from the decomposing phases. On the other hand, Mburu also found that areas of enhanced G-phase formation near boundary carbides also corresponds to a lower degree of spinodal decomposition, indicating that the presence of carbides significantly alters the kinetics of ferrite embrittlement [37], [50].

The influence of the G-phase on the mechanical properties of bulk CDSS, including specifically CF–3 and CF–8, is still a subject of debate. Multiple authors claim that the presence of the G-phase does affect the mechanical properties to varying degrees [53], [54], but no definitive indication of G-phase effects independent of the spinodal decomposition has been made. It is possible that the G-phase only has a significant effect on properties in tandem with the spinodal structure of the ferrite. In general, the presence and potential coarsening of additional physically distinct phase particles at grain (domain) boundaries is known to cause strengthening and embrittlement in metallic materials [55], [56].

Specifically, silicides in steels and other metals such as Ti alloys have a known embrittling effect [57], [58]. In this research, correlations of the presence of the G-phase to mechanical properties will be investigated.

v. $M_{23}C_6$ Carbides

Stainless steels are known to contain a variety of carbide phases, notably Cr-carbides [4]. However, based on the compositions and heat treatments, many of these carbides are not stable in DSS systems like the CF–3 and CF–8 steels studied here. Based on phase diagrams and CALPHAD calculations, there appear to be no carbides for which formation is thermodynamically favorable at in the 475 °C embrittlement range [59], [60]. However, the casting and treatment processes undergone during production of the steels cover a much wider range of higher temperatures, and carbides have been observed in DSS despite the presence of a solution treatment step. In general, based on the compositions of these steels, the most commonly encountered carbides are of the $M_{23}C_6$ stoichiometry, where the M is predominantly Cr, but can be substituted by other elements such as Fe [60], [61]. $Cr_{23}C_6$ carbides have been investigated in stainless steels notably by Southwick and Honeycombe [62], who report their crystal structure as cubic and containing a cube-on-cube orientation relationship with f.c.c. austenite grains.

The effects of carbides on mechanical deformation of steels in general has been widely studied [4], [62]–[64]. Wang, et al. and Zheng, et al. report a marked increase in tensile strength and a marked decrease in fracture toughness with the presence of $M_{23}C_6$ carbides in high manganese austenitic stainless steels [65], [66]. These property changes were accompanied by increased evidence of crack propagation and brittle failure in the steels. Furthermore, multiple studies have indicated that coarsening of the $M_{23}C_6$ carbides in the

DSS microstructure may be occurring [67], [68]. Coarsening of boundary precipitates can have varied effects, but in general can be expected to affect the mechanical deformation [69]. A recent study on $M_{23}C_6$ coarsening in a ferritic stainless steel has shown that the presence of other phases, such as the Laves phase in a ferritic stainless steel, can significantly affect the kinetics of carbide coarsening [70]. The effects of carbides at the duplex phase boundaries can also affect the kinetics of the ferrite decomposition. Mburu [50] and Hamaoka [67] have shown that the development of the G-phase and spinodal decomposition are different near boundaries containing carbides.

vi. Other Aging Factors

This study focuses on the effects of thermal aging on CF–3 and CF–8 DSS. However, operational conditions in a commercial nuclear environment may include other embrittlement factors such as irradiation and corrosion. Typically, irradiation effects are known to cause damage to metals and change properties by methods such as creation of point defects, creation of higher order defects such as dislocations and voids, and void swelling [71]. Additionally, the energy provided by the irradiation process can promote the kinetics within the atomic structure of materials, in this case promoting diffusion leading to spinodal decomposition and the formation of the G-phase [4], [72]. Thus, irradiation can significantly speed up and increase the severity of embrittlement of operational DSS. Austenitic steels similar to the austenite matrix in these DSS have been shown to undergo significant void swelling, much more than in comparable ferritic/martensitic steels [2]. However, ferritic steels are prone to embrittlement and the acceleration of embrittlement kinetics by irradiation. Hence the duplex steels would be expected to undergo both processes in an irradiation environment.

Another significant challenge in structural DSS for nuclear applications is the presence of a corrosive environment. The common usage of these alloys as cooling pipes, valves, and pressure vessels means that these materials are exposed to water and/or steam at elevated temperatures and pressures for extended periods of time. Hence, a major cause of failure is due to phenomena such as stress corrosion cracking (SCC) [2]. While both the ferrite and austenite meet the criteria for "stainless" steel, the austenite is somewhat less susceptible to corrosion and the decomposition of the ferrite has been shown to enhance its susceptibility to corrosive factors [72]. The corrosion and related cracking behaviors are factors of water chemistry, temperature, stress, DSS phase compositions, ferrite content, spinodal decomposition, and microstructure [71]. Due to the complexity of these factors, a large (and growing) body of literature exploring the effects and mitigation techniques of corrosion on DSS exists, but is beyond the scope of the current study.

C. Mechanical Systems Overview

i. Previous Studies on CDSS

Previous studies on these alloy systems focus largely on the well-established embrittlement during thermal aging below ~475-500 °C (known as 475° embrittlement) [5], [14], [29], [73], [74]. This embrittlement is commonly shown via a significant decrease in Charpy impact energy and a corresponding increase in Vickers microhardness values [7], [13], [26], [73]. Some thorough mechanical studies performed in the past 30 years have been performed, notably those performed by Chopra, et al. in the early 1990s [7], [26], [75] and more recently by Li, et al. and Byun, et al. [6], [73], [76] have shown significant changes in CVN, hardness, tensile properties, and ductility with increasing aging time and temperature within the embrittlement range. Bonnet, et al. showed that there is a distinct

correlation of CVN values with the ferrite percentage within the microstructure at constant aging time of 10,000 h at 400 °C, and doesn't show a leveling out of the curve until close to 40 vol.% ferrite [77]. Several other researchers have performed similar studies, and a good collection of the CVN data is plotted by Chung (1991), showing similar values of around 40 vol.% ferrite and a range of the DBTT shift occurring between 280 °C and 350 °C aging temperature [5], [9]. At the testing temperature, the DBTT has been shown to shift to higher temperatures (i.e. embrittlement) dependent on the aging temperature, where for accelerated aging (~350 °C – 425 °C) room temperature testing is no longer occurring on the upper shelf by 1500 h in CF–3 [5]. Similarly, many investigations report the aging evolution of tensile properties, where the ultimate tensile strength (UTS) is demonstrated to increase consistently with aging time and temperature [73], [76]. Reports of the yield strength vary, with some not reporting it at all, others reporting a slight increase, and yet others reporting a fairly constant value for various DSS [13], [73], [76].

Several studies, including those of Li [76] and Bonnet [77], report the progression of hardness with aging, including ferrite vs. austenite hardness by use of Vickers microhardness testing. The values show that the hardness of the steels is unequivocally increasing with progressive aging, with the largest changes occurring with respect to the ferrite phase. This test is fairly localized, but the scale of the indents is large enough that confidence in the ability of the indentation to capture only the single phase can be fairly low. In order to obtain more confidence in these values, a smaller-scale indentation using instrumented nanoindentation has been performed by Li, et al., but only using a small subset of tests and without reporting such data as the progression of nanohardness or elastic modulus [76]. More thorough studies by nanoindentation have been performed on the

ferrite and austenite phases of DSS not investigated in this study, such as by Dakhlaoui, et al. on a UR45N steel and Gadelrab, et al. on a UR50 steel, but these investigations do not characterize the effects of aging on the indentation properties [78], [79].

Attempts have been made to characterize the aging kinetics of the steels based on the evolution of the mechanical properties. Pumphrey and Akhurst (1990) estimated "activation energy" of the embrittlement using CVN data, determining the energy to be highly dependent on alloy composition where (normalized) values fall between 50-90 kJ/mol [13]. Similarly, Chung (1991) and Chopra (1994) estimated "activation energy" and fracture toughness of some CDSS using CVN data and again found a large dependence on composition [9], [75]. However, while these methods capture the engineering equivalents of the energy input into the system causing embrittlement over time, they do not capture the true kinetics of diffusion occurring within the ferrite nanostructure. For example, the application of Arrhenius behavior to a CVN curve means that Q value corresponds to the change in the fracture mechanics energy and crack propagation as they evolve alongside the microstructure, but not to the diffusion of the elements during ferrite decomposition. Estimation of the true diffusion-kinetic phenomena based on diffusion has been performed related to this current project by Mburu based on APT compositional data [50]. These changes are of great importance when considering nuclear structural materials, as the integrity of nuclear systems must be absolutely upheld in the face of a wide array of potential failure events. Hence, experimentation has clearly shown that the properties of the unaged materials do not solely suffice to meet the design requirements over an extended period of time since the material properties in response to both slow (e.g. quasistatic tensile testing) and faster strain rates (e.g. CVN) are not constant.

Past investigations have also been performed regarding the micro- and nanostructural phenomena related to DSS embrittlement. As mentioned above, the seminal initial discussion of spinodal decomposition was presented by Cahn and Cahn and Hilliard for the Fe-Cr system, which is a fairly close analog to the ferrite phase of a DSS [31], [32]. Many of the early studies on DSS using TEM and APT have focused on the decomposition of the ferrite phase. Miller and Bentley performed TEM and APT on CF–8 and CF–8M steels, revealing the presence of the spinodal α and α' phases, as well as the G-phase following aging at 400 °C to as much as 70,000 h [40]. A subsequent series of investigations by Miller, et al. greatly expanded on the initial investigations of spinodal decomposition of Fe-Cr alloys, showing the structure and decomposition kinetics in detail [42], [80]. More recently, Pareige, et al., Soriano-Vargas, et al., and Mburu, et al., among others, have applied today's current experimental capabilities to provide considerable new insights into the structural and compositional evolution of the spinodal domains [37]–[39], [81].

Somewhat less experimental information is available on the G-phase in these steels. Hamaoka, et al. provide insightful information regarding the G-phase and carbides in the CF–8 steels, showing that the spinodal decomposition and G-phase kinetics are closely inter-related [67]. Mburu, et al., show that the carbides and boundary elemental segregation also affects the degree of decomposition of the spinodal and G-phase [37]. However, there is very little data available at this time regarding the properties of the G-phase precipitates, and discussion of the dependence of segregation of G-phase forming elements versus the actual nucleated precipitation of G-phase on aging is ongoing.

ii. Composites, Micromechanics, and Mechanisms

For many purposes of this study, mechanical description of this system is best accomplished through the lens of composite material theory, where the DSS is a metal matrix composite (m.m.c.) with an austenite matrix and ferrite reinforcement. This allows for straightforward description of stress and strain transfer and partitioning through established methods for a particulate reinforcement in a continuous matrix [10], [12], [82]–[84]. In general, a two-phase metallic system such as the CF–3 and CF–8 DSS discussed here can be simply described where the austenite phase acts as the metal matrix and the ferrite phase acts as the reinforcement. This follows from the work of Ankem et al. regarding the behavior of α/β-titanium alloys [85], [86], where it was established that stress transfer between phases in metal alloys can be simply described for elastic behavior and near the yield point/elastic limit. The results discussed in this paper seek to provide insight into the interaction between the ferrite and austenite phases in duplex stainless steel systems, and to elucidate possible mechanisms for both ferrite hardening and bulk embrittlement.

For a simple fibrous composite, the extreme limiting cases correspond to conditions of constant stress and constant strain where the fibers align with the loading direction or are perpendicular to the loading direction, respectively [10]. In both cases, assuming a strong interface between the matrix and the reinforcement, elastic stress is transferred from a less stiff matrix phase to the stiffer phase, thus mitigating the effect of applied stress on the bulk material by reducing the amount of strain induced for the same amount of applied stress. In the constant strain assumption, the applied tensile load is aligned with fiber reinforcement, maximizing the interfacial area over which stress transfer occurs, thus

maximizing the amount of stress transfer by the equation: $E_c = V \cdot E_f + (1 - V)E_m$, where V is the volume fraction of the fibers, E_c is the elastic modulus of the composite, and the subscripts *f* and *m* refer to the fibers and the matrix, respectively. Conversely, stress transfer is minimized in the condition where the fibers are perpendicular to the applied tensile load, as the reinforcement/matrix interface is minimized for regions of non-zero applied stress. This case is described by $E_c = \frac{E_f \cdot E_m}{V \cdot E_m - (1-V)E_f}$. For the case of randomly oriented particulate reinforcement, the resulting stress transfer must fall somewhere in between these predicted values for a given volume fraction.

The general principles are related to the idea that multiphase alloys, especially those of a particulate phase within a matrix phase, can be modeled as a composite system with a matrix and particulate reinforcement. It follows that the constant stress and constant strain assumptions of composite behavior can be applied to model these systems, where the particulate structure should fall somewhere between the values predicted by these expanded rule-of-mixtures calculations [10]. In such a system, stress is transferred from the less stiff phase to the more stiff phase (inverse for strains), resulting in non-uniform stress and strain fields and the creation of interaction stresses ($\Delta\tau$) between the phases, Figure 3. These fields determine bulk applied stress and local onset regions of yielding, which depend on the elastic stiffness and yield strength of both components [10].

Numerous studies have shown that the δ (and α/α') ferrite is elastically stiffer than the γ-austenite phase in common DSS [53], [78], [79], [87]. Thus, in the case of ferrite grains reinforcing the austenite matrix in a duplex stainless steel, significant stress transfer can be expected during tensile loading, to a greater or lesser extent depending on the local orientation of the ferrite grains with respect to the loading condition. While it has important

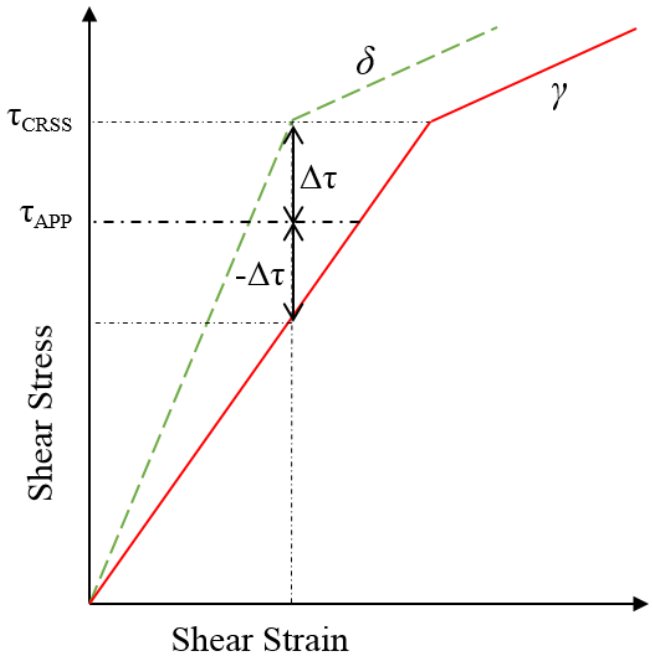

Fig. 3. A schematic shear stress vs. shear strain diagram showing the effect of interaction stresses ($\Delta\tau$) between two phases of a different stiffness. In this case, the plastic properties (yield strength and strain hardening) are assumed to be identical, thus resulting in yielding of the stiffer (δ) phase prior to yielding of the less stiff (γ) phase. Figure after Ankem, et al. [40].

implications wholly within the elastic region of both phases, this behavior becomes very significant once the yield point of one (or both) of the phases is approached. As can be observed in Figure 3 (adapted for this specific system from *Ankem, et al.*), the stress transfer can lead to the proportional limit of one phase being reached at either higher or lower applied strains than occurs during deformation of the single phase material. This is, of course, the fundamental reasoning behind adding a high-modulus reinforcement to a traditional composite – the stress is transferred to the reinforcement, which if it also has a higher yield strength than the matrix, results in yielding of the bulk system at a higher

applied stress than in the single-phase matrix material. This phenomenon occurs just as readily in multi-phase stainless steels, such as CF–3 and CF–8 DSS.

For these material systems, analysis of these elastic behavior phenomena provide great insight into the early deformation behavior and near-yield phenomena. However, after yielding of a material, the mechanical behavior is no longer controlled by linear interactions. The strain hardening portion of deformation, from the proportional limit of the material (initial deviation from elasticity) to the ultimate tensile strength (onset of non-uniform deformation) is governed by plasticity mechanisms – simplified to dislocation slip and twinning [56]. In order to analyze the deformation behavior of in the region of plasticity, it is necessary to understand the microstructure and their potential effects on deformation. In the case of the DSS, both phases are initially very ductile, and therefore are expected to fail by void formation and coalescence [56]. However, as the ferrite hardens during aging, the bulk steel also begins to lose strength and ductility. It is well established that the presence of grain and phase boundaries leads to inhibition of slip. Furthermore, during the embrittlement of a material, these same additional boundaries can provide locations of stress concentration, leading to deformation phenomena. The presence of the ferrite phase as a reinforcement materials during elastic deformation can thus lead to points of failure initiation during plastic deformation.

It is also necessary to understand that the duplex ferrite and austenite phases are not the only phases present in the materials. The presence of carbides at phase boundaries can greatly affect the plastic deformation of steels by precipitation hardening effects [55]. Additionally, the ferrite decomposition results in α and α' domains of varying boundary strength and in precipitation of G-phase precipitates within the ferrite phase. In general, the

introduction of domain boundaries between the phases can introduce coherency strains, the changes in local solid solution compositions can result in solution hardening/softening, Cr-rich regions may take on the nature of a Cr lattice and potentially act as a precipitate barrier, and the formation of G-phase at the domain boundaries may act as precipitates for hardening purposes [33], [34], [88]. Each of these potential mechanisms can act as barriers to dislocation motion or twin formation, resulting in hardening effects of the ferrite and bulk embrittlement.

D. NANOINDENTATION

To help establish the micromechanical relationships between the duplex phases, it is important to establish the individual properties of each phase. The use of instrumented nanoindentation testing is becoming an increasingly popular and reliable technique to obtain some of this data, particularly in the elastic region. Quantities such as the elastic modulus and hardness of a material down to nanoscale (indents on the order of ~100 nm diameter) can now be reliably obtained by nanoindentation methods [89]. These values are immensely useful in determining the composite deformation behavior and can be used as input data for more complex computational models, such as FEM modeling. Equally insightful (and useful) would be the determining of plastic properties such as yield strength and strain-hardening exponent on the local microstructure level. However, there is still much to be learned regarding these techniques, which are still on the cutting edge of mechanical testing technology.

The relationship between indentation and elastic properties was initially discussed by Tabor [90]. Later, Oliver and Pharr [91] presented a method (henceforth referred to as the Oliver and Pharr, or O&P, method) to determine the elastic modulus and hardness of a

single-phase grain from the load-displacement curve of a sharp nanoindentation test that has been implemented in ASTM Standard E2546–07 [92]. More recently, nanoindentation has been employed to measure plastic properties, such as the strain-hardening exponent, *n*, and yield strength, σ_y, of metals and alloys that obey power-law strain-hardening behavior. Dao, et al. formulated a reverse analysis method (henceforth referred to as the Dao method) combining a dimensionless analytical approach with experimental nanoindentation data and tested its validity on 6061-T6511 and 7075-T651 aluminum (Al) alloys [93]. Ogasawara, et al. applied a modified approach to the Dao method (henceforth referred to as the Ogasawara method) in order to obtain the strain-hardening exponent and yield strength of a wider range of alloys that obey power-law strain-hardening behavior, including brass, gold (Au), copper (Cu), and Al specimens [94].

The method developed by Oliver and Pharr and adapted into the standard for obtaining the elastic modulus of a given material is a general constitutive model based on experimental analysis of material behavior under standard Berkovich tip indentation load. This behavior, particularly relevant to metals, assumes that the unloading behavior is linear in the elastic region of recovery upon removal of the tip. The slope of this linear region, the stiffness, *S*, of the material, is defined by the equation **(1)** $S = \frac{dP}{dh} = \frac{2}{\sqrt{\pi}} E^* \sqrt{A}$, where $\frac{dP}{dh}$ is the change of load (P) with indentation depth (h), E^* is the reduced modulus, and A is the contact area. The contact area is determined based on the geometry of the Berkovich probe tip and an extrapolated indentation depth based on a comprehensive series of experimental data. Once the value of E* is determined from the solution to equation (1), the value is input into equation **(2)** $E^* = \left[\frac{1-\nu^2}{E} + \frac{1-\nu_i^2}{E_i}\right]^{-1}$ and the value of E for the tested material is obtained. Using this method, the calculation for nanohardness is a

straightforward hardness calculation of the form **(3)** $H = \frac{P_{max}}{A}$, which is the same as the calculation for Vicker's microhardness.

The Dao method begins from the same assumption as the O&P method for the linearity of the unloading curve and determination of the value of stiffness, $\frac{dP}{dh}$. However, this method is based on an engineering analysis approach using dimensionless equations derived from a subset of nanoindentation data obtained from certain materials – in this case: cubic metals. These require a simultaneous solution of dimensionless equations **(4)** $\frac{1}{E^*\sqrt{A_m}}\frac{dP}{dh} = c^*$ and **(5)** $\frac{P_{ave}}{E^*} = \frac{1}{E^*}\left(\frac{P_m}{A_m}\right) = \Pi_4\left(\frac{h_r}{h_m}\right)$, where A_m is the projected contact area, c^* is a constant based on tip geometry ($c^*_{Berkovich} = 1.167$), P_m is the maximum load, and Π_4 is one of six dimensionless equations based on fitting to experimental indentation data. Solving these equations based on the data results in values of E* and $\frac{P}{A}$, which can then be solved for *E* and *H* by equations (1) and (3). Please see Dao, et al. for full calculations [93].

The Dao and Ogasawara methods take this dimensionless approach to attempt to find plastic properties as well. As mentioned above, these methods follow the assumption based on approximation of the loading data to parabolic form, $P = Ch^2$, where C is the curvature of the loading curve. Then, using the equation **(6)** $C = \sigma_{0.033}\Pi_1\left(\frac{E^*}{\sigma_{0.033}}\right)$, where $\sigma_{0.033}$ is an estimation of stress at a value of 0.033 strain is applied, followed by a series of further dimensionless equations to solve for *n* (strain hardening exponent) based on the elastic modulus and stiffness. Finally, σ_y is calculated based on the plasticity equation **(7)** $\sigma_{0.033} = \sigma_y(1 + \frac{E}{\sigma_y 0.033})^n$. The Ogasawara method follows a very similar structure for determining n and σ_y, but with a unique set of dimensionless equations based on alternate data and using a representative stress value of $\sigma_{0.0115}$. The Ogasawara method does not outline a method

for determining the elastic modulus, so the value for *E* used to determine the plastic properties was the same as the one used in the Dao method. The reader is referred to the original publications for full calculation details [93], [94].

In an effort to obtain reliable micromechanical data for input into the FEM model, this investigation focuses on utilizing the Oliver and Pharr and Dao methods to determine the elastic properties of the CF–3 and CF–8 CDSS constituent phases from their nanoindentation load-displacement curves. The results for the elastic modulus and hardness are obtained by these two methods and compared. Additionally, the viability of determining the plastic properties by the Dao and Ogasawara methods for the constituent phases of these CDSS is investigated for the unaged steels. Following the evaluation and comparison of the methods, the effects of thermal aging on the elastic moduli and nanohardness are measured and analyzed.

E. Finite Element Methods

Finite element methods (FEM) are a fundamental and extremely useful engineering tool that can be used to describe a host of materials and mechanical systems. FEM concepts are built on the concept that obtaining a continuous solution over an entire area or volume of a complex system can range from computationally challenging to near impossible. Hence, FEM utilizes a mesh structure consisting of nodes and elements over with the calculations are performed. Essentially, FEM algorithms are utilized to account for applied boundary conditions, loads, material properties, and model geometries, and systematically obtain a solution for the desired quantity for each element. Then the solution can be output for each element or each node, or statistically applied to estimate the solution over the continuous surface or volume. The number of elements can range from a few to the

millions, and selection of elements can determine the accuracy, resolution, and computation time required to describe the system. As a result, FEM modeling methods provide an extraordinarily flexible approach to investigating mechanical deformation of a system, and the capabilities only increase with the steady increase of available computing power [95].

The foundations of using FEM modeling based on the microstructure of the alloys can be traced back to the work of Ankem, et al [10], [85], [96] and the necessity of including material models into what was (and still is) a predominantly mechanical engineering platform. FEM is well-equipped to describe such composite systems, and has been used frequently to analyze increasingly more complex composite systems with a high level of accuracy. Greene and Ankem, Neti, et al., and Rao and Ankem have utilized FEM to determine the effect of grain size and microstructure on mechanical properties such as tensile deformation, creep, and damping in dual-phase titanium alloys with much success [85], [86], [96]. These same methods by FEM can be readily applied to other two-phase (or more) systems, for which the DSS steel systems are an excellent fit, provided that the properties of the individual phases can be found. Furthermore, the models can be easily expanded to include plasticity theory [95], [97].

FEM software is often used to model the mechanical behavior of a system, and as such provides many of the tools needed to investigate the micro-mechanics of a multi-phase system. However, it is important to note that the underlying material models in ANSYS do not reflect any mechanistic behavior or atomistic properties of a material, and such effects as atomic interactions, dislocation slip, or sub-grain formation are not applicable to these models. However, the fundamentals of mechanical interactions are essentially the same on

all length scales above atomic. Thus FEM can be used to model micro-mechanical behavior of materials and can be used to provide great insight into the local deformation behavior such as stress-strain distributions, but additional analysis must be used to supplement the FEM results to elucidate the fundamental deformation mechanisms.

As a result of the fundamentals of composite behavior, the interaction between the ferrite and austenite phases in the bulk microstructure can be calculated by FEM to determine the overall effects on bulk behavior. Recently, studies have applied finite element method (FEM) models to realistic microstructural simulations in both 2- and 3-dimensions [98]–[101]. Paul (2013) and Sun, et al. (2009) used real-2-D microstructure representations to elucidate likely regions of failure in ferritic-martensitic and transformation-induced plasticity (TRIP) alloy systems [100], [102]. Clear contour plotting of the stress and strain within local regions provide insight into the contributions of microstructural features to bulk deformation and failure. An increasing body of work is forming in the literature regarding these real-microstructure FEM simulations, and this author has recently published work on the topic, utilizing experimental local property measurements by nanoindentation and FEM calculations to compare the bulk elastic modulus of the microstructure with that measured by bulk tensile testing [98]. Furthermore, FEM can analyze the effects of boundary precipitates on bulk properties and predict the most likely regions of failure and most likely slip systems to activate during a particular deformation event. Each of these methods can be used to cheaply and effectively make predictions and support experimental data.

II. MATERIALS AND THERMAL AGING PARAMETERS

CF–3 and CF–8 cast duplex stainless steels are characterized by their primary two microscopic phases: body-centered cubic (b.c.c.) δ-ferrite islands in a face-centered cubic (f.c.c.) γ-austenite matrix, Figure 4. These steels follow the standard compositional requirements of ASTM A351-14 [103] for austenitic and ferritic-austenitic stainless steel castings, where the iron (Fe) lattice is supplemented by significant amounts of Cr (~20 wt.%) and Ni (~8 wt.%) for phase stability and corrosion resistance. The full composition of the steels investigated in this study can be found in Table 1, as measured by optical emission spectroscopy.

The microstructure of the CF–3 and CF–8 steels is determined by the chemical composition and processing steps performed on the as-received material. The material here referred to as "as-cast" or "unaged" is based on the ASTM standard A351–14 [103], which specifies tolerances for austenitic castings used for "pressure-containing parts", such as those used in the commercial nuclear industry. The DSS studied here were received in the casting and processing condition laid out by this standard and meets the required tolerances. The ferrite volume percentage is determined by chemical composition, as is elaborated upon in Chapter I, and by the heat treatments. In general, the duplex microstructure is formed as the initial δ-ferrite phase is cooled into the region of austenite stability, and some ferrite is retained due to the chemical composition and time constraints [17], [104]. This is occurring during the casting process and also during the 2 h solution treatment process, which takes place in the γ-austenite (or $\gamma+\delta$) region of the phase diagram for these steels. The final measured result for as-cast steels in the "unaged" condition in

this study is approximately 10 vol.% ferrite in both steels, as presented in more detail in Chapter IV.

The steels utilized in this research are statically cast and subsequently solution treated at 1040 °C for 2 hours, followed by a water quench. 17.8 cm x 3.3 cm x 2.9 cm (7.0 in. x 1.3 in. x 1.1 in.) rectangular keel block specimens were received in this condition (referred to as "unaged") and machined into 5.8 cm x 1.6 cm x 1.6 cm (2.3 in. x 0.6 in. x 0.6 in.) and 8.9 cm x 1.6 cm x 1.6 cm (3.5 in. x 0.6 in. x 0.6 in.) blanks for aging and machining into mechanical testing specimens. Due to the stainless nature of the specimens, no significant scale was observed on the metal surfaces following thermal aging or water quenching. Due to the relatively small width and height of the specimens blanks, fairly low aging temperatures (as compared to the melting point of the steels), and fast cooling process, no significant structural gradient from the exterior to the center-line of the specimens is expected. Regardless, specimens for mechanical testing and microscopy evaluation were taken from the interiors of the specimen blanks following aging and quenching.

Table 1. Nominal composition (wt.%) of the CF–3 and CF–8 steels used in this study.

		Composition (wt.%)						
Steel	**Source**	**Fe**	**Cr**	**Ni**	**Si_{max}**	**Mn_{max}**	**Mo_{max}**	**C_{max}**
CF–3	ASTM A351	Balance	17.0–21.0	8.0–12.0	2.00	1.50	0.50	0.03
	Measured	69.52	19.69	8.40	0.98	1.07	0.28	0.02
CF–8	ASTM A351	Balance	18.0–21.0	8.0–11.0	2.00	1.50	0.50	0.08
	Measured	69.44	19.85	8.30	0.97	0.99	0.35	0.06

Table 2. Thermal aging conditions and associated nomenclature.

Unaged	**280 °C**	**320 °C**	**360 °C**	**400 °C**
4300 h	A1	A2	A3	A4
8600 h	B1	B2	B3	B4
12900 h	C1	C2	C3	C4
17200 h	D1	D2	D3	D4

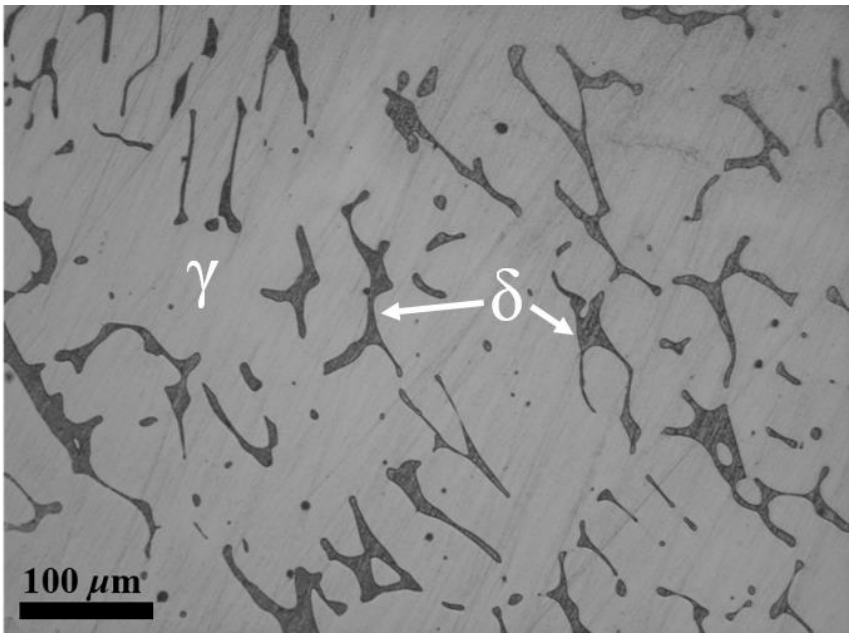

Fig. 4. Optical micrograph of the CF–3 microstructure showing the networked ferrite islands in the austenite matrix.

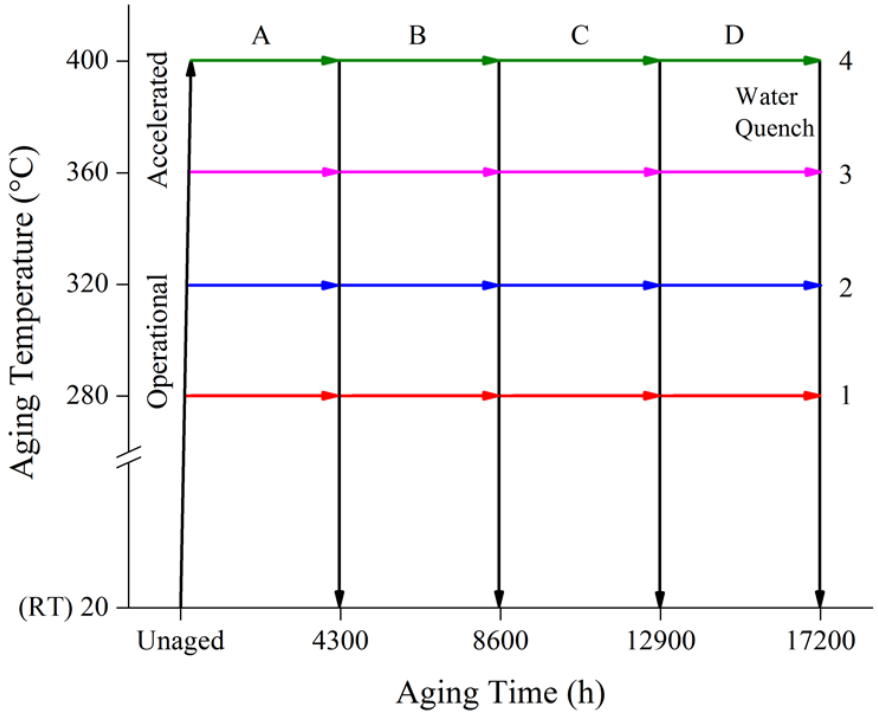

Fig. 5. Schematic of the thermal aging heat treatment process following solution treatment at 1040 °C for 2 h.

Thermal aging was performed on specimen blanks in benchtop laboratory furnaces in air at operational (280 °C, 320 °C) and accelerated (360 °C, 400 °C) temperatures for time steps of 4300 h, 8600 h, 12,900 h, and 17,200 h. The general aging parameters can be schematically found in Figure 5. A nomenclature system, Table 2, has been developed that will be used throughout this document for simplicity, where letters A, B, C, D refer to the aging steps and trailing numbers refer to the aging temperatures. Hence, CF–3 A1 refers to a CF–3 specimen aged at 280 °C for 4300 h, CF–8 C4 refers to a CF–8 specimen aged at 400 °C for 12,900 h, etc. At the end of each 4300 h time step, specimen blanks were removed from the laboratory furnaces, water quenched at room temperature, and machined into mechanical test specimens for CVN and tensile testing following the standard requirements presented in the following chapters. Additional un-deformed material was utilized for microscopy, nanoindentation, and other analysis techniques by preparation techniques listed in the following chapters.

The operational temperatures were selected to approximate the actual service conditions of DSS components in commercial light water reactors, and the accelerated temperatures were selected based on expectations of similar thermodynamic behavior but faster kinetics, which can be used to approximate the same conditions in the operational steels at more advanced times. In more specific terms, the accelerated aging steps are chosen such that they fall in the same region of the phase diagram as the DSS would experience in service. Thus, time-dependent processes such as diffusion, nucleation, growth and coarsening can by accelerated due to the increased thermal energy, while the formation of additional phases not formed under service conditions are precluded. These accelerated kinetics can be described by the simple Arrhenius relationship defining the

temperature dependence of diffusion: $D = D_0 \exp\left[-\frac{Q}{RT}\right]$, where D_0 is the diffusion constant, Q is the activation energy, R is the gas constant, and T is the absolute temperature [30]. To compare the effects of temperature, the ratio equivalent aging times can be taken as $\frac{t_2}{t_1} = \exp\left[\left(\frac{Q}{R}\right)\left(\frac{1}{T_2} - \frac{1}{T_1}\right)\right]$.

Note: Use of accelerated aging temperatures ranging from 350 °C – 400 °C is common in DSS alloys, but some questions remain as to the validity of the higher aging temperatures with regard to the in-service conditions. This question is examined in more detail in the Discussion, Chapter VI.

III. MECHANICAL TESTING

A. MECHANICAL PROPERTIES AND AGING TRENDS

Since embrittlement is an observable manifestation of changes in micro- and nano-structure, thorough measurement of the aging evolution of the steels is a valuable assessment of the structural changes and rates of change (i.e. kinetics) occurring in the system. Bulk mechanical testing entails (predominantly) established methods, basic machining, and straightforward interpretation of data, making it an excellent tool for achieving fast, reliable results. The data collected can provide guidance for additional in-depth study of local properties and small-scale characterization. Generally, the structural changes in the CF–3 and CF–8 systems will be discussed in the following chapters, but the first indications of these changes can be seen clearly in the results presented here. Furthermore, in operational service the mechanical properties must meet the necessary specifications for safe operation, thus making evaluation of the mechanical properties a crucial component of overall characterization of the system.

In this investigation, quasi-static tensile tests were performed at room temperature following quenching from each aging temperature at each 4300 h aging step. Additional tensile tests were performed at operational temperatures (300 °C) on smaller scale specimens for a selected subset of aging conditions. The results, when combined with established room temperature Charpy V-notch impact test (CVN) values, clearly demonstrate the progression of thermal aging embrittlement, strengthening, and the influence of compositional and structural differences between the two steels. The resulting trends clearly correspond with evolution of the structure on multiple length scales. As has been established in previous studies, the resulting trends can be interpreted in ways that

elucidate structure-property relationship and aid in predicting the behavioral evolution of the system [7], [13], [14], [75].

i. EXPERIMENTAL METHODS

a. Room Temperature Quasi-static Tensile Testing

Tensile test specimens were machined following specifications established in ASTM E8-13a [105] for cylindrical specimens with dimensions containing a 6.35 mm (0.25 in.) gauge diameter and a 25.4 mm (1.0 in.) gauge length, Figure 6. The cylindrical specimens

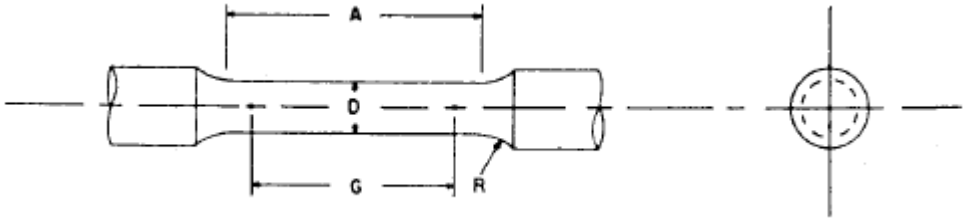

Fig. 6. Schematic diagram of the cylindrical tensile specimen used for this study. The gauge length, G, is 1 in. and the gauge diameter, D, is 0.25 in.

are machined with threaded ends on either side of the gauge which are then screwed into the tensile test fixtures. The specimens were deformed at room temperature in tension using an Instron® model 8502 test frame and model 8800 controller in the Materials Testing Laboratory (MTL) at UMD. A preload of ~250 N was applied prior to initiation of each test to relieve slack in the specimen fixtures and reduce spring-back during the strain-rate controlled tests. Real-time strain measurements were obtained and utilized to apply a strain-rate control rate of 0.00025 s^{-1} using a calibrated Instron® extensometer with a 1 in. gauge length. Upon approaching the strain limit of the extensometer (50%), the strain gauge was removed and testing was completed to fracture using a crosshead speed control

rate of 0.006125 mm s^{-1}. 0.2% offset yield stress (σ_y), proportional limit (σ_{PL}), ultimate tensile strength (UTS), and ductility were measured following standard procedures laid out in the ASTM standard. Figure 7 is a schematic demonstrating a general stress-strain curve and the engineering properties that can be obtained therewith. Errors are calculated as twice the standard error of the mean.

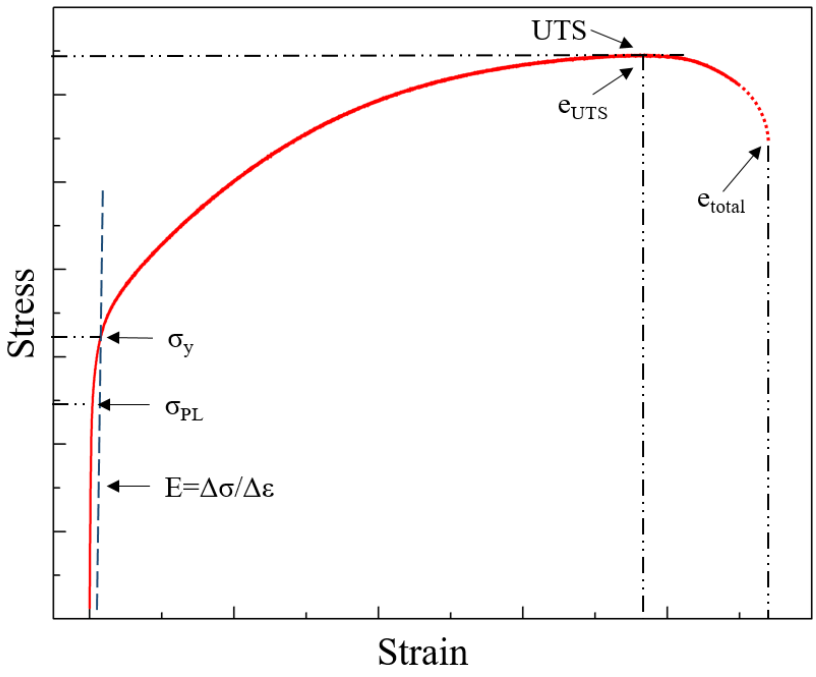

Fig. 7. Schematic diagram of a typical DSS stress-strain curve with the tensile properties labeled.

The ductility of the specimens is measured in three different ways: total elongation (%el), strain at necking (e_{UTS}), and percent reduction of area (%RA). The values of e_{UTS} are measured directly from the engineering stress-strain curves as schematically shown in Figure 7. The %el values were measured by marking the initial gauge length as delineated by the extensometer and measuring the final elongated length by a standard caliper.

Likewise, the %RA values were measured using a standard caliper and averaging the maximum and minimum diameter of the necked region following fracture.

Experimental Note: Due to minor equipment issues encountered during the early testing of the unaged bulk tensile specimens, the initial values calculated for these samples in the elastic and proportional limit region were suspect. Therefore, new specimens of the CF–3 and CF–8 steels were prepared and tested to improve upon the values obtained for elastic modulus and proportional limit. The average of two retests for both CF–3 and CF–8 were taken and reported for elastic modulus and proportional limit, replacing the initial measurements for the unaged steels. The plastic values such as offset yield strength, UTS, and ductility values were all validated for the initial tests and the results closely match those of the re-test specimens.

b. Elevated Temperature Quasi-static Tensile Testing

Flat/plate-type tensile specimens were machined for testing at operational temperatures following S1 tensile geometry with gauge dimensions are 5.3 mm x 1.2 mm x 0.80 mm (0.20 in. x 0.05 in. x 0.03 in.), Figure 8, using a wire EDM. Due to the small size and

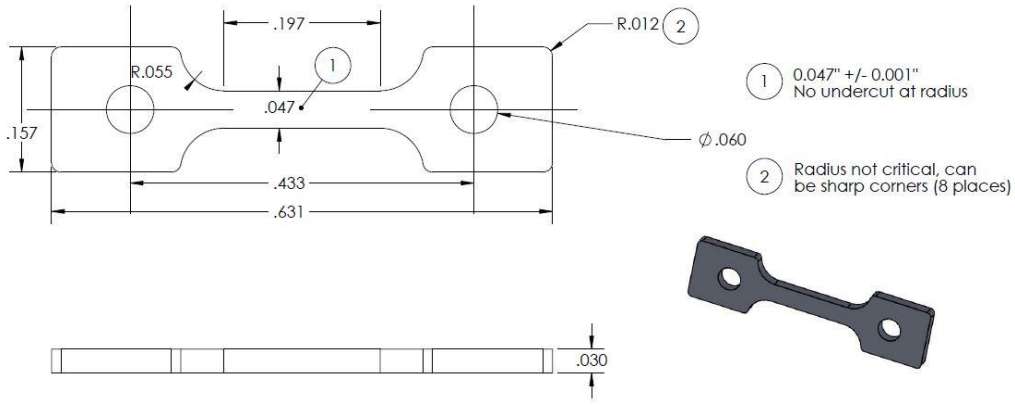

Fig. 8. Schematic diagram of the S1 tensile geometry.

resulting difficulty in machining, precise measurements of the gauge dimensions of each specimen were taken prior to testing and utilized in the final calculations. Testing was performed with assistance using an MTS model 880 tensile frame and 250 kN load cell at Los Alamos National Laboratory. A furnace chamber fitted to the fixtures was placed around the test apparatus where the specimen was mounted and the temperature was increased to 300 °C and monitored by a calibrated type-k thermocouple. Each test was performed at a strain rate of 10^{-3} mm/mm/s following stabilization of the temperature to 300 ± 5 °C. Due to constraints pertaining to the test apparatus, tests were terminated following initiation of necking (i.e. UTS) but prior to fracture. Errors are calculated as twice the standard error of the mean.

c. Charpy V-notch Impact Testing (CVN)

CVN specimens were prepared in accordance with specifications established in ASTM E23-12c [106] for each aging condition. 55 mm x 10 mm x 10 mm (2.17 in. x 0.39 in. x 0.39 in.) CVN specimens include a 45° notch to serve as a stress concentration point for consistent initiation of fracture in each specimen, Figure 9. Each specimen was impacted at room temperature using a Tinius Olsen IT406 impact test frame in the Modern Engineering Materials Instructional Laboratory (MEMIL) at the University of Maryland, College Park (UMD). Three specimens were tested for each aging condition after 4300 h and 8600 h. Four specimens were tested for each aging condition after 12,900 h and 17,200 h. Impact energy is measured as the energy absorbed by the specimen during fracture from the initial energy of 300 ft-lbs (407 J). The resulting fracture morphologies were analyzed by SEM (Chapter IV) to interpret the transition to less ductile behavior following embrittlement. Errors are calculated as twice the standard error of the mean.

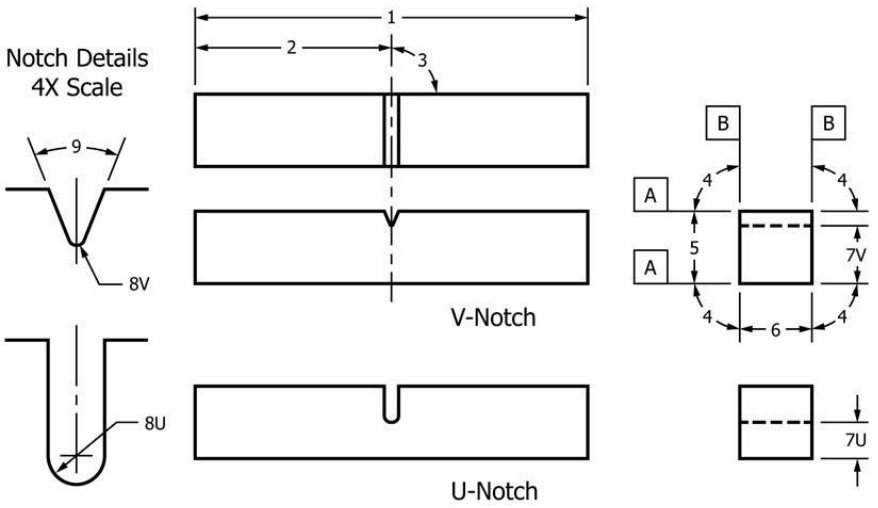

Fig. 9. Schematic diagram of the Charpy V-notch specimens with a notch angle of 45 ° used in this study.

d. Nanoindentation Testing

The local elastic modulus and nanohardness of the constituent ferrite and austenite phases were measured by instrumented nanoindentation. Prior to indentation, specimens of minimum 2 mm thickness were polished to a 0.05 μm surface finish. Nano-indents were made using a Hysitron 900 Triboindenter equipped with a diamond Berkovich tip in the MEMIL laboratory at UMD. The indenter was calibrated using a standard quartz specimen. The indentation load function consisted of a 15 s loading time to 4000 μN, 10 s of holding time, and 15 s of unloading to 0 μN for a total load time of 40 s, Figure 10. Analysis was performed following the Oliver and Pharr method [91], [92] taking the slope of 20% to 95% of unloading curve. Individual indents were performed in 12 different locations in each phase of both steels for all aging conditions. Each indentation location was selected randomly (within each phase to accommodate local anisotropy resulting from crystal

orientation and the results were averaged. Reported error is twice the standard error of the mean.

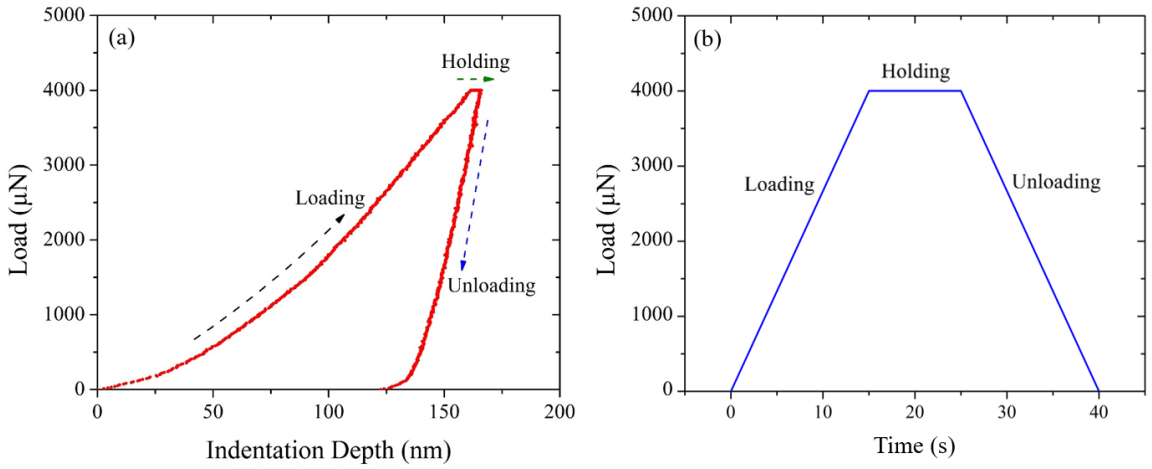

Fig. 10. (a) A representative nanoindentation load-displacement curve (unaged CF–3 austenite) obtained using **(b)** the indentation load function.

ii. RESULTS

a. *Room Temperature Quasi-static Tensile Testing*

Analysis of engineering materials requires measurement of the fundamental properties and evaluation of these properties over time. In general, tensile testing performed at a fairly low strain rate (i.e. quasi-static) is the standard method for the most commonly reported properties of metals, such as strength and ductility. Careful analysis of the resulting deformed specimens and corresponding stress-strain curves reveals proportional limit (σ_{PL}) and yield strength (σ_y), percent elongation (%el.) and reduction of area (%RA), ultimate tensile strength (UTS), and elastic modulus (Young's modulus, E). Each of these properties is dependent on microstructural properties such as grain size and precipitate phases, albeit in different ways and to different degrees. Thus, the results elucidate differences between

the CF–3 and CF–8 steels corresponding to their compositional and structural differences. Differences resulting from the evolution of the structures due to aging are made apparent and can be correlated to the micro- and nano-scale evolution of the CDSS during aging.

Stress-strain curves for the room temperature tests are shown in Figure 11. The curves follow the same shape and trends as shown schematically in Figure 7, and the following quantities are derived accordingly and listed in Table 3.

i. Elastic Modulus

The elastic modulus of the bulk materials can be estimated by taking the slope of the initial linear portion of the stress-strain curve, Figure 7, where the linear response to loading is indicative of purely elastic behavior and the strain is fully recoverable. Therefore, the slope of the line is equal to the elastic modulus (Young's modulus) $E = \frac{\sigma}{\varepsilon}$. The results for elastic modulus calculated directly from the stress-strain curves for each aging condition are shown in Table 3 and a sample calculation using an unaged CF–3 specimen can be found in Figure 12. The *E* values calculated for the unaged CF–3 and CF–8 are 189 GPa and 170 GPa, respectively. The measured *E* values for the aged bulk specimens show little change up to 17,200 h at the operational and accelerated testing temperatures. Elastic modulus is dependent on bonding between atoms and can change within a material due to changes in the solid solution composition or changes in bonding types [56]. The modulus of bulk specimens shows little change because the composite modulus depends on a modified rule of mixtures of the duplex phases and there is no significant change in the elastic modulus of either phase during aging. Since the ferrite volume fraction is quite small within the matrix, the matrix elastic properties dominate the bulk elastic properties, and thus the *E* values predominantly reflect the structural constancy

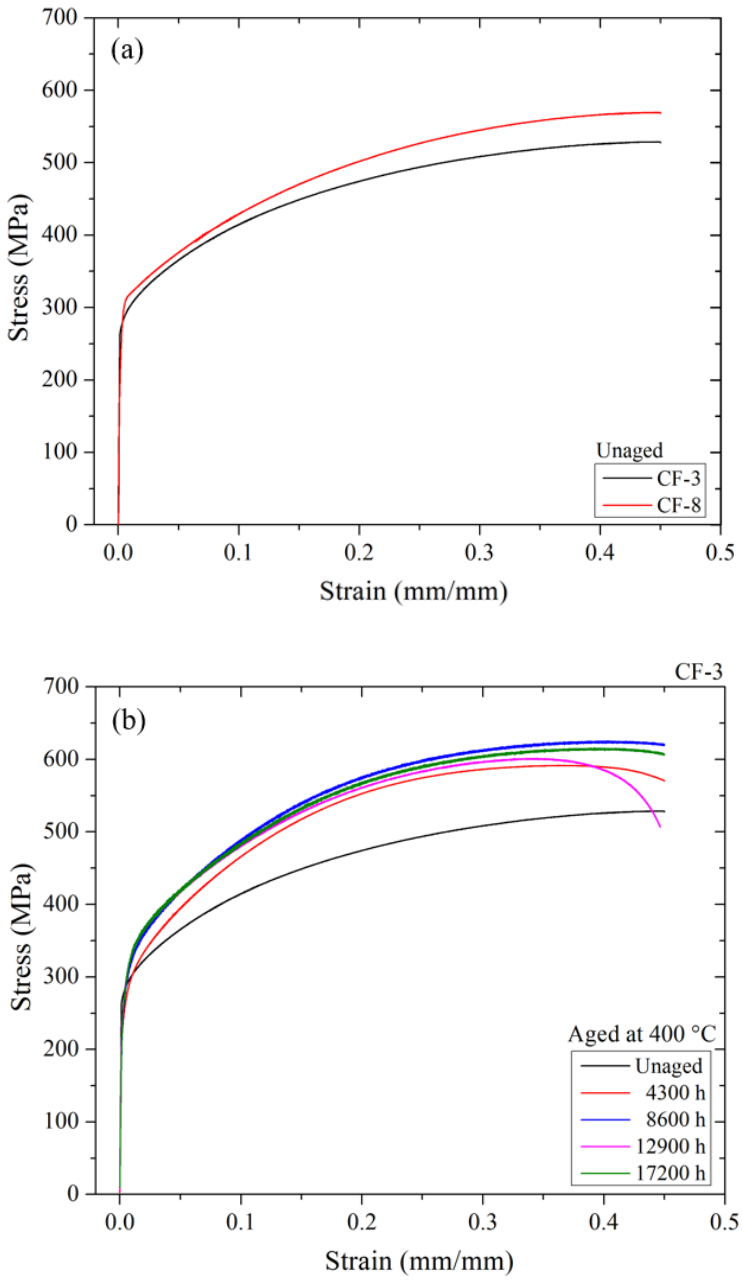

Fig. 11. Tensile stress-strain curves of **(a)** the unaged CF–3 and CF–8 steels and **(b)** a representative set of curves demonstrating the effect of aging on the tensile behavior.

Table 3. Measured tensile properties for the CF–3 and CF–8 steels at each aging condition tested at room temperature.

DSS	E *GPa*	σ_y *MPa*	σ_{PL} *MPa*	UTS *MPa*	e_{UTS} *mm/mm*	%el *%*	%RA *%*
CF3 Unaged	189.1	280	165	530	>0.45	61	83
CF3 A1	200.3	255	116	530	>0.45	75	88
CF3 A2	193.4	254	124	560	>0.45	62	83
CF3 A3	154.2	258	135	595	0.40	51	78
CF3 A4	168.1	250	145	590	0.37	51	78
CF3 B1	172.1	281	142	565	0.43	58	74
CF3 B2	159.9	271	148	565	~0.45	57	80
CF3 B3	151.6	279	133	610	0.37	59	78
CF3 B4	157.2	265	145	625	0.40	51	77
CF3 C1	185.1	275	151	561	>0.45	58	72
CF3 C2	189.0	272	154	562	0.42	59	80
CF3 C3	223.0	281	153	598	0.40	48	76
CF3 C4	204.4	266	138	600	0.33	42	67
CF3 D1	189.1	280	146	535	0.38	48	78
CF3 D2	182.6	256	142	595	0.45	60	79
CF3 D3	166.7	267	143	575	0.39	52	74
CF3 D4	164.6	273	148	620	0.44	55	65
CF8 Unaged	169.6	286	164	570	>0.45	60	80
CF8 A1	158.1	280	165	570	>0.45	61	81
CF8 A2	184.8	276	216	575	0.40	58	78
CF8 A3	152.1	260	117	595	0.40	65	78
CF8 A4	158.5	244	107	595	0.38	54	73
CF8 B1	173.7	269	161	570	>0.45	66	76
CF8 B2	138.1	267	139	585	0.44	55	74
CF8 B3	155.8	260	118	605	0.43	56	77
CF8 B4	121.6	263	140	620	0.45	55	65
CF8 C1	155.6	266	144	565	>0.45	66	77
CF8 C2	177.1	280	137	595	0.45	59	74
CF8 C3	166.5	270	132	610	0.37	57	72
CF8 C4	167.8	271	140	620	0.43	54	69
CF8 D1	175.7	285	148	585	0.44	56	71
CF8 D2	159.0	279	142	595	0.42	52	74
CF8 D3	162.3	283	150	630	0.43	53	74
CF8 D4	168.3	277	148	635	0.4	50	70

of the matrix. It is noted that the measured value of elastic modulus of CF–8 is lower than that of CF–3 by about 20 GPa. This is consistent with the findings of Ledbetter and Austin for a 304 austenitic stainless steel similar to the austenite matrix in this study, which found that addition of interstitial carbon serves to decrease the elastic constants of the steel [107]. The local elastic moduli of the individual ferrite and austenite phases are discussed later in Chapter III, and their influence is highlighted in Chapter V (FEM) and Chapter VI (Discussion).

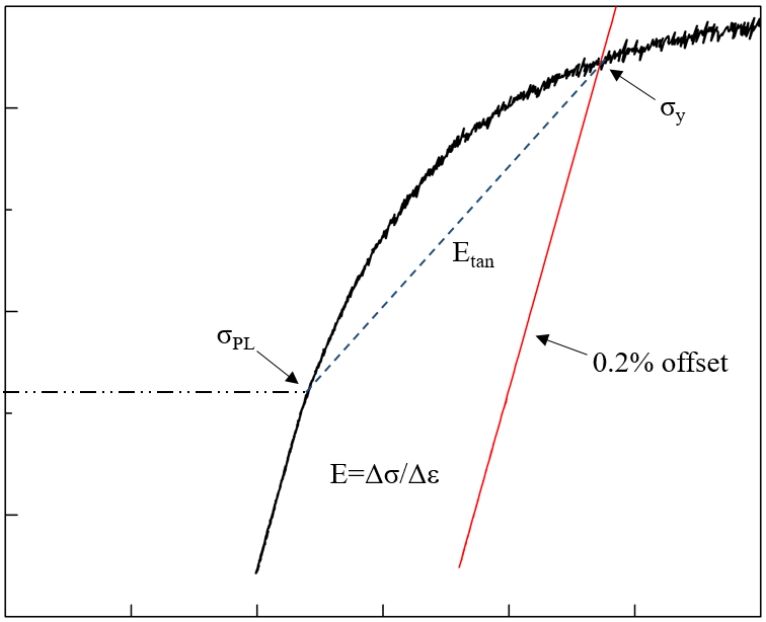

Fig. 12. Representative schematic of the elastic/near yield bulk behavior of a CF–3 stress-strain curve.

The values obtained for the elastic modulus, *E*, of the re-tested unaged specimens were 188 GPa for CF–3 and 179 GPa for CF–8, which are similar to the values reported above, with similar comparative trends. Since the initial values were previously reported in the literature and are confirmed by the re-tests to be reliable, the initial values will be utilized for later discussions.

ii. Tensile Yield Strength and Proportional Limit

The yielding behavior of structural components – especially materials in used in harsh environments and that must maintain integrity under a variety of conditions – is critical for determining the long-term operation and safety of the system. In many cases, yielding is considered failure of the material, at which point the best-case scenario means that the component must be replaced at considerable expense. The yield strength, σ_y, and proportional limit, σ_{PL}, are generally used to express similar quantities: the stress required to permanently deform the material. σ_y is utilized as the standardized engineering term, and for all metals is calculated precisely from the stress-strain curve where the 0.2% strain offset fit of the linear elastic region intersects the strain-hardening portion of the curve. This method is ideal for reporting strength and using it for comparison with regulations and other engineering materials.

The strain hardening portion of the curve occurs after the curve deviates from linearity and the strain is no longer recoverable. The specific point where the curve deviates from linear behavior is known as the proportional limit (or elastic limit), and is the real point of onset of permanent deformation. Thus σ_{PL} is more difficult to obtain precisely and must be interpreted from the data, but is more useful from a real behavior perspective. As a result of this, the proportional limit is also the more accurate quantity to use during computational modeling, such as by FEM. The calculation of both values is shown schematically in Figures 7 and 12. The 0.2% offset yield strengths and proportional limits for each aging condition are shown in Table 3.

Plots of the effects of aging on σ_y for the bulk specimens at room temperature for CF–3 and CF–8 steels are presented in Figure 13(a) and Figure 13(b), respectively. The initial

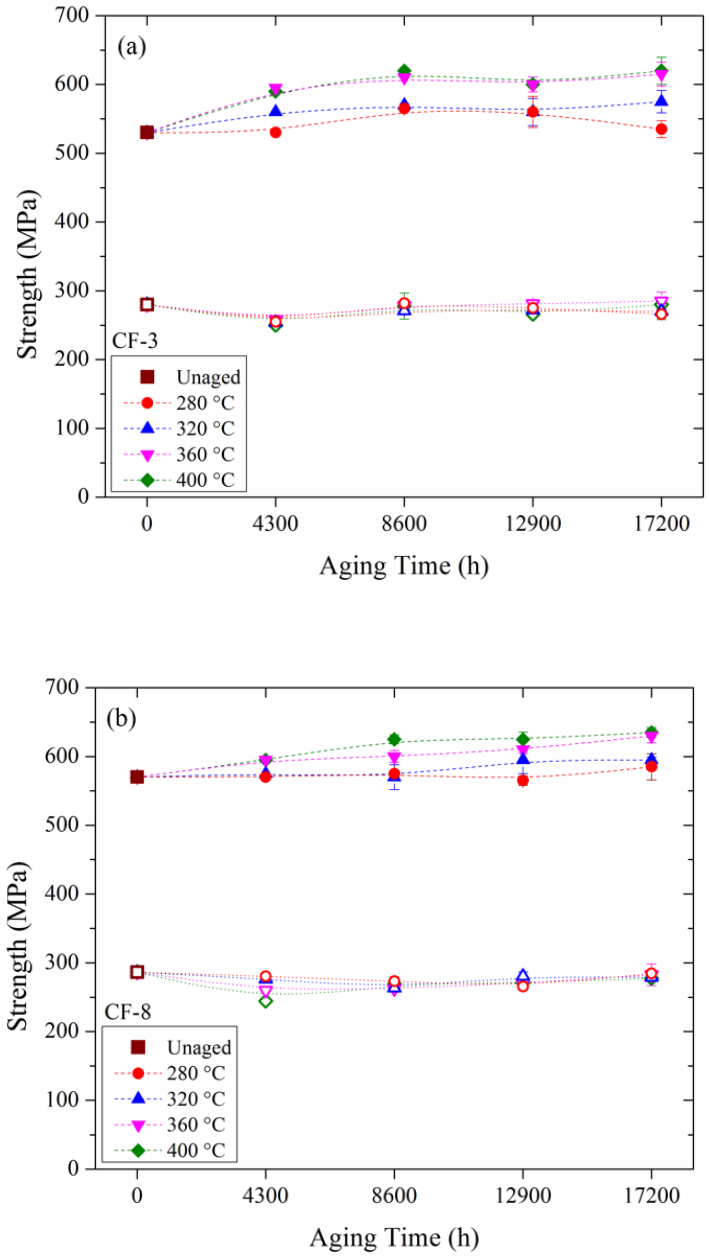

Fig. 13. Bulk tensile test results for ultimate tensile strength and 0.2% offset yield stress as a function of time and temperature for **(a)** CF–3 and **(b)** CF–8.

values in the unaged condition are 280 MPa for CF–3 and 286 MPa for CF–8. As can be observed in Figure 13, there is little change in the offset yield strength with aging for either steel. The yield strength values measured at the most extreme aging conditions, 400 °C and 17,200 h, are very slightly lower than the unaged values: 273 MPa and 277 MPa for CF–3 and CF–8, respectively. Likewise, the other aging temperatures up to 17,200 h all result in values within 8% of the unaged condition. Interestingly, there is a noticeable dip in the yield strength values of the CF–3 steel following aging at all temperatures to 4300 h which is not observed in the CF–8. However, all the values are subsequently recovered in future aging steps, and the cause of this phenomenon is not understood. It is possible that there is a real phenomenon occurring here to decrease the yield strength that is somehow mitigated by the presence of the carbides or interstitial carbon in the CF–8, but it is also possible that this is somehow resulting from experimental effects. Further investigation of the yielding phenomena of the CF–3 in the first year of aging is recommended for future study.

Values were also measured for the proportional limit, σ_{PL}, at each aging condition, Figure 14. The values of σ_{PL} obtained for the unaged condition are 165 MPa for CF–3 and 164 MPa for CF–8. Like the offset yield stress, there is little difference between the steels. However, the proportional limit values appear to follow a slight decreasing trend with aging time in both steels, though the variation in the values is larger than that of the offset yield stress. The D4 aged specimens (400 °C, 17,200 h) each exhibit values of 148 MPa for σ_{PL}, which constitutes a drop of ~10%. There also appears to be an apparent dip in the data following the first aging step at 4300 h similar to that observed in the offset yield stress of CF–3, which supports the possibility of this trend resulting from a real phenomenon during aging.

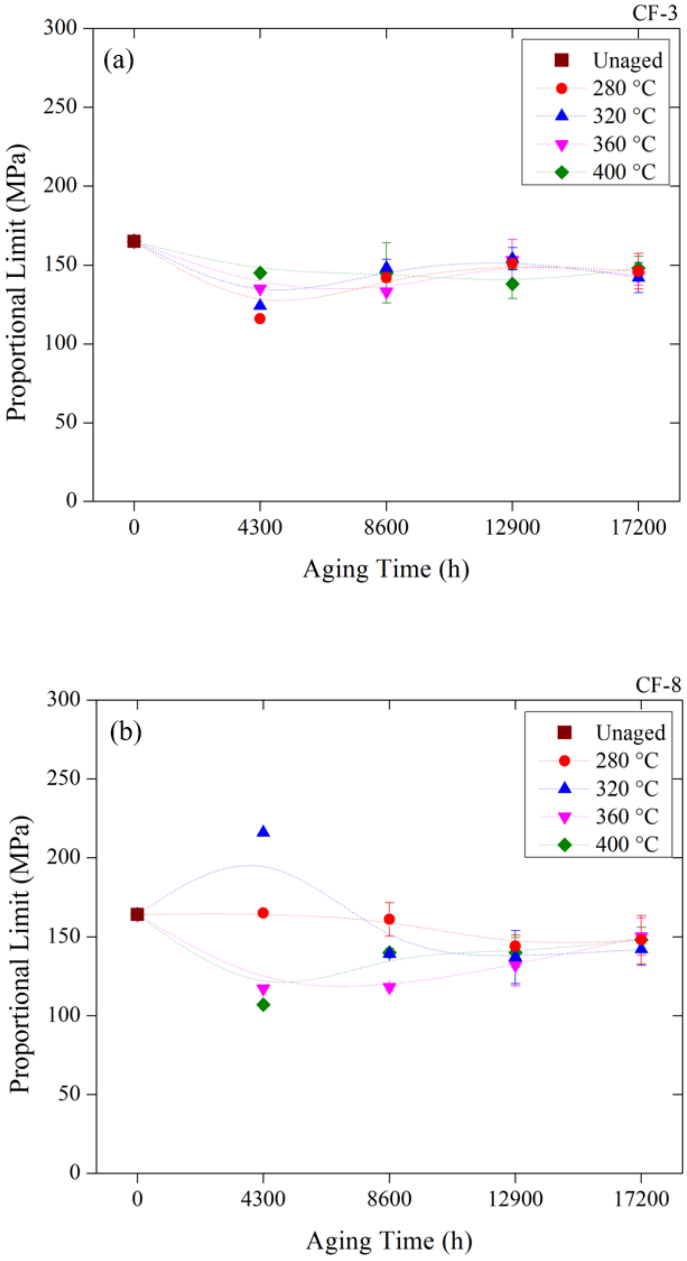

Fig. 14. Bulk tensile test results for proportional limit as a function of time and temperature for **(a)** CF–3 and **(b)** CF–8.

iii. Ultimate Tensile Strength

Unlike the yield strength of the bulk materials, the ultimate tensile strength (UTS) is dependent on each of the phases present in the microstructure. UTS is the strength corresponding to the maximum point on the engineering stress-strain curve, Figure 7, beyond which the engineering stress required to progress to each additional strain increment begins to decrease. This corresponds to the onset of necking in the specimen, and the true strain corresponds to the strain hardening exponent, *n*, of the true stress – true strain curve. The strain hardening behavior leading to this maximum is dependent on dislocation slip, which is characteristic of plastic behavior. Dislocation motion can be hindered, thus increasing strength, in a variety of ways. In this system, the presence and subsequent hardening of the island ferrite phase is expected to serve as a barrier to slip. Additionally, difference in composition leading to different solid solution concentrations and differences in phase structure can be expected to present non-negligible differences between the CF–3 and CF–8 steels.

The results for the UTS of the steels at every aging condition are listed in Table 3, and can be directly observed from the stress strain curves, Figure 11. First, from the comparison of the CF–3 and CF–8 UTS values prior to aging, it is evident that the CF–8 UTS of 570 MPa, is 7.5% higher than the CF–3 UTS of 530 MPa. This reflects the differences in C concentration in each steel. As will be presented in later chapters, the $M_{23}C_6$ carbide is shown to be present only in the CF–8, where the C concentration is three times higher than in the CF–3. The presence of carbides at phase boundaries is a known strengthening mechanism in stainless steels, and thus is the most likely cause of the larger UTS values. Carbon (C) interstitial atoms also can affect the strength of a steel and may have a smaller

role in the strengthening of the CF–8. It is also noted that since the unaged yield strength of the two steels are similar, the increased UTS in the CF–8 also indicates that the degree of strain-hardening in the unaged CF–8 is higher than in the CF–3.

Following aging, as can be expected with the changes in structure, the UTS of both steels changes as a function of time and temperature, Figure 13. As time and temperature increase, the results clearly indicate an increase in UTS in both steels. This corresponds to the increase in hardness, H, of the ferrite phase, Figure 20, which increases the amount of precipitation hardening – i.e. the energy required for dislocations to slip past/through the ferrite phase [108]. By 17,200 h, the UTS of CF–3 has increased to 535 MPa and 620 MPa for 280 °C and 400 °C, respectively. The UTS of CF–8 has increased to 585 MPa and 635 MPa, respectively. These results also indicate that the increase in UTS for CF–3 is greater than the increase in UTS for the CF–8 steel. In fact, following aging at 400 °C for 17,200 h, the UTS values are very similar between steels (~2.4%), indicating that the increase in UTS for CF–3 is much greater than that for CF–8 at the accelerated temperatures. Furthermore, only very slight increases are observed in the specimens aged at 280 °C for up to 17,200 h, whereas the largest changes are observed at the highest accelerated temperature of 400 °C. This is expected due to the faster diffusion kinetics resulting in microstructural changes, but may also be indicative of additional processes occurring during the aging evolution. This phenomenon, where the CF–3 properties at accelerated temperatures are evolving faster than those of the CF–8 is paralleled by the CVN results presented below.

iv. Ductility

Ductility values were calculated based on three different criteria: elongation at necking (%el_{UTS}), total elongation (%el), and reduction of area (%RA), Table 3. In the unaged condition, both steels exhibit considerable ductility by all measurements. For CF–3, the measured values are 61% total elongation and 83% reduction in area. For CF–8, the corresponding values are 60% total elongation and 80% reduction in area. Note that in the cases of the more ductile specimens early in the aging process, the strain at necking exceeded the limits of the extensometer, so these values are simply reported as ~45 %el_{UTS} or >45 %el_{UTS}. The aging trends for CF–3 and CF–8 %el and %RA are presented in Figure 15. Following aging at the D4 condition (400 °C, 17,200 h), the values are reduced relatively modestly in CF–3 to 55 %el and 65 %RA and in CF–8 to 50 %el and 70 %RA. There is more significant variation in results than was found for the strength properties of the steels, but specimens aged at operational temperatures generally demonstrate similar or less significant decreases in ductility than specimens aged at accelerated temperatures for each time step. This is consistent with other mechanical property results and with the expectations due to faster diffusion kinetics at higher temperatures.

The ductility measurements demonstrate that while a reduction in ductility is observed in following aging, the degree of ductility reduction is considerably less than the change in ductility of the CVN specimens. Due to the quasi-static nature of the tensile tests, the mobile dislocations are given time to nucleate, slip, and overcome obstacles, unlike in the relatively high strain rate CVN tests. Thus, even following aging at the accelerated temperatures up to two years, the tensile specimens still show a high degree of ductility, which is also reflected in analysis of the fracture surfaces presented in the next chapter.

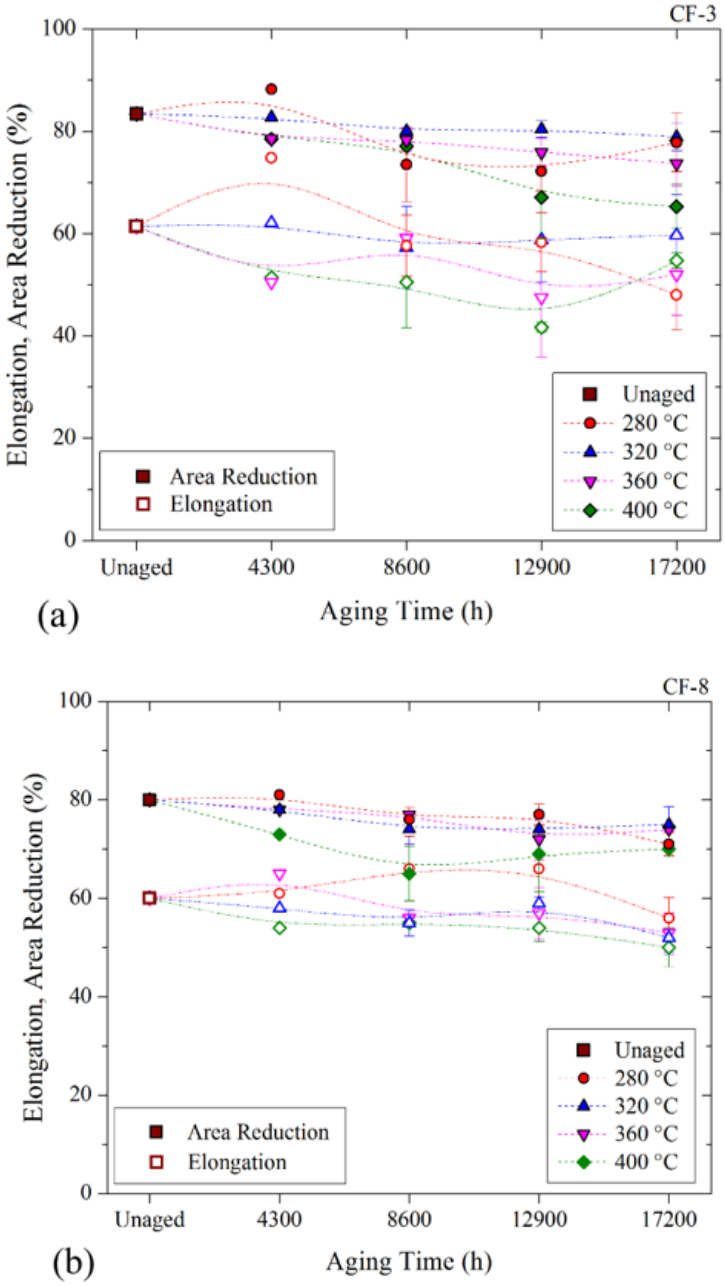

Fig. 15. Bulk tensile test results for ductility as a function of time and temperature for **(a)** CF–3 and **(b)** CF–8.

v. Elevated Temperature Quasi-static Tensile Testing

The previously discussed results provide a good degree of insight into the strengthening and embrittlement behavior of the steels with progressively higher thermal aging temperatures and times. The room temperature tests, however, do not fully account for the real operational conditions under which CF–3 and CF–8 components in nuclear power infrastructure would be subjected to outside stresses. Specifically, the temperature of the steels remains elevated during operation and would therefore be subjected to loads at these temperatures. Thus, quasi-static tensile tests were performed at 300 °C on a select subset (Table 4) of the CF–3 and CF–8 steels in order to assess their strength and behavior under operational conditions. The subset was chosen to incorporate the effects of both aging time and aging temperature to capture a representative dataset in the operational temperature range.

Table 4. 300 °C tensile properties for the DSS at following aging at selected conditions.

Test	**Aging Time**	**Aging Temp.**	**σ_y**	**UTS**	**e_{UTS}**
300 °C	***h***	***°C***	*MPa*	*MPa*	*mm/mm*
CF3 Unaged	-	-	174	383	0.31
CF3 A4	4300	400	175	388	0.33
CF3 B4	8600	400	182	393	0.28
CF3 C4	12900	400	181	394	0.27
CF8 Unaged	-	-	173	397	0.40
CF8 A1	4300	280	156	364	0.32
CF8 A2	4300	320	173	367	0.32
CF8 A3	4300	360	168	367	0.34
CF8 A4	4300	400	160	357	0.28
CF8 B2	8600	320	156	388	0.46
CF8 B4	8600	400	166	399	0.31
CF8 C2	12900	320	165	378	0.44
CF8 C4	12900	400	171	412	0.35

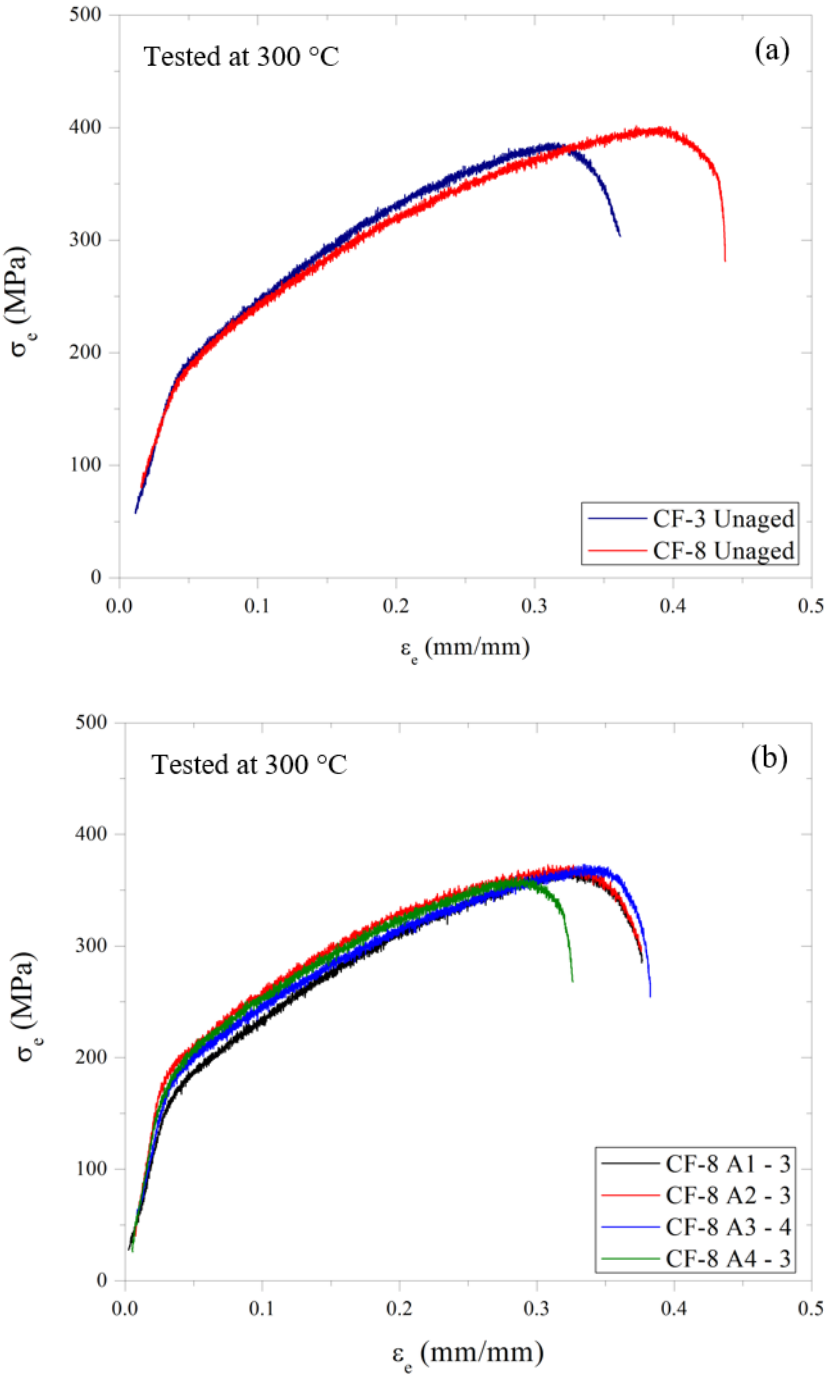

Fig. 16. Tensile stress-strain curves of **(a)** the unaged CF–3 and CF–8 steels and **(b)** a subset of CF–8 curves demonstrating the effect of aging on the tensile behavior at 300 °C.

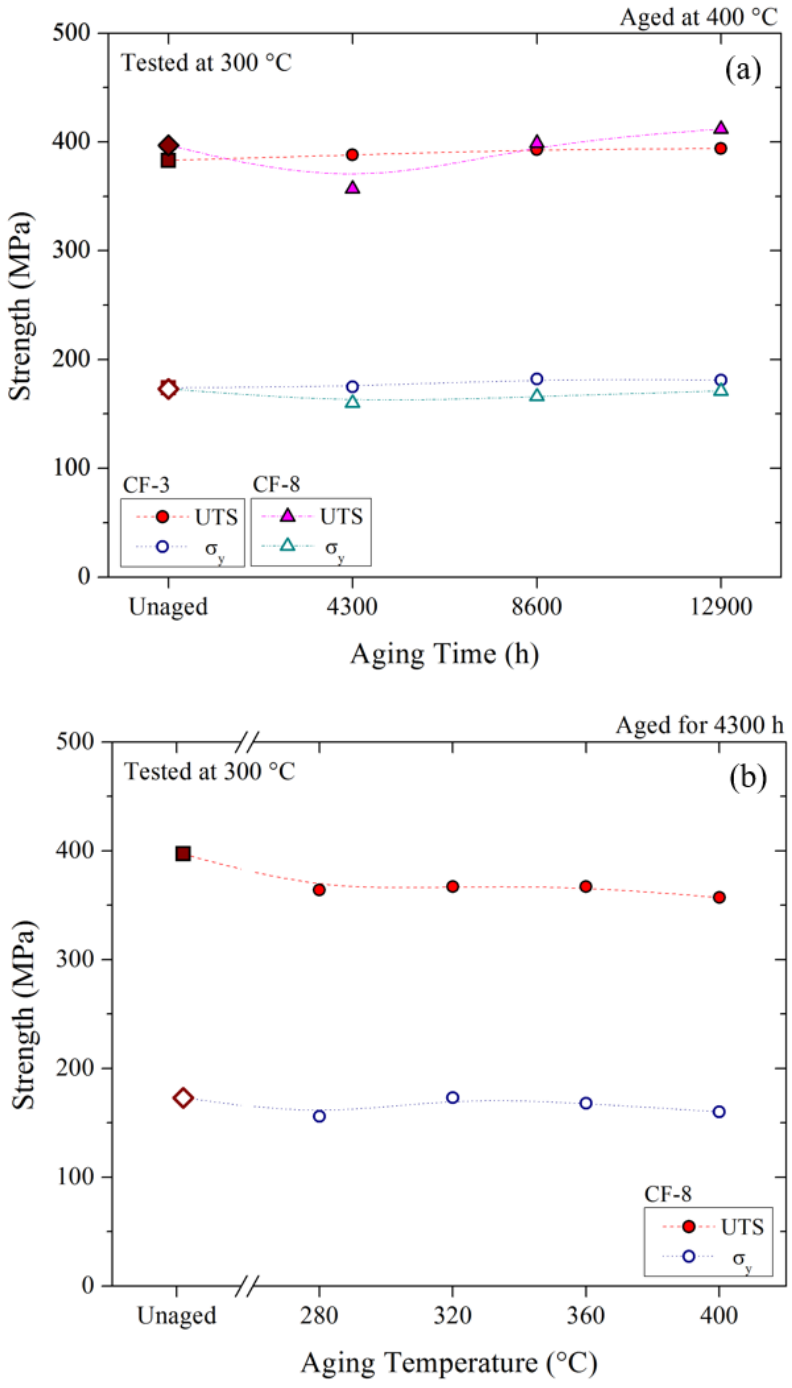

Fig. 17. Bulk tensile test results tested at 300 °C for ultimate tensile strength and 0.2% offset yield stress as a function of time for **(a)** CF–3 and CF–8 aged at 400 °C and as a function of temperature for **(b)** CF–8 aged for 4300 h.

The results for σ_y, UTS, and $\%el_{UTS}$ are listed in Table 4. As is demonstrated by the tensile stress-strain curves in Figure 16, there are limited clear trends of increasing strength and decreasing ductility with aging time at 300 °C. The initial unaged values for offset yield strength and UTS are 174 MPa and 383 MPa, respectively for CF–3, and 173 MPa and 397 MPa, respectively for CF–8. Plots of σ_y and UTS versus aging time, Figure 17, illustrate the effects of aging on tensile strength of the steels. It is apparent that there is little change in the yield strength of either steel resulting from aging under any condition when tested at 300 °C. There is an increase in the UTS to as much as 412 MPa following aging at 400 °C for 12,900 h in CF–8, but the increase is not as substantial at 300 °C as is found when tested at room temperature. In the case of the CF–3 steel, there is little significant increase in UTS, reaching only 397 MPa. Values measured for ductility follow similar trends. The initial unaged values for $\%el_{UTS}$ are 31% and 40% for CF–3 and CF–8, respectively. Though the aged values show a fair amount of variation, in general the trends are for fairly constant values, with the longest aged and highest temperature specimens tested in this manner (400 °C, 12,900 h) having measured $\%el_{UTS}$ values of 27% and 35% for CF–3 and CF–8, respectively.

In comparison to the room temperature tests, the tests performed at 300 °C show consistently lower strength as expected. The unaged values for σ_y are 61% (106 MPa) lower at 300 °C than at room temperature for CF–3, and 65% (113 MPa) lower for CF–8. Similarly, the unaged UTS values are 39% lower (150 MPa) for CF–3 and 43% (170 MPa) lower for CF–8. This is expected due the easier dislocation mobility in metals at elevated temperatures, and the ductility values are similarly reduced. Though the room temperature values are most directly relevant to the present study, as they clearly indicate the

fundamental embrittlement and strengthening of the steels following aging. However, the tensile measurements at 300 °C correspond more closely to the actual operational conditions of the steels in commercial nuclear systems.

vi. Charpy V-notch Impact Testing (CVN*)*

A classic test of embrittlement in metal alloys possessing a ductile-to-brittle transition (e.g. materials possessing a b.c.c crystal structure), is Charpy V-notch impact testing. The CVN tests occur at a reasonably high-strain rate, thus promoting typical brittle behavior at room temperature such as crack propagation over ductile void coalescence due to the limitations of dislocation slip at higher strain rates and lower temperatures. Thus, a decrease in dislocation mobility following aging is readily evident at CVN testing rates. Typically, austenitic stainless steels are more ductile than their ferritic counterparts [109], and the DSS investigated in this study are typically very ductile because of the ~85% – 90% by volume austenite matrix. Generally, as the microstructure evolves during thermal aging of the DSS and dislocation mobility is impeded by hardening of the b.c.c. ferrite island phase, the CVN values are expected to decrease significantly as a result of a shift in the ductile to brittle transition curve [73].

The room temperature Charpy impact results, Figure 18, show initial CVN values for both CF–3 and CF–8 that are characteristic of very ductile behavior. The maximum value that can be obtained by the impact test frame is 300 ft-lbs (407 J). The CF–3 unaged specimens absorb 289 ft-lbs (392 J) and the CF–8 unaged absorb 233 ft-lbs (317 J). Following thermal aging, the CVN results following thermal aging exhibit dependence of the embrittlement on aging time and a strong dependence on aging temperature. The accelerated aging temperatures, 360 °C and 400 °C, result in a large drop in the impact

energy absorbed at the first aging time of 4300 h (~0.5 years) to 162 ft-lbs (220J) and 108 ft-lbs (147 J), respectively. Similarly for CF–8 at these temperatures, the CVN values are 148 ft-lbs (200 J) and 112 ft-lbs (152 J), respectively. At subsequent aging time steps, the values continue in a slowly decreasing progression to 17,200 h, where the CVN values for CF–3 and CF–8 reach 58 ft-lbs (79 J) and 80 ft-lbs (108 J), respectively, for aging at 400 °C. Specimens aged at 400 °C for the CF–3 and CF–8 show a drop in CVN energy from greater than 300 J to less than 100 J during a time period of just two years, thus demonstrating the substantial effect of decomposition on the bulk mechanical behavior of the steels.

Following aging at operational temperatures, a drop in CVN values is also evident up to 17,200 h, but these aging temperatures do not result in the same initial large decrease in impact energy. Following aging for 4300 h at 280 °C and 320 °C, CVN values for CF–3 drop to 249 ft-lbs (338 J) and 253 ft-lbs (342 J), respectively, and values for CF–8 fall to 249 ft-lbs (338 J) and 181 ft-lbs (245 J), respectively. After the final aging step at 17,200 h, values for CF–3 fall further to 226 ft-lbs (306 J) and 184 ft-lbs (249 J), respectively. The CF–8 CVN values fall to 179 ft-lbs (243 J) and 143 ft-lbs (194 J), respectively. Hence, at these operational temperatures, the CVN data follows the generally decreasing trend of the accelerated temperatures but without the initial large drop at 4300 h. It can be reasonably expected that the drop in impact energy at more extended operational times should approach the drop achieved at shorter times at the accelerated temperatures. It is also noted that the unaged and operational CVN values for CF–3 are consistently higher than the corresponding values for the CF–8 steels, but following accelerated aging to longer times the CF–3 values are lower than CF–8, indicating a faster rate of embrittlement for CF–3.

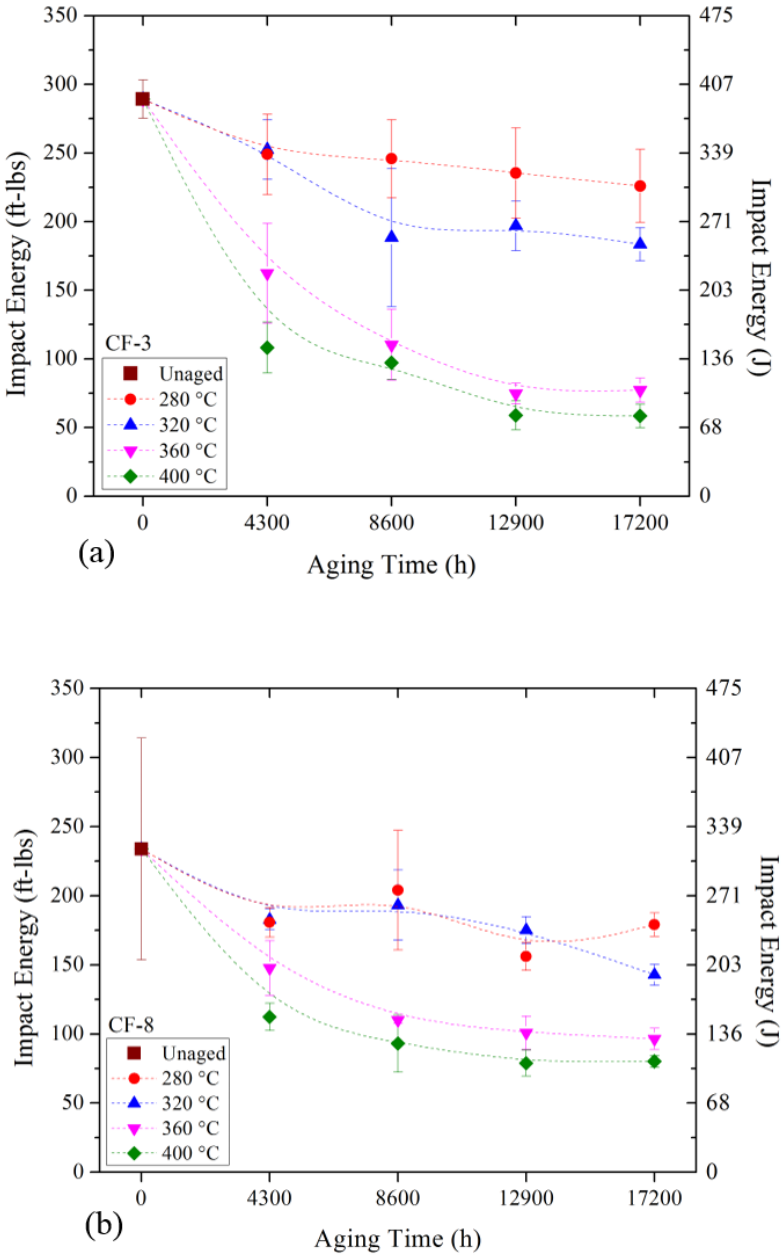

Fig. 18. Charpy V-notch impact testing results as a function of time and temperature for **(a)** CF–3 and **(b)** CF–8.

vii. Nanoindentation Modulus and Hardness

Nanoindentation testing was performed to evaluate the changes in the local ferrite and austenite properties occurring concurrently with the progression of general embrittlement of the bulk steels. Indents were performed measuring the elastic modulus and nanohardness values at each aging condition. The initial unaged condition shows that the elastic modulus, *E*, of the ferrite is larger than that of the austenite in both steels. The measured values of *E* for the unaged condition are 222 GPa and 204 GPa for ferrite and austenite, respectively, in CF–3, and 226 GPa and 211 GPa, respectively, in CF–8, and are consistent with previously reported results [98].

The trends in the elastic modulus data in each steel are presented in Figure 19. The elastic modulus for each phase remains approximately constant at both operational and accelerated temperature aging up to 17,200 h. Following aging at the highest temperature and longest time (400 °C for 17,200 h), the elastic moduli of the phases in CF–3 are measured as 220 GPa for the ferrite and 203 GPa for the austenite. The corresponding modulus values for CF–8 are 230 GPa and 201 GPa for ferrite and austenite, respectively. These values are nearly identical to those of the unaged specimens, even for the specimens with expectations of the most aging evolution, and the same trend holds true for each of the other aging conditions.

Measurements of nanohardness values, *H*, Figure 20, show that the hardness values of the ferrite and austenite are very similar in the unaged condition, 5.18 GPa and 4.95 GPa, respectively, for CF–3; and 5.28 GPa and 5.67 GPa, respectively, for CF–8. Similar to the *E* values, the *H* values in the austenite remain approximately constant during aging, though they appear to show more scatter in the data than that of the ferrite. The values for the

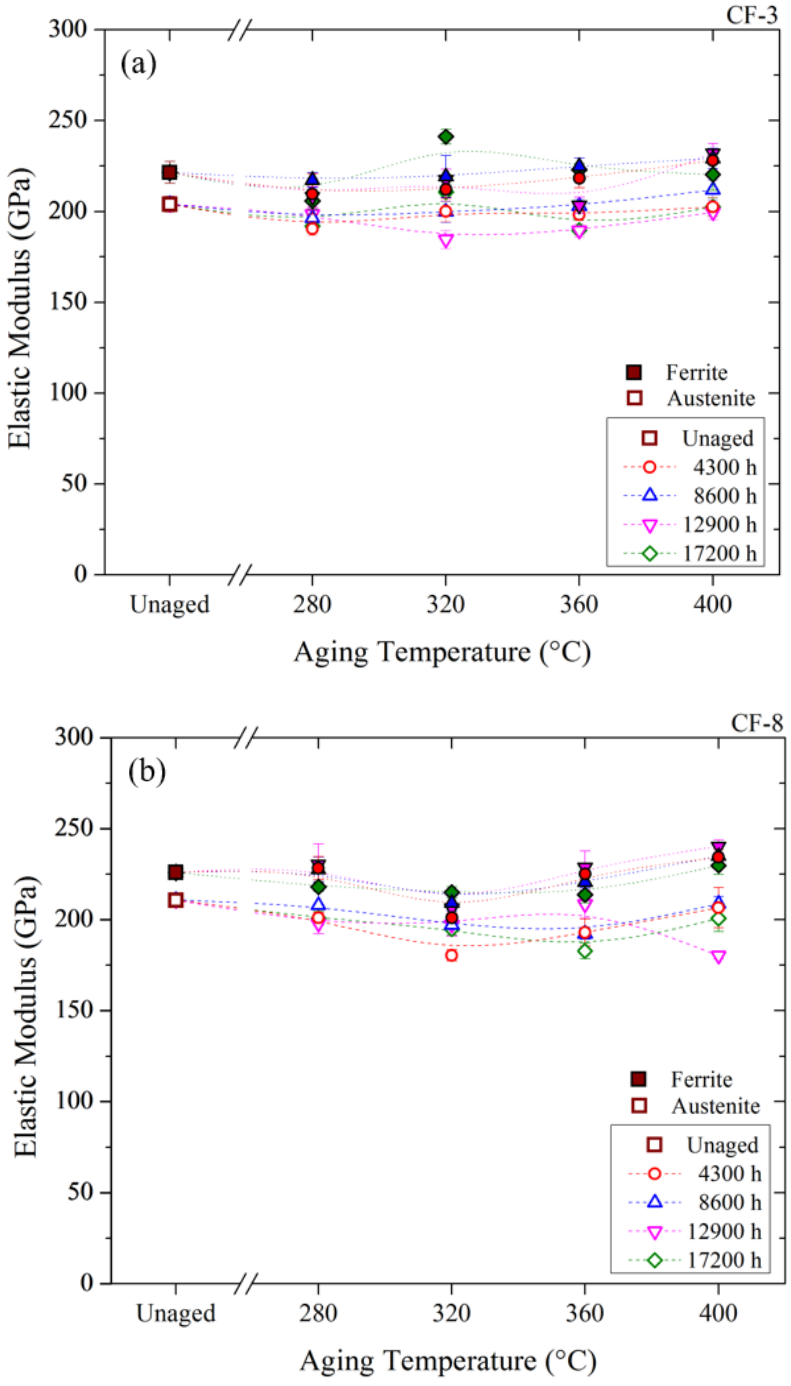

Fig. 19. Evolution of elastic modulus of the ferrite and austenite phases with aging temperature for each of the four aging times for **(a)** CF–3 and **(b)** CF–8 DSS.

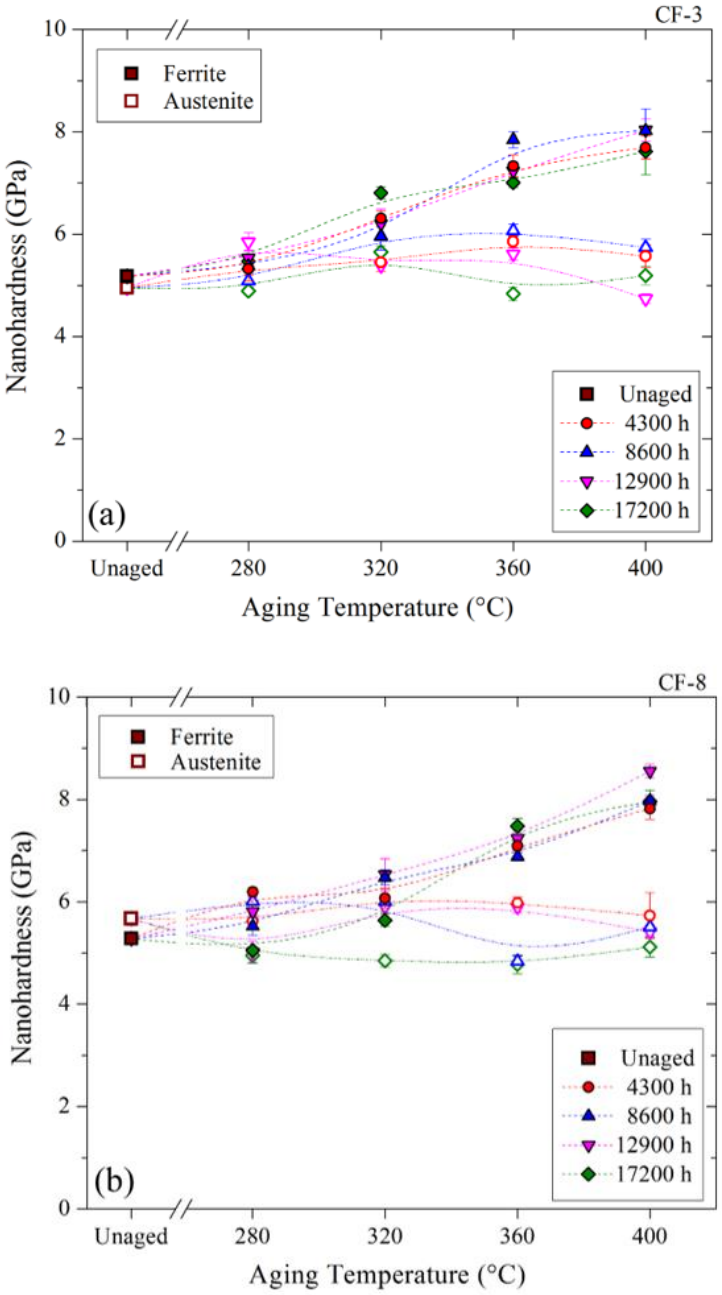

Fig. 20. Evolution of nanoindentation hardness of the ferrite and austenite phases with aging temperature for each of the four aging times for **(a)** CF–3 and **(b)** CF–8.

austenite phase of the specimens aged 400 °C for 17,200 h are 5.19 GPa and 5.12 GPa for CF–3 and CF–8, respectively. In contrast, the ferrite hardness values are observed to significantly increase during aging at accelerated temperatures, with increasing *H* values corresponding to increasing aging temperature and aging time. The values corresponding to the highest temperature and time in the ferrite phase are measured as 7.62 GPa and 7.96 GPa for CF–3 and CF–8, respectively, signifying hardness increases of 47% and 60%. However, at 280 °C, the ferrite nanohardness in either steel shows little change up to 17,200 h (5.47 GPa for CF–3, 5.02 GPa for CF–8), similar to the much smaller change in UTS and CVN values at this lower operational temperature. Furthermore, it is noted that unlike the bulk mechanical properties, the local ferrite hardness changes more in the CF–8 steel than in the CF–3, indicating that the microstructural changes within the ferrite may be occurring more significantly in the CF–8. These trends provide significant insight into the mechanisms of embrittlement in the steels, as discussed in the ensuing chapters.

B. Nanoindentation Investigation and Method Comparison

Bulk mechanical testing results demonstrate the effects of aging of the steels on the macro scale, and clearly show the progression of embrittlement that can occur during operation of CF–3 and CF–8 in nuclear power plant environments. However, the nature of the bulk testing means that only the cumulative effects of changes in the existing phases (and possible formation of new phases) in the microstructure are observable in the results. The nanoindentation technique, which is continually evolving and improving in scope and accuracy [110], allows for specific phases to be selected independently for testing – in this case the f.c.c. austenite matrix and b.c.c. ferrite islands – and evaluated mechanically for

elastic modulus and local indentation hardness. Due to the consistently evolving indentation analysis methods, the desired accuracy of elastic results for input into FEM models, and the desire to obtain similarly accurate results in the plastic deformation regime, an in-depth investigation into two common elastic methods and two common plastic methods has been performed.

i. EXPERIMENTAL METHODS

Results were analyzed by three different methods, with two goals in mind: 1. evaluate the aging evolution of the constituent duplex phases, allowing for comparisons between aging times, aging temperatures, phases, and compositions; and 2. provide experimental property data that can be used as input values in finite element method (FEM) models of the microstructure for improved confidence in the model results. Instrumented nanoindentation provides an established technique to measure the elastic properties of metals and alloys by permitting selection of a single-phase grain. The methods utilized here follow the most established method for determining elastic modulus and hardness, that produced by Oliver and Pharr [91], and a more recently developed method, based on the work of Dao, et al. [93]. Furthermore, two dimensionless analysis methods for determining the yield strength and strain hardening exponent based on data collected on real alloys systems is examined, the first of which is based again on the work of Dao, et al. and the second by Ogasawara, et al. [94]. Additional details regarding the background of these methodologies are available in Chapter I.

A load-displacement curve taken from a single indent in the austenite phase of the unaged CF–3 steel, Fig. 10(a), illustrates the response of the phase during the 3-step indentation process, Fig. 10(b). The responses of the ferrite and austenite phases in both

the CF–3 and CF–8 steels follow qualitatively similar trends, but vary quantitatively corresponding the variation in properties resulting from material differences and aging evolution (and embrittlement). The loading segment of the curve exhibits a parabolic shape following an approximately square relationship between load and depth, as discussed below. During the 10 s hold at maximum load, a slight increase in indentation depth is observed. The unloading curve segment decreases approximately linearly until the load approaches 0 μN. This initial linear part of the unloading curve is assumed to demonstrate entirely elastic behavior as it measures linear recovery of the phase during timed (15 s) removal of the Berkovich tip [93]. The unloading stiffness, *S*, which is used to determine the elastic modulus, *E*, of each phase in both steels at each aging time was calculated as the slope of the unloading segment of the curve from 100% of the maximum applied load, P_{max}, and fitting the following 67% of the curve (i.e. $1.00 \times P_{max}$ to $0.33 \times P_{max}$) applied in the Hysitron software by a linear least squares method [111]. The *S* value is utilized in the calculation of the reduced modulus, E^*, in both the Oliver and Pharr and Dao methods. The quantity E^* is a function of the elastic modulus and Poisson's ratio of the indenter tip, E_i and ν_i, and the modulus and ratio of each phase, *E* and *ν*, by the relationship: $E^* = \left[\frac{1-\nu^2}{E} + \frac{1-\nu_i^2}{E_i}\right]^{-1}$, where ν is assumed to be 0.29 for both phases in these CDSS [112]. The quantity E^* is related to the indentation load-displacement curve by a projected area of elastic contact, *A*, and the quantity *S*. Although the mean stiffness value of each phase is the same in both the Oliver and Pharr and Dao methods, the quantity *A* is obtained by different calculations leading to slightly different values of *A*, Table 5. An estimate of the elastic contact area is determined from the geometry of the Berkovich indenter and the maximum indentation depth, h_{max}, in the Oliver and Pharr method [91], and it is determined

by simultaneously solving a system of two equations for the quantities A and E^* in the Dao method [93].

Table 5. Mean values of the elastic parameters in the ferrite and austenite phases of the CF–3 and CF–8 CDSS derived from the individual load-displacement curves and by the Oliver and Pharr (O&P) and Dao methods.

Material		**Measured**			**Calculated**	
DSS	Phase	h_{max} *(nm)*	P_{max} *(μN)*	S *(μN/nm)*	$A^{O\&P}$ *($nm^2 \cdot 10^{-5}$)*	A^{dao} *($nm^2 \cdot 10^{-5}$)*
CF–3	Ferrite	173.9	3995.5	169.4	7.84	8.14
	Austenite	176.0	3995.5	166.0	8.02	8.50
CF–8	Ferrite	176.6	3994.3	171.1	8.11	8.50
	Austenite	176.0	3994.5	162.5	7.96	9.22

Results for the initial testing of the unaged specimens were determined for the elastic properties by both the Oliver and Pharr and Dao methods, and the results were compared. Further, the plastic properties were investigated by the Dao and Ogasawara methods with mixed success, and the validity of these models for the DSS in this study is discussed. The elastic results were used subsequently as inputs in the original FEM model of the duplex microstructure presented in Chapter V. Nanoindentation testing of the aged specimens was conducted at a later date using a different Berkovich tip. In order to maintain consistency of trends and data, the unaged specimens were re-tested during the aged specimen testing, and the updated unaged data applied to the discussion of nanoindentation trends. Furthermore, the values tested for this set used a range of 20% – 95% of the unloading slope to calculate the stiffness. These values were compared to the same data calculated by the range of 33% – 100%, and the difference was found to be insignificant for these

materials. The results related to the study of the aging trends of the nanoindentation properties are presented above in Chapter III, Section A.

ii. RESULTS

a. Elastic Methods Comparison

The values of the elastic modulus, *E*, for each phase in both the CF–3 and CF–8 CDSS are solved by the above equations and the results of the unaged tests are illustrated in Figure 21. Two methods, those formulated by Oliver and Pharr and by Dao, et al., were utilized to determine the elastic modulus and nanoindentation hardness of δ–ferrite and γ–austenite in CF–3 and CF–8. The measured values for the elastic modulus, *E*, by the Oliver and Pharr method are $E^{\delta}_{CF-3} = 185.3$ GPa, $E^{\gamma}_{CF-3} = 178.6$ GPa, $E^{\delta}_{CF-8} = 183.4$ GPa, and $E^{\gamma}_{CF-8} = 173.1$ GPa. The Dao method results for elastic modulus are $E^{\delta}_{CF-3} = 176.6$ GPa, $E^{\gamma}_{CF-3} = 166.7$ GPa, $E^{\delta}_{CF-8} = 175.3$ GPa, and $E^{\gamma}_{CF-8} = 153.6$ GPa. The mean elastic modulus calculated using the Dao method agrees to within 12% of the Oliver and Pharr method elastic modulus for the f.c.c. γ–austenite phase in both steels, and to within 5% for the b.c.c. δ–ferrite phase in both the CF–3 and CF–8. The mean elastic modulus calculated following Dao, et al. is consistently lower in value than the Oliver and Pharr method results by approximately between 8 and 20 GPa, Figure 21, which can be attributed to the different estimates of the projected contact area. In general, the elastic moduli determined by the two methods are in good agreement and the mean elastic modulus of the ferrite phase is greater than that of the austenite phase by approximately 10 GPa in both the CF–3 and CF–8 stainless steels. The elastic moduli results obtained in this investigation for the unaged duplex phases are also qualitatively similar to those reported by Gadelrab, et al. for a Uranus 50 duplex stainless steel, where values of 199.5 GPa and 183.9 GPa were obtained

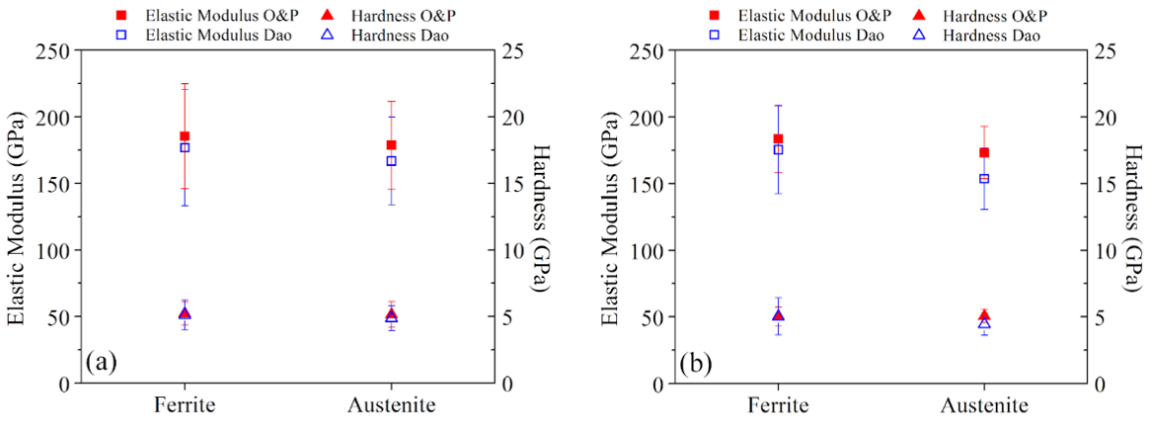

Fig. 21. Results for local elastic modulus and nanohardness for the unaged ferrite and austenite phases using both the Oliver and Pharr and Dao methods for **(a)** CF–3 and **(b)** CF–8.

for the ferrite and austenite phases, respectively, when applying the Oliver and Pharr method [79]. Guo, et al., however, reported slightly greater values of 216 GPa and 194 GPa for the ferrite and austenite phases, respectively, in a Z3CN20-09M duplex stainless steel, although their methodology for calculation was not specified [53]. Furthermore, the results obtained here indicating that the elastic modulus of the ferrite is greater than that of the austenite phase for CF–3 and CF–8 stainless steels are consistent with reported results in other duplex stainless steels.

Both the Oliver and Pharr and Dao methods have also been implemented to calculate the nanoindentation hardness, *H*, of the constituent duplex phases in both the CF–3 and CF–8 stainless steels, Figure 21. Nanoindentation hardness values are measured in the same manner as in Vickers microhardness tests, except that the indentation area is directly measured in the Vickers test and a projected area of contact is utilized the nano-hardness calculations. In both methods, the nanoindentation hardness is calculated directly from the

quantity P_{max} and the quantities $A^{O\&P}$ and A^{Dao}, Table 5. The calculated mean H values of both phases in both stainless steels are slightly greater than 5 GPa when using the Oliver and Pharr method. The Dao method calculations show that the mean hardness of the b.c.c. δ–ferrite phase for both steels agree closely with those from the Oliver and Pharr method. However, the mean nano-hardness values of the f.c.c. γ–austenite phase are between 5% and 10% lower than those calculated using the Oliver and Pharr method. Hence, it appears that there is a sensitivity to structure in at least one of these calculation methods.

Though the results for the elastic modulus indicate that ferrite is stiffer than austenite in these steels, the ferrite phase mean nanoindentation hardness is approximately the same as that of the austenite phase. The Dao method shows a greater difference in the quantity H between the two phases of the steels when compared to the Oliver and Pharr method. This could be demonstrative of a real physical difference in nanoindentation hardness between phases that the Dao method is better suited toward evaluating due to its use of experimentally measured data from a variety of metals and alloys in developing the dimensionless equations [93]. Alternatively, the difference could be caused by the nanoindentation data for the b.c.c. δ–ferrite phase falling within the dimensional analysis limitations of the Dao method better than the data from the f.c.c. γ–austenite phase. In contrast, the Oliver and Pharr method does not rely on calibration to experimentally measured data and is expected to apply more universally [91].

b. Plastic Properties by Dao and Ogasawara Methods

Values of the Dao representative stress, $\sigma_{0.033}$, were determined to be 3181 MPa and 3368 MPa for the δ–ferrite and γ–austenite phases, respectively, for the CF–3 steel. Comparable values of 3311 MPa and 3299 MPa were calculated for $\sigma_{0.0115}$ for the ferrite

and austenite phases, respectively, in the CF–3 steel by the Ogasawara method. Both methods obtained qualitatively similar results for the CF–8 steel. Tensile testing performed on the CF–3 and CF–8 steels determined the bulk UTS as 530 MPa and 570 MPa at greater than 45% elongation. For the Dao and Ogasawara methods, the predicted stresses at 3.3% and 1.15% plastic elongation, respectively, are nearly an order of magnitude larger than the bulk UTS values at greater than 45% elongation, which is not physically reasonable. When the representative stress values are used in the dimensionless equations to determine the quantities n and σ_y, the results reflect the fact that the values for the quantity σ_r are too large. In a majority of cases the equations failed to return a value for the quantity n between 0 and 1, Figure 22. The values that could be determined for the quantity n varied widely. Furthermore the calculation of yield stress is a function of both the representative stress and strain-hardening exponent, and thus σ_y could not be calculated when the quantity n was indeterminate. The σ_y values that could be calculated tended to be unreasonably high following the trend for high values of the quantity σ_r. In addition, the bulk yield strength of the unaged CF–3 and CF–8 stainless steels was measured as 280 MPa and 286 MPa, respectively, which is significantly lower than the few values that could be determined for the quantity σ_y of each phase. Guelorget, et al. reported a similar issue when applying the Ogasawara method to a 316L austenitic stainless steel, which has a composition similar to the austenite phase of the CF–3 and CF–8 DSS [87].

Based on these data, the equations were unable to return a solution for the quantity σ_y when using the Ogasawara method. Additionally, a study performed by Harvey, et al. that characterized a nanocrystalline Al-Mg alloy concluded that the Dao method reliably determined the elastic modulus, but finds that the results obtained for the quantities n and

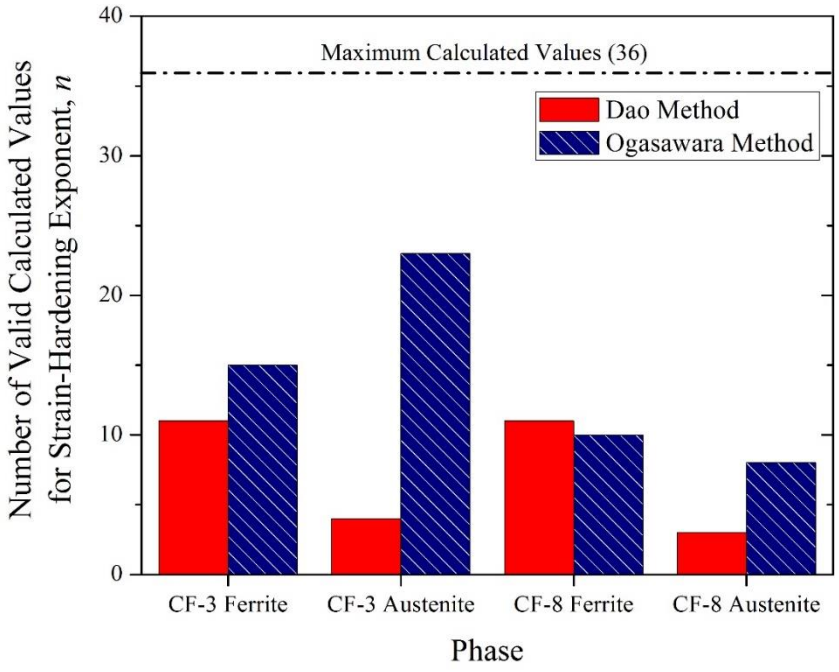

Fig. 22. The number of valid calculated strain-hardening exponent, n, values that are between 0 and 1 for both the ferrite and austenite phases in CF–3 and CF–8 using the Dao and Ogasawara methods. The maximum number of successfully calculated n values is 36 in each phase.

σ_y by both Dao and Ogasawara methods differ significantly between methods and vary considerably depending on the exact microstructure, thereby indicating that the difficulties in applying both methods are not limited to stainless steels [113]. The Dao method was, however, successfully implemented in the aforementioned nanoindentation study of a Uranus 50 duplex stainless steel and reasonable values for the yield stress and power-law strain-hardening exponent were determined [79]. These varying reports could be a result of several possible deviations from the region of applicability of the Dao and Ogasawara methods for some alloys, which include validity for Dao when $n \leq 0.3$ or $0.3 < n \leq 0.5$ and $\frac{\sigma_y}{E^*} < 0.03$ and for Ogasawara when $0 \leq n \leq 0.5$ and $3 \leq \frac{\bar{E}}{\sigma_r} \leq 3300$ (where $\bar{E} =$

$\frac{E}{1-\nu^2}$). The authors state that the solutions outside of these parameters are subject to greater variation and there exists the possibility of a non-unique solution. Furthermore, it is possible that the b.c.c. δ–ferrite phase and the f.c.c. γ–austenite phase in the CF-3 and CF-8 CDSS do not follow power-law strain-hardening behavior. Since alloys that follow power-law behavior were used to calibrate the dimensionless functions in the aforementioned methods, alloys that deviate from power-law behavior may not result in an accurate value for the quantity σ_r and thus the quantities n and σ_y would be indeterminate or not physically real.

IV. MICROSCOPY AND MICROSTRUCTURE

A. INTRODUCTION

The previous chapter has established experimentally several changes in the deformation behavior of the duplex stainless steels that occur during thermal aging. It is fundamental, however, that mechanical behavior is directly influenced by the structure of a material. Thus, in order to determine the origins of the mechanical behavior changes, the corresponding structural evolution of the steels must be observed and analyzed. There are a huge variety of potential techniques that are available for such studies, but a few have been chosen as optimal to characterize the CF–3 and CF–8 steels in this work.

In general, review of the extant literature and common understanding of these materials systems shows that observation of multiple length scales is crucial to capture the full extent of structural evolution. For example, the duplex phases (austenite and ferrite) are present on the micron (μm) scale, $M_{23}C_6$ carbides in these steels tend to be on the order of hundreds of nanometers (nm), and spinodal decomposition and G-phase formation in the ferrite tend to be below twenty nanometers in scale, especially at lower aging times and temperatures [37], [67]. Furthermore, identification of phases and important structural data (e.g. crystal structure, lattice parameter, etc.) are best obtained by structural observation, such as diffraction techniques, while decomposition and other forms of elemental segregation are best observed via compositional analysis. With information of both of these types, valuable information regarding the structural changes and associated kinetics can be carefully analyzed, and important information regarding the mechanisms of mechanical behavior evolution can be discerned.

In this work, a combination of multi-scale microscopy techniques, including optical microscopy (OM), scanning electron microscopy (SEM), and transmission electron microscopy (TEM) have been utilized for conventional visual analysis of the structure of the steels at various stages of thermal aging. Furthermore, selected area electron diffraction (SAED) available through TEM is utilized to analyze multi-scale structural details, electron backscatter diffraction (EBSD) analysis is used to investigate crystallographic orientation, and energy dispersive spectroscopy (EDS) is performed for basic compositional analysis. Additionally, high resolution nano-scale compositional analysis by atom probe tomography (APT) was performed as a part of this project to characterize elemental segregation near the phase boundaries. New analysis methods were developed to quantify the extent of spinodal decomposition of the ferrite phase and the formation of G-phase precipitates. The APT experiment and analysis were performed primarily by Ms. Sarah Mburu of the University of Maryland and Dr. Daniel Perea of Pacific Northwest National Laboratory. The detailed description of this work can be found in other published work [37], [50], [114], but some results are presented here as they aid significantly to the analysis and discussion of the structure-property relationships of the CF–3 and CF–8 steels.

B. Specimen Preparation and Experimental Methods

i. Optical Microscopy

Metallography and optical (light) microscopy was performed on the CF–3 and CF–8 specimens before aging in order to observe and analyze the basic duplex microstructure. A subset of aged specimens was also prepared and observed by the same methodology to evaluate larger scale changes in microstructure volume fractions or morphology.

CF–3 and CF–8 specimens from various aging conditions were cut into blanks for machining and further reduced to approximately 10 mm × 10 mm × 3 mm. Reduced specimens were cold mounted in epoxy for metallographic examination. The specimens were ground (180, 320, 600, and 1200 grit paper) and polished with colloidal alumina using standard metallographic preparation procedures to 0.3 μm or 0.05 μm surface finish. Chemical etching was performed using Kalling's reagent No. 1 (33 mL HCl, 33 mL ethanol, 33 mL water, 1.5 g $CuCl_2$) at room temperature to reveal the duplex microstructural features. Optical micrographs were obtained using a Buehler ViewMet Inverted Metallograph equipped with a digital recording device.

The volume percentage (fraction) of the unaged b.c.c. δ–ferrite and face-centered cubic (f.c.c.) γ–austenite phases in the microstructure were determined employing three different methodologies: (1) manual point counting in accordance with the ASTM E562-11 standard, (2) digital counting of pixels using the Image–J version 1.50b software in accordance with the ASTM E1245-03 standard, and (3) the Schoefer diagram based on composition in accordance with the ASTM A800-14 standard [18], [19], [115]. The percentages determined by methods (1) and (2) were measured by utilizing 20 optical micrographs from each steel as specified in the standards. Volume percentages of aged specimens at 280 °C and 400 °C to 17,200 h were evaluated by method (1) to investigate any potential change in the ferrite volume percentage during thermal aging.

ii. Scanning Electron Microscopy – Fractography

Scanning electron microscopy (SEM) is a technique utilizing the effects of an electron beam interacting with a specimen to image the surface morphology. This technique has a much better resolution than traditional optical microscopy, with modern

instruments typically capable of imaging on the order of 10 nm or smaller. In this study, SEM functionality has been utilized to investigate the fracture morphology of the fracture surfaces of failed tensile and CVN specimens to gain insight into the deformation behavior and failure modes of the steels. This technique allows for imaging of complex surface morphologies and provides valuable data related to phase and elemental makeup due to contrast differences related to the electron scattering.

SEM was performed on the fracture surfaces of CF–3 and CF–8 steels of selected aging conditions following failure by CVN testing and tensile testing. A Tescan XEIA Plasma FIB/SEM operating in SEM mode (located in the UMD AIMLab) was used to image each fracture surface. All fractographs were collected in field mode at 10 kV.

SEM fractography was performed on a selected subset of specimens from different aging conditions in an effort to obtain a representative sample set consisting of various microstructures. The primary focus of the fractography results for both the tensile and CVN fracture surfaces is placed on unaged specimens and specimens aged at the lower and upper bound temperatures (280 °C and 400 °C, respectively) for 17,200 h. Given what is known about the microstructures and presented here in this chapter, this allows for comparison of fracture behavior between specimens containing un-decomposed ferrite (unaged) vs. decomposed ferrite (aged), presence of G-phase (400 °C) vs. no confirmed G-phase (280 °C), and presence of carbides (CF–3) vs. no carbides (CF–8).

iii. Electron Backscatter Diffraction

Electron backscatter diffraction (EBSD) is an electron beam technique closely related to SEM. When a scanning electron beam is incident upon a sample, some of the electrons are backscattered. For electrons backscattered near the Bragg angle of the

material, electron diffraction can occur, resulting in crystal orientation information being transmitted in the form of Kikuchi pattern [116]. Special EBSD detectors implemented in and SEM are able to capture the diffracted backscattered electrons, allowing for a scanning beam to be analyzed to determine the crystallographic information of the material. Hence, important structural information and (due to the scanning beam) detailed crystallographic maps can be generated, reflecting important structural information such as orientation, misorientation, plastic deformation, etc. [116], [117]. The fundamental output of the EBSD scans are orientation maps based on the inverse pole figure (IPF) technique, providing detailed surveys of the distributions of the phase/grain orientations within the microstructure.

In this study, the crystallographic orientations and microstructure misorientation distributions resulting from tensile plastic deformation of the unaged γ–austenite and δ–ferrite phases were investigated by the EBSD technique. This experiment was performed at Los Alamos National Laboratory using an FEI Inspect Field Emission Gun (FEG) scanning electron microscope (SEM) instrument equipped with a TSL EBSD detector. Specimens taken from the transverse section of the tensile specimen gauge lengths were prepared by standard metallographic techniques followed by jet electropolishing using a solution of 5 vol.% perchloric acid in methanol at approximately –30 °C with an applied voltage of 23 V. Experiments were performed on a 70° pre-tilted holder at an accelerating voltage of 20 kV and aperture size of 50 μm. The EBSD scans were performed at two different magnifications with a scanned area of either ~0.25 μm × ~0.5 μm or ~0.75 μm × ~1.5 μm and a step size for data collection of 0.4 μm and 1.2 μm, respectively. Data analyses were performed using TSL OIM software.

Kernal average misorientation (KAM) studies were conducted using an exclusion angle of 5° and considering the second nearest neighbors. The KAM analysis technique provides inside into the misorientation of the crystal structure at a given point, as defined by the scanned kernel of the defined size. The orientation is then compared with a pre-defined number of nearest neighbors in order to determine the local misorientation, or difference in the orientation from the local average orientation. This technique regarding the local misorientation is a good indicator of the level of plastic deformation, and can be correlated to plastic strain and dislocation density [116]. KAM studies performed here on the deformed tensile specimens elucidate local trends in the deformation behavior during plastic loading, and can be used to find areas of high and low strains, identify differences between steels, and additional evidence related to deformation of the duplex structures.

Grain orientation spread (GOS) analyses were performed using a 5˚ tolerance angle. Similarly to the KAM maps, the GOS maps provide a measure of the crystallographic misorientation of the microstructure. However, instead of providing a local measured based on nearest neighbors, the GOS maps relate the average misorientation within an entire grain. The average crystallographic orientation of a grain is calculated, and the misorientation of each kernel with respect to the average is calculated, with the averaged misorientation of the entire grain resulting in the GOS map. This shows a less localized visualization of plastic strain than is observed in the KAM maps, but the GOS maps show clearly which grains during deformation show a greater extent of plastic deformation (and dislocation density), and which undergo less deformation. The resulting GOS maps can be usefully compare to the orientation maps to determine the various effects of orientation anisotropy and the contribution to the deformation of the composite phases. This also

provides similar maps to those obtained computationally by FEM of the real microstructures, as presented in Chapter V.

iv. Transmission Electron Microscopy

In order to effectively study the structure of crystalline materials on length scales smaller than ~5 μm, transmission electron microscopy (TEM) is commonly used. TEM, as compared to scanning electron microscopy (SEM) has a much better resolution – in the case of current instrumentation, even individual atoms can be resolved in certain cases [118]. Additionally, in comparison with techniques like atom probe tomography (APT), TEM lacks the compositional data available from APT but is able to provide crystallographic information like crystal structure, lattice parameter, and grain orientation that APT cannot discern. Hence, TEM is a valuable resource for locating and identifying b.c.c.-ferrite and f.c.c.-austenite regions, carbides at the phase-interfaces, and other structurally mature phases that may be present in the duplex stainless steel micro- and nano-structures, such as G-phase precipitates.

Unlike SEM, where the scattered electrons from the specimen surface are collected for observation, TEM collects the electrons transmitted through the specimen. Thus, the prepared specimens must be very thin, generally <100 nm, in order to transmit enough electrons to achieve a clear image. To achieve this, specimens for TEM study were cut into thin slices approximately 1 cm x 1 cm x 0.5 mm and cold-mounted using a quick-set acrylic. They were then mechanically ground using 320 grit and 600 grit grinding paper until thinned to ~100-200 μm and polished to 1200 grit to achieve a smooth surface on both sides. After removing the polished sample from the mount, 3 mm diameter disks (standard for conventional TEM specimen holders) were mechanically punched out from the thinned

specimens. The disks were then mounted on the surface of sample holders using crystal bond and further polished by conventional methods to ~25-40 μm thickness.

In the unaged condition, single jet electropolishing was utilized following mechanical thinning. CF–3 and CF–8 samples were mounted in a SouthBay Model 550 Electrolytic Jet Thinning Instrument and polished at a voltage of 20 V for ~10-12 minutes using an electrolyte solution of 10% perchloric acid in acetic acid cooled using dry ice. The specimen was inverted every 2-3 minutes to allow approximately equal etching on both sides by the single jet. Following thinning by electropolishing, final thinning to perforation and cleaning was performed using a Fischione model 1010 ion milling system. Specimens were milled at 5 kV and 3 mA at an angle of 15 ° until a perforation was observed, then cleaned at 2.5 kV and 2 mA at an angle of 8° for 10 minutes.

Following aging, a subset of conditions was chosen for TEM analysis: CF–3 and CF–8 aged at 280 °C for 17,200 h, at 360 °C for 17,200 h, and at 400 °C for 8600 h and 17,200 h were selected for TEM analysis. Due to a variety of factors including a change in the etch rate of the ferrite phase and equipment availability, aged specimens were prepared by dimpling instead of electropolishing. After mechanical thinning as described above, each specimen was mounted with crystal bond and thinned using a brass dimpling wheel as part of a SouthBay model 515 dimpling system. Each specimen was dimpled for ~25 minutes using 0.3 μm diamond paste until a distinct dimple was formed. Following dimpling, specimens were milled in the Fischione model 1010 ion mill at 5.5 kV, 7 mA, and 15 ° angle until perforation. Following perforation, specimens were cleaned in the ion mill at 2.5 kV, 3 mA, and 10 ° for 10 minutes and then 2 kV, 2 mA, and 8° for 5 minutes. Additionally, one specimen (CF–8 aged at 400 °C for 17,200 h) was prepared

professionally by FEI in Portland, OR using state-of-the-art focused ion beam (FIB) techniques.

Two TEMs were utilized in this work, both located in the Advanced Imaging and Microscopy Laboratory (AIMLab) at the University of Maryland. The primary microscope used for conventional imaging, electron diffraction, and bright/dark field imaging is a JEOL JEM 2100 LaB_6 TEM. A JEM 2100 FEG (field emission gun) TEM was also utilized for slightly higher resolution and energy dispersive x-ray spectroscopy (EDS) capabilities.

v. Atom Probe Tomography

Atom probe tomography (APT) is a state-of-the-art technique providing data of individual atomic distributions within a small region of a specimen. Conical specimen tips are evaporated using voltage or laser pulses, and a sensitive detector is used to determine the composition (by mass/charge ratio) and location of the elemental mass within the 3-D sample. Thus, an extremely detailed 3-D compositional reconstruction can be created. Modern APT techniques can successfully detect millions of atoms for reconstruction, providing unprecedented insight into the atomic distributions within a material [119]. As part of this characterization study, Mburu, et al. have performed comprehensive APT studies of the ferrite/austenite interfaces of the CF–3 and CF–8 steels, providing in-depth details of the elemental distributions within the ferrite, austenite, carbides, and boundaries of the steels, as well as stepwise documentation of the progression of diffusional processes occurring during thermal aging [50]. While no real structural data is obtained by APT, the compositional maturation of spinodal decomposition and G-phase can be clearly observed by this data. These data are extremely relevant to the evolution of the mechanical properties of the steels, and provide insight into the mechanisms of embrittlement.

Specimens for APT analysis were first fabricated using an FEI Helios Nanolab 600 dual beam FIB/SEM instrument following standard lift-out and sharpening procedures. Atom probe tomography was performed using a CAMECA Local-Electrode Atom Probe (LEAP®) 4000 instrument at the Environmental Molecular Sciences Laboratory (EMSL) at Pacific Northwest National Laboratory (PNNL) [120]. APT data were collected along the ferrite/austenite phase interfaces for each aging condition using a specimen tip base temperature of 40 K, DC voltage pulse ratio of 15%-20%, evaporation rate of 0.015 ions per pulse, and background pressure of 10^{-11} Torr (10^{-8} Pa). Data analysis of the ferrite included analysis of spinodally decomposed α and α' domains to determine the mean wavelength (domain size) and mean amplitude (degree of concentration fluctuation) following procedures developed by Mburu, et al. [37], [114], and the full details of the methodology are presented in those texts.

C. Results

i. Optical Microscopy

An optical micrograph of the CF–3 steel, Figure 4, illustrates an example microstructure consisting of a network of island-shaped *δ*–ferrite phase (dark color) in the continuous *γ*–austenite matrix phase (light color). The microstructure of the CF–8 steel has a qualitatively similar appearance to that of the CF–3 steel. This microstructure is consistent with those reported in the literature of a steel with a composition similar to CF–8, with a ferrite content of less than 20% by volume [6], [121].

The b.c.c. *δ*–ferrite phase volume percentage of the CF–3 steel is greater than the CF–8 steel when measured by the three aforementioned methods, Table 6. By the manual point counting method, the CF–3 steel ferrite volume percentage is 11.5 ± 1.1 vol.% while that

Table 6. Ferrite volume percentage in the unaged CF–3 and CF–8 duplex stainless steels as determined by three different methods.

	Ferrite Volume Percentage (%)		
Steel	Manual Point Counting [ASTM E562-11]	Digital Counting of Pixels [ASTM E1245-03]	Schoefer Diagram [ASTM A800-14]
CF–3	11.5 ± 1.1	12.1 ± 1.0	18 ± 6.3
CF–8	9.1 ± 0.9	10.0 ± 0.4	14 ± 4.8

of the CF–8 steel is 9.1 ± 0.9 vol.%. The digital counting method results in a ferrite volume percentage of 12.1 ± 1.0 vol.% for the CF–3 steel and 10.0 ± 0.4 vol.% for the CF–8 steel. The Schoefer method based on the CF–3 and CF–8 nominal compositions predicts ferrite volume percentages of 18 ± 6.3 vol.% and 14 ± 4.8 vol.%, respectively. The Schoefer diagram is based on Cr equivalency and Ni equivalency values, where the magnitude of each element's contribution to the b.c.c.-forming chromium equivalency term, Cr_{eq}, and f.c.c.-forming nickel equivalency term, Ni_{eq}, affect the formation of either the δ–ferrite or the γ–austenite phase, respectively [114]. The CF–3 steel has a Cr_{eq}/Ni_{eq} ratio of 1.34, whereas the CF–8 steel has a ratio of 1.25, resulting in a larger expected ferrite volume percentage in the former. Since the Schoefer diagram is not specific to the CDSS used in this study and is based on generalized composition and element equivalency data of many duplex stainless steels, the values measured by the manual point counting method and the digital counting of pixels method are likely more accurate. The directly measured values are, however, within the range determined by the Schoefer diagram for both steels.

Cursory investigations of the volume fractions of the aged specimens at the highest temperature and longest aging time (400 °C, 17,200 h) were performed by manual point

counting methods. These calculations determined that the volume percentages of the aged specimens did not significantly vary during thermal aging up to 17,200 h, showing only variation by ±2 % from the unaged specimens. Qualitative evaluation of the microstructures also shows no readily evident changes in morphology or distribution of the duplex phases on the micron scale, so characterization focus was applied to the sub-micron scale, as in the following sections.

ii. Scanning Electron Microscopy – Fractography

Fractography was performed on the fracture surfaces of failed standard cylindrical tensile specimens and failed standard Charpy v-notch (CVN) impact specimens using SEM. Specimens representing the unaged condition and aged for 17,200 h (~2 years) at 280 °C and 400 °C were selected for CF–3 and CF–8 steels with both tensile and CVN failures to compare the evolution of the fracture behavior after aging at operational and accelerated temperatures at low and high strain rates, respectively. Furthermore, tensile specimens aged at 360 °C for 4300 h and 8600 h were selected for both steels to compare the effects of G-phase formation from the unaged condition.

Analysis of the fracture surfaces of the unaged tensile, Figure 23, and CVN, Figure 24, specimens reveals overwhelmingly ductile behavior in both steels. The fractographs exhibit widespread and fairly uniform dimples and corresponding columnar complements, indicative of void creation and coalescence representative of a ductile fracture mode. Additionally, there are some larger fissures present, likely corresponding to void coalescence and resulting crack propagation. The presence of a fairly high volume fraction of particularly deep dimples suggests particulate initiation and promotion of void coalescence that likely corresponds to the presence of the ferrite phase islands within the

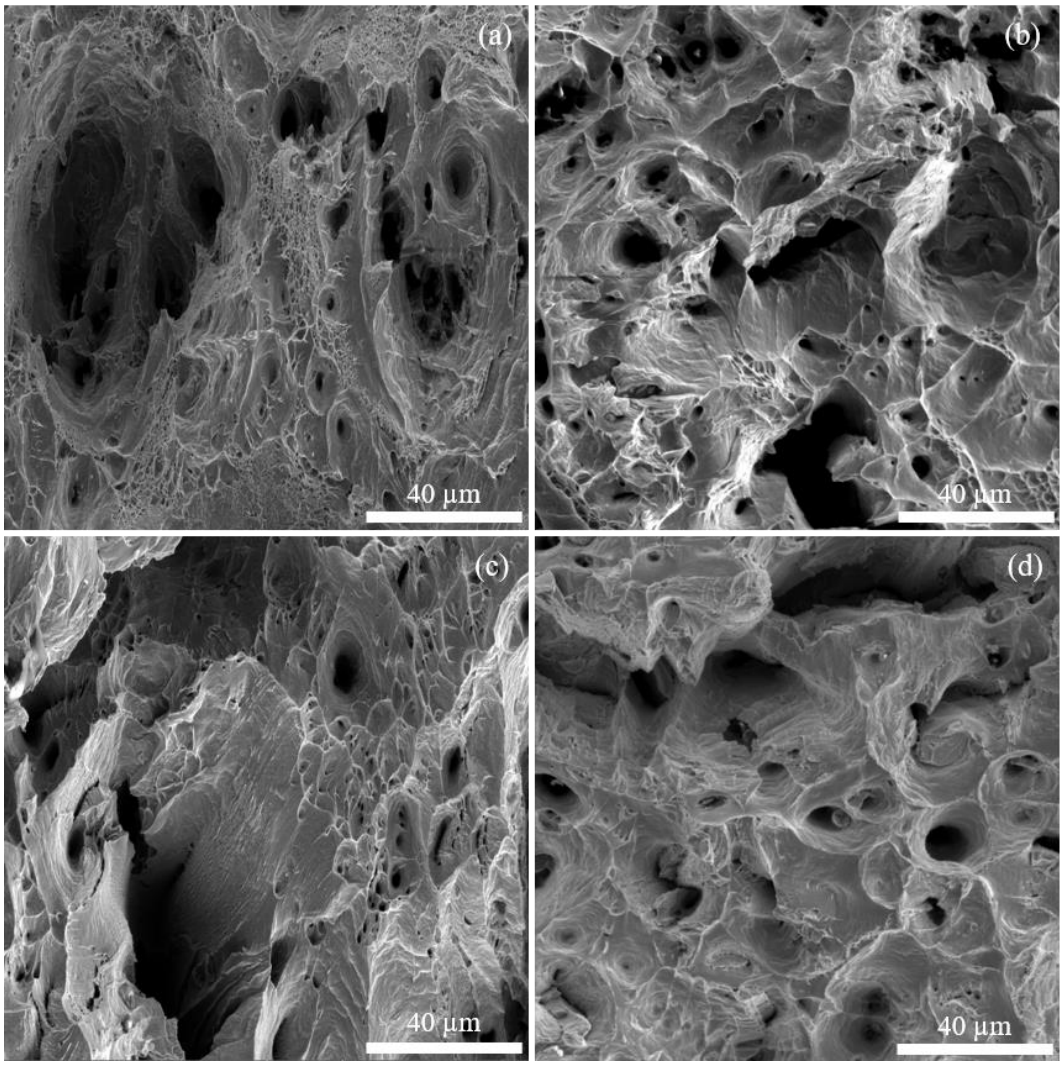

Fig. 23. SEM fractographs of tensile specimens at 2 kx magnification comparing the fracture behavior in CF–3 in the **(a)** unaged condition and **(b)** aged at 400 °C for 17,200 h; and CF–8 **(c)** unaged and **(d)** aged at 400 °C for 17,200 h.

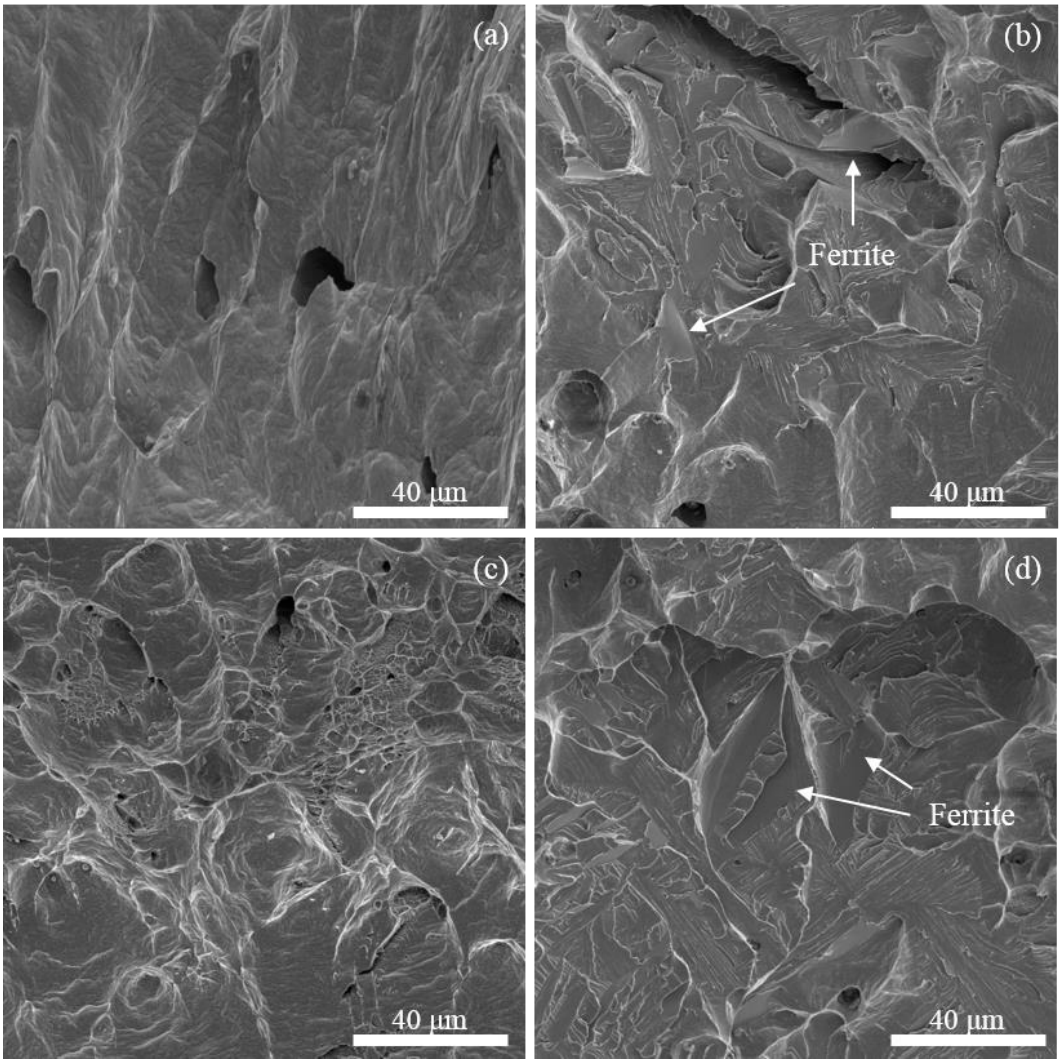

Fig, 24. SEM fractographs of CVN specimens at 2 kx magnification comparing the impact fracture behavior in CF–3 in the **(a)** unaged condition and **(b)** aged at 400 °C for 17,200 h; and CF–8 **(c)** unaged and **(d)** aged at 400 °C for 17,200 h. Following aging, exposed ferrite facets are visible.

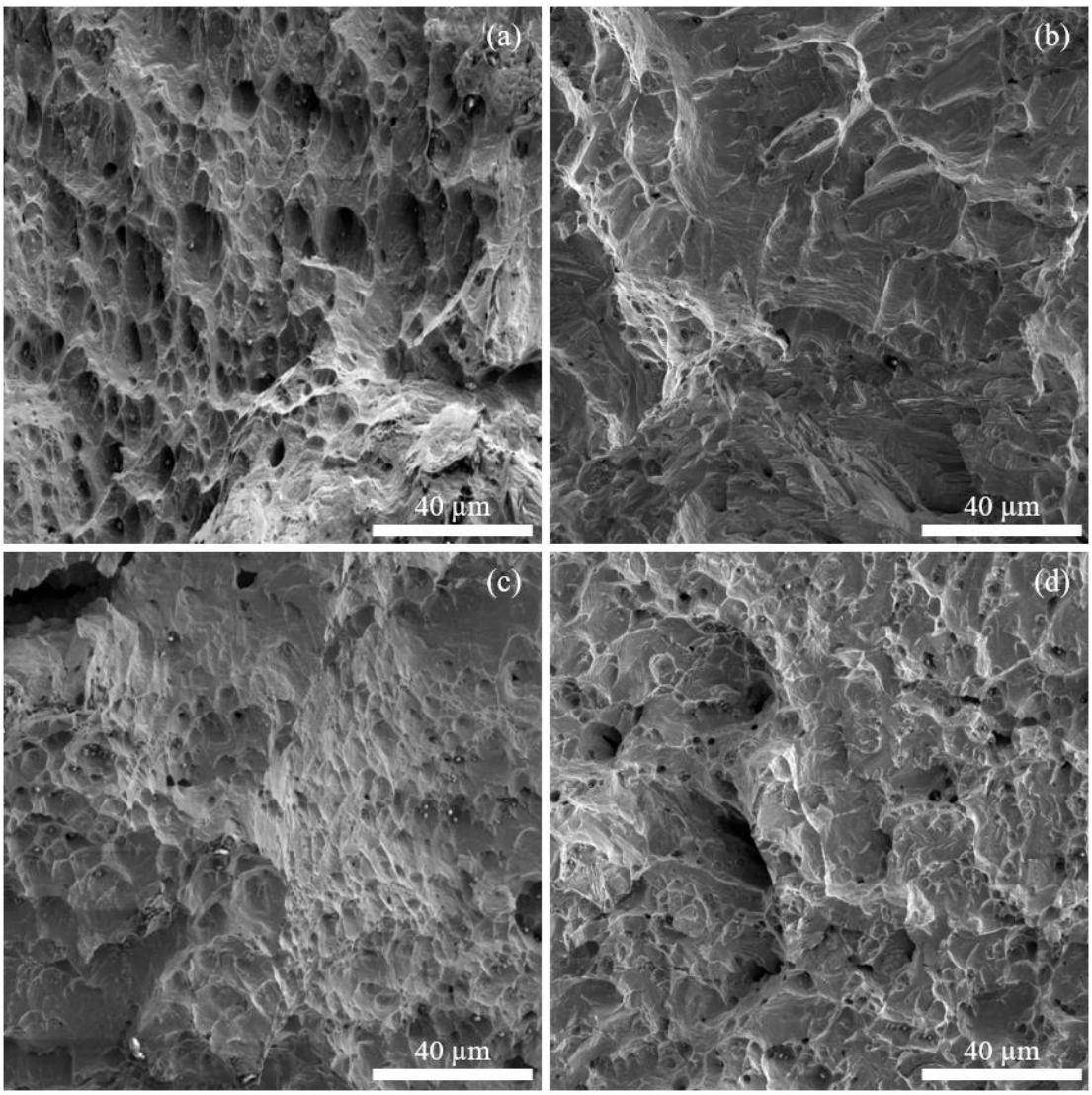

Fig. 25. SEM fractographs of CVN specimens at 500x magnification comparing the impact fracture behavior in CF–3 in the **(a)** unaged condition and **(b)** aged at 400 °C for 17,200 h; and CF–8 **(c)** unaged and **(d)** aged at 400 °C for 17,200 h.

austenite matrix [99], [122]. Little evidence of shear/cleavage or intergranular fracture is evident, but the CF–8 steel contains more shear indicators, which suggests the influence of the $M_{23}C_6$ carbide phase at the ferrite/austenite phase boundaries.

Analysis of the aged specimens indicates more variety in the appearance of the fracture surfaces. In the case of the tensile specimens, the aging condition D1 (280 °C for 17,200 h) for both steels is still dominated by ductile behavior. Characteristic dimpling and columnar structuring are still widespread in the D1 condition as well as in the D4 (400 °C for 17,200 h) condition, though there is more evidence of cleavage, characterized by flat surfaces and sharp ridges corresponding to brittle fracture [123]. Although a greater degree of cleavage fracture is evident in the D4 as opposed to the D1, both aging conditions in the tensile specimens for both steels are dominated by ductile failure. Comparison of the CF–3 and CF–8 steels during aging, Figure 25, shows a greater propensity for large fissures (ductile tearing corresponding to void coalescence [123]) and cracks (corresponding to cleavage) in the CF–8 from the unaged through all the observed aging conditions, likely as a result of the addition of the interphase carbides which are hard and brittle, serving as void and crack nucleation sites. The A3 and B3 conditions (360 °C for 4300 h and 8600 h, respectively) exhibit similarly ductile behavior to the unaged conditions, except for a larger amount of larger fissures present, which still appear to correspond more to ductile behavior.

Prior to aging, the fracture surfaces show no clear features delineating preference for failure related to any particular duplex phase. In the case of the aged specimens, there is still widespread evidence of ductile-type failure, but there are large regions of smoother, brittle-type failure indicative of significant embrittlement. There is also evidence in the SEM micrographs of exposed facets of ferrite indicative of brittle failure of the ferrite

grains, similar to the mechanisms proposed by Marrow and Harris [122]. This is consistent with ferrite hardening and embrittlement.

Analysis of the CVN specimens in the aging conditions D1 and D4 shows a greater difference in fracture behavior from the unaged baseline than seen in the tensile specimens. The D4 CVN specimens in both steels show significant regions of cleavage and brittle fracture, demonstrated by flat and sharp regions. In many cases at high (2kx) magnification, the ferrite island phase is observable, likely following interdomain cracking within the decomposed ferrite. Both of the steels in both aging conditions still exhibit regions of characteristic ductile behavior, but the proportion of brittle damage is markedly higher in the CVN specimens than in the correspondingly aged tensile specimens. This fractographic result is consistent with the observed mechanical testing results, which show a much larger drop in high strain-rate ductility (CVN impact energy) than the ductility drop during quasi-static loading (tensile elongation).

iii. Electron Backscatter Diffraction

Electron backscatter diffraction (EBSD) provides a straightforward and useful method for investigating the crystal orientations (and misorientations) of the phases and grains within the DSS microstructure. EBSD scans were performed on the unaged CF–3 and CF–8 steels before and after tensile deformation in order to characterize the original microstructure and the effects that extensive plastic deformation have on the orientations of the phases and grains. The orientation maps presented by inverse pole figure (IPF) color maps of the unaged and undeformed CF–3 are presented in Figure 26 (a) – (c), showing the overall orientations and the ferrite and austenite orientations separately, for clarity. The equivalents for CF–8 are presented in Figure 27 (a) – (c).

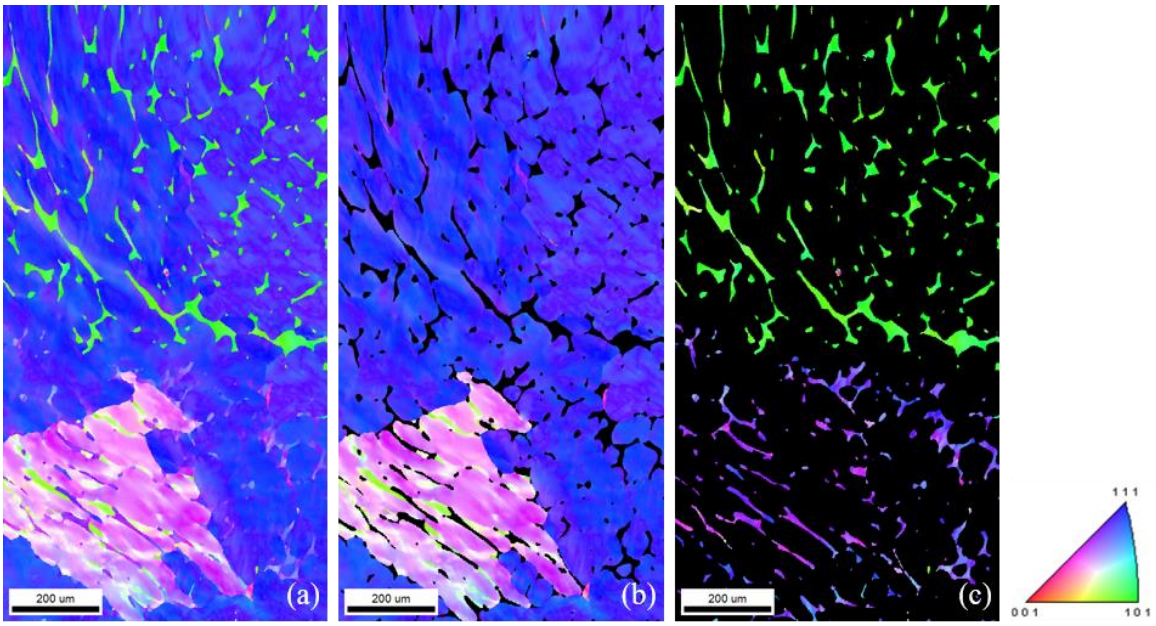

Fig. 26. IPF EBSD maps of unaged CF–3 microstructure showing **(a)** full orientation map, **(b)** map of just the austenite phase, and **(c)** map of just the ferrite phase for clarity.

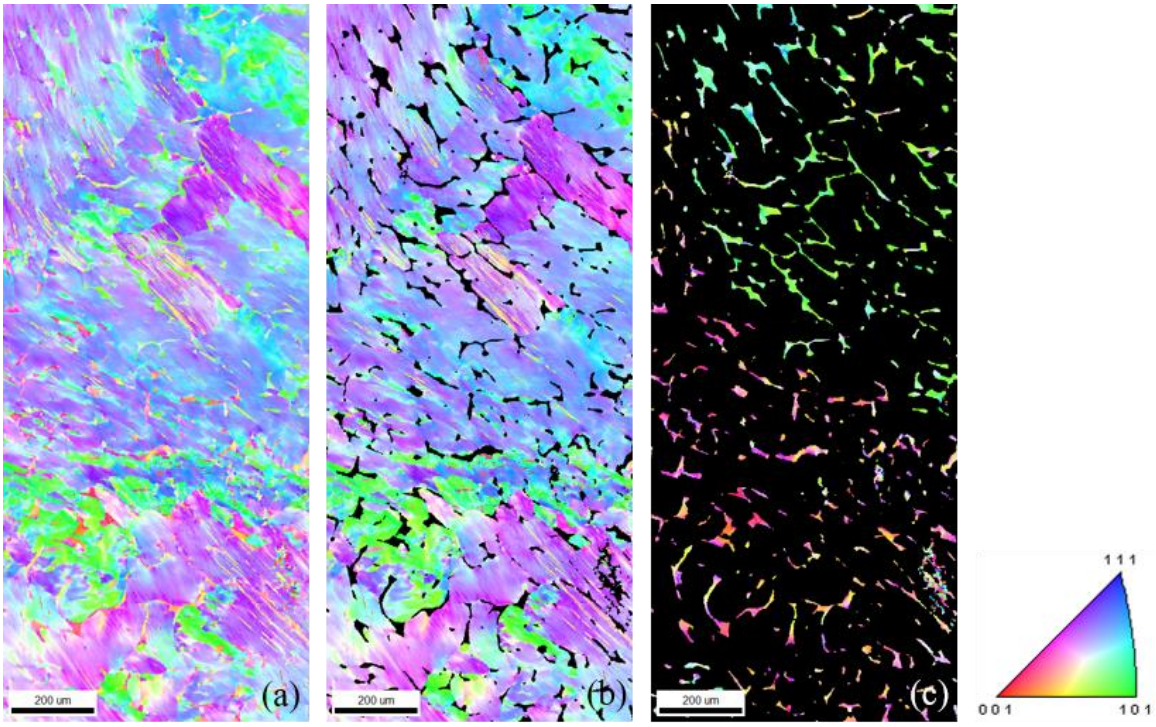

Fig. 27. IPF EBSD maps of unaged CF–8 microstructure showing **(a)** full orientation map, **(b)** map of just the austenite phase, and **(c)** map of just the ferrite phase for clarity.

It can be observed from these figures that the grain size of the austenite phase is large, with only two grains separated by a large angle boundary (blue vs. pink coloration) visible. Furthermore, it can clearly be observed that nearly all of the ferrite islands within the each austenite grain share the same orientation. Referring to the IPF orientation legend for the CF–3 steel, it can be seen most clearly that for the blue austenite grain with a {111}-type orientation, the ferrite grains contained within the matrix have largely green coloration. This corresponds to a {101}-type orientation, which fulfills the Kurdjamov-Sachs orientation relationship expected for these phases in the DSS. All other ferrite/austenite grains are expected to exhibit this same relationship criterion. Furthermore, it is noted that within the large blue austenite grain region there are some areas, such as the lower right corner of the IPF images, where the ferrite orientation differs from that in the upper portion of the image. It is possible that the similarly oriented ferrite grains comprise a continuous network in 3-dimensions, but the islands with different orientations demonstrate discontinuities in the ferrite network.

The kernel average misorientation (KAM) maps of undeformed and 45% strained CF–3 specimens, Figs. 28(a) – (b), and CF–8 specimens, Figs. 28(c) – (d), respectively, illustrate the misorientation distribution within the microstructures. The undeformed CF–8 exhibits greater misorientation than the undeformed CF–3 steel. One likely contributor to the measured difference between the undeformed steels is the greater nominal concentration of C in the CF–8 and the presence of the aforementioned $M_{23}C_6$-type carbides at the heterophase interfaces. Additionally, both CF–3 and CF–8 exhibit greater misorientation at the δ–ferrite/γ–austenite interfaces than in the interior of the grains in the undeformed condition, which indicates a higher dislocation density at these locations [34].

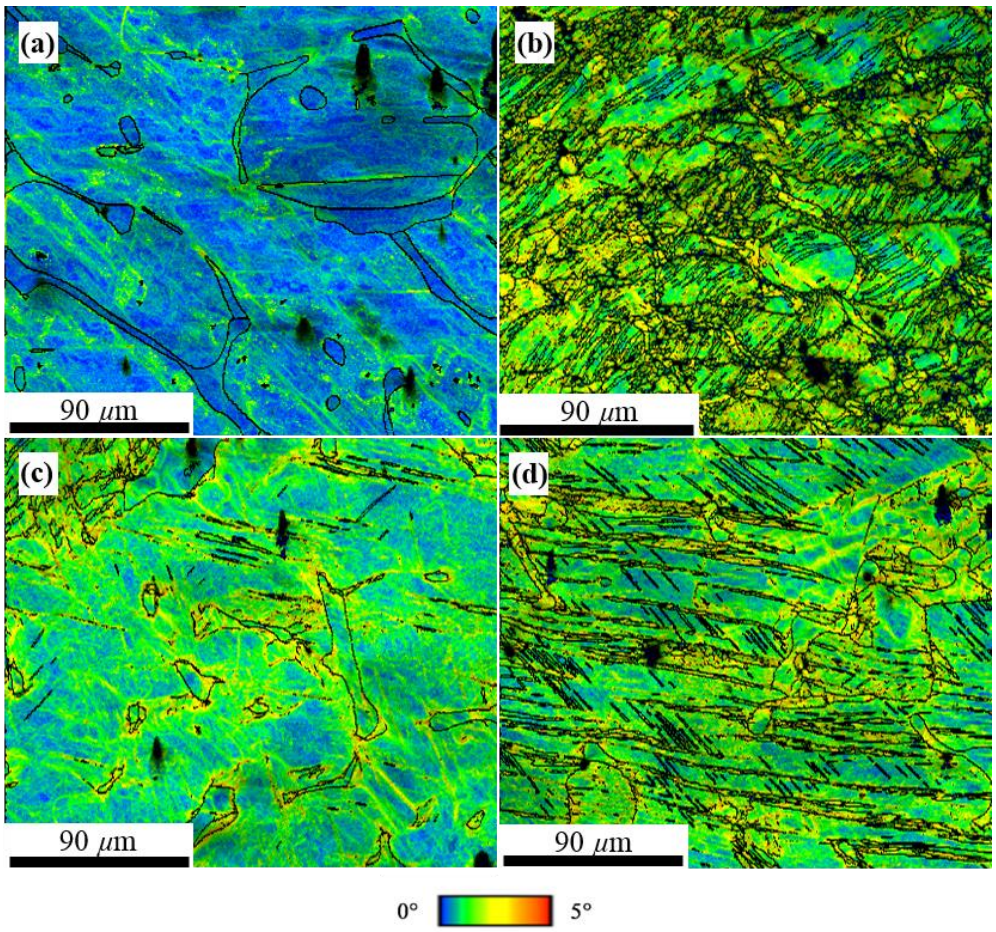

Fig. 28. KAM EBSD maps of **(a)**,**(b)** CF–3 and **(c)**,**(d)** CF–8 DSS in the **(a)**,**(c)** undeformed state and in the **(b)**,**(d)** failed tensile specimens.

The KAM maps after non-uniform plastic deformation, Figs. 28(b) and (d), illustrate that the amount of misorientation has increased in both steels. Furthermore, plastic deformation leads to deformation of the grains, an increase in the quantity of high-angle boundaries, and formation of subgrain structure throughout the microstructure of both steels. Furthermore, qualitative analysis of the KAM maps suggests that the degree of refinement and number of regions exhibiting a higher degree of misorientation is more significant in the CF–3 than in the CF–8 steel, suggesting that structural factors exist in the CF–8 to mitigate plastic deformation.

Grain orientation spread (GOS) maps of the deformed specimens can be used to identify the regions of largest plastic deformation (strain) by revealing the grains with the greatest average misorientation. GOS maps of both unaged steels were taken at cross-sections of the tensile specimens 0.5 in. from the necked region, Fig. 29(a),(c), and 0.15 in. from the centerline of the necked region, Fig. 29(b),(d). The former of these locations corresponds to uniform plastic deformation to 45% strain, and the latter corresponds to >45%, non-uniform strain past the UTS of the specimen. Original grain and phase boundaries can be clearly observed in the uniformly deformed specimens by the GOS map, where the level of strain can be seen to vary between phases and grains. The largest and smallest strains in this case are observed in ferrite islands, and the plastic strains of the austenite tend to be more intermediate. This is consistent with the strain partitioning results predicted by the anisotropic FEM model of the duplex microstructure presented in Chapter V. Furthermore, distinct differences can be observed between the uniformly deformed CF–3 and CF–8 specimens. The CF–8 results include a significantly higher maximum average misorientation (12.2° vs. 7.1°) and the apparent onset of subgrain formation, which is not observed in the CF–3. In the GOS maps taken near the necking point, both steels show similar distributions of minima and maxima in the ferrite with intermediate values for the austenite grains. In both specimens, significant subgrain formation is observed in the non-uniform region. Interestingly, the maximum average misorientation for the CF–3 is nearly double that of the GOS map taken far from the neck, but the CF–8 specimens show similar values near and far from the neck. This may suggest that the carbon effects in the CF–8 have a greater influence on the uniform deformation, but a stabilizing influence on non-uniform deformation.

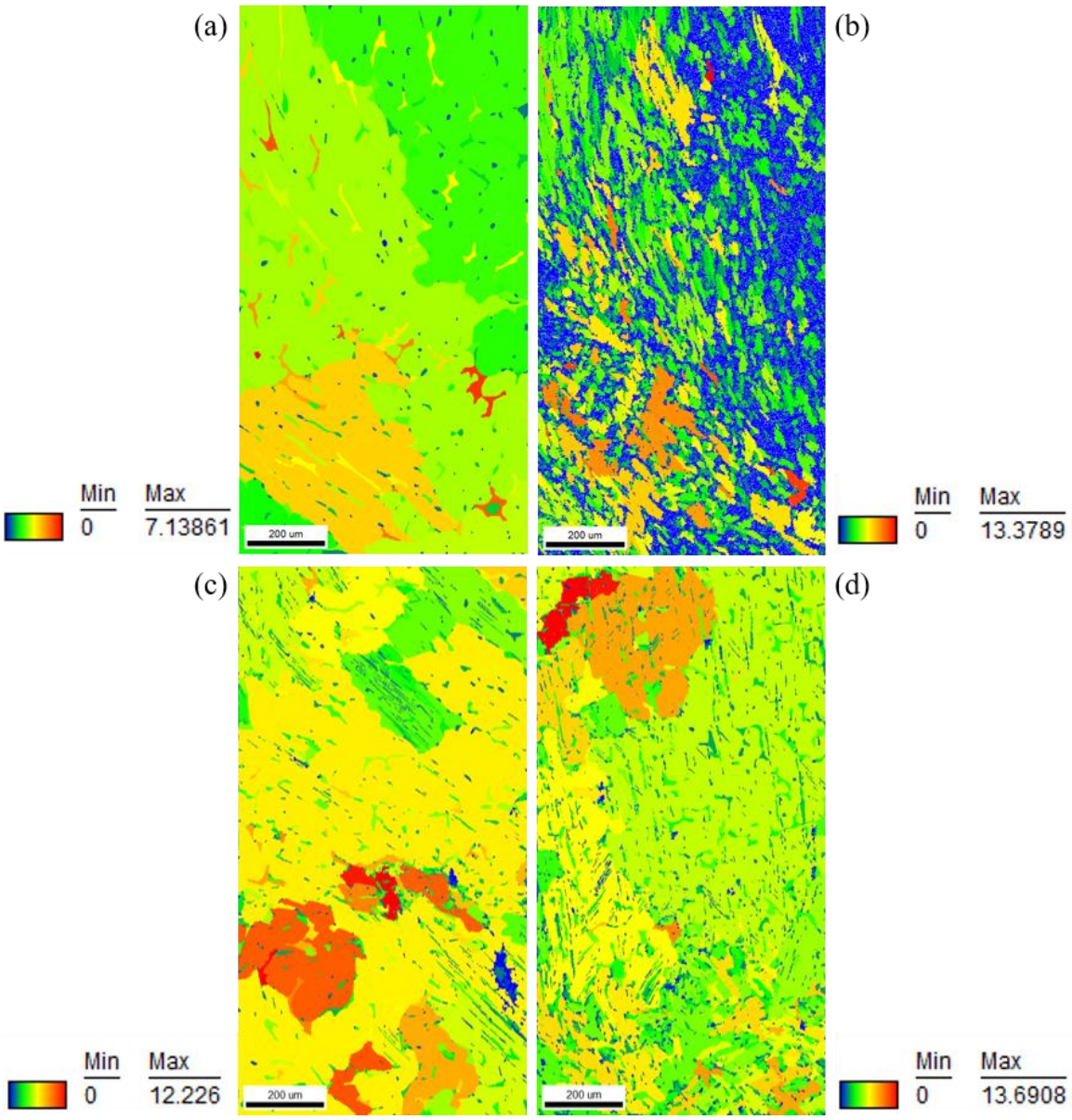

Fig. 29. GOS EBSD maps of unaged **(a),(b)** CF–3 and **(c),(d)** CF–8 tensile specimens deformed **(a),(c)** uniformly and **(b),(d)** non-uniformly to failure within the gauge length.

iv. Transmission Electron Microscopy

a. Unaged CF–3 and CF–8

The unaged CF–3 and CF–8 specimens prepared by electropolishing and ion milling were observed by conventional TEM imaging and selected area electron diffraction (SAED). Phase boundaries were identified qualitatively and diffraction patterns were recorded at zone axes on each side of the boundary. Due to both phases consisting of a cubic crystal lattice, indexing of the diffraction patterns was necessary to definitively identify each phase as b.c.c. ferrite or f.c.c. austenite. Calculation of the lattice parameters of each phase from multiple diffraction patterns and zone axes results in mean values of $a_{fer} = 0.289\ nm$ and $a_{aus} = 0.372\ nm$. These values match quite closely with the values reported by Redjaimia, et al of $a_{fer} = 0.287\ nm$ and $a_{aus} = 0.354\ nm$ [124]. Detailed analysis of the interiors of each phase reveal no additional lattice diffraction spots within either phase or at the boundaries that would correspond to the presence of additional phases within the duplex phases. Furthermore, conventional and high resolution (HR) imaging of the interior of either duplex phase, reveal no additional contrast or interfaces which could be indicative of additional tertiary phases of significant volume fraction present in the unaged microstructure aside from the presence of carbides at the phase interfaces in CF–8, as discussed below.

The δ–ferrite/γ–austenite interfaces in both unaged steels were observed by conventional TEM and SAED. The interfaces of the unaged CF–3 steel were straight and uniform and did not exhibit carbide precipitates as demonstrated by the lack of superlattice reflection spots in the SAED pattern, Fig. 30(a). Carbides were also not observed within the interiors of the b.c.c. δ–ferrite phase or the f.c.c. γ–austenite phase at locations away

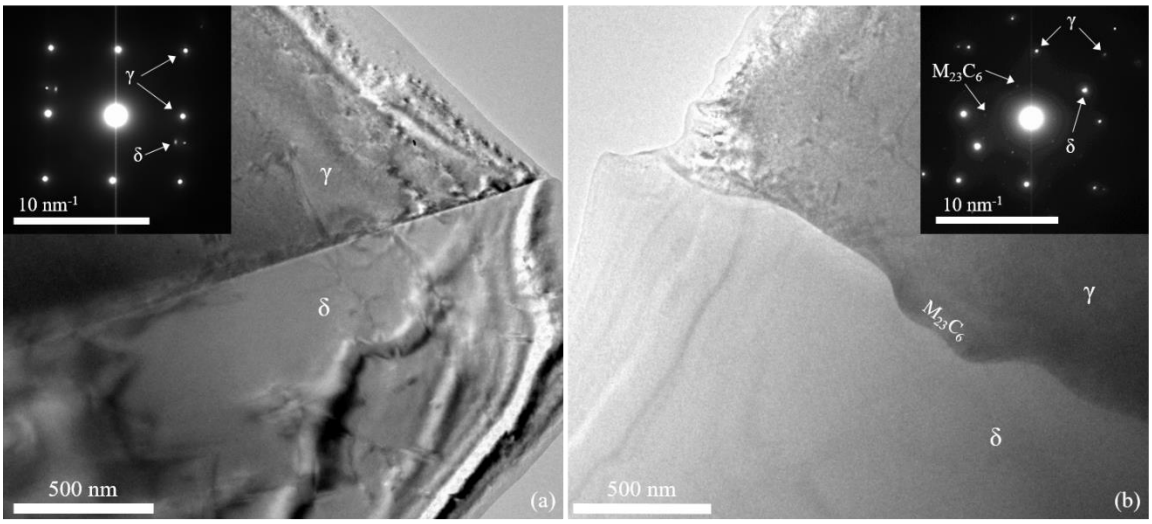

Fig. 30. Conventional TEM images of the δ–ferrite/γ–austenite heterophase interface in **(a)** CF–3 and **(b)** CF–8 duplex stainless steels with (insets) SAED patterns along the γ–austenite [001] zone axis.

from the interfaces. The lack of carbides in the CF–3 microstructure is most likely due to the low nominal C concentration of 0.02 at.% (max for the alloy is 0.03 at.%), Table 1. In contrast, the interfaces in the CF–8 steel demonstrate noticeable deviation from the smooth linearity observed in the CF–3 steel, Fig. 30(b), and SAED patterns taken at the interfaces along the [001] (Fig. 30(b) inset) and $[\bar{3}01]$ (Fig. 31(c)) *γ*–austenite zone axis reveal the presence of f.c.c. superlattice diffraction spots indicative of an $M_{23}C_6$ carbide phase. These spots are not present in the SAED patterns of the interior of either the *δ*–ferrite or *γ*–austenite grains in either steel or along the boundaries in the CF–3 steel. Additionally, the superlattice pattern exhibits a cube–cube orientation relationship (OR) – $\{111\}_\gamma \| \{333\}_{M_{23}C_6}$, $\langle 110\rangle_\gamma \| \langle 330\rangle_{M_{23}C_6}$ – with the *γ*–austenite phase. Hence, the $M_{23}C_6$ precipitates in the form of elongated carbide particles can be clearly seen at the interface during conventional TEM imaging when the specimen is tilted along a *γ*-austenite zone

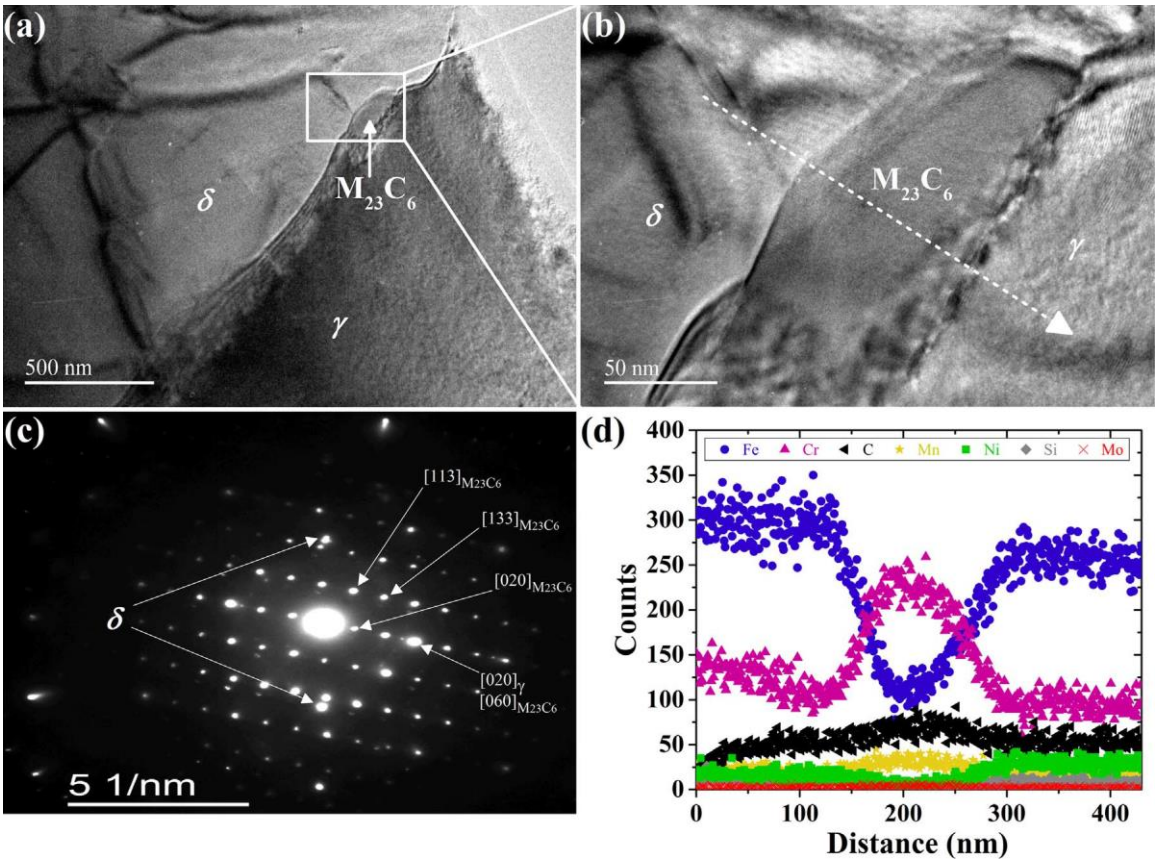

Fig. 31. (a) – (b) Conventional TEM images of an $M_{23}C_6$ carbide observed at the heterophase interface in CF–8 duplex stainless steel with **(c)** associated SAED pattern of the f.c.c. carbide along the γ–austenite/$M_{23}C_6$ [301] zone axis and **(d)** TEM-EDS scan results of element concentrations taken along a 430 nm line across the $M_{23}C_6$ carbide from the δ–ferrite phase to the γ–austenite phase along the dashed arrow.

axis, but appear primarily as undulations in the phase boundary when observed along a ferrite zone axis.

Figure 31(a),(b) depicts a conventional TEM image of one such $M_{23}C_6$ carbide, with an observed length of around 230 nm and width of 90 nm. Other carbides of the same type were observed at multiple different heterophase interfaces in CF–8, and exhibit similar

morphology to the one illustrated in Figure 31. These observations are consistent with those made by Southwick and Honeycombe [62] for $M_{23}C_6$ carbides in a different DSS of similar composition. The lattice parameter, $a_{M_{23}C_6}$, was measured as 1.10 nm in this study, which is slightly greater than the reported experimental value of $a_{M_{23}C_6} = 1.07$ nm [62], and is similar to other values reported in the literature in the approximate range of $a_{M_{23}C_6} = 1.05 - 1.10$ nm [125], [126] for an $M_{23}C_6$ carbide, where M = Cr. The lattice parameter is known to be subject to small variations due to differences in chemical composition.

An EDS line-scan was taken from the interior of the δ–ferrite phase across a representative $M_{23}C_6$ carbide and ending in the interior of the γ–austenite phase, Figure 31(d). The EDS results illustrate that the carbide is enriched in Cr and C, and contains smaller quantities of Mn, Ni, Mo, and Si. The carbide is depleted in Fe as compared to either duplex phase, though Fe is still present. Furthermore, EDS line scan and mapping reveals a depletion of Cr in the b.c.c. δ-ferrite lattice over a distance of approximately 50 nm from the interface. These observations support APT observations that the carbide contains metallic elements other than Cr, APT results indicating that the presence of Cr-rich carbide precipitates significantly alters the chemistry of the adjacent phases, and prior experimental observations in another steel containing Cr [68]. In addition, recent first principles calculations illustrate that Fe can substitute on the Cr lattice forming a $Cr_{23-x}Fe_xC_6$ carbide [125], [127]. The cohesive energy of an $M_{23}C_6$ carbide with $Cr_{19}Fe_4C_6$ stoichiometry is calculated, however, to be -8.095 eV, and thus the stability is slightly less than that of the $Cr_{23}C_6$, which has a calculated cohesive energy of -8.404 eV. Thus, it is likely that during aging, Cr diffusion into the carbide and Fe diffusion out of the carbide is ongoing.

b. Carbides in the Aged Steels

In the case of these duplex steels, CALPHAD calculations and published characterization work suggest that precipitation and formation of new carbides is not favorable at temperatures within the 475 °C embrittlement range. However, due to the presence of $M_{23}C_6$ carbides in the unaged CF–8 steels, it is important to investigate the effects that aging has on the boundary carbides in this study. Thorough analysis of the CF–3 steel specimens aged at 280 °C, 360 °C, and 400 °C reveal no evidence of carbides present at any boundaries or within either duplex phase, Figure 32. As in the unaged steels, the boundaries are uniformly smoothly linear and show no deviations or undulations indicative of boundary carbides as observed in the CF–8 specimens. Furthermore, SAED at the boundaries of each of the specimens reveal no diffraction spots corresponding to carbides along either austenite or ferrite zone axes.

TEM analysis of the aged CF–8 specimens, again aged at 280 °C, 360 °C, and 400 °C for 17,200 h, as well as aged at 400 °C for 8600 h show the presence of $M_{23}C_6$ carbides in all cases. Conventional TEM images with associated diffraction patterns are presented in Figure 33, where it can be observed that the cube-on-cube OR with the austenite phase is maintained as in the unaged condition. Calculation of the mean lattice parameter of the carbides at the highest aging temperature and longest aging time (400 °C, 17,200 h) results in a value of $a_{M_{23}C_6} = 1.09\ nm$, which is consistent with the value in the unaged CF–8 and with literature reports [62], [125], [126].

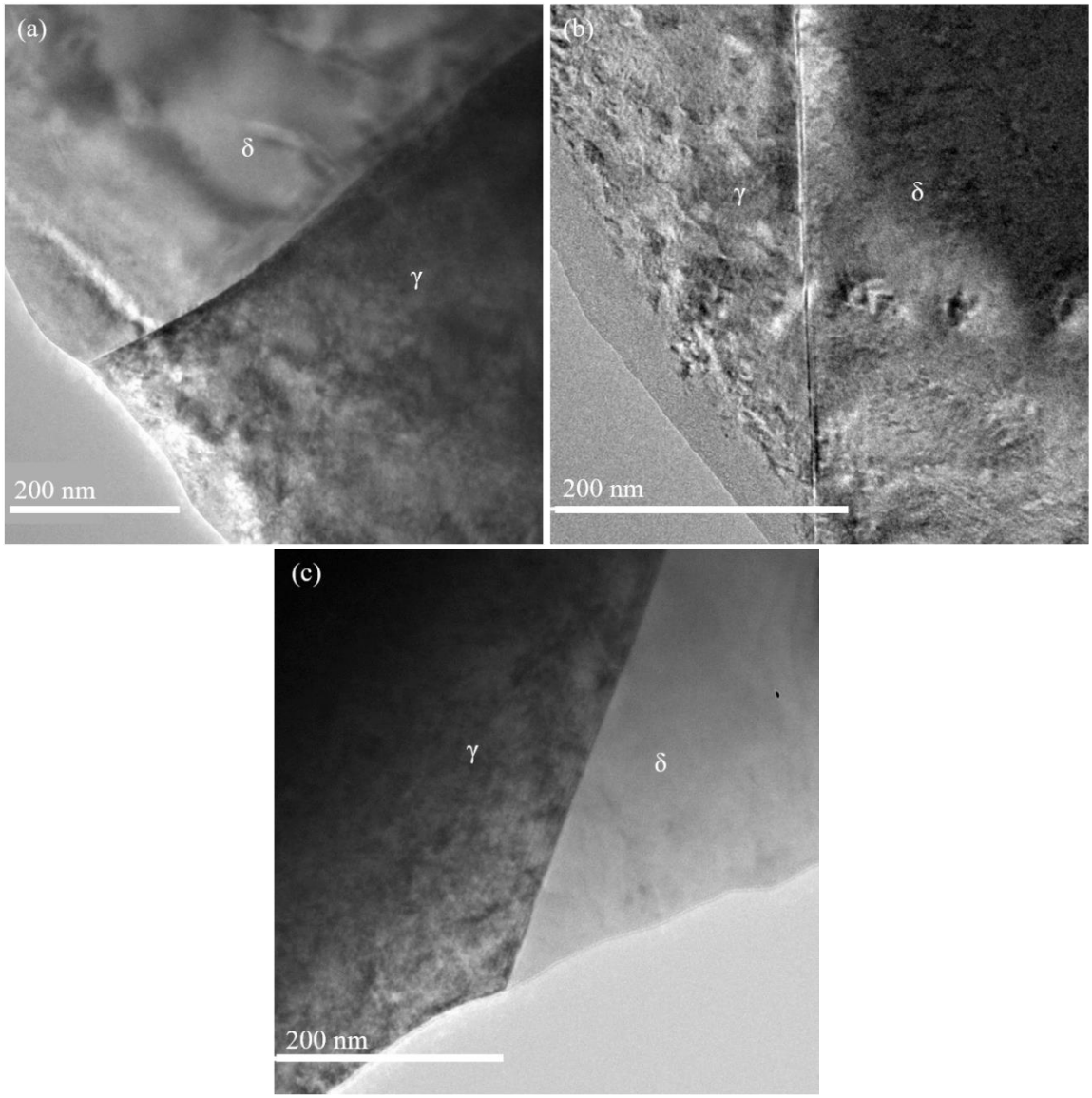

Fig. 32. Conventional TEM images of ferrite/austenite phase boundaries for CF–3 steels at **(a)** 280 °C, **(b)** 360 °C, and **(c)** 400 °C for 17,200 h.

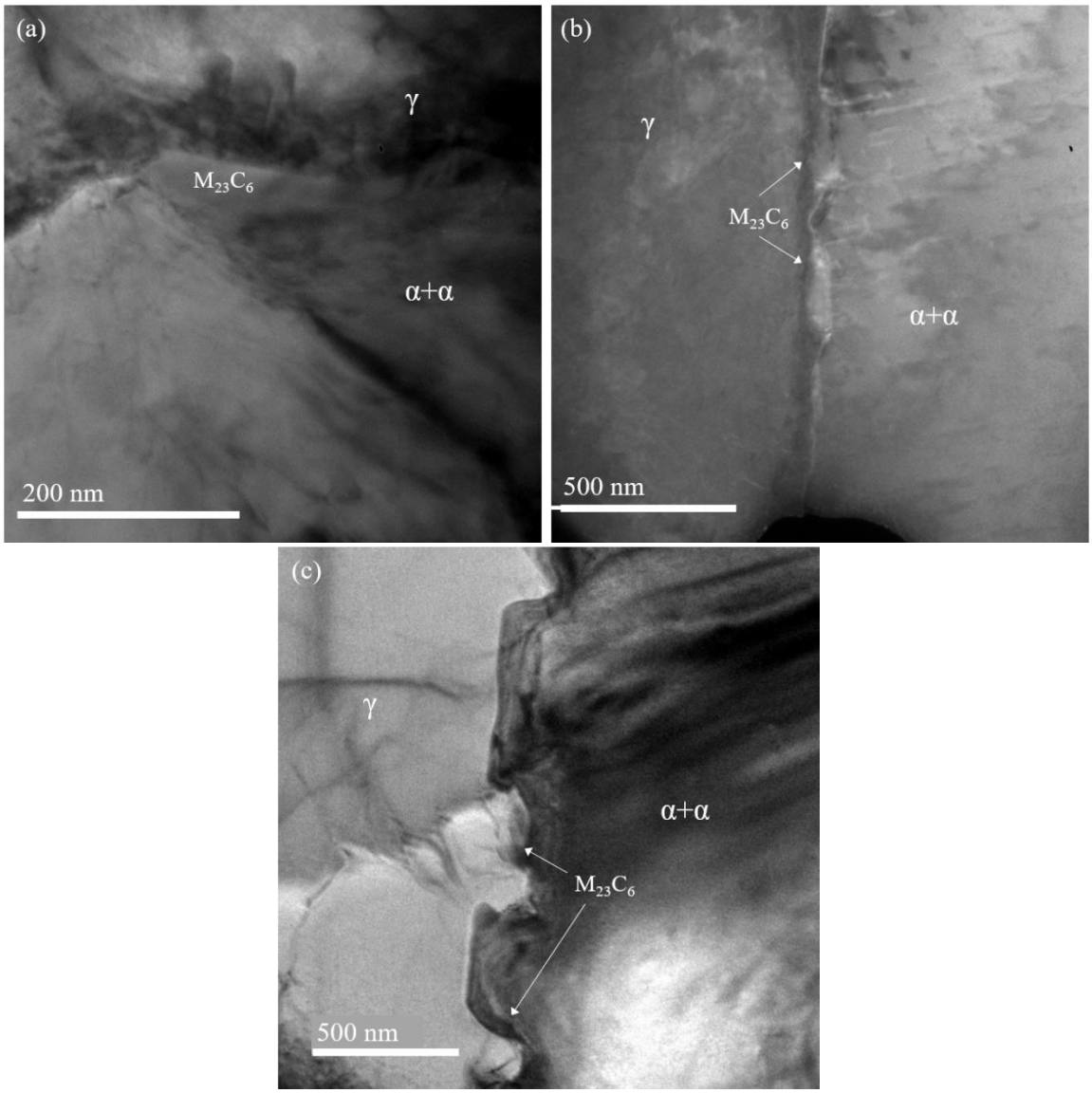

Fig. 33. Conventional TEM images ferrite/austenite phase boundaries for CF–8 steels at **(a)** 280 °C, **(b)** 360 °C, and **(c)** 400 °C for 17,200 h.

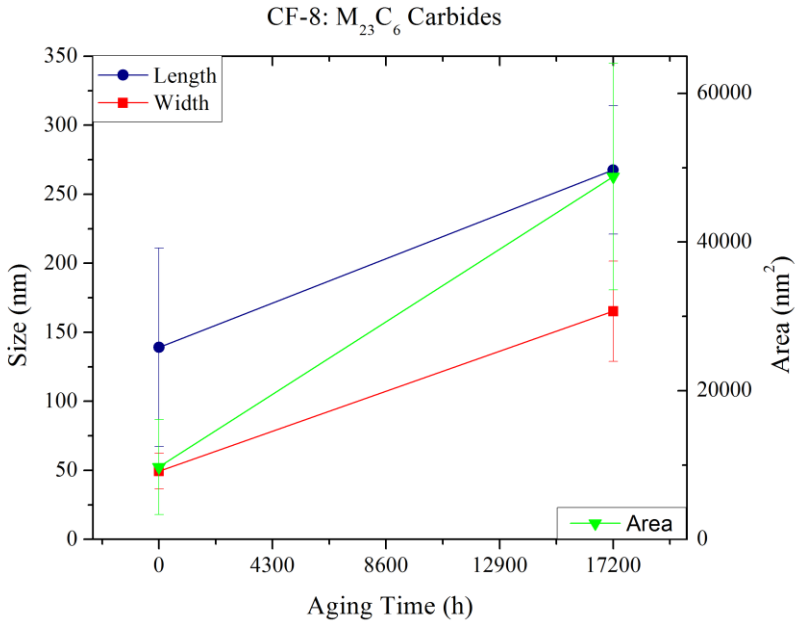

Fig. 34. General changes in carbide size and distribution in CF–8 prior to aging and after aging at 400 °C for 17,200 h.

Qualitative analysis suggests that while formation or dissolution of the carbides does not appear to be occurring, there is a noticeable coarsening of the carbides. While carbides in these steels are typically not assumed to be nucleating at the temperatures studied here, carbides nucleated during the casting and treatment process may not dissolve in this temperature range. Figure 34 shows the approximate spacing and size of the carbides observed in the CF–8 specimens at each condition, and seems to indicate that the spacing is getting smaller. However, due to the small field of view of the TEM and the limited number of boundaries and orientations that have been observed, the data presented in Figure 34 is not statistically significant enough to draw definite conclusions from.

Generally, these measurements were made using dark field images taken by isolating the electrons transmitted through a single carbide diffraction spot, only illuminating the carbides along a particular austenite/carbide zone axis. Dark field images

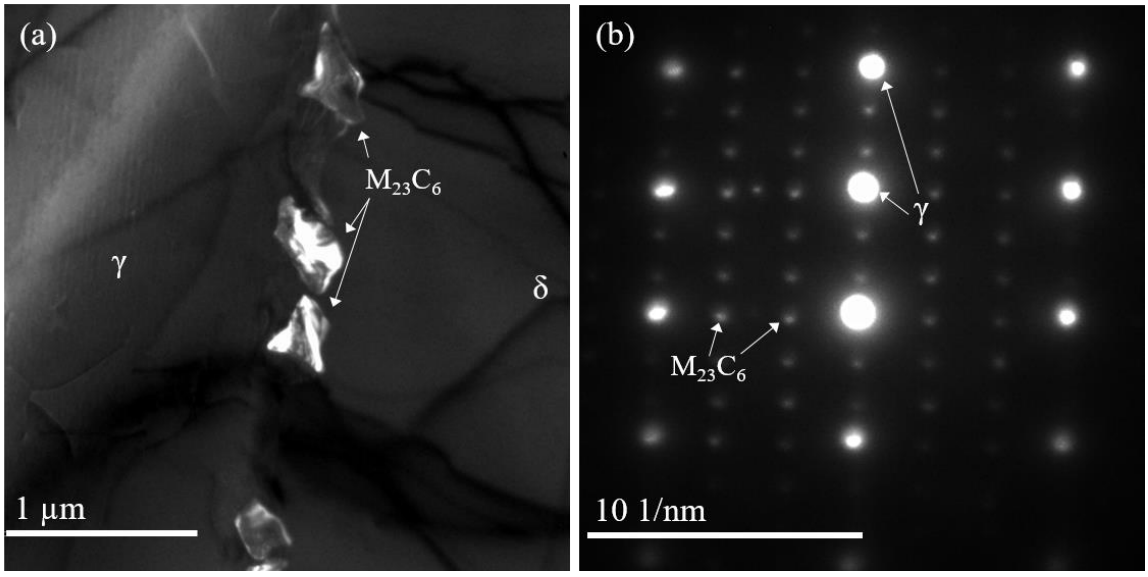

Fig. 35. Dark field TEM images of ferrite/austenite phase boundaries for CF–8 showing the altered morphology and distribution of boundary carbides following thermal aging at 400 °C for 17,200 h.

presented in Figure 35 for different conditions seem to qualitatively confirm the early stages of coalescence of carbides indicative of traditional coarsening, where the volume fraction of the phase remains constant but diffusion of precipitate-forming elements (in this case primarily Cr and C) along the phase boundaries causes the growth of large particles at the expense of smaller, less stable particles. TEM studies present in the literature, notably Hamaoka, et al. [49], [67], for longer aging times support the presence of coarsening mechanisms for the carbides during the aging of DSS. An additional observation is that the aging carbide precipitates appear to be "drifting" into the body of the austenite phase, indicating a shift in the location of the ferrite/austenite phase boundaries. This could be explained inter-diffusion of Fe, Cr, and Ni between the austenite and ferrite phases during aging as a means to increase compositional stability in each phase, since it has been shown that Fe and Ni are enriched in the austenite and Cr is enriched in the ferrite [20]. This may

also be indicative of the formation of the γ′ austenite phase at the boundaries, which then encroaches on the ferrite regions.

c. Additional Phases in the Aged Steels

The APT investigations performed during this study and presented predominantly by Mburu and Mburu, et al. [37], [50], indicate the clear chemical segregation of elements on the nano-scale within the ferrite phase. This is constituted by spinodal decomposition of the ferrite into Fe-rich α and Cr-rich α′ domains ($\delta \rightarrow \alpha + \alpha'$) in both steels under all aging conditions, and by segregation of G-phase forming elements to α/α′ domain boundaries. In the TEM, the decomposition reaction is difficult to observe due to the close similarities in atomic mass and lattice parameter of Fe and Cr, and the resulting small mismatch between the α and α′ domains. Generally, evidence of the spinodal reaction in DSS is said to be indicated by a mottled contrast of slightly lighter and darker regions corresponding to each domain. G-phase formation, however, is a nucleation and growth process of a different crystal structure (f.c.c.) within the matrix (b.c.c.). However, in the early stages of formation, the nucleation may not yet have occurred, resulting only in contrast between the Ni-Si-Mn-etc. rich G-phase forming zones and the ferrite matrix. Furthermore, even in the case of nucleation, the small size (~5-10 nm radius) and potentially small volume fraction can mean a very small effect on the diffraction patterns and very diffuse lattice spots. Specimens selected for TEM were each observed in detail within the ferrite phase (as determined by SAED) along multiple zone axes and under different beam conditions in order to discern the presence of decomposed domains or G-phase phase forming zones or precipitates.

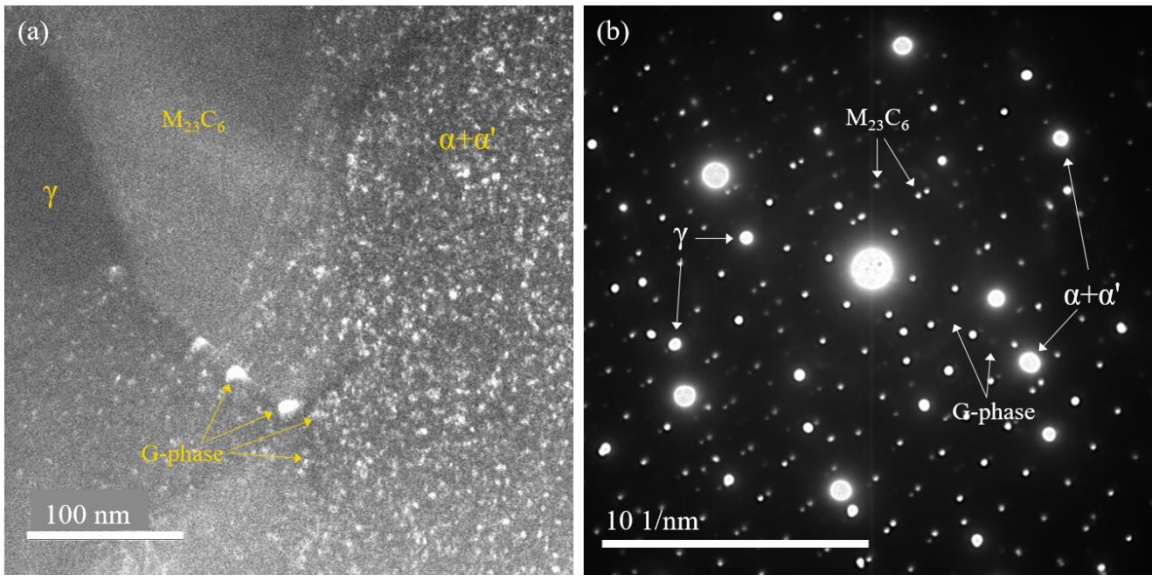

Fig. 36. (a) Dark field TEM image of ferrite/austenite phase boundaries for CF–8 D4 showing the presence of carbides and G-phase. **(b)** SAED image showing diffraction spots corresponding to all four phases.

Of the aged TEM specimens, the best contrast and most conclusive data was obtained for the CF–8 steel aged at 400 °C for 17,200 h, Figure 36. This specimen was prepared by focused ion beam techniques, and as a result is very uniform in thickness. However, the downside to this is that only one ferrite grain is observable. This specimen, also referred to as CF–8 specimen D4, is observed to contain α+α'-ferrite, γ-austenite, $M_{23}C_6$ carbides, and G-phase precipitates, all of which are visible in dark field imaging along the ferrite/austenite phase boundary, Figure 36. Using this dark field technique, diffraction spots corresponding to the carbides and G-phase are isolated to transmit the electron diffracted through these phases in particular, highlighting their presence in the nanostructure. Figure 36 shows a fairly high density of G-phase precipitates, increasing closer to the carbide boundary. These precipitates in the interior of the ferrite match the morphology (approximately spherical), distribution, and size (~4-10 nm) expected from

reports for similar materials and long aging times in the literature [46], [52], [98]. The SAED pattern, Figure 36(b), corresponding to the image, shows diffraction spots for all four phases along the ferrite/G-phase $[20\bar{1}]$ zone axis (ZA), and the austenite/$M_{23}C_6$ $[10\bar{1}]$ ZA. This confirms the cube-on-cube OR for the f.c.c. austenite with the complex f.c.c. carbide and the cube-on-cube OR for the b.c.c. ferrite with the f.c.c. G-phase. The lattice parameters for each of the four phases each support their identification as such, and are consistent with previously reported values: $a_{\alpha+\alpha'} = 0.29\,nm$, $a_{\gamma} = 0.36\,nm$, $a_{M_{23}C_6} = 1.07\,nm$, and $a_{G-phase} = 1.15\,nm$. The value for $a_{G-phase}$ is the least available in the literature and can vary due to the wide range of possible compositions for the G-phase in stainless steels, but the measured value of 1.15 nm is consistent with the available information [47], [49]. It can also be observed that there are several larger precipitates located directly at the ferrite/carbide boundary. These precipitates possess the same contrast as the smaller interior G-phase particles and are likely larger G-phase particles formed at the readily available nucleation sites available at the boundary by G-phase forming elements concentrated at the boundaries and/or ejected by the carbides during aging. Due to the size of these particles, it is possible that they are further along in structural development and possess a clearer diffraction signature, which could help to explain why this specimen is the only specimen for which clear G-phase diffraction spots could be discerned.

The corresponding CF–3 specimen, (400 °C, 17,200; D4), is shown by APT to exhibit a higher degree of spinodal decomposition by both wavelength and amplitude Figure 41. Furthermore, the presence of clusters of G-phase forming elements has been observed by APT. In the TEM specimens, observation of the ferrite by bright field imaging,

Figure 37, reveals contrast corresponding to segregated G-phase clusters. These clusters show similar size (~4-10 nm) and morphology (~spherical) to that observed for the CF–8 D4 specimen. The particles appear to be more widely distributed than in the CF–8 near the carbides, which supports the conclusions drawn by APT that G-phase volume fraction increases near the ferrite/carbide boundary [50]. There are no carbides present at the phase boundaries, and thus no larger G-phase particles are observed at ferrite/carbide interfaces. Analysis of SAED patterns, Figure 37 (inset), reveals diffraction spots corresponding to ferrite and austenite, but no additional diffraction spots are observed. High resolution (HR) TEM images of the ferrite phase along the ferrite zone axis shows significant mottling of contrast of the approximate size and morphology of the spinodally decomposed α and α' domains. However, as the lattice parameters of both decomposed domains are very similar and they are coherent, diffraction confirmation was not achieved.

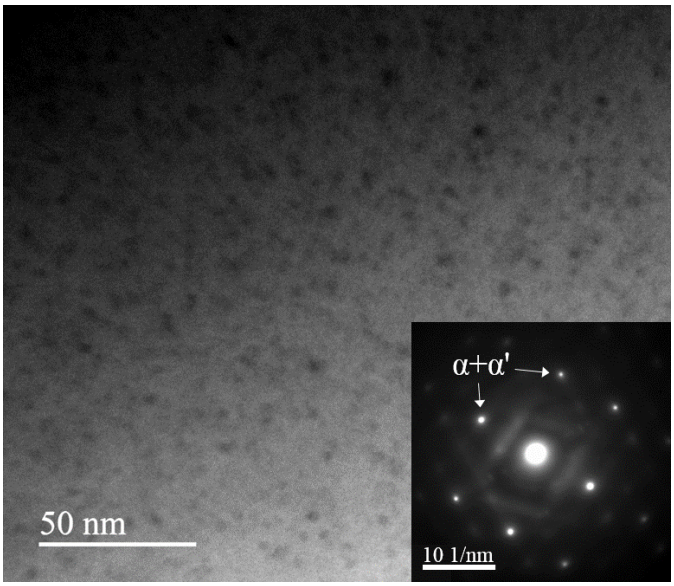

Fig. 37. Bright field TEM image of ferrite phase for CF–3 D4 showing contrast appearing to correspond to the G-phase and (inset) SAED pattern along a ferrite zone axis within the ferrite phase.

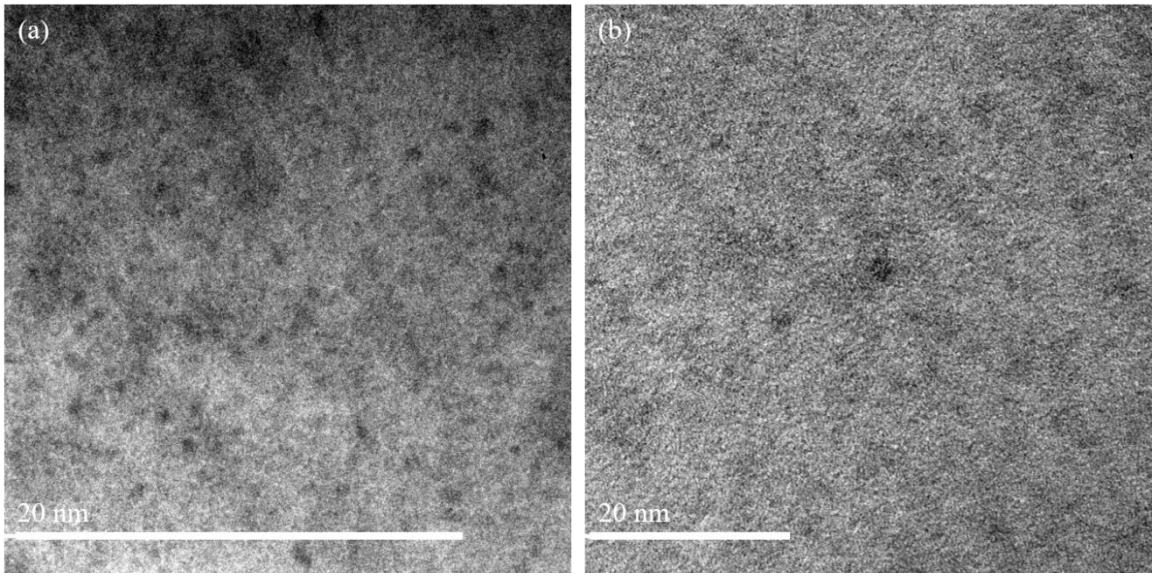

Fig. 38. Conventional TEM images of ferrite phase in **(a)** CF–3 B4 and **(b)** CF–8 B4 showing contrast appearing to correspond to the G-phase.

CF–3 and CF–8 B4 specimens (aged 400 °C, 8600 h) were observed through similar TEM techniques. Conventional TEM images of these specimens, Figure 38, show contrast corresponding to particles of the expected size and morphology for the G-phase, but at a fairly low density. As a result, no diffraction evidence or other conclusive evidence for structurally mature G-phase particles was found, but the TEM images support the presence of G-phase clusters as noted by APT.

D3 specimens of both steels (360 °, 17,200 h) – at a lower accelerated temperature than the B4 specimens, but double the aging time – exhibit similar evidence to that of the B4 specimens. In these cases, dark field images showing some contrast were able to be captured, implying that there may be some more formed G-phase particles than exist in the B4 specimens, but SAED patterns were too diffuse to obtain absolute confirmation of the presence of G-phase. Similar G-phase cluster and mottled contrast were obtained by conventional imaging were observed to those of the previous samples.

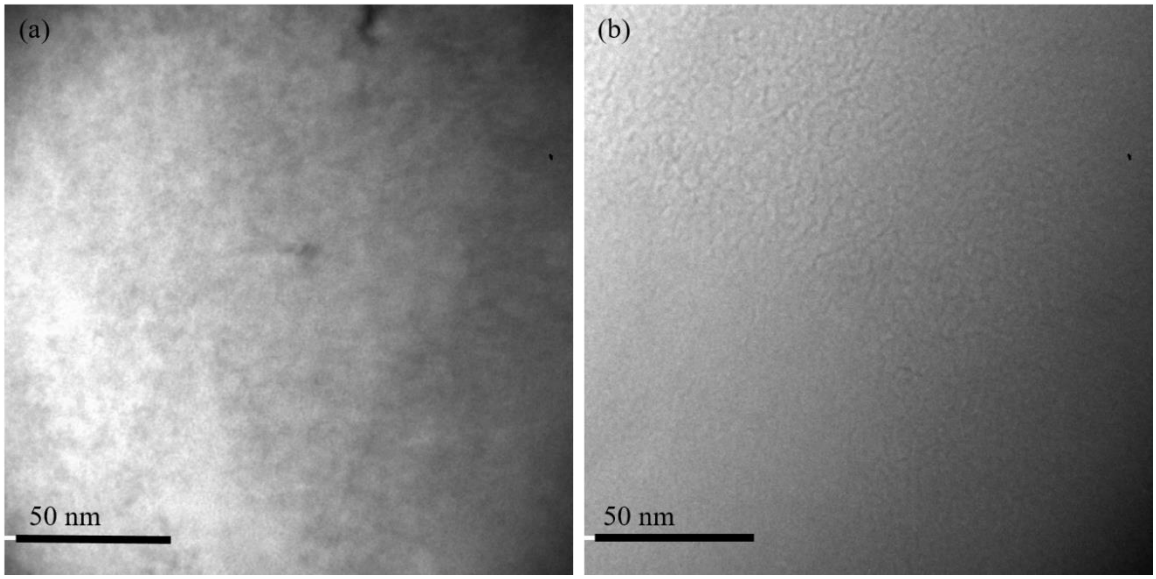

Fig. 39. Bright field TEM images of ferrite phase in **(a)** CF–3 D1 and **(b)** CF–8 D1 showing no significant contrast indicative of G-phase.

Finally, D1 specimens for both steels (280 °C, 17,200 h) were observed using the same methods, Figure 39. Unlike the other specimens, no evidence of unusual contrast was observed that would correspond to the G-phase clusters. This not only supports the APT data that no significant G-phase formation is occurring at the 280 °C aging temperature by 17,200 h, but it also supports the implication that the contrast observed in the other specimens corresponds to real aging phenomena and not to specimen preparation or typical micrographs for these steels. As stated before, carbides were observed in the CF–8 D1 steel but not in the CF–3 D1 steel, and only SAED patterns corresponding to the ferrite, austenite, and carbides were observed.

v. Atom Probe Tomography

Atom probe tomography (APT) was performed at the ferrite-austenite phase interfaces for each aging condition to analyze the nano-scale effects of spinodal

decomposition [37], [114]. The calculation of mean wavelength, λ, and mean amplitude, A, are based on comparison of the local Fe and Cr fluctuations to their mean compositions in the ferrite phase. Multiple regions of interest (ROI) are taken measuring 30 nm x 3.2 nm x 3.2 nm, Figure 40(a), and the Fe and Cr concentrations are measured along the length of the ROI, Figure 40(b). A and λ of the α' domains are measured as the distance between Cr peaks and the difference between the Cr peaks and the mean Cr concentration, respectively. The full methodology is provided in the aforementioned publication and comprehensive analysis is the subject of ongoing work, but some straightforward results are presented here in an effort to elucidate correlations between the spinodal decomposition of the ferrite, the ferrite hardness, and evolution of the bulk mechanical properties.

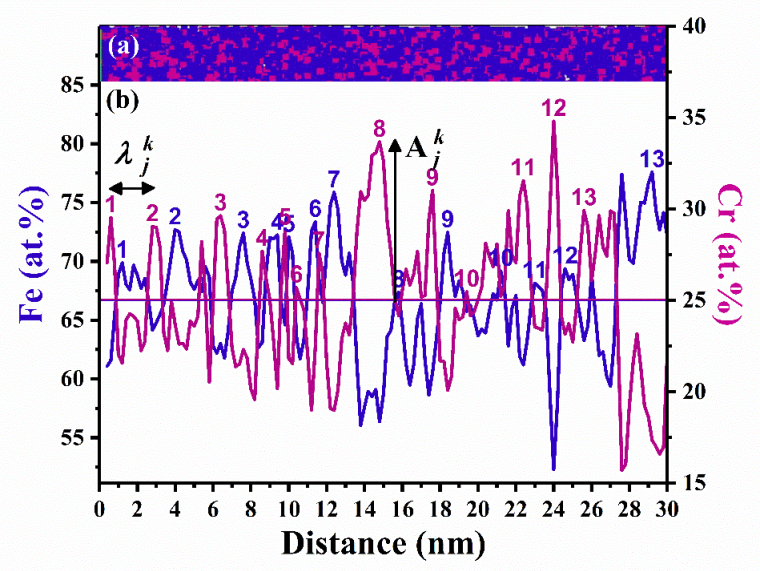

Fig. 40. Fluctuations of iron (Fe, blue) and chromium (Cr, magenta) concentrations along an **(a)** ROI taken in the ferrite of an unaged CF-3 APT tip. **(b)** Corresponding Fe and Cr concentration profiles illustrate the deviation of the Fe-rich α and Cr-rich α' domains from the mean elemental concentrations. *[50], [128]*

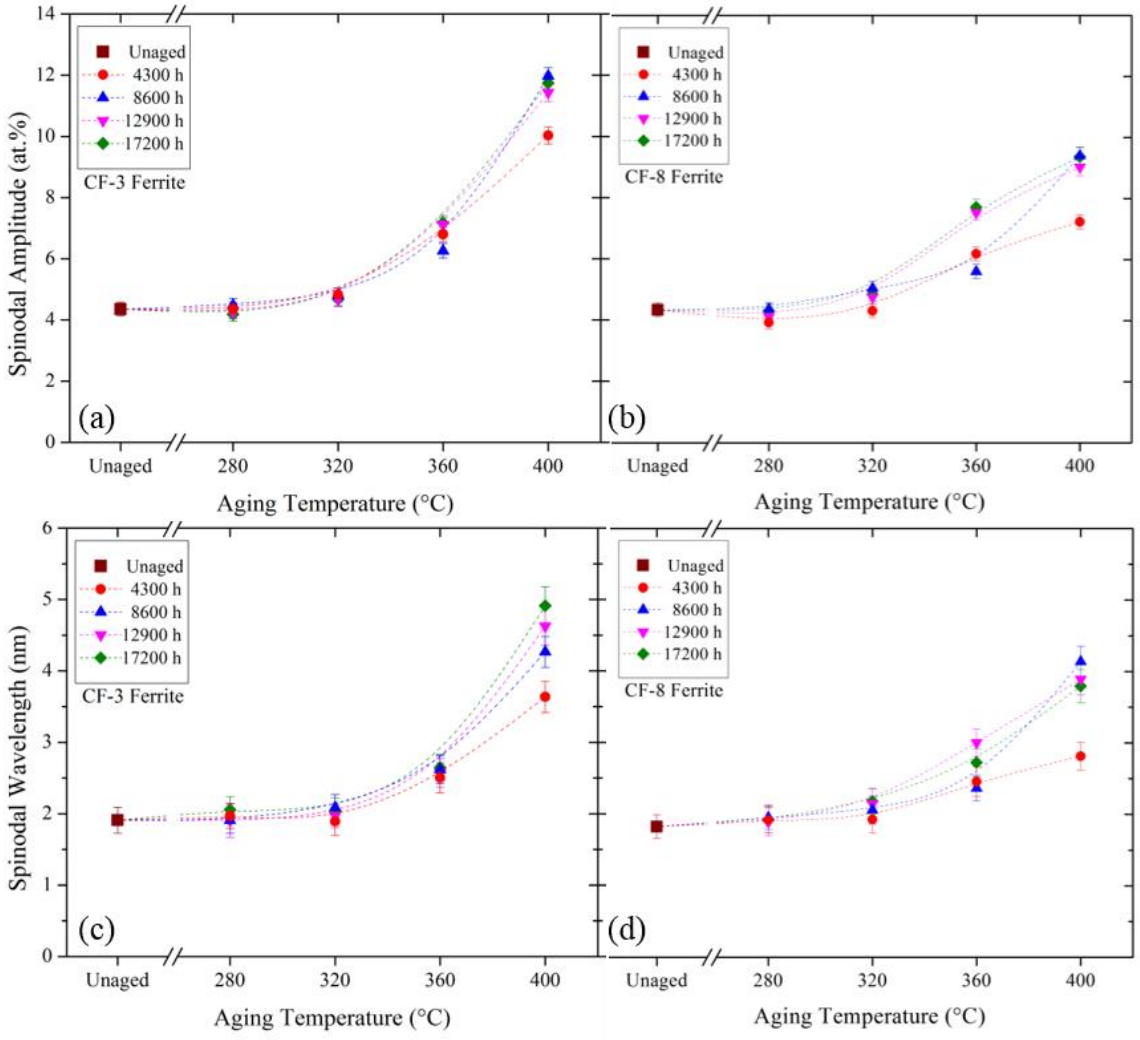

Fig. 41. Effects of aging temperature on the decomposition of the ferrite phase measured by APT on **(a)** spinodal amplitude of CF–3, **(b)** spinodal amplitude of CF–8, **(c)** spinodal wavelength of CF–3, and **(d)** spinodal wavelength of CF–8 DSS.

As previously reported, some incipient spinodal decomposition is observed in the unaged condition, likely having formed during quenching from the solution treatment process, resulting in spinodal wavelengths of 1.91 nm and 1.83 nm in the unaged state for CF–3 and CF–8, respectively [37]. The corresponding unaged amplitudes are 4.35 at.% and 4.36 at.%, respectively. During aging at 280 °C, the spinodal mean amplitude, *A*,

Figures 41(a) – (b), and spinodal mean wavelength, λ, Figures 41(c) – (d), show little change up to 17,200 h, matching the trends in ferrite nanohardness, Figures 20(a) – (b). Following aging up to 17,200 at 280 °C, the Cr wavelength and amplitude in the CF–3 ferrite were 2.06 nm and 4.18%, respectively. The corresponding values for the Cr wavelength and amplitude in the CF–8 ferrite were 1.93 nm and 4.32%, respectively. In contrast, the progression of spinodal decomposition is significant at the accelerated aging temperatures. Following aging up to 17,200 h at 400 °C, the Cr wavelength and amplitude in the CF–3 ferrite were 4.91 nm and 11.74%, respectively. The corresponding values for the Cr wavelength and amplitude in the CF–8 ferrite were 3.80 nm and 9.38%, respectively.

As can be observed by comparing the wavelength and amplitude values of the two steels, the incipient spinodal properties are approximately the same in the unaged condition. However, the degree of decomposition is larger in the CF–3 steel following aging at accelerated temperatures, where both the wavelength and the amplitude are larger than in the corresponding specimens of CF–8. This indicates that the diffusion kinetics are different between the two steels during aging under the same conditions. Furthermore, the trends for increasing wavelength and amplitude are both continuing to increase beyond the ~2 year aging step, though the rate of increase is beginning to level at the longer aging times.

V. FINITE ELEMENT METHOD MODELING

A. INTRODUCTION

The goal of this chapter is to utilize finite element method (FEM) modeling to study the mechanical effects of aging embrittlement on the microstructure of a structural duplex stainless steel. In the previous chapters, experimental methods for measuring the bulk and local mechanical properties, as well as characterization of the microstructure were utilized to observe the real system in a comprehensive way. However, experiment methods such as these are limited in that they require destructive testing of a limited amount of material, which means that including the cost of the material and the time commitment of aging, certain things such as possible loading conditions must be carefully selected. Furthermore, for experimental testing important characteristics such as crystal orientation cannot be changed, and it can be very difficult and expensive to measure the stresses and strains during deformation in-situ. FEM modeling provides a method for repeatable and highly adaptable analysis of the stress-strain distributions of the bulk material and within the microstructure on multiple length scales. With the creation of accurate model geometries, material properties can be changed, different crystal orientations explored, and important deformation trends pinpointed in a way that is considerably less feasible by experiment.

In order to understand and predict the changes in deformation behavior that occur during thermal aging, it is useful to understand the effects of properties and structural changes on the local stress and strain distributions within the microstructure. FEM models can show these local distributions resulting from an applied stress state, allowing regions of high stress and strain to be elucidated and enabling predictions to be made for the locations of yielding and failure under applied deformation. Such models have been created

in two dimensions (2-D) for dual-phase (ferritic-martensitic) [100] and duplex (ferritic-austenitic) [98] stainless steels for various assumptions of isotropy and elastic behavior. These models can be used to predict regions of high elastic stress (likely locations for yielding or brittle failure), high hydrostatic stress (likely locations for ductile failure), and high local strains [129], [130]. As the measured properties change during the formation of nanometer-size phases in within the ferrite phase, these local stress and strain distributions will change, giving insight into the changing bulk mechanical behavior of the CF–3 and CF–8 steels during service in nuclear systems. Furthermore, FEM can be applied on multiple length scales, thus allowing for geometric representations of nanostructural, microstructural, and bulk changes to be analyzed and correlated.

For this project, 2–D isotropic FEM models and a 3–D anisotropic model have been developed based on the real microstructure of CF–3 and CF–8 CDSS at multiple length scales. The effects of aging embrittlement of the δ–ferrite phase on the local elastic and plastic stress and strain distributions are evaluated. The ferrite properties have been varied to reflect the effects of longer aging times on the material, and the results are analyzed based on applied tensile loads and accurate constraints. When available through experiment, structure and properties obtained from this study have been directly implemented in the FEM models for the highest level of accuracy. Where properties are required but not experimentally obtained during the course of this work, the necessary quantities have been determined from the literature. The evolution of the elastic and plastic property inputs for δ–ferrite has been incorporated through both external and internal results. The γ–austenite properties are assumed to remain the same throughout the aging process, which is commonly accepted to be true in these CDSS systems, and is supported

in the previous chapters [4], [14], [76]. The FEM results shed light on the effects of thermal aging of the CDSS during operation in commercial nuclear plants and will aid in prediction of likely yielding and failure locations due to stresses in the microstructure under applied loads, but the methodologies presented here can also be readily applied to a wide range of multi-phase materials systems for similar analyses.

B. Computational Methods

i. General Modeling Details

a. Model Geometry, Mesh, and Constraints

Each of the FEM model geometries presented in this chapter was created using the same fundamental method. Images of real microstructures were obtained as micrographs by optical microscopy, electron microscopy, or atom probe tomography and utilized as a template to duplicate the structure on the relevant length scale to the maximum possible accuracy. These micrographs were converted to binary pixelated images using public domain ImageJ software (available through NIH) [131]. Binary raster images were converted to vector image files using RasterVect® v.21.5 software, where the phase and grain boundaries could be treated as point-defined linear segments. Vectorized images were imported into modeling software (AutoCAD® 2016), visually adjusted for accuracy and reduction of non-real sharp angles that could result in computational artifacts, and converted to appropriate file types for upload into ANSYS® Mechanical APDL finite element modeling software. ANSYS® software utilized was initially Mechanical APDL v.15.1, and was updated each year through ANSYS® v.18.2. For geometry consistency, files imported to ANSYS® consisted of keypoints and line segments only, and areas (for 2-D) and areas and volumes (for 3-D) were added directly in the APDL window.

Following completion of the model geometries and ensuring continuity of the highest order geometric features (areas or volumes, as required), element types were selected and applied to the model. The element types vary depending on model geometry and the desired calculations, see sections below for specifics. Next, model material properties were assigned to the highest order features. Finally, the FEM mesh was created, consisting of nodes and elements as defined by the element type. Each mesh size and shape was selected to minimize errors and artifacts and to maximize the resolution (notably at phase boundaries) while maintaining feasible computation times. At times ANSYS® SmartSize functionality was used, but when this was not achieving a desired mesh, manual mesh sizing was utilized.

For these models, numerous boundary conditions are possible depending on the desired real life loading condition desired for replication. For this study, boundary conditions were applied to simulate a thin slice of a tensile specimen at the center-line, Figure 42. The bottom row (or plane, for 3-D) of nodes is constrained in the y-direction (tensile direction), with the bottom center node constrained in the x (nodes along the x and z centerlines, for 3-D) direction to prevent movement while allowing for contraction due to Poisson's effects. A uniform displacement (constant strain) was applied to the top row (or plane) of nodes to simulate the effect of a tensile displacement on the microstructure where the phase interfaces are strong in order to simulate a strain-rate controlled tensile test [10], [85]. The applied displacements were varied to the desired regions of the stress-strain curve of the materials to observe the distributions of the local stresses and strains within the microstructure at various stages of tensile deformation.

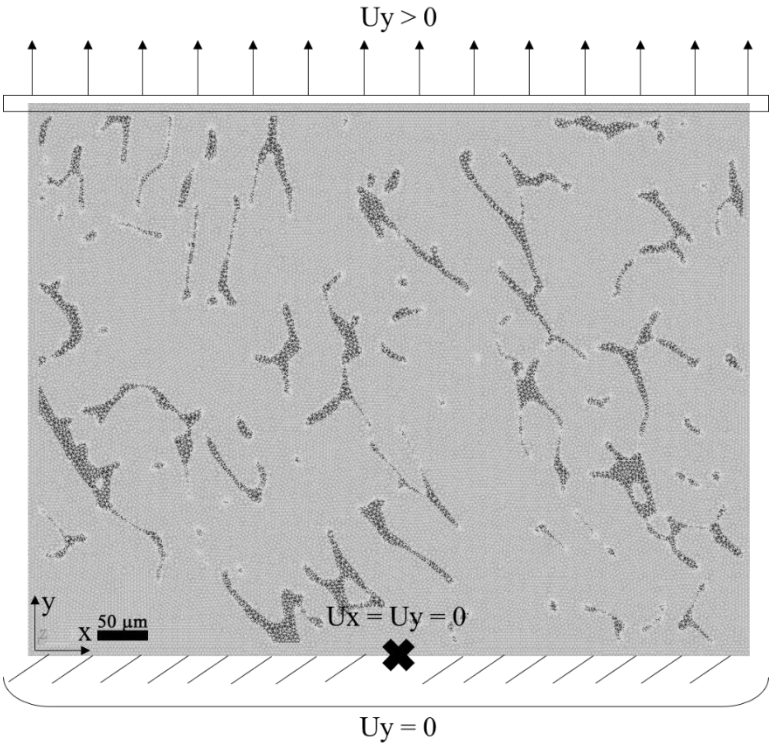

Fig. 42. Schematic diagram of the standard constraints applied to the 2-D FEM models.

b. Model Validity Checks

In order to verify the validity of the FEM results, each model must be checked for consistency of results with respect to the loads and constraints, and with respect to the mesh size of the model. Due to the fundamentals of the finite element method, the solution to the problem is only as good as its setup. Possible issues that can arise are artifacts due to abnormalities in the geometry or shape irregularities in the mesh, or artifacts (or outright failure) due to abnormal physics resulting from the setup of the constraints and loading conditions. Each of the models used in this research was checked systematically for these issues, and corrections to the model were made in response to any irregularities.

To check for the validity of the boundary conditions, the general shape (rectangles of the same dimensions) were tested as single phase and bi-crystal models with uniform

properties. These simplified geometries were then given the same desired boundary conditions described in the previous section, and displacements were applied. Control input material properties such as elastic modulus and Poisson's ratio were applied, and the solution results were tested for consistency with the governing equations. The resulting the x and z-strains must be uniformly equivalent to the expected values corresponding to contraction by Poisson's ratio and the stress distributions predicted by Hooke's Law, $\sigma = E \cdot \varepsilon$, in the y-direction must be uniform and equal to the expected values.

A similar method is used to check the model geometry for consistency. In this case, the actual model geometry is used, but uniform properties are applied to all areas/volumes (i.e. phases). The y-stresses in the tensile directions must match the Hooke's law solution in the elastic region, and the x-stress distribution must show uniformity relating to Poisson's ratio. Often the models show local variations reflecting artifacts caused by the constraint conditions, mesh, and geometry, but the values are ~10 orders of magnitude smaller than those in the y-direction and are therefore negligible.

The dependency of the results on the mesh size and structure can be a real concern, especially for a complex model. To test the mesh size, a mesh is selected for a microstructure given an appropriate element size and number of nodes to achieve the desired resolution, and the mesh generator is optimized to eliminate warnings or errors. Then meshes of similar sizes both larger and smaller than the desired size are generated, and the same constraint solutions are obtained for each one. Upon comparison of the solutions, the values must be consistent. Significant changes in the solution due to small variations in the mesh size indicate a non-negligible mesh-size dependency and a new mesh size is selected in a more stable size region.

ii. Individual Model Specifics

a. Unaged Isotropic Model

i. Material System and Properties

A two-dimensional FEM model based on the real ferritic-austenitic duplex microstructures of each of the CF–3 and CF–8 steel was developed based on optical micrographs taken of the microstructures of the unaged specimens, Figure 4 for CF–3 (CF–8 is qualitatively similar). These models were developed on the scale of hundreds of microns, thus it only incorporates the ferrite and austenite phases. Phase material properties were investigated in the elastic deformation region of the stress-strain curve, and the properties applied to the system were obtained directly through instrumented nanoindentation presented in Chapter III. Due to the scale of the model, the randomness of the orientation distributions from the bulk scale of the real tensile specimens, and the randomness of the obtained nanoindentation data, the models here are defined as isotropic for both phases. The input properties, Table 7, are to satisfy the linear/elastic/isotropic mechanical model, and include the elastic modulus, E, and Poisson's ratio, ν, of the ferrite and the austenite. As in the nanoindentation procedure, Poisson's ratio is assumed to be 0.29 for both phases [112].

Table 7. Input properties for 2-D isotropic CF–3 and CF–8 duplex microstructure models.

DSS	Phase	Elastic Modulus (Pa)	Poisson's Ratio
CF–3	Austenite	$178.6 \cdot 10^9$	0.29
	Ferrite	$185.3 \cdot 10^9$	0.29
CF–8	Austenite	$166.7 \cdot 10^9$	0.29
	Ferrite	$176.6 \cdot 10^9$	0.29

ii. Model and Parameters

2-D FEM models of the unaged CF–3 and CF–8 microstructures were developed in the ANSYS® Mechanical APDL version 16.2 software. The optical micrographs of the duplex microstructures, were converted to vector format using RasterVect version 21.5 software and the vectorized microstructure images were meshed in the ANSYS® software using a triangular Solid, Plane 183 element, Figure 43 (CF–3). There are six nodes per element and the elemental edge dimension is 0.075 units (equivalent to ~3.2 μm). The elastic material model properties of the ferrite and austenite phases utilized in the FEM model were obtained by instrumented nanoindentation, Table 7. The applied displacement was equivalent to 0.1% strain, which is within the elastic deformation region of the stress-strain curve, ensuring modeling of the purely elastic behavior of the steels.

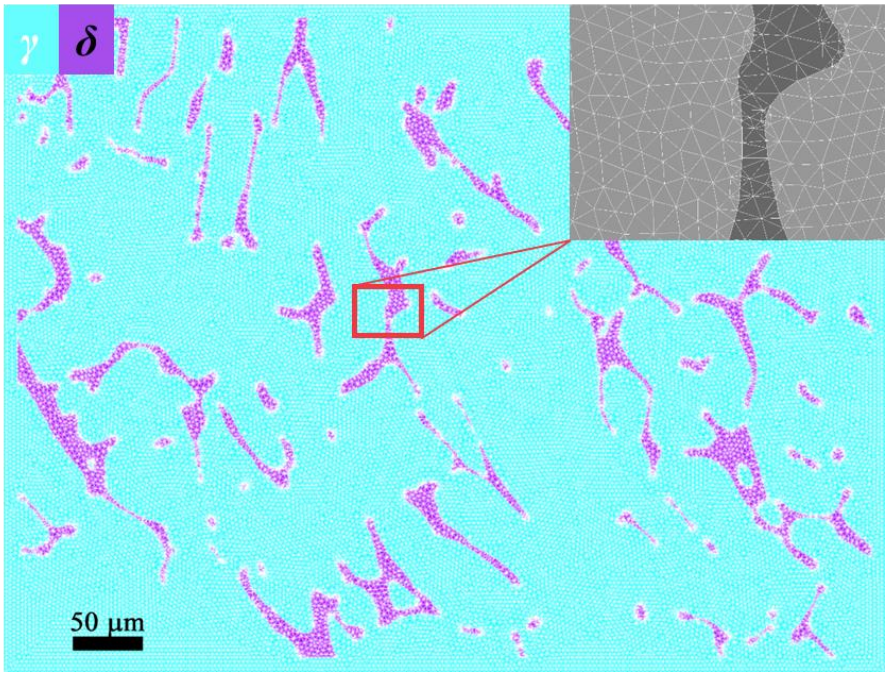

Fig. 43. 2-D isotropic duplex microstructure model including mesh and phases of CF–3.

iii. Model Checks

The constraints were checked by single crystal tests with defined properties of $E = 200\ GPa$ and $\nu = 0.29$, and by a bi-crystal with defined properties of $E_1 = 200\ GPa$, $E_2 = 220\ GPa$, and $\nu_1 = \nu_2 = 0.29$ and found to be consistent with the governing equations.

The model geometry, constraints, and mesh were tested with all phases defined by properties of $E = 200\ GPa$ and $\nu = 0.29$. The y-direction solution was found to match exactly to the governing equations. The x-direction solutions were found to result in stresses ~10^{11} Pa smaller than the y-direction stresses, meaning these variations are negligible.

The mesh size dependency in increments of 0.01 from 0.055 to 0.095 around the defined element size of 0.075 units was evaluated and found to be negligible.

b. Unaged Anisotropic Model (3D)

i. Material System and Properties

The isotropic elastic modulus, *E*, of the CF–8 steel has been determined by instrumented nanoindentation using an assumed Poisson's ratio, *v*, of 0.29 [98]. However, in this study, it is desirable to utilize the anisotropic elastic (compliance) matrix due to the local anisotropy present in the material as a result of different crystalline orientations. These orientations are essentially random in a specimen of a large enough volume, but in a small enough region of interest (ROI), the random variations will balance to the isotropic condition, and therefore the anisotropy must be taken into account. The anisotropic stiffness matrix for the ferrite and austenite phases in an SAF 2304 duplex stainless steel system was obtained from the literature and utilized here, Table 8 [132]. Furthermore,

though the overall orientation of the grains is random in this material, there is a known orientation relationship (Kurdjamov-Sachs relationship, where $\{111\}_\gamma \| \{110\}_\delta$ and $\langle 1\bar{1}0\rangle_\gamma \| \langle 1\bar{1}1\rangle_\delta$) between the ferrite islands and austenite matrix. It can be seen in the electron backscatter diffraction (EBSD) orientation map, Figure 27, that the larger austenite grains contain ferrite islands of a consistent orientation following this orientation relationship.

Table 8. Compliance constants for both phases applied to the 3-D anisotropic model.

Ferrite ($\cdot 10^{-11}\ Pa^{-1}$)				**Austenite ($\cdot 10^{-11}\ Pa^{-1}$)**			
x-orientation	**S11**	**S12**	**S44**	**x-orientation**	**S11**	**S12**	**S44**
100	0.715	-0.259	0.859	100	0.988	-0.382	0.820
101	0.443	-0.077	1.585	111	0.348	-0.062	1.460
101 + 15° Rot.	0.477	-0.111	1.483	111 + 15° Rot.	0.388	-0.102	1.340

ii. Model and Parameters

The FEM modeling and analysis was performed using ANSYS Mechanical APDL v.17.1 software. A three-dimensional (3-D), anisotropic FEM models was created for the CF–8 steel in the unaged and aged conditions. The models have been created based on the real 2-D microstructures of the steels observed via EBSD. The 3rd dimension is added as a thickness of 0.036 units (5% of the height), in order to allow for calculation and observation of stresses and strains in the z-direction, which are important due to the application of the 3-D anisotropic elastic properties (in an isotropic system, the x and z results will be equivalent). The models were created using AutoCAD v.14.2 subsequently imported into ANSYS for meshing. Independent geometric volumes were created for each individual ferrite phase grain, and these volumes are incorporated as islands within two continuous volume austenite matrices. The volumes were meshed using triangular 3-D elements of

type *Solid 20-node 186* using the ANSYS Smart Size feature, which utilizes an algorithm to determine the best functional mesh size for optimal nodal distribution and computation time, Figure 44. A Smart Size of 5, corresponding to a mid-size mesh setting, was utilized for this work.

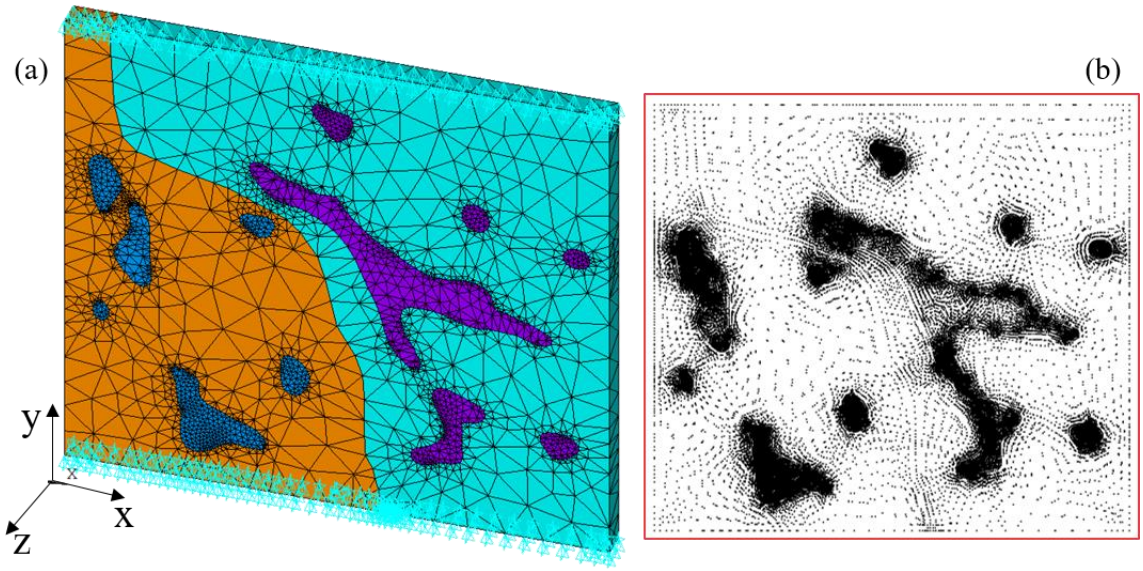

Fig. 44. Meshed CF–8 microstructure **(a)** elements and constraints and **(b)** corresponding nodes with an added-thickness third dimension to accommodate anisotropy.

The properties, as discussed in Chapter III, were included in the ANSYS materials models as *Elastic-Anisotropic, Plastic-Bilinear* material properties, and the ferrite grains were rotated with the respect to the austenite matrix following the K-S orientation relationship and the EBSD results. Rotations of the compliance matrices were performed using equations derived for crystalline cubic anisotropic structures [133]:

(1) $S'_{11} = S_{11} - 2(S_{11} - S_{12} - 0.5 \cdot S_{44})(m_1^2 n_1^2 + l_1^2 n_1^2 + l_1^2 m_1^2)$

(2) $S'_{12} = S_{12} + (S_{11} - S_{12} - 0.5 \cdot S_{44})(l_1^2 l_2^2 + m_1^2 m_2^2 + n_1^2 n_2^2)$

(3) $S'_{44} = S_{44} + 4(S_{11} - S_{12} - 0.5 \cdot S_{44})(l_2^2 l_3^2 + m_2^2 m_3^2 + n_2^2 n_3^2)$.

Loads and constraints were added to the system in a manner representative of a slice of constant thickness taken from a tensile specimen, where the bottom of the model corresponds to the center plane of a real specimen. The loading condition was applied in the form of a uniform y-displacement to each node on the top plane of the plane equal to 0.050%, 0.075%, and 0.100% strain, or 0.000362, 0.000543, and 0.000724, y-unit displacements, respectively.

iii. Model Checks

In order to check the loads and constraints, the completed geometric model is meshed as normal, but each of the 4 individual phase orientations was assigned the same isotropic properties. An elastic modulus of 200 GPa and Poisson's ratio of 0.29 were used in this case. The applied load was a displacement of 0.000724 units, equivalent to 0.118% strain (the unit value was rounded off) was applied along the y-direction. The finite element analysis results reveal that the output y-strain is uniformly equal to 0.00118, which is consistent with the paper calculations.

In this case, the mesh size dependency was tested by using the final model geometry, constraints, and properties, but with progressively coarser meshes (i.e. progressively smaller numbers of elements) as determined by Smart Size. The Smart Size 5 that was used in the forthcoming results was changed to size 2, 5, and 10 in order to determine whether the number of nodes significantly affects the results. Maximum stress differences of about 3-5 MPa were found between the 3 finest meshes (1, 2, and 5), where the magnitude differences show no real trend and appear to be determined to a small error by the actual elemental distributions and some random variation. However, there are large differences seen been the 3 finer meshes and the coarse mesh size 10, indicating that there is a mesh

size dependence beginning somewhere above smart size 5. This results in different locations for maximum and minimum values, as well as non-negligible magnitude changes. However, since mesh size 5 was utilized for the results presented here, mesh size can safely be ruled out as a significant influence in the results.

c. Aged Isotropic Microstructure – Plasticity Near Yield

i. Material System and Properties

The properties of the duplex steels near the yielding point are interesting for two reasons: because the yielding of a structural material is oftentimes considered failure, resulting in the need for replacement, and because the tensile results of the steels in this study show that there is little-to-no evolution of the yield strength during thermal aging. Since yielding is a local mechanical phenomenon, it is worthwhile to use the FEM technique to explore the effects of the changing local phase properties on the evolution of the yielding behavior. In this study, the 2-D isotropic model previously developed to observe the elastic deformation behavior of the unaged CF–3 steel is adapted to explore the near-yield behavior of the microstructure.

The material model used for this model calculation consists of a linear/elastic/isotropic model for the elastic portion of deformation, with the addition of a Mises Plasticity model. The overall model utilizes a bi-linear form, where the deformation after yielding is considered to also follow a linear form, with a slope known as the tangent modulus (E_{tan}). This approximation holds well at small strains near the yield point. Note that for the FEM model purposes, the yield point is defined as the proportional limit, not at the offset engineering yield stress. The required properties input into the FEM material models are available in Table 9. The elastic modulus of both the ferrite and austenite phases

Table 9. Input properties for the bilinear models of the unaged and aged steels.

DSS	Phase	Elastic Modulus *(Pa)*	Poisson's Ratio	Yield Strength *(σ_{PL}; Pa)*	Tangent Modulus *(Pa)*
CF–3 Unaged	Austenite	$204.0 \cdot 10^9$	0.29	$165 \cdot 10^6$	$570.4 \cdot 10^7$
	Ferrite	$221.5 \cdot 10^9$	0.29	$165 \cdot 10^6$	$570.4 \cdot 10^7$
CF–3 Aged	Austenite	$204.0 \cdot 10^9$	0.29	$165 \cdot 10^6$	$570.4 \cdot 10^7$
	Ferrite	$221.5 \cdot 10^9$	0.29	$350 \cdot 10^6$	$570.4 \cdot 10^7$

were determined by nanoindentation and the Poisson's ratio was assumed to be 0.29 for both phases. Some assumptions were made to describe the yield behavior of the individual phases, as reliable values were not available through the nanoindentation testing or in the literature. In general, it is commonly noted that most metals, including stainless steels, possess a linear relationship between yield strength and hardness, $H = m \cdot \sigma_y$ [90], [134]. Thus, taking this assumption and noting that the nanohardness of the ferrite and austenite are very similar to one another in the unaged condition, it can be assumed that the yield strengths of the two phases are approximately equal. Thus the initial unaged yield stress has be set for both phases to the bulk proportional limit measured from the tensile tests. Likewise, the value of E_{tan} for each phase was defined by a linear approximation of the strain hardening between the proportional limit and 0.2% offset yield strength on the tensile curve. Since the hardness of the austenite is shown not to change during aging, the yield strength of the austenite is held constant. The ferrite nanohardness of the CF–3 steel increases 47% during aging to the longest aging time at the highest aging temperature, which based on these assumptions results in the ferrite yield strength (σ_{PL})increasing 47% from 165 MPa to 350 MPa. Assuming that the local proportional limit and offset yield stress increase the same amount for the ferrite, the tangent moduli are assumed not to change during thermal aging.

ii. FEM Model and Parameters

A 2-dimensional (2-D) geometry based on the real microstructure of the CF–3 duplex stainless steel was created using AutoCAD software and uploading into ANSYS v17.2. This same microstructure geometry model was previous utilized to analyze the elastic deformation behavior of the unaged steel and a more detailed account of the geometry procedures can be found in the above section for the 2-D Isotropic Model. The loading constraints were also generally the same, where a zero constraint was applied to the bottom nodes and a constant strain was applied in the y-direction on the top nodes. However, in order to capture the onset of local yielding, the loading was divided into ~100 substeps of ~0.002% y-strain. The substeps corresponding to the onset and progression of yielding were identified and the data for that set of substeps were analyzed.

The material model phase properties were obtained from the nanoindentation data just as in the elastic isotropic model. For consistency of comparison, the 2-D isotropic model based on the unaged CF–3 microstructure was implanted for both the unaged and aged models, excepting that the properties were updated to reflect the aging evolution of the ferrite phase, Table 9. At the time of the adaptation of this model to investigate the near-yield behavior, updated values of the elastic modulus of each phase were available and implemented.

iii. Model Checks

The models presented in this section possesses the same geometry, mesh, and constraints as those presented above for the 2-D elastic isotropic model, and therefore the same checks that apply above apply here. The model was successfully validated

immediately prior to running these solutions, including implementation of the bi-linear elastic/plastic properties.

d. 2-D Isotropic Model – Carbides and Phase Boundaries

i. Material System and Properties

The FEM models presented in the previous sections contain structural geometries on the order of hundreds of microns (μm). At this scale, only the duplex ferrite and austenite phases are resolved in the micrographs and feasibly resolved in the model geometry. However, the mechanical behavior of the regions near the phase boundary can be affected by structural components on a smaller scale. For the CF–8 system, the phase boundaries are found by TEM in Chapter 3 to be occupied by regularly occurring $M_{23}C_6$ carbides. In order to investigate the stress-strain effects at the boundaries and the effects of the carbides, a new model is warranted at this reduced scale.

New FEM models were thus created including the ferrite and austenite phases, with known properties as determined by nanoindentation. However, due to the scale of the $M_{23}C_6$ carbides on the order of ~100 nm, experimental determination of their properties was outside the reach of this project. Properties of Cr carbides in stainless steels were thus obtained from the literature. Mburu, et al. [37], report the composition of the unaged carbide in the C –8 steel to contain approximately $Cr_{14}Fe_9C_6$ stoichiometry. Han, et al. [126], report a Young's modulus value for a very similar stainless steel carbide of stoichiometry $Cr_{15}Fe_8C_6$ of $E = 352.3\ GPa$ and a Poisson's ratio of $\nu = 0.31$ determined by ab-initio calculations. These elastic property values were utilized for the carbides in the FEM models of the CF–8 boundaries containing carbides.

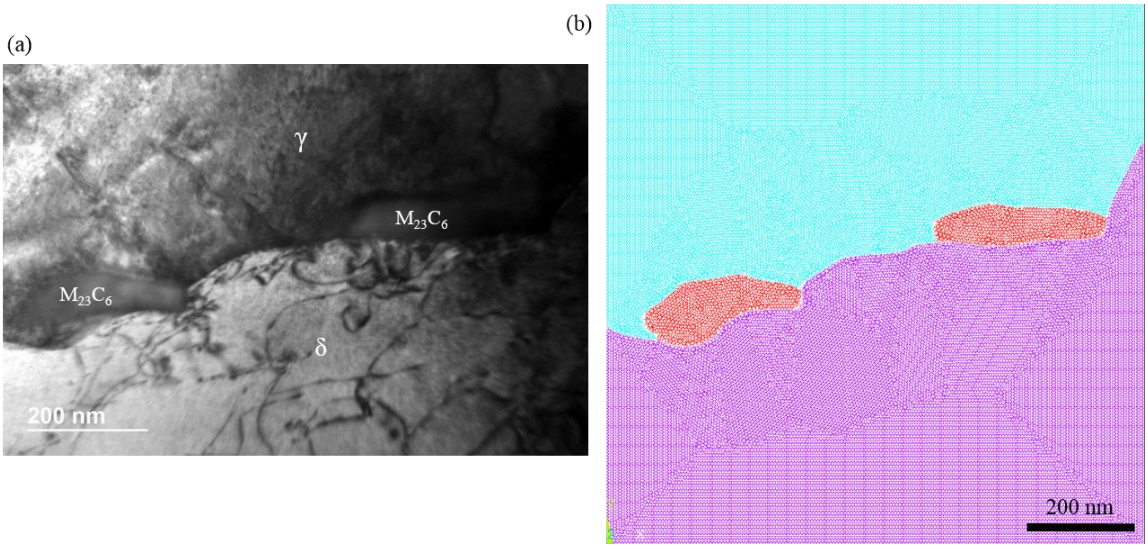

Fig. 45. (a) TEM micrograph of a representative CF–8 microstructure phase boundary and **(b)** corresponding meshed FEM model of the boundary area with carbides.

ii. FEM Model and Parameters

FEM models of the phase boundaries were created for the CF–8 steel based on TEM micrographs of the unaged steel, Figure 45. This particular micrograph was chosen because it was deemed to be the most representative of the size, morphology, and distribution of the boundary carbides of the unaged CF–8 steel, respectively. Both models (one including carbides at the boundary, one excluding them) are square of corresponding to real dimensions of 1 μm x 1 μm. The models were meshed with the 2-D Solid Plain 183 elements for a total of 131,089 nodes. The boundary conditions include constraints equivalent to those applied to the previous isotropic models, simulating a slice at the centerline of tensile specimen. The loading condition consisted of a uniform y-displacement equivalent to 1% strain. The isotropic model was limited to elastic behavior.

iii. Model Checks

The constraints were checked by single crystal tests with defined properties of $E = 200\ GPa$ and $\nu = 0.30$, and by a bi-crystal with defined properties of $E_1 = 200\ GPa$, $E_2 = 225\ GPa$, and $E_3 = 500\ GPa$, and $\nu_1 = \nu_2 = 0.30$ and $\nu_3 = 0.20$ and found to be consistent with the governing equations.

The model geometry, constraints, and mesh were tested with all phases defined by properties of $E = 200\ GPa$ and $\nu = 0.29$. The y-direction solution was found to match exactly to the governing equations. The x-direction solutions were found to result in stresses ~10^{10} Pa smaller than the y-direction stresses, meaning these variations are negligible.

The mesh size dependency in increments of 0.02 from 0.03 to 0.07 around the defined element size of 0.05 units was evaluated and found to be negligible.

Table 10. Elastic input properties for the ferrite, austenite, $M_{23}C_6$, α, and α' phases. [126], [135]–[138]

DSS	Phase	Elastic Modulus *(Pa)*	Poisson's Ratio	Method	Source
CF–3	Austenite	$204.0 \cdot 10^9$	0.29	Nanoindentation	Chapter III
	Ferrite	$221.5 \cdot 10^9$	0.29	Nanoindentation	Chapter III
	α	$214.8 \cdot 10^9$	0.29	Various	[132,133,134]
	α'	$245.9 \cdot 10^9$	0.29	Various	[132,133,134]
	G-phase	$209.0 \cdot 10^9$	0.40	Ultrasonic	[135]
CF–8	Austenite	$210.8 \cdot 10^9$	0.29	Nanoindentation	Chapter III
	Ferrite	$225.9 \cdot 10^9$	0.29	Nanoindentation	Chapter III
	$M_{23}C_6$	$352.3 \cdot 10^9$	0.31	Ab-Initio	[123]

e. 2-D Isotropic Model – Decomposed Ferrite

i. Material System and Properties

While the original isotropic model of the duplex microstructure was several orders of magnitude larger than the scale required adequately demonstrate the boundary carbides, the boundary model consisting of 1000 nm x 1000 nm geometry is much too large to present the nanoscale decomposition products within the ferrite. The spinodal decomposition wavelengths (domain sizes) are on the order of 2 – 5 nm for the α and α' phases. Furthermore, inclusion the G-phase precipitates observed at the accelerated aging condition are typically around 4 – 10 nm in size. Therefore, an additional isotropic model representing these phases was created, to fully cover the effects of embrittlement across the DSS length scales.

The decomposed nanostructure consists of two networked domains of α and α', which form a metal matrix/metal reinforcement composite system not unlike that observed on the microscale for the duplex structure. The elastic modulus and Poisson's ratio were approximated from the literature for the Fe-Cr system, where the relatively compositions of Fe and Cr from which the properties were obtained were based on the APT-determined amplitudes. Experimental data for Fe-Cr systems ranging from pure Fe to pure Cr were compiled from multiple sources [SSS], and the intermediate values required for the α and α' compositions of the CF–3 D4 (400 °C, 17,200 h) were interpolated from the data, Table 10. In general, based on the compiled literature data, the elastic modulus is expected to steadily increase with increasing Cr composition, and the Poisson's ratio is expected to decrease over the same range. A model including G-phase precipitates is also presented, with the G-phase properties, Table 10 being derived from the elastic properties of the most

similar nickel silicide that could be found in the literature: a Ni_3(Si,Ti) silicide possessing the same crystal structure (cubic $L1_2$) and a very similar stoichiometry to the G-phase [138].

ii. FEM Model and Parameters

FEM models were created based on the real decomposed nanostructure of the CF–3 D4 aging condition (400 °C, 17,200 h). The real nanostructure was based off of a thin slice of a 3-D APT reconstruction depicting the Fe and Cr distributions and elemental Ni segregations, Figure 46. Two models were created with the same spinodal structure, with one containing G-phase particles and the other containing no G-phase. Both models are rectangular of real dimensions 48.9 nm x 34.8 nm. The model meshes were formed with triangular Solid Plane 183 elements containing 205,295 nodes with G-phase and 204,492 nodes without G-phase. The boundary conditions include constraints equivalent to those applied to the previous isotropic models, simulating a slice at the centerline of tensile specimen. The loading condition consisted of a uniform y-displacement equivalent to 1% strain, and the isotropic model was limited to elastic behavior.

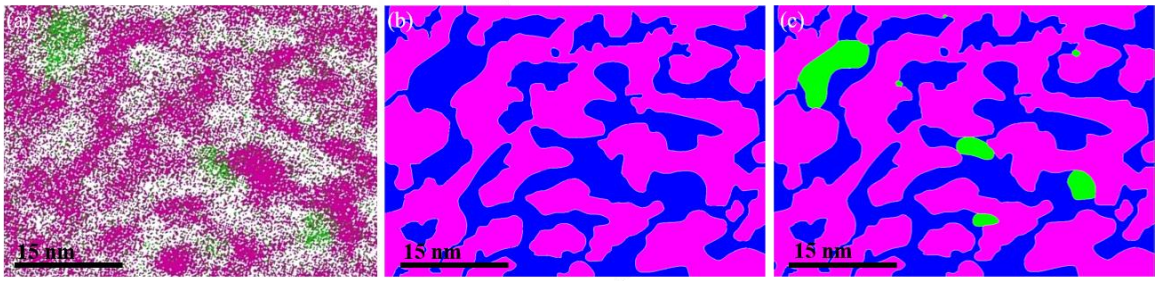

Fig. 46. (a) APT reconstruction of the decomposed CF–3 microstructure and corresponding FEM models of the spinodal area **(b)** without and **(c)** with G-phase.

iii. Model Checks

The constraints were checked by single crystal tests with defined properties of $E = 200\ GPa$ and $\nu = 0.30$, and by a bi-crystal with defined properties of $E_1 = 200\ GPa$, $E_2 = 225\ GPa$, and $E_3 = 300\ GPa$, and $\nu_1 = \nu_2 = \nu_3 = 0.30$ and found to be consistent with the governing equations.

The model geometry, constraints, and mesh were tested with all phases defined by properties of $E = 200\ GPa$ and $\nu = 0.30$. The y-direction solution was found to match exactly to the governing equations. The x-direction solutions were found to result in stresses ~10^{10} Pa smaller than the y-direction stresses, meaning these variations are negligible.

The mesh size dependency in increments of 120 from 120 to 360 around the defined element size of 240 units was evaluated and found to be negligible.

C. RESULTS

i. Unaged Isotropic Model (2-D)

The FEM results for the example CF–3 and CF–8 microstructures in Figs. 47(a) – (d) illustrate the effects of applied elastic deformation on the *δ*–ferrite and *γ*–austenite phases. Contour plots of the von Mises stresses determined by FEM, Figs. 47(a) – (b), demonstrate higher *δ*–ferrite phase stresses (yellow, orange, and red contours) and the lower *γ*–austenite phase stresses (blue and green contours). The highest stresses (red contours) occur in the narrowest regions of the ferrite phase. Similarly, the von Mises strains, Figs. 47(c) – (d), exhibit significant heterogeneity in both steels' microstructures. In general, the strains are greater in the *γ*–austenite phase (green, yellow, orange, and red contours) than in the *δ*–

ferrite phase (blue contours). The maximum stress determined by FEM for this applied deformation condition is 188 MPa for CF–3, Fig. 47(a), whereas it is 187 MPa for CF–8, Fig. 47(b). In both cases, the stresses determined from the FEM model are about 100 MPa less than the bulk engineering yield stress. The maximum von Mises strain is calculated as 0.1028 % in the CF–3 steel, Fig. 47(c), and 0.1043 % in the CF–8 steel, Fig. 47(d). The bulk elastic modulus calculated from the FEM model by using the stress in the y–direction and the applied strain are 179.3 GPa and 174.1 GPa for CF–3 and CF–8, respectively, which are within 6% of the experimentally measured bulk values.

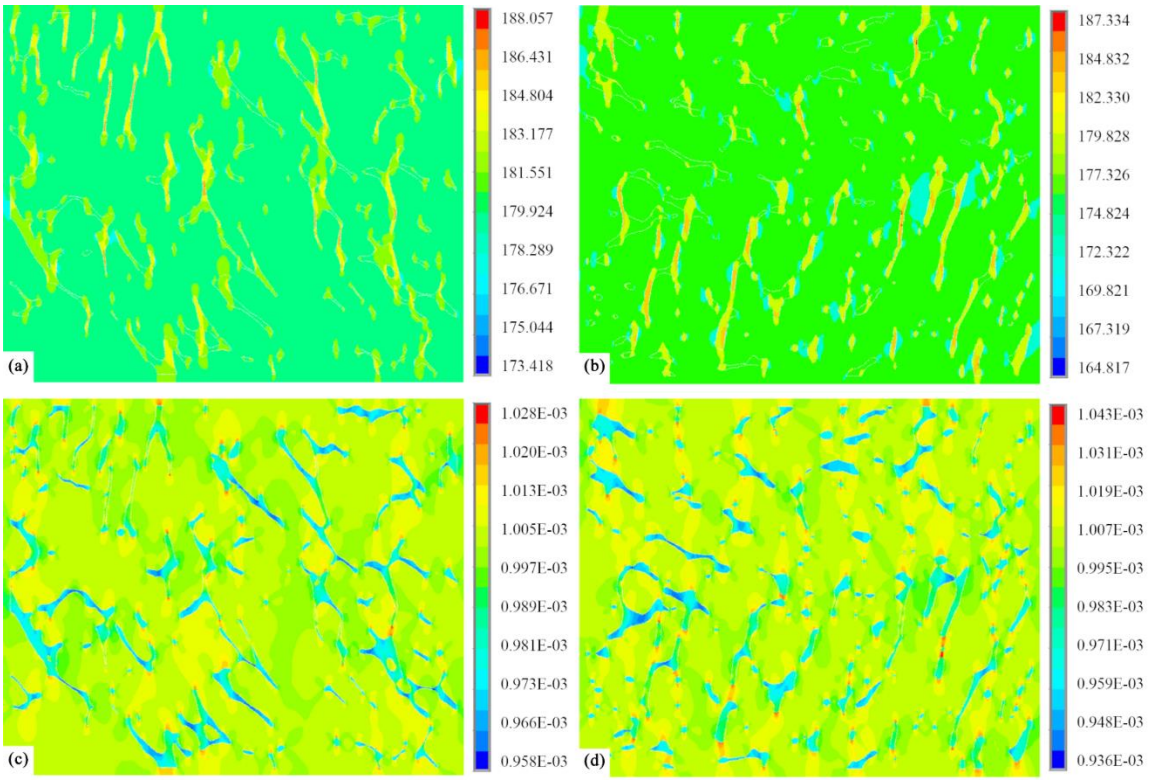

Fig. 47. Von Mises **(a)**,**(b)** stress and **(c)**,**(d)** distributions for the **(a)**,**(c)** CF–3 and **(b)**,**(d)** CF–8 duplex microstructure models.

Since the von Mises elastic stresses and strains exhibit significant heterogeneity in the microstructure of both steels, the average stresses and strains in each phase were calculated in order to quantify the visual results by determining partitioning ratios of the form $\sigma_\gamma/\sigma_\delta$ and $\varepsilon_\gamma/\varepsilon_\delta$, which permit direct comparison of the ferrite and austenite response. The partitioning ratios of the von Mises stresses $(\sigma_\gamma/\sigma_\delta)$ for CF–3 and CF–8 are 0.984 and 0.978, respectively, which indicates that the stresses are higher in the ferrite phase. The partitioning ratios of the von Mises strains $(\varepsilon_\gamma/\varepsilon_\delta)$ indicate that the strains are higher in the austenite phase, where the ratios are 1.022 and 1.038 for CF–3 and CF–8, respectively. Furthermore, the stress and strain distributions are influenced by differences in morphology of the microstructures in the steels. The CF–3 exhibits greater stress and strain homogeneity in the matrix phase away from the heterophase interfaces when compared to CF–8. Larger areas of uniform coloration in the relatively unconstrained regions of the austenite matrix phase away from the heterophase interfaces can be observed in Figs. 47(a) and 47(c) when compared to Figs. 47(b) and 47(d).

In these steels, both phases are considered to be ductile [139] and thus both phases are expected to deform plastically. The regions exhibiting the highest von Mises stresses and strains are the most likely locations for the onset of yielding. Since the yield stress values for the constituent phases could not be determined in the present study by nanoindentation due to limitations of the extant models, the plastic stress and strain distributions were not investigated by FEM in this study. Analysis of the nanohardness and misorientation distributions related to the plastic strain after deformation of the CF–3 and CF–8 steels suggests that the strengths of the constituent phases are similar. Since the elastic deformation stresses are found to be higher in the δ–ferrite phase than in the γ–austenite

phase, and assuming equal values for the yield stress, the ferrite phase would plastically deform prior to the austenite phase. However, the actual location for the onset of yielding will depend on the exact magnitude of the yield stresses relative to the stress and strain distributions in the microstructure and will be influenced by local anisotropy.

ii. Unaged Anisotropic Model (3D)

The micromechanical response of the material under applied tensile loading gives valuable information about the loading behavior of the CF–8 steel at the microstructural level. In this model, tensile displacements equivalent to 0.050%, 0.075%, and 0.100% strain were applied in the y-direction of the model. The y-direction is equivalent to the $[1\bar{1}0]$ direction in material 1 (f.c.c. austenite), $[1\bar{1}\bar{1}]$ direction in material 2 (b.c.c. ferrite), and a rotation of 15° from those directions, respectively, about the z and y axes for materials 3 and 4. Plots of the von Mises stress and strain distributions, Figure 48 (a) and (b), are important for analyzing the potential yielding locations in the microstructure with these orientations, assuming validity of the von Mises Criterion.

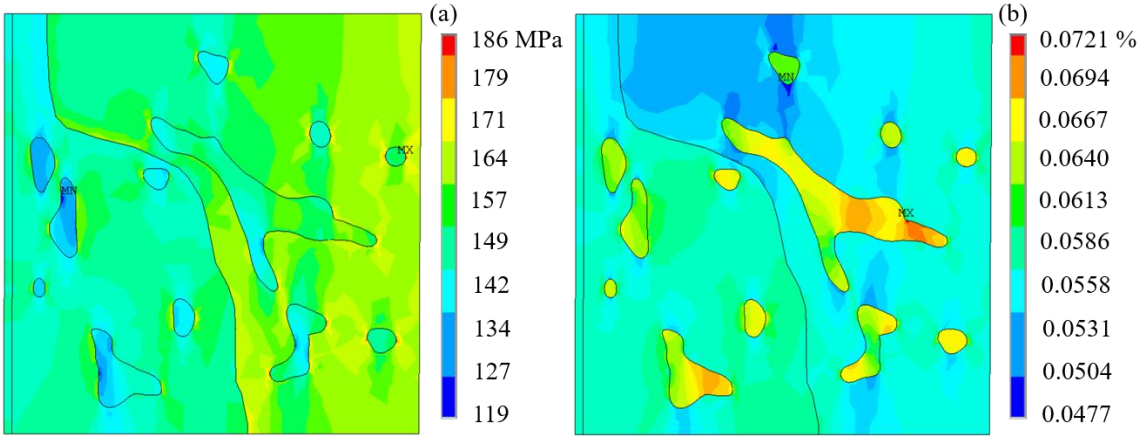

Fig. 48. Von Mises **(a)** stress and **(b)** strain distributions for the CF–8 3-D anisotropic duplex microstructure model.

The von Mises stress distribution for an applied displacement equal to 0.050% strain, Figure 48 (a), shows a range of stresses varying from a minimum value of 119 MPa located in the ferrite (material 4) to a maximum value of 186 MPa located in the austenite (material 1). The maximum value is 100 MPa lower than the expected engineering yield stress (286 MPa) of either phase in the unaged condition, and thus the results are fully within the elastic region for this condition. The maximum von Mises stresses are located within the austenite phase near the phase boundaries with the ferrite islands, and reflect the effect of interaction stresses at the phase interfaces. Furthermore, there is a directional component to the maximum stress regions. These areas with high stress concentrations are located primarily along interfaces that are parallel to the loading direction where transfer of the stress across the interface is most significant, and thus likely causes large stresses along the interface itself, which in this model is assumed to the much stronger than the yield strength of either phase. The minimum von Mises stresses are concentrated with the ferrite phase, mostly in the material 3 and 4 region that is rotated an additional 15° from the right side of the model. As for the maximum stresses, the minimum stresses have a directional component and are located in the narrower regions of the ferrite which are aligned with the loading direction. This can be attributed to the greater amount of interface area aligned with loading, allowing for a greater amount of stress transfer to occur.

The von Mises strains show results following similar reasoning to the stress distributions. The von Mises strains range from a minimum value of 0.0569% located in the austenite region (material 1) to a maximum value of 0.0854% in the ferrite region (material 4). As expected, these locations complement the directionality and locations of the maximum and minimum strains. Essentially, the largest strains can be expected in

regions with less stiffness in the loading direction and less ability to transfer stress to the stiffer regions, i.e. regions of ferrite that are narrow and aligned perpendicular to the loading direction. This can clearly be seen to be the case in Figure 48(b). Likewise, the lowest strains can be expected in regions of material with higher stiffness in the given loading direction, also where less stress transfer can occur. This can be clearly seen in the regions of lowest strain in the figure, which are in the austenite regions near phase boundaries perpendicular to the loading direction.

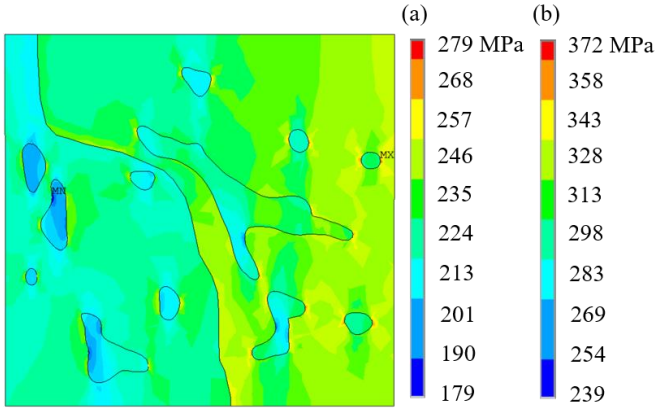

Fig. 49. Von Mises stress distributions for the CF–8 3-D anisotropic duplex microstructure model at **(a)** 0.075% and **(b)** 0.100% applied strain.

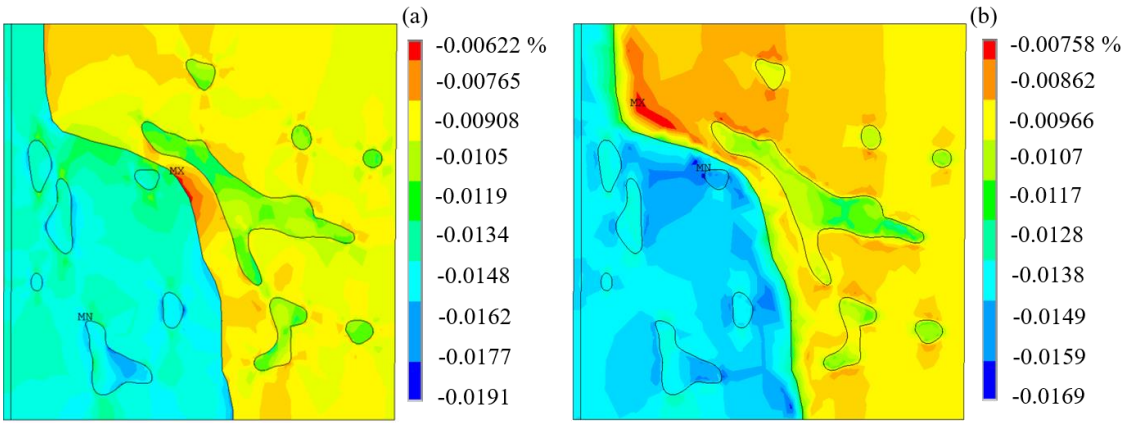

Fig. 50. (a) x elastic strain and **(b)** z elastic strain distributions for the CF–8 3-D anisotropic duplex microstructure model.

One of the most important pieces of information that can be predicted by the FEM analysis is the locations of the onset of yielding within the microstructure. As the von Mises criterion is assumed to be valid for this system, the locations for initiation of plastic deformation will be the regions where the von Mises stress first meets and exceeds the yield stress for the given phase. The yield stresses have not been incorporated into the model itself, but values for yield stress in the unaged condition (286 MPa for both phases) and the aged condition (286 MPa for austenite and 376 MPa for ferrite) can be considered when observing the von Mises stress contour plots at 0.075% and 0.100% strain, Figure 49 (a) and (b). In all cases for these orientations and loading conditions, it will be expected that austenite will yield before ferrite, as can be seen in the von Mises stress plots. The yielding will initially occur in the highest stress regions along the phase boundaries parallel to the loading direction, first in grain 1 and then later in grain 3. In the unaged case, the ferrite phase will likely begin to yield fairly soon after, as the yield stresses are the same and the overall stress range is within 100 MPa. However, in the aged condition, there will likely be a significant difference in the time/total load applied between when the austenite and ferrite phases yield, which can dramatically affect the deformation behavior, and may contribute to the change in failure mode observed after aging [8].

The effects of anisotropy can be seen most clearly in the plots of x and z-elastic strain, Figure 50 (a) and (b). In these contour plots, there can be seen a very large difference in coloration and corresponding to large, fairly uniform differences in strain magnitudes between the austenite grain on the right (material 1) and the austenite grain on the left (material 2). Since the scale of this model is on the order of ~100 μm, these variations are expected to balance over the bulk scale, and thus approximate isotropic behavior. However,

these results clearly show that on the local level, the anisotropic effects of the elastic properties are non-negligible. The x-strains in maximum region of material 3 are around 0.0169% (compressive), compared to the minimum compressive strains of 0.0076% in material 1. Similar behavior is observed for the x-stress distributions. These differences, and similar discrepancies in the z-stresses and strains, indicate significant differences in the calculations of the von Mises stresses, and thus predicted yielding locations in the material. This contributes to the results seen in the von Mises stress distributions, Figure 48(a), where of the 4 different granular orientations investigated here, the yielding is expected to occur first in material 1, an austenite grain where the $[1\bar{1}0]$ direction is parallel to the loading direction.

iii. Aged Isotropic – Elastic/Plastic Near Yield

FEM simulations of tensile deformation up to just past the elastic limit were run for a 2-D CF–3 microstructure with properties corresponding to two aging conditions: unaged and D4 (400 °C, 17,200 h). The applied y-displacement was segmented into substeps, and these substeps were analyzed to determine the relevant near-yield data. Since the elastic data was analyzed for the isotropic elastic model earlier in Chapter IV, the elastic results prior to yield follow the same trends and contours as reported there and are not revisited in this section. The goal of these models is to investigate the differences in local isotropic yield behavior of the microstructure before and after extended aging, where the effect of the ferrite hardening is known to affect the bulk behavior of the steels, but where little change is observed in the bulk tensile yield stress measured throughout aging.

a. Unaged CF–3

The onset of yielding is most clearly observed in the substep progression of contour plots for the von Mises plastic strain of the model microstructures. The von Mises plastic strains for unaged CF–3 model, Figure 51, are uniformly zero (blue coloring) up to 0.072% strain (substep 63), indicating that the microstructure is deformed purely in the elastic regime to this point. This is confirmed by the corresponding maximum von Mises stress at substep 63, $\sigma_{VM}^{max} = 163.2$ MPa, which is less than the yield strength for either phase (which are the same for the unaged specimen, $\sigma_y^{\gamma} = \sigma_y^{\delta} = 165$ MPa. At the next substep, the applied strain is increased to 0.073 % strain (substep 64) and the corresponding contour plot, Figure 51(b), shows a small region of non-zero von Mises plastic strain. The maximum values of von Mises stress and plastic strain at this point are $\sigma_{VM}^{max} = 165.3$ MPa and $\varepsilon_{VM}{}_{pl}^{max} = 1.46 \cdot 10^{-6}$. This region corresponds to the first local yielding location observed in the model, and is located within the ferrite phase, and in a grain of the ferrite with a fairly narrow, elongated structure aligned with the tensile direction. This initial yielding location is consistent with the observation of maximum stress location from the elastic isotropic model, and is consistent with the expected composite material behavior for constituent phases with different elastic moduli but the same yield stress. The calculated value of the bulk measured von Mises stress corresponding to the onset of local yielding in the steel is $\sigma_y^{bulk} = 148.9$ MPa.

The following substeps, Figure 50(c)-(f) demonstrate the progression of yielding throughout the ferrite phase, continuing to occur locally in regions of ferrite aligned with the tensile direction and highly constrained by the phase interfaces. By 0.080 % applied strain (substep 70), nearly all of the ferrite has yielded, and yielding has begun to be

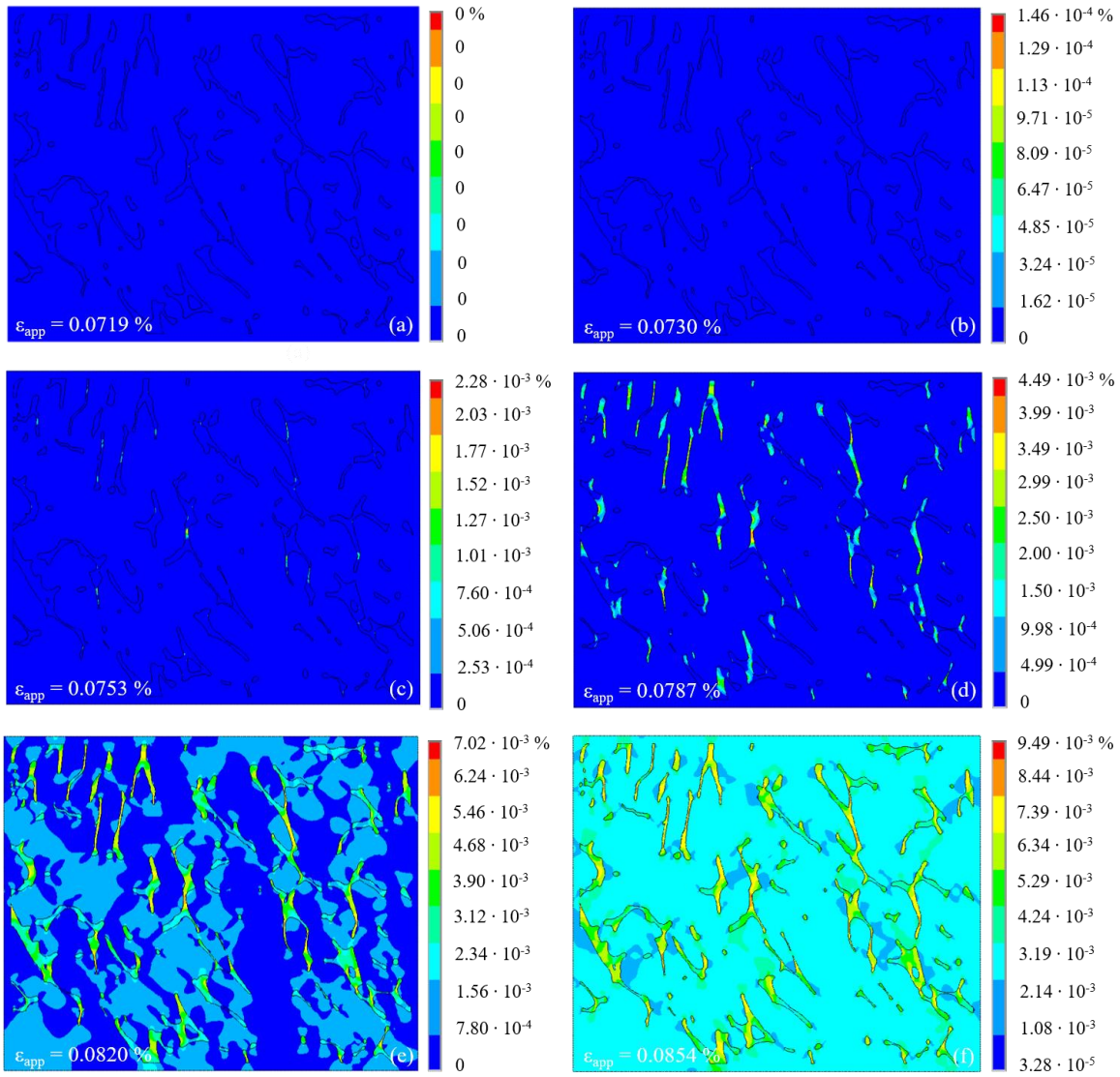

Fig. 51. Progression of von Mises plastic strain distribution in the unaged microstructure of CF–3 unaged DSS under applied load over progressive substeps from **(a)** 0.0719 % applied strain – **(f)** 0.0854 % applied strain.

recorded in regions of the austenite. At this substep, the average plastic von Mises strain in the ferrite is $\varepsilon_{VM}{}_{pl,\delta}^{avg} = 5.30 \cdot 10^{-5}$, which is about 5 times larger than the maximum von Mises strain in the austenite $\varepsilon_{VM}{}_{pl,\gamma}^{max} = 1.61 \cdot 10^{-5}$ and more than two orders of magnitude greater than the average in the austenite $\varepsilon_{VM}{}_{pl,\gamma}^{avg} = 1.19 \cdot 10^{-7}$. At this point, the ferrite is

overwhelmingly governed by the tangent modulus of the bilinear curve, while most of the austenite is still in the elastic regime. By substep 75 (0.085 % applied strain), Figure 50(f), essentially all the microstructure is yielded and both phases are deforming following the equivalent tangent modulus equations estimated from the bulk data.

b. Aged CF–3

The FEM model of the CF–3 aged at 400 °C for 17,200 h is designed to provide insight into the yielding behavior of the most advanced degree of aging studied in this investigation. The microstructure utilized for the geometry was held the same as that developed for the unaged CF–3 to facilitate direct comparison of the results of the aged to the unaged. However, the yield strength of the ferrite phase was adjusted in the aged model to account for the hardening behavior. Hence in the aged model, the ferrite elastic modulus and yield strength are both greater than the corresponding austenite properties.

Again, the onset of yielding is most clearly observed in the substep progression of contour plots for the von Mises plastic strain of the model microstructures. The von Mises plastic strains for aged CF–3 model, Figure 52, are uniformly zero (blue coloring) up to 0.076% strain (substep 67), indicating that the microstructure is deformed purely in the elastic regime to this point. This is an increase of 0.004% strain from the unaged condition before yielding occurs. The corresponding maximum von Mises stress at substep 67, $\sigma_{VM}^{max} = 173.6$ MPa, is greater than the yield strength for the austenite phase (which is the same for the unaged specimen, $\sigma_y^{\gamma} = 165$), but is located in the ferrite phase and below its yield stress, $\sigma_y^{\delta} = 350$ MPa. The corresponding maximum von Mises stress recorded in the austenite phase is $\sigma_{VM,\gamma}^{max} = 164.7$ MPa, which is just below the yield stress. Thus, this substep captures the final moments before local yielding occurs.

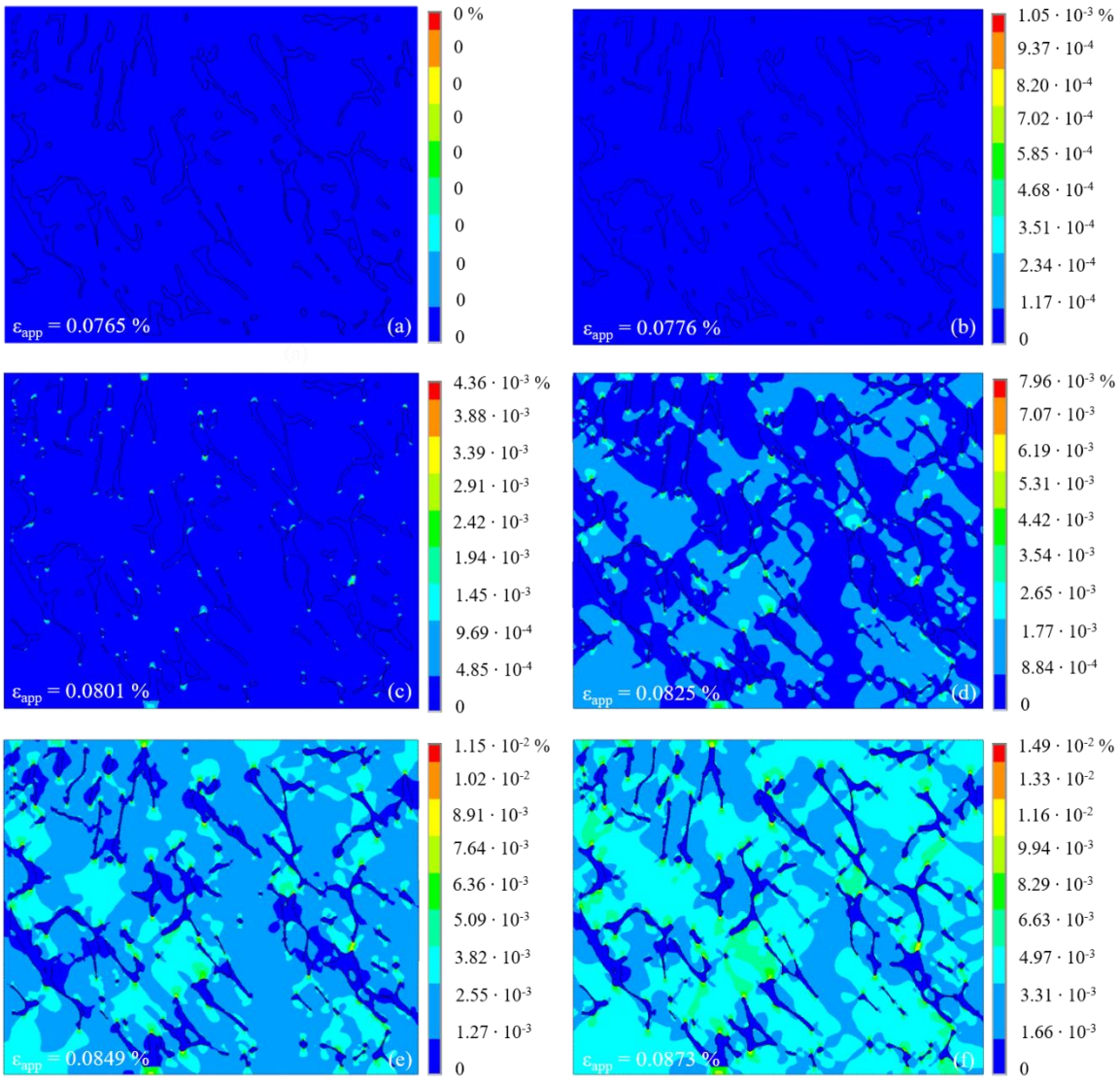

Fig. 52. Progression of von Mises plastic strain distribution in the aged microstructure of CF–3 unaged DSS under applied load over progressive substeps from **(a)** 0.0765 % applied strain – **(f)** 0.0873 % applied strain.

The next substep, at applied strain of 0.078 % strain (substep 68), Figure 52(b), shows a small region of non-zero von Mises plastic strain – the onset of local yielding. The maximum values of von Mises stress and plastic strain at this point are $\sigma_{VM,\gamma}^{max} = 165.8$ MPa and $\varepsilon_{VM}{}_{pl,\gamma}^{max} = 1.05 \cdot 10^{-5}$ for austenite and $\sigma_{VM,\delta}^{max} = 176.2$ MPa and $\varepsilon_{VM}{}_{pl,\delta}^{max} = 0$. This

initial plastic deformation is observed to occur in the austenite phase. Unlike the unaged yielding in the interior of the ferrite phase, the initial aged yielding point is located in the austenite phase but adjacent to the interphase boundary. Similarly, however, the location is in a region highly constrained by phase boundaries and between two ferrite islands aligned with the tensile direction. The calculated value of the bulk measured von Mises stress corresponding to the onset of local yielding in the steel is $\sigma_y^{bulk} = 158.2$ MPa.

The ensuing loading substeps, Figure 51(c)-(f), indicate that the continuation of local yielding initiation is occurring in similarly constrained regions of austenite, and proceeding into progressively less constrained austenite regions. By substep 78 (0.090 % applied strain), essentially all of the austenite has yielded, and there is no corresponding plastic strain in the ferrite phase. The plastic strain in the austenite regions that showed the earliest onset of yielding are beginning to increase in plastic strain as high as $\varepsilon_{VM}{}_{pl,\gamma}^{max} = 1.84 \cdot 10^{-4}$ with a corresponding von Mises stress of $\sigma_{VM,\gamma}^{max} = 179.5$ MPa. The corresponding maximum von Mises stress in the ferrite phase is $\sigma_{VM,\delta}^{max} = 209.8$ MPa, which is still well below the yield strength of the decomposed phase. The ferrite did not begin to yield locally during the extent of applied deformation for this model, and based on the known moduli of the bilinear model will yield considerably later than the austenite phase in the aged specimen.

iv. 2-D Isotropic – Carbides and Phase Boundaries

2-D isotropic models of the CF–8 steel with a real area of 1 μm^2 were analyzed to investigate the effects of elastic deformation on the area in the vicinity of the ferrite/austenite phase boundaries. In this steel, $M_{23}C_6$ carbides are commonly present at the phase boundaries. Models of these boundaries containing carbides and lacking carbides

were solved in order to more clearly compare the effects that the carbides have on the deformation mechanics. Due to the anisotropic model geometry resulting from the approximately linear nature of the boundaries at this length scale, the 1% tensile elastic strain applied in the y-directions corresponds approximately to a constant stress composite loading condition.

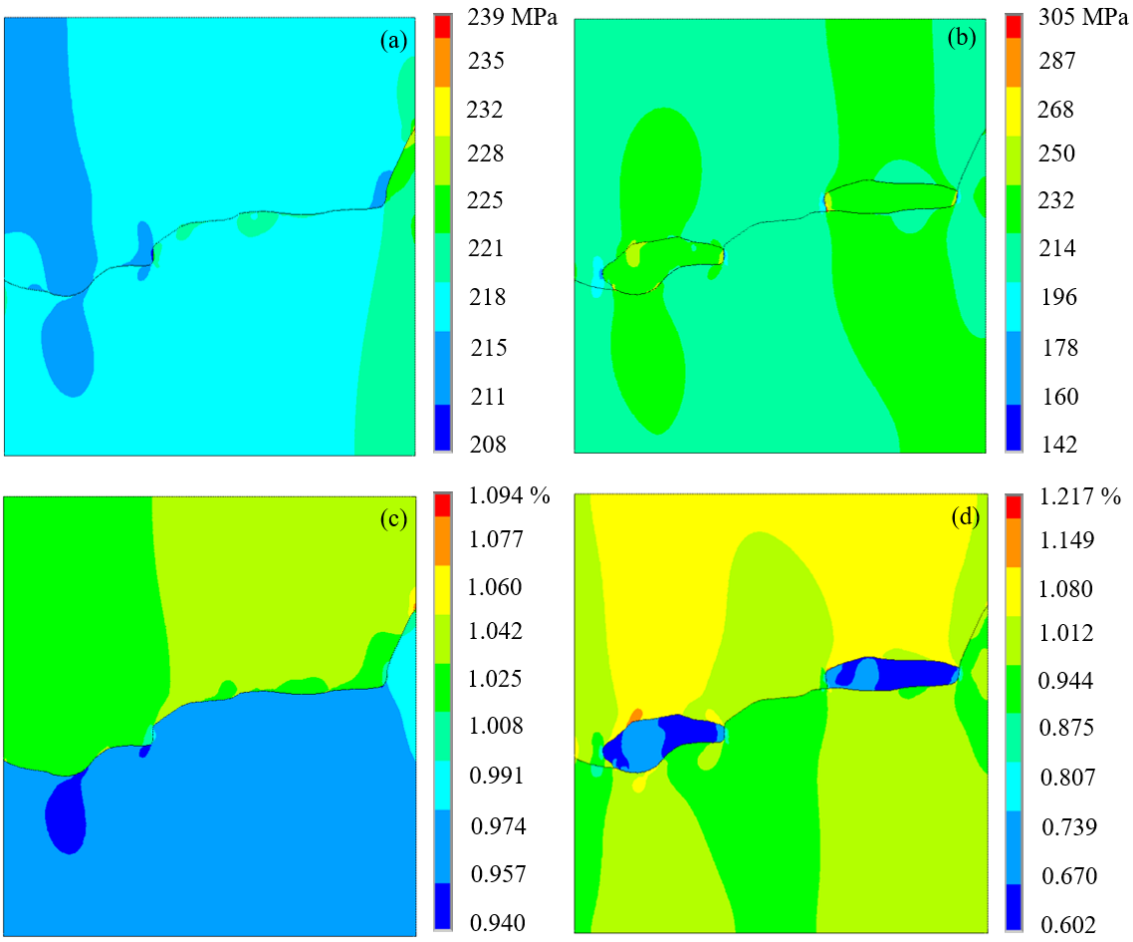

Fig. 53. Von Mises **(a)**,**(b)** stress and **(c)**,**(d)** strain distributions for the **(a)**,**(c)** CF–8 phase boundaries not containing carbides and **(b)**,**(d)** CF–8 boundaries containing carbides.

A comparison of von Mises contour plots in the CF–8 unaged boundary morphologies with and without carbides, Figure 53, shows that the stress distributions are significantly different with carbides present at the microstructure. The boundary lacking carbides with an applied y-displacement, Figure 53(a), exhibits a fairly uniform stress distribution along the boundary, with a total stress range from 208 MPa – 239 MPa. Due to the acute angle formed by the model boundary meeting the phase boundary, the stress concentrations at the edge of the model serve to increase the stresses calculated in this model, and the range across most of the boundary is fairly uniform in the range of 208 MPa – 218 MPa. The measured value of bulk stress in response to the 1% applied elastic strain is $\sigma_{bulk} = 222$ MPa. The minimum stress value is located at the boundary in the austenite phase, in a region aligned with the tensile direction.

In contrast, the presence of the boundary carbides, including non-artifact acute angles and the much stiffer carbide particles, Figure 53(b), covers a much larger range of 142 MPa – 305 MPa. The measured value of bulk stress in response to the 1% applied elastic strain is $\sigma_{bulk} = 222$ MPa. Here, the minimum and maximum stresses are location at the boundaries of the carbide, with the minimum stresses located in the austenite and maximum stresses located in the carbide. Due to the fact that the bodies of the carbides are located predominantly within the austenite phase, the ferrite boundary is much the same in the model containing carbides, resulting in a similar ferrite stress distribution. The average von Mises stress in the ferrite is 222 MPa when carbides are present and 219 MPa when carbides are not. Similarly, the average austenite stresses are 221 MPa when carbides are present and 218 MPa when carbides are not. For both models, the slightly stiffer ferrite contains slightly higher stresses due to stress transfer effects, and this discrepancy is

expected to be amplified for situations approximating the constant strain condition, where the boundary is more aligned with the tensile direction. The average stress of both duplex phases are higher in the model containing carbides, though the average stress of the carbides themselves, $\sigma_{carbide}^{avg} = 236$ MPa, is considerably higher than either duplex phase, as is expected due to their higher stiffness. Thus it is evident that the presence of the carbides in the CF – 8 substantially affects the properties of the phases near the boundaries, causing significantly greater heterogeneity in the stress distributions.

Similar to the results expected using composite theory and obtained by the isotropic model of the duplex microstructure, the trends for the strains, Figure 53(c),(d), are inverse to those of the stresses. In the same manner as the stress distributions, the range of strains is greater for the model containing carbides (0.60 % to 1.22 % vs. 0.94 – 1.09%), with the carbide-containing model possessing both the smallest and largest strains. Thus, the heterogeneity induced by the carbides near the boundaries is evident for the strains as well as the stresses. For the model containing carbides the average strains are 1.05 % in the austenite, 0.98 % in the ferrite, and only 0.67% for the carbides. In the model without carbides, the average elastic strains are 1.03% for the austenite and 0.97% for the ferrite. These result in austenite/ferrite strain partitioning ratios ($\varepsilon_\gamma / \varepsilon_\delta$) of 1.07 for both models in the approximately constant stress condition.

v. 2-D Isotropic – Decomposed Ferrite

The nanoscale structure of the material, despite being many orders of magnitude smaller than the duplex microstructure, has been shown by experiment to be fundamentally significant to the progression of bulk embrittlement of the DSS during thermal aging. APT analysis revealed the compositional segregation of the ferrite by spinodal decomposition

into Fe-rich and Cr-rich domains, as well as the potential for formation of cubic nickel silicide G-phase precipitates at the domain boundaries. Thus, as the final piece of the multi-scale modeling puzzle, FEM models based on the decomposed microstructure of the CF–3 are analyzed. Unlike the previous models which incorporated both duplex phases, the model geometries presented here relate to the interior of the ferrite phase only. However, as has become a common theme in this chapter, the decomposed ferrite structure takes the form of a multiphase metal-matrix composite material, and the due to this fact, the mechanical behavior results are expected to follow similarly to the previous isotropic analyses.

The von Mises stress distributions within the decomposed ferrite containing no G-phase is presented in Figure 54(a). The contours corresponding to the stress distribution between the Fe-rich α and Cr-rich α' domains bear more than a passing resemblance to the stress distributions on the micro-scale for the duplex microstructure. The applied 1% elastic strain condition results in estimated bulk stresses of $\sigma_{no\ G-phase}^{bulk} = 233$ MPa. Within the nanostructure, the stiffer Cr-rich phase acts as a reinforcement (analogous to the ferrite in the duplex structure), with an α/α' stress partitioning ratio $\sigma_{\alpha}/\sigma_{\alpha'} = 0.96$. This indicates clearly that the average stress in the Cr-rich α' domains is higher than in the Fe-rich α domains. Furthermore, the maximum stress observed in the α' is 21 MPa larger than that observed in the α (276 MPa vs. 255 MPa), which can have a significant effect on the yielding behavior of the ferrite, as was indicated by the isotropic near-yield model of the duplex phases. Qualitative observation of the stress distributions within the contour plot shows similar von Mises stress distributions to that of the duplex structure, as well, with the largest and smallest stresses occurring in regions constrained near boundaries and

aligned with the tensile loading direction. The heterogeneity of the stress distribution is also apparently anisotropic, with bands of various stress ranges aligned with the tensile direction.

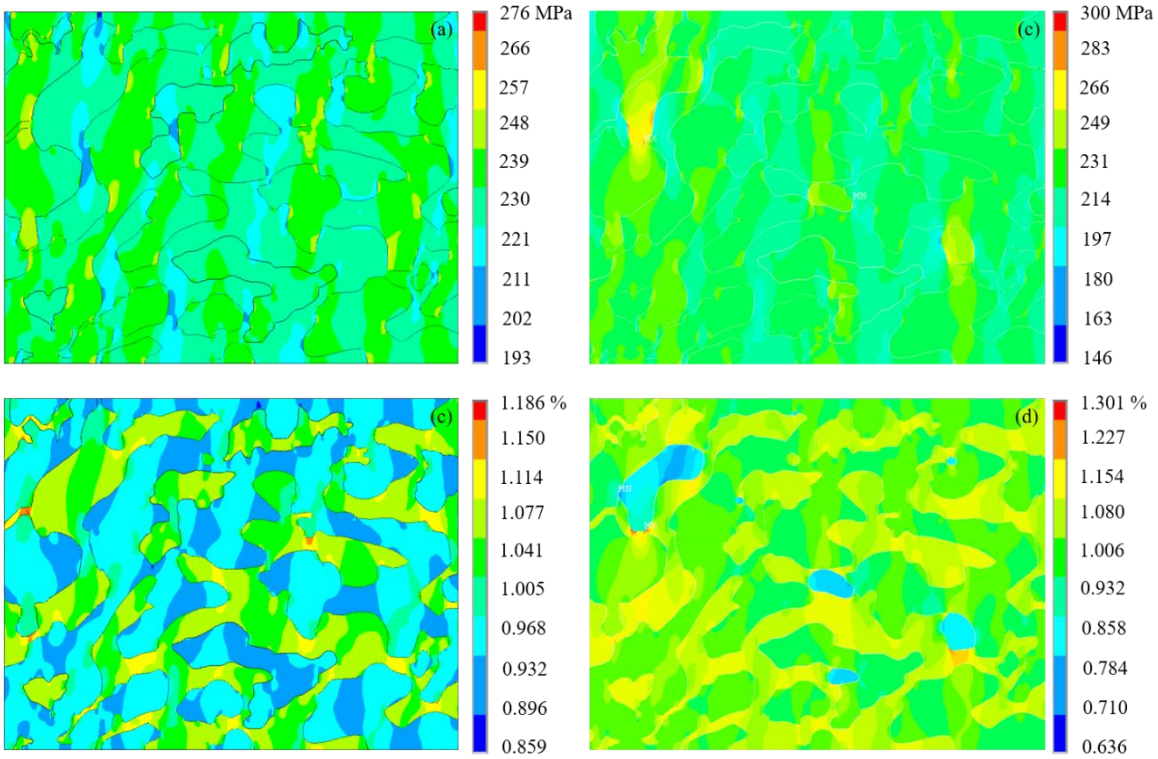

Fig. 54. Von Mises **(a)**,**(b)** stress and **(c)**,**(d)** strain distributions for the **(a)**,**(c)** CF–3 decomposed ferrite not containing G-phase and **(b)**,**(d)** CF–3 decomposed ferrite containing G-phase.

For the model of nanoscale ferrite containing G-phase particles, Figure 54(b), the stress distributions are altered by the presence of the precipitates within the inter-connected domain structure. As was observed for the carbides at the duplex phase boundaries, the presence of domain boundary precipitates is shown to significantly increase the heterogeneity of the stress (and strain) distributions. For this solution, the estimated bulk stress of $\sigma^{bulk}_{no\ G-phase} = 218$ MPa is much less than that calculated for the structure not

containing the G-phase, indicating that the presence of the G-phase particles serves to reinforce the microstructure in the elastic region and mitigate deformation of the ferrite phase under elastic loading. However, the G-phase has little effect on the stress partitioning, resulting in a value of $\sigma_\alpha/\sigma_{\alpha'} = 0.97$. As observed in the contour plot for the structure not containing G-phase, the G-phase containing nanostructure model contains banding characteristic of alignment with the tensile loading direction. Furthermore, the G-phase particles are shown to possess contours corresponding to higher stresses, which is expected due to the higher elastic modulus of the particulate phase. The average von Mises stress calculated for the G-phase is 238 MPa, which is significantly larger than $\sigma_\alpha^{avg} = 212$ MPa or $\sigma_{\alpha'}^{avg} = 220$ MPa.

As in the other isotropic composite models, the strain distribution trends, Figure 54(c),(d), are shown to be inverse of the trends for the stress distributions. The strains are lowest in the higher stiffness materials (α for the spinodal-only structure, G-phase for the model containing all 3 phases). The α/α' strain partitioning ratio for the spinodal-only structure is $\varepsilon_\alpha/\varepsilon_{\alpha'} = 1.10$ and for the G-phase containing structure is $\varepsilon_\alpha/\varepsilon_{\alpha'} = 1.09$, once again not showing a large effect due to the additional reinforcement. For the applied displacement equal to 1% bulk elastic strain, the average strains in the α-phase are the largest, $\varepsilon_\alpha^{avg} = 1.19\%$ and $\varepsilon_\alpha^{avg} = 1.30\%$, respectively. The lowest average strains are in the α' for the spinodal only model, $\varepsilon_{\alpha'}^{avg} = 1.12\%$, and in the G-phase for the G-phase containing model, $\varepsilon_{G-phase}^{avg} = 0.79\%$.

VI. DISCUSSION

A. INTRODUCTION

The preceding chapters provide a thorough characterization of the evolution of mechanical behavior and micro- and nano-structures of CF–3 and CF–8 stainless steels during thermal aging. A computational simulation of the real microstructures of the steels on multiple length scales by finite element method modeling has been presented, allowing for adaptable application of experimental data to obtain valuable insights into the structure-property relationships of the DSS. Each aspect of this research work provides unique data related to the effects of embrittlement of the duplex stainless steel systems. In an effort to expand on these results, the data obtained from each of the prior chapters can be used to provide critical information into the governing mechanisms of embrittlement on multiple length scales.

It has been established that the bulk embrittlement of the steels is caused by changes in the composite behavior of the duplex microstructure. These changes in behavior on the microscale are shown to be driven by changes in the nanoscale of the ferrite phase, and potentially by changes at the mesoscale at the ferrite/austenite phase boundaries. The goal of this dissertation is to investigate the effects of the spinodal decomposition process, formation of additional phases, and potential evolution of carbide morphology on the local ferrite and interphase behavior in CF–3 and CF–8 DSS, with emphasis on elucidating the effects of the ferrite embrittlement on the bulk mechanical behavior. While there has been some work in the past regarding explanations and mechanisms for the effect of the ferrite decomposition on bulk mechanical deformation, a majority of the existing studies regarding ferritic-austenitic DSS focus on the bulk mechanical testing results and the

kinetic mechanisms underlying the spinodal decomposition process. Notably, the effects of the degree of Fe-Cr segregation (spinodal amplitude) along with the possible nano-scale effects of G-phase forming zones or G-phase precipitates have not been fully elaborated upon. In this chapter, the effects of aging at operational and accelerated temperatures are explored through the various data presented in previous chapters and the results are discussed and correlated. Furthermore, the mechanical deformation results are examined mechanistically to form a more comprehensive picture of the influence of the local ferrite nanostructure on bulk mechanical behavior.

B. Bulk Mechanical Properties and Embrittlement

The mechanical properties investigated in Chapter III provide a large amount of data related to the progression of trends occurring during ongoing thermal aging. The bulk tensile results, Figures 13-15, show various phenomena dependent on material composition (CF–3 vs. CF–8), aging temperature (operational vs. accelerated), and aging time (unaged vs. 17,200 h). Note that for the sake of discussion, operational vs. accelerated temperatures will often be addressed generally, and evidence presented will be for 280 °C vs. 400 °C, respectively, unless otherwise stated.

Prior to the aging studies, there are discernable differences in mechanical properties between the CF–3 and CF–8 steels, most noticeably involving the UTS of the unaged steels and the ductility measured by tensile and Charpy impact testing. Unaged CF–8 is shown to possess a higher UTS and lower elastic modulus and Charpy impact energy than the unaged CF–3. It can be clearly observed from the compositions of the steels, Table 1, that while the Fe, Cr, and Ni concentrations in the steels are nearly identical, the CF–8 used in this study contains 3x the amount of carbon (0.06 wt.% vs. 0.02 wt.%; it is noted that the ASTM

designations "–3" and "–8" refer to the maximum allowed values of [C] permitted for these alloys). This difference in C – a known interstitial element [107] – can have profound effects on the mechanical behavior of the bulk materials and the constituent phases. The C atoms in solution result in strengthening of the lattice by introduction of stress and strain fields serving as an impediment to dislocation slip [56]. Additionally, C present above the solubility limit will be present in larger quantities at grain and phase boundaries, and can form carbide precipitates under the right conditions, as is observed for the CF–8 steel in Chapter IV. The presence of carbides is known to significantly affect plastic deformation behavior by impeding slip, and they can also serve as stress concentration points leading to crack propagation and embrittlement [108]. Finally, the presence of C interstitials in steels has been shown to decrease the elastic modulus of the steels [107]]. Thus, the elevated presence of carbon in the CF–8 steel explains essentially all of the differences observed between the steels, including higher UTS, lower elastic modulus, and lower CVN energy.

APT results obtained by Mburu, et al. have shown that the interstitial C atoms are located at a higher proportion in the austenite than in the ferrite in both the CF–3 and CF–8 steels in the unaged condition [50]. There is also evidence of a significant C concentration increase at the ferrite/austenite phase boundaries, with interface compositions reaching 1.0 at.% and 1.3 at.% for CF–3 and CF–8, respectively. The values measured in CF–3 are lower for both phases and the phase interfaces at all aging conditions as compared to the CF–8, corresponding to the lower bulk C concentration in CF–3. This supports the result that $M_{23}C_6$ carbides are not found to be present in the CF–3 specimens prior to aging or during aging up to 17,200 h. Following aging, at 400 °C for 17,200 h, the interface concentration

of C in the CF–8 increases to close to 5 at.% (away from the carbides) and the ferrite and austenite phases show approximately equal C concentrations. Both phases show increased C near the boundary following aging, indicating that significant amounts of carbon are diffusing to the phase interfaces. However, at the 280 °C aging temperature up to 17,200 h, there is little change observed in the near-interface C concentrations and the boundary concentration only shows an increase of ~0.1 at.%. This correlates well to the observed differences in bulk mechanical properties between the operational and accelerated temperatures. This provides evidence of the relation of diffusion kinetics to the TEM and APT observations that carbide coarsening (related to boundary diffusion) [Chapter IV] and carbide compositional changes (related to diffusion between the phase interiors and phase interfaces) [50] are evident at the accelerated temperatures but not significant at the operational temperatures up to 17,200 h.

During the progression of thermal aging, distinct trends are observed to be dependent on aging time and temperature, with the most significant changes occurring at the accelerated temperatures. The ultimate tensile strengths of both steels are shown to increase with increasing aging time and temperature, Figure 13. This is a result of hardening of the δ–ferrite phase due to spinodal decomposition, which can be considered analogous to precipitation hardening within the γ–austenite matrix phase. As the ferrite phase hardens or strengthens, the UTS of the bulk steel increases due to enhanced inhibition of dislocation slip at the ferrite boundaries with the austenite matrix. Contrary to the local nature of the yielding behavior, the UTS is governed by the aggregate effects of strengthening mechanisms throughout the bulk specimen, thus the local hardening of the ferrite increases

the bulk strength, even in the absence of structural or mechanical changes of the matrix phase.

In the case of the CVN behavior, there is a significant decrease in impact energy associated with aging, even at the lower operational aging temperatures. Since there is no change in the austenite phase nano- or microstructure during aging, the reduction in bulk ductility is a result of the nanostructural changes associated with hardening in the ferrite phase. The decrease in CVN values is observed at each aging temperature as early as 4300 h, and therefore embrittlement is initiated early in the aging process. Analysis of the fracture surfaces of the CVN specimens indicates brittle failure of the ferrite is occurring following aging in both steels. Since the ferrite is only ~8-12 vol.% of the bulk, brittle failure of ferrite most likely contributes to bulk failure by promoting stress concentrations and ductile failure in the austenite matrix, significantly reducing the energy absorbed during Charpy impact testing [122].

The spinodal decomposition serves to form a large number of coherent interphase (inter-domain) boundaries between α and α' domains within the decomposing ferrite, leading to multiple pathways for intergranular (inter-domain) crack propagation. In the early stages of aging, the inter-domain boundaries are relatively low-energy and are largely chemical in nature, with a coherent interface of the same crystallographic structure and very similar lattice parameters [33]. This is likely enough to promote more brittle fracture between the spinodal domains within the decomposing ferrite grains [38], as is evidenced by the decrease in CVN values at the operational aging temperatures and 4300 h aging times. As aging progresses, the lattice parameters are expected to diverge, decreasing the coherency of the domain boundaries [39].

At the accelerated aging temperatures, G-phase forming zones indicated by clusters of elements such as Ni, Si, and Mn are found to form at the spinodal domain boundaries [37]. These G-phase forming zones most likely promote strain fields and facilitate fracture initiation. In the case of more fully formed G-phase particles at longer aging times, the presence of distinct particles at the α/α' domain interfaces will cause stress concentrations which can significantly promote initiation of fracture in the decomposed ferrite phase [140]. The presence of these precipitates may play a significant role in embrittlement alongside the formation and maturation of the spinodal domain boundaries, and the influence of G-phase particles may dominate the ferrite fracture behavior at the accelerated aging temperatures and longer aging times.

In addition to possessing different initial properties, the CF–3 and CF–8 steels exhibit different trends during aging. During the course of thermal aging, the UTS of the CF–3 increases by 90 MPa (from 530 MPa to 620 MPa) at the highest aging temperature and longest time, compared to a corresponding increase of 65 MPa (from 570 MPa to 635 MPa) for CF–8. There are two possible explanations for this phenomenon. First, there are different or faster kinetics occurring in the CF–3 ferrite, resulting in a greater progression of spinodal decomposition in this steel. This is related to the presence of the carbides in the CF–8, which alter the composition and kinetic gradients present in the ferrite prior to and during aging. Second, there is a competing process in the CF–8 which offsets some of the hardening of the ferrite by spinodal decomposition and G-phase. The TEM results (Chapter IV) suggest that the possible mechanism behind this is the coarsening of the $M_{23}C_6$ carbides during aging, which results in greater carbide precipitate size, but decreased surface area occupied along the phase boundaries. Hence, this coarsening may cause weakening of

precipitate hardened phase boundaries simultaneous with the strengthening accompanying the decomposition of the ferrite.

There is an interesting trend in the ductility values of the CF–8 as compared to the CF–3, as well. In the case of the tensile tests, the initial total elongation values of the both steels are comparable in the unaged condition. However, following aging to 17,200 h at 400 °C, the total elongation drops 8% more for CF–3 than for CF–8, Figure 15. Hence, the lower carbon steel embrittles more quickly. This trend is seen more clearly in the CVN results, Figure 18. In the case of the CVN values, the initial impact energy in the unaged condition for CF–8 is lower than that of CF–3 by a significant amount. This can be explained by the presence of boundary carbides in CF–8 steel, which serve as stress concentration points and brittle failure sites, promoting failure at the ferrite/austenite interfaces. However, following aging to the longest aging time at 360 °C and 400 °C, the CVN values for CF–8 are larger than those under the same conditions for CF–3; i.e. the CF–3 steel has undergone a greater degree of embrittlement.

In order to understand these differences, it is noted that the spinodal wavelength and amplitude for CF–8, Figure 41(b) and (d), are lower than the corresponding values for CF–3, Figure 41(a) and (c), at the 360 °C and 400 °C temperatures at 17,200 h. Thus, it is likely that the presence of higher C concentrations and especially the presence of $M_{23}C_6$ carbides are affecting both the evolution of the ferrite phase and the embrittlement of the CF–8 steel. Since the $M_{23}C_6$ carbide composition is a Cr-carbide (~$Cr_{23}C_6$) [37], [62], it was previously shown that the region near the ferrite/austenite interfaces in CF–8 are depleted of Cr [63], [141]. This may alter the driving force of the spinodal decomposition and slow the kinetics of Fe and Cr un-mixing, thus resulting in a lower degree of decomposition. Furthermore,

the formation of G-phase clusters and precipitates is also affected. The APT observations of Mburu, et al. [23] suggest that there may be a greater quantity of G-phase clusters and precipitates near the heterophase ferrite/austenite interfaces when carbides are present than at locations away from it within the decomposing δ–ferrite phase after aging in CF–8. This is likely an effect of increased Ni and Si concentration within the Cr depleted zones in the ferrite phase and expulsion of Ni, Si, Mn, etc. from the boundaries where the carbides are formed. These results demonstrate that there may be competing effects related to the mechanical property degradation up to 17,200 h aging between decreased spinodal decomposition and increased G-phase formation.

Evaluation of the tensile test results of the steels tested at operational temperature (300 °C) demonstrates that there is a noticeable decrease in ductility for the unaged specimens compared to those tested at room temperature, the former of which show $\%el_{UTS}$ values of 31% and 40% for CF–3 and CF–8, respectively. This behavior is expected due to the increased defect mobility at higher temperatures, allowing dislocation slip to occur more readily [56]. Furthermore, aged specimens tested at 300 °C show little by way of significant trends and the tensile properties are relatively constant with aging time and temperature. This is consistent with the supposition that the ductile-to-brittle-transition temperature is near room temperature [5], [14]. If this is indeed the case, then even though the aging evolution results in a shift of the DBTT to lower temperatures, the 300°C testing of the materials is consistently occurring on the upper shelf of the DBTT curve. As a result, the embrittling processes up to 17,200 h do not appear to have a significant effect on material performance at operational temperatures.

C. YIELD BEHAVIOR

The relatively constant value of the bulk yield stress is an interesting result, especially since an increase in bulk UTS and nanohardness is observed at all aging conditions. In the case of the bulk specimens the consistency of these values may be attributed to the lack of changes in the austenite matrix during aging, as yielding behavior is governed locally and only requires one of the phases to reach the critical stress to yield. There is also not much difference between the values observed in the CF–3 versus the CF–8 steel at any given condition. The measured value of 286 MPa for CF–8 is only 6 MPa larger than measured for CF–3. These trends are more accurately borne out by measurement of the proportional limit, which demonstrate the real-behavior onset of plastic deformation, Figure 14, and shows that the proportional limits of the unaged steels are essentially the same. The slightly larger value of CF–8 offset yield stress may result from the higher C concentration in the CF–8, which results in a higher concentration of interstitial C and the formation of $M_{23}C_6$ carbides at the ferrite-austenite phase boundaries. Since the real onset of plastic behavior occurs at the proportional limit, the portion of the stress-strain curve from σ_{PL} to σ_y is technically subject to strain hardening, which can be increased by C effects and thus result in a higher offset yield stress. Furthermore, the presence of phase boundary carbides serve to act as a reinforcement material, where some of the applied stress is transferred due to its higher stiffness. However, the effect over this very small strain range may be very small, and the observed difference is essentially the same within expected experimental error. As mentioned above and discussed later, the presence of the discontinuous precipitate phase likely has little effect on the real yield strength.

The unaged ferrite and unaged austenite have very similar *H* values in both steels. Since it is commonly attributed that hardness and yield stress can be described by fairly simple mathematical relationships (generally assumed to be linear) [90], [134], this suggests that the yield strength of the ferrite is essentially equal to the yield strength of the austenite in the unaged state. Supposing that this is correct, bulk yielding would thus occur in the elastically stiffer ferrite phase first during tensile deformation of the unaged steels due to elastic interactions, Figures 3 and 55 [10], [82], [85]. Furthermore, this implies that upon hardening of the ferrite, the local ferrite yield strength increases correspondingly. Since the austenite hardness (and therefore yield strength) remains the same following aging, this can result in the critical stress being reached first in the austenite during deformation of the steels following aging. Because yielding is a local phenomenon instead of an aggregate effect across the steel (as in UTS or CVN), the bulk yield strength measured for the aged specimens now corresponds the yield strength of the austenite. Hence, the phase in which initial yielding occurs may change, but the measured value for the bulk yield strength is found to be fairly constant.

The 2-D isotropic FEM model created based on the real duplex microstructure was expanded to a bi-linear plastic behavior model following the Mises plasticity criterion in order to investigate this hypothesis, Chapter V. The results of the near-yield analysis based on the experimentally obtained hardness and tensile properties support the conclusion that the phase subjected to the local onset of yielding transitions from the stiffer ferrite to the less stiff austenite due to the increase of the local yield strength of the decomposing ferrite. The models show that the aged microstructure continues to exhibit stress partitioning to the ferrite, which becomes capable of enduring more elastic deformation after aging.

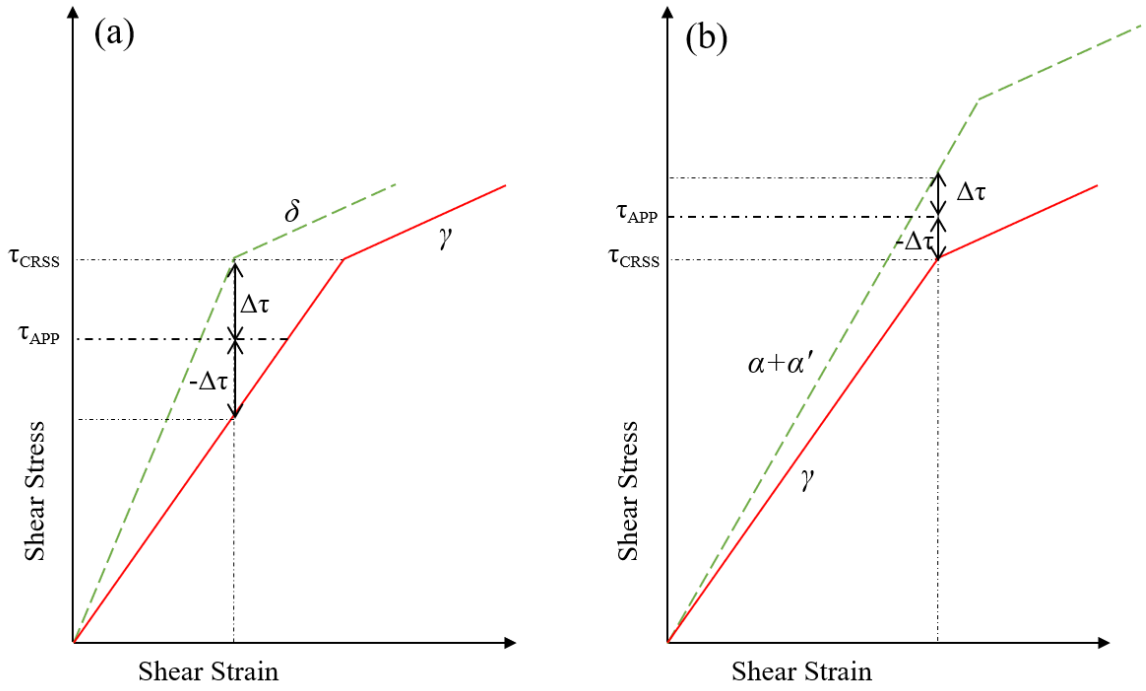

Fig. 55. Bilinear loading schematic based on Figure 3 showing the effects of raising the yield strength of the elastically stiffer phase (in this case, ferrite).

A duplex phase loading schematic describing this behavior is presented in Figure 55(a) for the unaged and Figure 55(b) for the aged structure. In the initial unaged microstructure, the interaction stresses result in the applied stress being disproportionately partitioned to the ferrite, and these interaction stresses result in the yield strength of the ferrite being reached first. However, following aging, Figure 55(b) clearly shows that upon increase of the yield strength of the ferrite phase, the interaction stresses of the ferrite are not enough to reach yielding before the yield strength of the austenite phase (which is the same as that of the unaged ferrite). This diagram also serves to explain the slight increase in bulk yield strength observed in the FEM models from the unaged to the aged state. Since the interaction stress relating to the stress transfer of the austenite is negative, and the stress

present in the austenite phase is actually less than the applied stress, the onset of yielding is actually occurring at a larger applied stress.

It is noteworthy that the composite behavior analysis and corresponding FEM results indicate that the bulk yield strength of the steel should actually increase during aging, if only by a small amount due to the similarity in the elastic moduli of the duplex phases. This behavior is not observed in the experimental tensile testing, where the σ_{PL} and σ_y values are observed to decrease to 4300 h, then recover to approximately the same as the unaged values at longer unaged times. The drop is most significant after aging at 400 °C, where decreases of approximately 11% and 15% are observed for CF–3 and CF–8, respectively. The yield strength decrease follows a consistent trend across aging temperatures at 4300 h. This consistency, combined with the relatively small error encountered during the bulk tensile testing suggests that this initial decrease and subsequent recovery is a real phenomenon. It is possible that the decrease is related to annealing of the steels during the initial stages of aging. Due to the duplex microstructure, it has been reported that there are residual stresses present in the steels following cooling after casting and solution treatment [142]. These stresses and associated dislocation density can be relaxed and reduced during extended exposure to elevated temperatures during aging (i.e. annealing) resulting in softening of the steels, similarly to the reported increase in Charpy impact energy for a similar DSS following annealing at 350 °C for up to 4 h [143]. However, this strength reduction is shown to be recovered at longer aging times. The subsequent increase in yield strength may be explained by the results obtained by FEM regarding the effect of hardening of the ferrite phase indicating that following extended aging there should be an increase in the bulk yield strength. Hence, the net result is that

little change in the bulk yield strength is observed up to 17,200 h. More work is suggested in this area regarding the short-term aging effects of near-yield behavior.

D. Effects of Ferrite Decomposition on Mechanical Behavior

As shown in the results in the previous chapters, there is a distinct correlation between the nanohardness and the progression of spinodal decomposition in the ferrite phase. There is likewise little to no change observed in the nanohardness or structure of the austenite phase. Thus, it is apparent that the changes in bulk behavior are driven by changes in the nanostructure of the ferrite phase. The hardening of the ferrite phase is clearly dependent in some manner on the degree of spinodal decomposition occurring during aging. Due to the miscibility gap in the Fe-Cr and Fe-Cr-Ni systems and the presence of a spinodal region, the b.c.c. δ–ferrite phase undergoes phase separation into continuous networks of Fe-rich α– and Cr-rich α′–domains [44]. This process also promotes segregation between the inter-domain boundaries of alloying elements such as Ni, Si, Mn (i.e. G-phase forming elements). Some theories as to the origin of the hardening have been put forward over the years, notably by Cahn (1963) [45], but the precise mechanism of the hardening has been difficult to ascertain. In general, the relatively small lattice mismatch at the α/α′ domain interfaces and the similar compositions of the two domains, especially at shorter aging times, tend to belie the large effect that the decomposition has on the local hardness and embrittlement. However at higher temperatures and longer aging times, the structural differences may be larger and have a significant effect on deformation behavior.

The results presented in this study with regard to the relationship between hardening and spinodal decomposition show two significant trends. First, when the spinodal wavelength (i.e. domain size) and spinodal amplitude (i.e. compositional

magnitude) of the α′ domains show little change at 280 °C, there is also little change in the nanohardness. Second, a significant increase in the hardness is measured when the wavelength and amplitude are shown concurrently to increase, Figures 20 and 41. At the 400 °C aging condition, all three quantities (λ, A, and H) exhibit significant increases with aging time. This includes a large increase from the unaged state to 4300 h and a smaller increase from 4300 h to 17,200 h, similar to the CVN results. Thus, at the aging times corresponding to the accelerated diffusion rates, the change in degree of spinodal decomposition of the ferrite and the ferrite nanohardness are closely correlated. Furthermore, the amplitude and wavelength of the ferrite phase in CF–3 increases more than those of in the CF–8 at 360 °C and 400 °C, corresponding to the greater decrease in CVN for the same conditions. This is indicative of a greater degree of decomposition leading to a greater degree of embrittlement between the two steels.

First, consider the potential effect of wavelength, or spinodal domain size, on the expected mechanical properties of the ferrite. In general, an increase in grain size and corresponding decrease in interfacial area per unit volume tends to lead to a lower hardness as dislocation slip and/or twinning can occur more freely [49]. However, this is contrary to the observed result where an increase in hardness corresponds to an increase in wavelength. Since the progression of spinodal decomposition with aging consists of both compositional and size changes, it is likely that this result is not a causative phenomenon, i.e. the wavelength increase is not promoting hardening and is simply occurring concurrently. This suggests that it is the compositional evolution – the spinodal amplitude and possibly the G-phase clusters and precipitates – that contributes to the increase in hardness. This supports the premise that the increasing segregation within the ferrite phase is leading to the physical

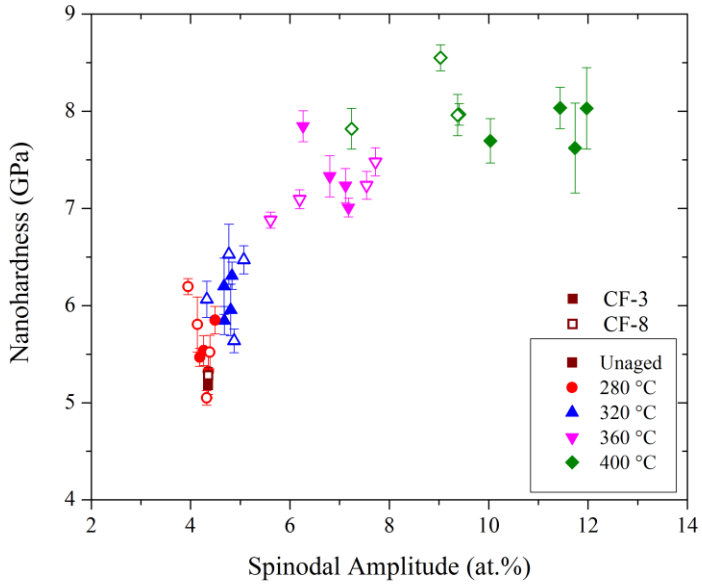

Fig. 56. Nanoindentation hardness values of the ferrite phase plotted as a function of the Cr concentration amplitude of the decomposed ferrite domains for both CF–3 (closed shapes) and CF–8 (open shapes) steels. Dependence on aging temperature is highlighted by different shapes/colors.

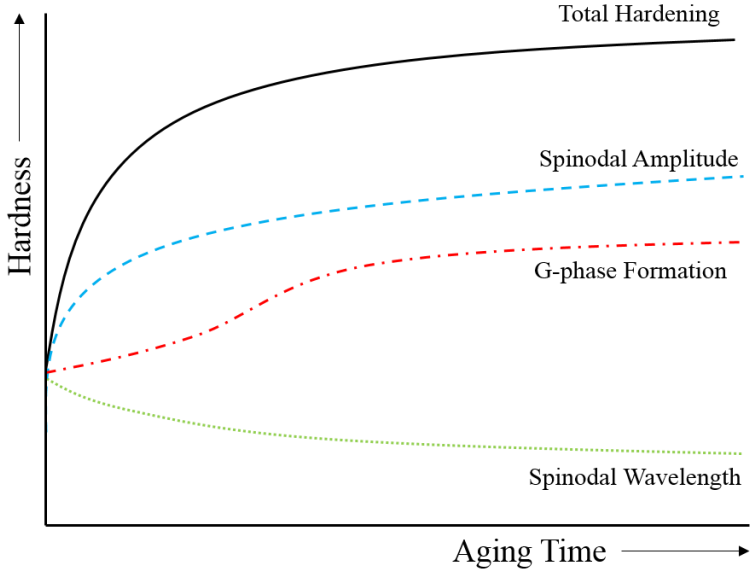

Fig. 57. Schematic diagram of possible hardening and softening mechanisms acting during decomposition of the ferrite phase.

mismatch at the domain boundaries. Figure 56 shows a plot of the evolution of the nanohardness in the ferrite versus the spinodal amplitude, which illustrates that the hardness increases rapidly with Cr amplitude increasing to approximately 7 at.%, but plateaus at higher concentration amplitudes. Since the domain size (wavelength) is increasing similarly during the aging process, the grain size effect may be serving to offset the compositional effects at more advanced stages of aging (seen at the accelerated aging temperatures), demonstrated schematically in Figure 57.

Cahn suggests that the principal operating mechanism of hardening by spinodal decomposition is the hindrance of dislocation motion or dislocation pinning by enhanced misfit and increased modulus differences located at regions with a higher degree of Fe or Cr enrichment, noting that this should occur in the regions of the domains where the degree of elemental segregation would be greatest [144]. Due to the different atomic radii and elastic moduli of Cr and Fe, the Cr-rich domains will contain a strain field resulting from lattice distortion from high concentration of substitutional Cr, as well as coherency strains at the domain boundaries resulting from the diverging lattice parameters at the α/α' inter-domain boundaries. In the case of a decomposing δ–ferrite phase, these lattice strains can introduce a barrier to dislocation motion both through the α'-phase and at the inter-domain boundaries, thus increasing the critical stress required to plastically deform the ferrite phase, i.e. hardening occurs.

While investigating the ferrite phase in a ferritic-martensitic steel, Terentyev, *et al.*, assume that the Cr-rich α′ phase acts as precipitated phase within the ferrite, essentially providing an Orowan-type impedance to dislocation motion where the dislocations move more easily in the Fe-rich α-phase and are slowed or pinned when coming into contact with

the Cr-rich α'-phase [88]. However, in the APT data presented here for aging times to 17,200 h, both phases still contain a majority Fe, meaning that the Cr-rich domain is still defined by a b.c.c. Fe lattice, yet with the α' domains possessing a larger concentration of Cr substitutional atoms. Hence, treatment of the α' domains as unique precipitates at this stage of aging may not be accurate for the CF–3 and CF–8 systems. It is, however, possible that either the α or α' domains are more difficult for dislocations to move in, and thus that some combination of the above effects is resulting in the obstruction to dislocation motion in the decomposing ferrite phase. Jenko, *et al.* [145], and Hsieh, *et al.* [146], performed TEM studies on dislocation motion within decomposed ferrite in duplex stainless steels and were able to show that the spinodal structure does affect the dislocation behavior and hinder dislocation motion, especially after aging at or above 350 °C. However, due to the length-scale of the domains, it is difficult to ascertain the exact mechanisms.

The effect of various stages of G-phase formation at the α/α' domain boundaries on the mechanical aging evolution remains an open question. These Ni-silicide precipitates, and the early stages of formation consisting of zones of enriched Ni and Si, have so far been observed in these steels at the given times only for the accelerated temperatures (i.e. at 360 °C and 400 °C) up to 17,200 h of aging [147]. The G-phase has previously been shown to form at dislocations and other areas of Ni and/or Si enrichment in the high diffusion flux regions at the α/α′ boundaries [59], [112]. The specimens containing G-phase zones and/or precipitates also correspond to the aging temperatures and times where the most significant hardness increases and ductility decreases have been observed (note that the size difference between the nanoindenter tip, ~100 nm, and the spinodal wavelength and G-phase forming zones and precipitates, ~2-10 nm, results in each ferrite indent including the combined

effects of α, α', and G-phase/zone regions). This suggests that hardening results from clustering and eventual nucleation of a physically distinct phase at the domain boundaries. Miller, *et al.*, report that the hardening is larger in magnitude in DSS than in the pure Fe-Cr-Ni system where the G-phase is not formed due to lack of significant Si concentrations [25]. Conversely, at least some hardening is reported during aging in the pure systems that undergo spinodal decomposition but form no additional precipitates, so G-phase must not be responsible for the entirety of the hardening effect in DSS. The possible effect of G-phase precipitation is also provided in the schematic in Figure 57, and it may be that formation of G-phase zones (and nucleation of those zones at later stages of aging) could be a major hardening mechanism competing with softening associated with the increase in domain wavelength.

During the course of this investigation, promising correlations have been explored regarding the presence of the formed G-phase in the decomposed ferrite and the evolution of the properties. Fractography was performed on deformed specimens shown by APT to contain G-phase elemental clusters and compared to those that were shown not to contain strong G-phase indicators. If the formation of the G-phase had a major effect on the fracture surfaces of the CF–3 phase this effect would be expected as differences between the unaged and A3 condition, as predicted based on the G-phase data obtained by atom probe tomography (APT). Likewise, a similar effect would be expected from the A3 to the B3 condition in the CF–8. The lack of significant differences observed between these conditions indicates that the G-phase, at least in its early stages, is not significantly affecting deformation behavior.

Similarly, investigation of the ferrite hardness and the bulk mechanical properties allow for direct comparison of all aging conditions, including those shown to contain G-phase and those without. There are strong correlations observed between both aging temperature and embrittlement and the presence of G-phase and embrittlement. Essentially, in specimens where significant ferrite hardening, bulk embrittlement, and mechanical strengthening were found to occur (i.e. at the accelerated temperatures), there are G-phase indicators present in the nanostructure. Furthermore, specimens that show little to no change in most mechanical properties (i.e. at 280 °C), no G-phase indicators are found, even when non-negligible spinodal wavelength and amplitude changes are present such as after aging at 320 °C. However, the development of the G-phase is shown to correlate strongly with increasing spinodal decomposition amplitude, and the two effects could not be fully isolated in this experiment. Furthermore, TEM analysis of the ferrite nanostructure was only able to confirm structurally precipitated G-phase in the CF–8 D4 specimen, meaning that despite the compositional indicators available from the APT results, the effect of G-phase elemental segregation versus nucleated G-phase precipitates is also unclear.

E. Validity of the Accelerated Aging Temperatures

The cumulative aging effects have been extensively observed at both operational temperatures and accelerated temperatures. Hence, it is of interest to compare the data at the various temperatures and attempt to determine the validity of the accelerated aging temperatures regarding prediction of the embrittlement of the DSS during operation at longer aging times. Focusing first on the evolution of the mechanical properties, there are distinct temperature-dependent differences in the trends occurring up to 17,200 h. In the case of the UTS and tensile ductility, the primary difference between the trends at 280 °C

and 400 °C are the rates of strengthening and ductility loss – which is consistent with expectation of accelerated kinetics. The CVN data show one additional difference early in the aging process. While all four aging temperatures exhibit a decrease in impact energy correlated to aging temperature, the accelerated temperatures (360 °C and 400 °C) show a large initial drop during the first 4300 h of aging that is not observed at the operational temperatures. On the local level, the ferrite results show no significant changes in the nanohardness up to 17,200 h at 280 °C, but very large increases (>47%) at 400 °C. Slight increasing trends are observed at 320 °C. Calculations of elastic modulus, yield strength/proportional limit, and 300 °C tensile properties show no significant trends, and thus are not useful in comparing aging temperatures.

Correlations in aging temperature effects based on the microstructure are similarly mixed. Spinodal decomposition is observed in all specimens. However, there is little evolution in the spinodal wavelength or amplitude at 280 °C up to 17,200 h, while there are major increases in both quantities at 400 °C. Since spinodal decomposition is a diffusion-based process, it is likely that the 280 °C specimens are undergoing increasing phase separation, just at a much slower rate than at 400 °C. The largest differences in nanoscale evolution between aging temperatures are the coarsening of the carbides (in CF–8) and the precipitation of the G-phase. Coarsening, similar to spinodal decomposition, is diffusion-dominated, and thus could be reasonably expected to approximate the accelerated temperatures at long aging times in the operationally aged specimens [30]. The G-phase, however, presents an additional problem in that the thermodynamic requirements for nucleation are not established (in contrast to the α, α', and $M_{23}C_6$ phases, which are confirmed in all specimens here). G-phase is only observed in the DSS specimens aged at

accelerated temperatures up to 17,200 h in this study, and specimens containing G-phase correspond closely to samples exhibiting the largest changes in mechanical properties. Furthermore, only one specimen (CF–8 aged at 400 °C for 17,200 h) was confirmed to contain structurally precipitated G-phase. The other specimens containing G-phase were only confirmed compositionally, and may represent elemental segregation without nucleation having occurred. APT studies by Mburu [50] have shown similar G-phase elemental segregation beginning to occur at 320 °C, but below the defined G-phase compositional threshold for confirmation.

Thus, based on these results obtained here up to 17,200 h, it is not possible to absolutely determine the validity of the accelerated aging temperatures. In general, it has been shown that embrittlement does occur to some degree at all four aging temperatures. However, differences observed between the properties and microstructure of the 280 °C aged and 400 °C aged specimens can be major. The 320 °C trends tend to correlate more closely to the 280 °C trends, and likewise the 360 °C trends correlate more closely to the 400 °C trends. However, the intermediate temperatures do lack the extremes observed at the minimum and maximum aging temperatures. It is possible – even likely – that the 360 °C aging temperature is a fairly accurate indicator of trends observed at 320 °C at longer aging times. It is also quite possible that this extends to 400 °C, as well. However, since very few real trends are observed at 280 °C aging, it is nearly impossible to determine whether any of the other temperatures can accurately predict the behavior at 280 ° C to 17.200 h of aging. Much depends on the potential for G-phase formation at the operational temperatures, as this will not only affect the mechanical properties but also the kinetics of spinodal decomposition. Future work is suggested to better validate the aging temperatures utilized

in this study, including short term aging to elucidate trends during early aging prior to 4300 h, and longer term aging studies, especially at the operational temperatures.

F. Finite Element Modeling and Composite Behavior

The structure-property relationships of the microstructure have been investigated in detail for the elastic deformation regime by FEM modeling. The models developed in Chapter V represent a reliable way to accurately predict the composite behavior of a multi-phase microstructure. These models also show the extremely useful versatility made available by modern FEM capabilities. The ability to accurately replicate real microstructures, add and remove phases and material properties, change the scale and resolution of the structure of interest, and change the crystal orientation and anisotropy present capabilities of calculation that far exceed simple execution by experiment. These FEM models have been used to show the micro-mechanical behavior of the elastic and near-yield regimes of the stress-strain curve for CF–3 and CF–8 duplex steels on the micro- and nanoscales, and are used to help analyze the trends encountered during aging.

For the case of the 2-D isotropic model of the duplex microstructure, the results clearly show that the ferrite and austenite phases undergo stress and strain partitioning. The heterogeneity of the stress and strain distributions can be explained by the difference in elastic modulus of the phases. The stiffer δ–ferrite phase will resist elastic deformation more than the γ–austenite phase. Thus, stress is transferred from the γ–austenite matrix to the δ–ferrite islands in order to maintain compatibility at the interfaces. Basic composites theory typically predicts the micromechanical behavior based on simplified descriptions of the microstructure: that of fibers aligned with or perpendicular to the loading direction, or of regularly distributed particulates [10]. However, in metallurgical systems consisting of

a complex microstructure, the morphology and distribution of the reinforcement phase will have a significant effect on the mechanics.

For the CF–3 and CF–8 duplex microstructures, the stresses are highest in ferrite islands that are elongated in a direction parallel to the direction of applied deformation. This occurs due to the mechanism by which the stresses or strains are transferred: across a strong phase interface [82]. The segments of the phase interface aligned with the tensile direction approximate the constant strain condition, where both phases are undergoing the same amount of displacement. Due to the nature of Hooke's law ($\sigma = E \cdot \varepsilon$, where E is the elastic modulus, a material constant), forcing the strain (ε) across the boundary to be constant means that the stress (σ) must adjust in order to maintain the integrity of the interface. Furthermore, Choi, et al., discusses this phenomenon in TRIP steel as an state of elevated stress triaxiality, where the constraints placed on the microstructure also result in higher stresses perpendicular to the applied deformation direction [129]. A larger value of the hydrostatic component of stress is expected in these locations as a result, which suggests that these are regions of interest for void initiation during the onset of ductile failure [56].

These behaviors are observed throughout the different elastic FEM models, and the resulting assumptions hold for each scale of analysis down to the decomposed ferrite nanostructure. As a result, analysis of the resulting stress and strain distributions from the FEM computations allows prediction of the behaviors of the DSS, including predictions of likely regions of failure. This is seen in the prior discussion on the yield stress, where the near-yield FEM models are shown to predict the parts of the microstructure most likely to contain the onset of local plastic deformation. On a broader scale, the areas of highest von

Mises stress during elastic deformation show the areas that are most likely to yield in the microstructures. This applies also to brittle materials, where areas of the highest stress concentrations are the likely initiation points for crack nucleation and brittle failure.

For the isotropic models, it is shown that these stress concentrations occur most readily in narrow regions of ferrite aligned with the tensile direction, as shown in the unaged models. Analysis of the models on different length scales such as the phase boundary model (not including carbides) and nanoscale decomposition models (not including G-phase), show that this holds true on the different scales. In general, the stresses are concentrated in regions highly constrained by the phase boundaries. In the unaged case, this is shown to indicate that highly constrained regions of ferrite will yield first. However, the micromechanics are not quite so simple. In the case of the yielding of the aged material, where the ferrite yield strength is assumed to increase proportionally with the hardness, the morphology and elastic stress-strain distributions are not changed, but the local yielding phenomena are shown to change. Hence, both the morphological constraints and the material properties must be considered.

The elastic FEM models of the ferrite nanostructure are remarkably analogous to the duplex microstructure models, excepting that the volume fractions of the spinodal domains are closer to 50/50. The elastic deformation of the nanostructure follows similar principles, and the stresses are transferred to the stiffer Cr-rich α' phase, with the corresponding strains transferred to the Fe-rich α phase. This suggests that the overall microstructure of the DSS can be approximated as layers of composite behavior, with the resulting “bulk” composite behavior of the decomposed ferrite then functioning as a single component of the duplex micro-mechanics. Hence, a flow can be utilized to create a stepwise process for modeling

a complex material from the nanoscale to the bulk. This method can be applied to any multi-scale material, and supplies a roadmap for future computational studies.

Real structures are often more complex than the original duplex microstructure models. For example, the CF–8 has been shown by TEM to contain $M_{23}C_6$ carbides at ferrite/austenite phase boundaries. The meso-scale boundary model of the CF–8 shows that these additional reinforcement particles, which possess higher elastic stiffness and much higher yield stress than either of the duplex phases [126], increase the heterogeneity of the stress-strain distributions. A similar effect is observed in the spinodal structure containing G-phase, where the ceramic G-phase particles at the domain boundaries fulfill the same role as the carbides. Furthermore, they introduce additional highly constrained boundary conditions that can result in locally enhanced stresses, thus promoting failure in these regions. Additionally, the addition of ceramic particles like carbides and G-phase are known contributors to failure, serving to cause stress and strain fields increasing local deformation and also failing in a brittle manner upon reaching their strength limits [15], [55], [108]. In contrast, the carbides also serve to inhibit slip and twinning during deformation of a bulk material and increase strain hardening, and thus have a mixed influence on deformation.

Additionally, as the models containing carbides (and G-phase) show, the ceramic particles serve as effective reinforcements during elastic deformation, absorbing a greater proportion of the applied stress. In the case of the schematics of the elastic interaction effects of two-phase composites, Figure 3 and 55, the effects of both phases are fairly straightforward. However, the inclusion of an additional phase complicates the interactions. In addition to affecting the morphology of the microstructure, the addition of

a third phase requires analysis of the interactions and stress transfer across three different phase boundaries: δ/γ, $\delta/M_{23}C_6$, and $\gamma/M_{23}C_6$ or α/α', α/G-phase, α'/G-phase. However, in these systems the boundary area of the original duplex phases or of the spinodal domains is much higher than those between the precipitates and either primary constituent, thus resulting in a fairly small effect of the precipitates on the stress/strain transfer. This is supported by the results for partitioning ratios for the models containing carbides and G-phase, which show the γ/δ and α/α' ratios are approximately the same with or without the inclusion of the extra particles. The mixed effects of the carbides on the bulk deformation can be observed in the mechanical properties comparisons between the CF–3 and CF–8 steels, where the CF–8 steel is determined to be stronger and more brittle than the CF–3 in the unaged condition. However, the steel containing the carbides shows less of a negative impact (i.e. embrittlement) due to thermal aging, as the presence of the additional phase serves to stabilize the deformation behavior through the previously discussed mechanisms.

The FEM analysis of anisotropic deformation also adds to the complex picture of deformation of the DSS. Previous work, as well as examination of the elastic constants (anisotropic and isotropic), indicate that the ferrite phase is generally elastically stiffer than the austenite phase [79], [87], [98], [112]. Hence, the observed results for the isotropic case and the expected results obtained via composites concepts indicate that stress is transferred from the austenite to the ferrite phase, thus resulting in higher stress in ferrite and higher strain in austenite. However, the anisotropic FEM results presented here indicate larger stresses in the austenite and larger strains in the ferrite. This supports the importance of investigating the micromechanical behavior on a small scale and without assuming isotropic behavior. Utilizing different grain orientations based on real measurements and

relationships, as well as assuming the random orientations of neighboring austenite grains, it is shown here that under these realistic loading conditions and granular orientations there will be locations within the unaged microstructure where austenite will be yielding before the ferrite. These results show that while, on average, the microstructural locations of yielding in the unaged condition will be located in the ferrite, this is not necessarily the exclusive case.

These results and corresponding discussion have primarily revolved around the micromechanics of the elastic regime and near-yield behavior. Insight into the specific stress-strain distributions during higher strain plastic micromechanical behavior of the steels is generally beyond the scope of this investigation. However, the EBSD analysis performed in Chapter IV not only provides valuable structural data that can be utilized in creation of FEM models (as performed for the 3-D anisotropic model), but also provides insight into the local plastic deformation behavior of a microstructure. As such, the KAM and GOS maps can provide very similar data to that which is obtained from the FEM models, but for much more extensive degrees of plastic deformation than were applied to the FEM models in this study. Accurate analysis of large amounts of plastic strain by computational modeling requires advanced implementation of plasticity theory that were beyond the scope of this investigation. However, the EBSD methods provide real structural data in manner similar to the contour plots of created to show the FEM stress-strain distributions. As seen from the GOS maps of the 45% deformed unaged tensile specimens, Figure 29(a) – (d), there is no clear trend regarding the location of high or low misorientation based on the grain or phase structure. Thus, GOS analysis illustrates that the greatest local misorientation can be located in either the ferrite phase or the austenite

phase. This suggests that the extent of plastic deformation is similar in both phases. Similarly, the KAM maps indicate that, in addition to the formation of sub-grain structure, the plastic strains are greatest near the phase boundaries. This is likely an effect of the additional constraints put on the deformation due to the presence of strong interfaces, but in the plastic regime is also indicative of geometrically necessary dislocations, dislocation pileup, and stacking faults [116].

In terms of the operational functionality of DSS components, the FEM results reveal a large quantity of valuable information related to deformation and failure. The models demonstrate that the stress and strain partitioning is related to the micro- and nano-structures, which results in stress concentrations in regions of high morphological constraint. These regions can thus be identified as likely regions of failure in service, where ductile yielding or crack initiation is most likely to occur. Furthermore, the addition of phases into the micro- and nano-structures results in changes in these concentrations. For example, the addition of carbides at the ferrite/austenite interfaces serves to significantly increase the heterogeneity and elevate the local stress concentrations near boundaries that can promote failure under the right conditions. These stress concentrations can also provide local regions of increased susceptibility to stress corrosion cracking and other complex failure modes.

In contrast to the indicators of embrittlement mechanisms, the FEM models also demonstrate a blueprint for designing microstructures where failure can be mitigated. Depending on the desired applications and likely service failure modes, such additions of carbides and G-phase could serve to strengthen the material and transfer stresses away from the weaker regions of microstructure, such as from the ferrite and austenite phases to the

higher yield strength carbides. The anisotropic FEM models and the plastic EBSD results indicate that there is an orientation and local morphological effect on the distribution of deformation on the microstructure, and such results can be used to guide processing and alloy development to help reduce local regions of lower strength failure. In general, these results demonstrate that the complexity of analyzing potential deformation and failure mechanisms in service at different possible locations, strain rates, and stages of deformation can be simplified by the FEM process, and that the bulk mechanical properties commonly surveyed for material selection in nuclear infrastructure can be explained and predicted computationally for better adaptation to specific systems.

VII. CONCLUSIONS

A. SUMMARY

This research addresses gaps in understanding regarding the thermal aging embrittlement of cast ferritic-austenitic duplex stainless steels that are commonly used in commercial nuclear power systems. CF–3 and CF–8 duplex stainless steels (DSS) were obtained and thermally aged in a laboratory setting for up to 17,200 h (~2 years) at operational (280 °C, 320 °C) and accelerated temperatures (360 °C and 400 °C). A thorough set of mechanical and structural characterization was performed allowing for in-depth analysis of the thermal aging evolution of these structural stainless steels in service environments. Experimental techniques such as mechanical testing and electron microscopy have been supplemented by state-of-the-art finite element method (FEM) modeling to provide a more comprehensive understanding of the structure-property relationships within these steels, both in the unaged and long-term aged conditions. The influence of the duplex ferrite and austenite phases have been investigated by both experiment and FEM computation based on accurate microstructures and properties, and the effects of decomposition of the ferrite phase on the bulk embrittlement of the steels have been explored in detail. In summary, the work performed over the course of this project provides a clear, thorough approach to characterization of this material system with regard to its embrittlement in service in nuclear systems, and the results and analysis have provided valuable insights into the mechanisms governing the evolution of the structure and properties of the CF–3 and CF–8 steels during thermal aging.

B. CONCLUSIONS

Several important conclusions have been drawn from the results and analysis presented in the previous chapters:

1. Thermal aging evolution of the micro- and nano-scale structure leads to significant changes in the elastic and plastic deformation behavior of the CF–3 and CF–8 steels. Based on the known effects of precipitation hardening, particulate reinforcement, and elasto-plastic deformation, it is clear that bulk embrittlement of the steels is predominantly caused by the structural evolution of the ferrite phase during thermal aging.

2. Bulk embrittlement in both the CF–3 and CF–8 steels occurs to varying degrees at each of the four aging temperatures. Charpy V-notch impact energy (CVN) decreases at all aging temperatures and aging times, while tensile ductility (%el, %RA) decreases and ultimate tensile strength (UTS) increases for both steels. Differences in evolution of mechanical properties and fracture surfaces indicate that the effects of aging embrittlement are more significant at higher strains rates (i.e. CVN) than at lower strain rates (i.e. quasistatic tensile testing).

3. SEM fractography of the failed specimens following CVN and tensile testing shows significant embrittlement following accelerated aging. Exposed facets of ferrite in regions that failed in a brittle manner, especially in the CVN fracture surfaces, strongly supports the hypothesis that ferrite hardening leads to bulk embrittlement.

4. Nanoindentation analyses of the local ferrite and austenite phases by the Oliver and Pharr method and Dao method show good agreement for determination of the local elastic properties of the unaged steels. The Dao and Ogasawara dimensionless analysis methods

for determination of yield and strain hardening behavior are found to be unreliable for these DSS systems.

5. The evolution of ferrite nanohardness correlates closely to the increasing wavelength and amplitude of the Cr-rich α' spinodal domains, as determined by APT. The largest increases in nanohardness occur under the same aging conditions as the largest increase in element segregation (spinodal amplitude), and no significant change in hardness is observed when the spinodal amplitude remains relatively unchanged.

6. The presence of $M_{23}C_6$ carbides in CF–8 leads to significant differences in mechanical properties versus the CF–3 steels. The carbides are shown to undergo coarsening during aging and, due to their potential influence on kinetics of decomposition in the G-phase, appear to mitigate the progression of bulk embrittlement in the CF–8 at accelerated aging temperatures.

7. The presence of G-phase coincides closely with the progression of embrittlement of the steels. Experimental and FEM analysis of the ferrite nanostructure provides strong evidence that precipitated G-phase particles affect the mechanical properties of the duplex phases and bulk steels. Due to the close association between degree of spinodal decomposition and G-phase formation, direct correlation of the presence of G-phase to the embrittlement of the steels remains elusive.

8. The accelerated aging temperatures are shown to not be good predictors of operational aging up to 17,200 h. Trends in structural evolution such as increasing degree of spinodal decomposition, G-phase precipitation, and carbide coarsening are not easily comparable between the accelerated and operational temperatures to this time. Trends in mechanical properties lead to the same conclusion.

9. FEM models developed based on the real microstructures of the steels show that in the isotropic materials systems (i.e. the real systems, on average), stress is transferred preferentially to the ferrite phase and strain is partitioned in the austenite phase. On the nanostructural level, stress is found to be transferred to the Cr-rich α' phase and strain to the Fe-rich α phase. Models including carbide and G-phase precipitates show that the presence of these phases greatly increases the heterogeneity of the stress and strain distributions in their vicinity.

10. The elastic modulus difference between the ferrite and austenite phases leads to differences in yielding behavior between the unaged and long-term aged conditions. FEM models indicate that the local onset of yielding during deformation of the microstructure may change significantly during ferrite hardening, with the local yield point changing phase preference following ferrite decomposition.

11. Based on anisotropic FEM modeling, local yielding behavior in the unaged steels can occur in either phase depending on crystal orientation, phase morphology, and the applied loading conditions. EBSD analysis of specimens confirms similar behavior in the plastic regime at high levels of permanent deformation. Thus, in the unaged state, the local phase morphology and orientation dominate the deformation behavior.

C. FUTURE WORK

The above conclusions represent the overall success of this research work in advancing the body of knowledge related to the specific CF–3 and CF–8 stainless steels, and ferritic-austenitic duplex stainless steels in general. Several key results based on the microstructural evolution of the steels during aging and the resulting micro-mechanical relationships have been elucidated using a mixture of established methods and state-of-the-

art techniques and technology. However, as with any project, the scope of work for this project precluded complete characterization of every aspect of these important material systems. Therefore, future work is planned/suggested to continue to unlock the unknowns and advance the technologies presented in this dissertation.

First, more targeted and thorough investigation into the validity of the accelerated aging temperatures (especially 400 °C) for describing the thermal aging of the DSS systems during operation. An investigation including longer term aging (> 2 years) and more short term aging steps (between 0 and 4300 h) is recommended to maximize the ability to compare verify the thermodynamic comparability and correlate the aging kinetics, respectively. Furthermore, additional investigation into the effects of the carbides on the thermal aging evolution of the structure and properties of the steels is suggested. The results of this investigation indicate that the higher carbon concentration and the presence of boundary carbides significantly affects the properties of the steels and the kinetics of aging embrittlement in the CF–8 versus the CF–3. More precise investigation of the mechanisms could lead to insights to improve material selection and processing.

Two more studies are recommended concerning the mechanical deformation of the steels. Direct observation of the effect of the G-phase on mechanical deformation of the decomposed ferrite remains elusive. Investigations of the ferrite deformation by such methods as in-situ tensile testing in a TEM are recommended, as the local effects of the G-phase particles (and spinodal domains) on dislocation slip (or twinning) can be directly observed. Finally, regarding the FEM studies, further work is planned regarding the incorporation of more advanced plasticity and anisotropic modeling. Addition of such factors as grain and phase boundary effects can provide significant insight into the plastic

deformation behavior on the microstructure level. As the current FEM study focuses on elastic and simple near-yield behavior, expansion of the model to included permanent deformation is the next logical step in the model progression.

VIII. References

[1] P. A. Kharecha, C. F. Kutscher, J. E. Hansen, and E. Mazria, "Options for Near-Term Phaseout of CO2 Emissions from Coal Use in the United States," *Environ. Sci. Technol.*, vol. 44, no. 11, pp. 4050–4062, Jun. 2010.

[2] S. J. Zinkle and G. S. Was, "Materials challenges in nuclear energy," *Acta Materialia*, vol. 61, no. 3, pp. 735–758, Feb. 2013.

[3] M. F. Ashby and M. Smidman, "Materials for Nuclear Power Systems," Granta Design, 1 MFA, 2010.

[4] K. H. Lo, C. H. Shek, and J. K. L. Lai, "Recent developments in stainless steels," *Materials Science & Engineering R*, vol. 65, pp. 39–104, 2009.

[5] T. S. Byun, Y. Yang, N. R. Overman, and J. T. Busby, "Thermal Aging Phenomena in Cast Duplex Stainless Steels," *JOM*, vol. 68, no. 2, pp. 507–516, 2016.

[6] S. L. Li *et al.*, "Microstructure evolution and impact fracture behaviors of Z3CN20-09M stainless steels after long-term thermal aging," *Journal of Nuclear Materials*, vol. 433, no. 1–3, pp. 41–49, Feb. 2013.

[7] O. K. Chopra and W. J. Shack, "Mechanical properties of thermally aged cast stainless steels from Shippingport reactor components," U.S. Nuclear Regulatory Commission, Argonne National Laboratory, NUREG/CR-6275, 1995.

[8] H. M. Chung and O. K. Chopra, "Microstructures of Cast-Duplex Stainless Steel After Long-Term Aging," in *Proc. Second Int. Symp. on Environmental Degradation of Materials in Nuclear Power Systems - Water Reactors*, Monterey, CA, 1985, pp. 287–292.

[9] H. M. Chung, "Evaluation of Aging of Cast Stainless Steel Components," U.S. Nuclear Regulatory Commission, Argonne National Laboratory, ANL/CP--70872, DE91 014013, 1991.

[10] S. Ankem, H. Margolin, C. A. Greene, B. W. Neuberger, and P. G. Oberson, "Mechanical properties of alloys consisting of two ductile phases," *Progress in Materials Science*, vol. 51, pp. 632–709, 2006.

[11] I. L. Mogford, "The deformation and fracture of two-phase materials," *Metallurgical Reviews*, vol. 12, no. 1, pp. 49–68, 1967.

[12] S. Kuang, Y. Kang, H. Yu, and R. Liu, "Stress-strain partitioning analysis of constituent phases in dual phase steel based on the modified law of mixture," *International Journal of Minerals, Metallurgy and Materials*, vol. 16, no. 4, pp. 393–398, Aug. 2009.

[13] P. H. Pumphrey and K. N. Akhurst, "Aging kinetics of CF3 cast stainless steel in temperature range 300-400°C," *Materials Science and Technology*, vol. 6, pp. 211–219, 1990.

[14] H. M. Chung and T. R. Leax, "Embrittlement of laboratory and reactor aged CF3,CF8, and CF8M duplex stainless steels," *Mater. Sci. Technol.*, vol. 6, no. 3, pp. 249–262, Mar. 1990.

[15] T. Gladman, "Precipitation hardening in metals," *Materials Science and Technology*, vol. 15, no. 1, pp. 30–36, 1999.

[16] M. Pohl, O. Storz, and T. Glogowski, "Effect of intermetallic precipitations on the properties of duplex stainless steel," *Materials Characterization*, vol. 58, no. 1, pp. 65–71, Jan. 2007.

[17] S. Kim and Y. Kim, “Estimation of Thermal Aging Embrittlement of LWR Primary Pressure Boundary Components,” *Journal of the Korean Nuclear Society*, vol. 30, no. 6, pp. 609–616, 1998.
[18] “ASTM Standard E562-11. Standard Test Method for Determining Volume Fraction by Systematic Manual Point Count,” ASTM International, West Conshohocken, PA, ASTM Standard E562-11, 2011.
[19] “ASTM Standard A800/A800M -14. Standard Practice for Steel Casting, Austenitic Alloy, Estimating Ferrite Content Thereof,” ASTM International, West Conshohocken, PA, ASTM Standard A800/A800M-14, 2014.
[20] R. P. Kolli *et al.*, “Characterization of Element Partitioning at the Austenite/Ferrite Interface of As Cast CF-3 and CF-8 Duplex Stainless Steels,” *Microsc. Microanal.*, vol. 21, no. Suppl 3, pp. 365–366, 2015.
[21] W. Hoffelner, “Damage assessment in structural metallic materials for advanced nuclear plants,” *J Mater Sci*, vol. 45, no. 9, pp. 2247–2257, Feb. 2010.
[22] C. R. F. Azevedo, “Selection of fuel cladding material for nuclear fission reactors,” *Engineering Failure Analysis*, vol. 18, no. 8, pp. 1943–1962, Dec. 2011.
[23] R. L. Klueh and A. T. Nelson, “Ferritic/martensitic steels for next-generation reactors,” *Journal of Nuclear Materials*, vol. 371, no. 1, pp. 37–52, Sep. 2007.
[24] F. H. Hayes, M. G. Hetherington, and R. D. Longbottom, “Thermodynamics of duplex stainless steels,” *Materials Science and Technology*, vol. 6, no. 3, pp. 263–272, Mar. 1990.
[25] M. K. Miller, I. M. Anderson, J. Bentley, and K. F. Russell, “Phase separation in the Fe-Cr-Ni system,” *Applied Surface Science*, vol. 94, pp. 391–397, Mar. 1996.
[26] O. K. Chopra and A. Sather, “Initial Assessment of the Mechanisms and Significance of Low-Temperature Embrittlement of Cast Stainless Steels in LWR Systems,” U.S. Nuclear Regulatory Commission, Argonne National Laboratory, NUREG/CR-5385, ANL-89/17, 1990.
[27] G. Bonny, D. Terentyev, and L. Malerba, “On the alpha-alpha’ miscibility gap of Fe-Cr alloys,” *Scripta Materialia*, vol. 59, pp. 1193–1196, 2008.
[28] E. Martinez, O. Senninger, C.-C. Fu, and F. Soisson, “Decomposition kinetics of Fe-Cr solid solutions during thermal aging,” *Physical Review B*, vol. 86, p. 224109–(1–13), 2012.
[29] S. S. Brenner, M. K. Miller, and W. A. Soffa, “Spinodal Decomposition of Iron-32 at.% Chromium at 470 °C,” *Scripta Metallurgica*, vol. 16, no. 7, pp. 831–836, 1982.
[30] D. A. Porter and K. E. Easterling, *Phase Transformations in Metals and Alloys*, 2nd ed. USA: Taylor and Francis, 2004.
[31] J. W. Cahn, “On Spinodal Decomposition,” *Acta Metallurgica*, vol. 9, no. 9, pp. 795–801, 1961.
[32] J. W. Cahn and J. E. Hilliard, “Spinodal Decomposition: A Reprise,” *Acta Metallurgica*, vol. 19, pp. 151–161, 1971.
[33] S. Baghsheikhi, “Spinodal decomposition in the binary Fe-Cr system,” Masters Thesis, Royal Institute of Technology, Stockholm, Sweden, 2009.
[34] J. W. Cahn, “Phase Separation by Spinodal Decomposition in Isotropic Systems,” *Journal of Chemical Physics*, vol. 42, no. 1, pp. 93–99, 1965.

[35] G. Bonny, D. Terentyev, and L. Malerba, “New Contribution to the Thermodynamics of Fe-Cr Alloys as Base for Ferritic Steels,” *J. Phase Equilib. Diffus.*, vol. 31, no. 5, pp. 439–444, Oct. 2010.
[36] Y.-Y. Chuang and Y. A. Chang, “A thermodynamic analysis and calculation of the Fe-Ni-Cr phase diagram,” *Metallurgical Transactions A*, vol. 18, no. A, pp. 733–745, 1987.
[37] S. Mburu *et al.*, “Effect of aging temperature on phase decomposition and mechanical properties in cast duplex stainless steels,” *Materials Science and Engineering: A*, vol. 690, pp. 365–377, Apr. 2017.
[38] C. Pareige *et al.*, “Kinetic study of phase transformation in a highly concentrated Fe-Cr alloy: Monte Carlo simulation versus experiments,” *Acta Materialia*, vol. 59, pp. 2404–2411, 2011.
[39] J. Emo, C. Pareige, S. Saillet, C. Domain, and P. Pareige, “Kinetics of secondary phase precipitation during spinodal decomposition in duplex stainless steels: A kinetic Monte Carlo model – Comparison with atom probe tomography experiments,” *Journal of Nuclear Materials*, vol. 451, no. 1, pp. 361–365, Aug. 2014.
[40] M. K. Miller and J. Bentley, “APFIM and AEM investigation of CF8 and CF8M primary coolant pipe steels,” *Materials Science and Technology*, vol. 6, no. 3, pp. 285–292, Mar. 1990.
[41] J. W. Cahn, “The later stages of spinodal decomposition and the beginnings of particle coarsening,” *Acta Metallurgica*, vol. 14, no. 12, pp. 1685–1692, 1966.
[42] M. K. Miller, J. M. Hyde, A. Cerezo, and G. D. W. Smith, “Comparison of low temperature decomposition in Fe-Cr and duplex stainless steels,” *Applied Surface Science*, vol. 87, pp. 323–328, Mar. 1995.
[43] Z. Yan, Y. Li, X. Zhou, Y. Zhang, and R. Hu, “Evolution of nanoscale Cr-rich phase in a Fe-35 at.% Cr alloy during isothermal aging,” *Journal of Alloys and Compounds*, vol. 725, pp. 1035–1043, Nov. 2017.
[44] N. Pettersson *et al.*, “Nanostructure evolution and mechanical property changes during aging of a super duplex stainless steel at 300 °C,” *Materials Science and Engineering: A*, vol. 647, pp. 241–248, Oct. 2015.
[45] K.-H. Park, J. C. LaSalle, L. H. Schwartz, and M. Kato, “Mechanical Properties of Spinodally Decomposed Fe-30 wt.% Cr Alloys: Yield Strength and Aging Embrittlement,” *Acta Metallurgica*, vol. 34, no. 9, pp. 1853–1865, 1986.
[46] W.-Y. Chen, M. Li, X. Zhang, M. A. Kirk, P. M. Baldo, and T. Lian, “In situ TEM study of G-phase precipitates under heavy ion irradiation in CF8 cast austenitic stainless steel,” *Journal of Nuclear Materials*, vol. 464, pp. 185–192, Sep. 2015.
[47] I. Shuro, H. H. Kuo, T. Sasaki, K. Hono, Y. Todaka, and M. Umemoto, “G-phase precipitation in austenitic stainless steel deformed by high pressure torsion,” *Materials Science and Engineering: A*, vol. 552, pp. 194–198, Aug. 2012.
[48] A. Grytsiv *et al.*, “Crystal chemistry of the G-phases in the {Ti, Zr, Hf}–Ni–Si systems,” *Journal of Solid State Chemistry*, vol. 180, no. 2, pp. 733–741, Feb. 2007.
[49] T. Hamaoka, A. Nomoto, K. Nishida, K. Dohi, and N. Soneda, “Accurate determination of the number density of G-phase precipitates in thermally aged duplex stainless steel,” *Philosophical Magazine*, vol. 92, no. 22, pp. 2716–2732, Aug. 2012.

[50] S. Mburu, “Kinetics of Thermal Aging Embrittlement and the Associated Embrittlement of Cast Duplex Stainless Steels,” PhD Dissertation, University of Maryland, College Park, MD, 2017.
[51] Y. Matsukawa *et al.*, “The two-step nucleation of G-phase in ferrite,” *Acta Materialia*, vol. 116, pp. 104–113, Sep. 2016.
[52] C. Pareige, J. Emo, S. Saillet, C. Domain, and P. Pareige, “Kinetics of G-phase precipitation and spinodal decomposition in very long aged ferrite of a Mo-free duplex stainless steel,” *Journal of Nuclear Materials*, vol. 465, pp. 383–389, Oct. 2015.
[53] E.-Y. Guo, H.-X. Xie, S. S. Singh, A. Kirubanandham, T. Jing, and N. Chawla, “Mechanical characterization of microconstituents in a cast duples stainless steel by micropillar compression,” *Materials Science & Engineering A*, vol. 598, pp. 98–105, 2014.
[54] G. Liu, Y. Wang, S. Li, K. Du, and X. Wang, “Deformation behavior of thermal aged duplex stainless steels studied by nanoindentation, EBSD and TEM,” *Materials at High Temperatures*, vol. 33, no. 1, pp. 15–23, Jan. 2016.
[55] H. Gleiter and E. Hornbogen, “Precipitation hardening by coherent particles,” *Materials Science and Engineering*, vol. 2, no. 6, pp. 285–302, Mar. 1968.
[56] G. E. Dieter, *Mechanical Metallurgy*, SI Metric. Singapore: McGraw-Hill, 1988.
[57] S. Ankem, D. Banerjee, D. J. McNeish, J. C. Williams, and S. R. Seagle, “Silicide Formation in Ti-3Al-8V-6Cr-4Zr-4Mo,” *Metallurgical Transactions A*, vol. 18A, pp. 2015–2025, 1987.
[58] T. Takasugi, “Microstructural control and mechanical properties of nickel silicides,” *Intermetallics*, vol. 8, no. 5, pp. 575–584, May 2000.
[59] S. Anthonysamy *et al.*, “Gibbs energies of formation of chromium carbides,” *MMTA*, vol. 27, no. 7, pp. 1919–1924, Jul. 1996.
[60] N. I. Medvedeva, D. C. Van Aken, and J. E. Medvedeva, “Stability of binary and ternary M23C6 carbides from first principles,” *Computational Materials Science*, vol. 96, pp. 159–164, Jan. 2015.
[61] Y. Liu, Y. Jiang, J. Xing, R. Zhou, and J. Feng, “Mechanical properties and electronic structures of M23C6 (M = Fe, Cr, Mn)-type multicomponent carbides,” *Journal of Alloys and Compounds*, vol. 648, pp. 874–880, Nov. 2015.
[62] P. D. Southwick and R. W. K. Honeycombe, “Precipitation of M23C6 at austenite/ferrite interfaces in duplex stainless steel,” *Metal Science*, vol. 16, no. 10, pp. 475–482, Oct. 1982.
[63] K. Kaneko *et al.*, “Formation of M23C6-type precipitates and chromium-depleted zones in austenite stainless steel,” *Scripta Materialia*, vol. 65, no. 6, pp. 509–512, Sep. 2011.
[64] D. H. Jack and K. H. Jack, “Invited review: Carbides and nitrides in steel,” *Materials Science and Engineering*, vol. 11, no. 1, pp. 1–27, Jan. 1973.
[65] L. J. Wang, L. Y. Sheng, and C. M. Hong, “Influence of grain boundary carbides on mechanical properties of high nitrogen austenitic stainless steel,” *Materials & Design*, vol. 37, pp. 349–355, May 2012.
[66] L. Zheng, X. Hu, X. Kang, and D. Li, “Precipitation of M23C6 and its effect on tensile properties of 0.3C–20Cr–11Mn–1Mo–0.35N steel,” *Materials & Design*, vol. 78, pp. 42–50, Aug. 2015.

[67] T. Hamaoka, A. Nomoto, K. Nishida, K. Dohi, and N. Soneda, “Effects of aging temperature on G-phase precipitation and ferrite-phase decomposition in duplex stainless steel,” *Philosophical Magazine*, vol. 92, no. 34, pp. 4354–4375, Dec. 2012.
[68] J. Janovec, A. Vyrostkova, and M. Svoboda, “Influence of tempering temperature on stability of carbide phases in 2.6cr-0.7mo-0.3v steel with various carbon content,” *MMTA*, vol. 25, no. 2, pp. 267–275, Feb. 1994.
[69] M. A. Neri and R. Colás, “Analysis of a martensitic stainless steel that failed due to the presence of coarse carbides,” *Materials Characterization*, vol. 47, no. 3, pp. 283–289, Sep. 2001.
[70] Q. Gao *et al.*, “Precipitates and Particles Coarsening of 9Cr–1.7W–0.4Mo–Co Ferritic Heat-Resistant Steel after Isothermal Aging,” *Scientific Reports*, vol. 7, no. 1, p. 5859, Jul. 2017.
[71] S. Şahin and M. Übeyli, “A Review on the Potential Use of Austenitic Stainless Steels in Nuclear Fusion Reactors,” *J Fusion Energ*, vol. 27, no. 4, pp. 271–277, Dec. 2008.
[72] F. Iacoviello, F. Casari, and S. Gialanella, “Effect of ‘475 °C embrittlement’ on duplex stainless steels localized corrosion resistance,” *Corrosion Science*, vol. 47, no. 4, pp. 909–922, Apr. 2005.
[73] T. S. Byun, N. R. Overman, and T. G. Lach, “Mechanical Properties of Model Cast Austenitic Stainless Steels after Thermal Aging for 1500 Hours,” U.S. Department of Energy, Pacific Northwest National Laboratory, M2LW–16OR0402152, 2016.
[74] S. M. Dubiel and J. Żukrowski, “Phase-decomposition-related short-range ordering in an Fe–Cr alloy,” *Acta Materialia*, vol. 61, no. 16, pp. 6207–6212, Sep. 2013.
[75] O. K. Chopra, “Estimation of Fracture Toughness of Cast Stainless Steels During Thermal Aging in LWR Systems,” U.S. Nuclear Regulatory Commission, Argonne National Laboratory, NUREG/CR-4513, Rev. 1, ANL-93/22, 1994.
[76] S. Li, Y. Wang, S. Li, H. Zhang, F. Xue, and X. Wang, “Microstructures and mechanical properties of cast austenite stainless steels after long-term thermal aging at low temperature,” *Materials & Design*, vol. 50, pp. 886–892, Sep. 2013.
[77] S. Bonnet, J. Bourgoin, J. Champredonde, D. Guttmann, and M. Guttmann, “Relationship between evolution of mechanical properties of various cast duplex stainless steels and metallurgical and aging parameters: outline of current EDF programmes,” *Materials Science and Technology*, vol. 6, pp. 221–229, 1990.
[78] R. Dakhlaoui, A. Baczmański, C. Braham, S. Wroński, K. Wierzbanowski, and E. C. Oliver, “Effect of residual stresses on individual phase mechanical properties of austeno-ferritic duplex stainless steel,” *Acta Materialia*, vol. 54, no. 19, pp. 5027–5039, Nov. 2006.
[79] K. R. Gadelrab, G. Li, M. Chiesa, and T. Souier, “Local characterization of austenite and ferrite phases in duplex stainless steel using MFM and nanoindentation,” *J. Mater. Res.*, vol. 27, no. 12, pp. 1573–1579, 2012.
[80] M. K. Miller, J. M. Hyde, M. G. Hetherington, A. Cerezo, G. D. W. Smith, and C. M. Elliott, “Spinodal Decomposition in Fe-Cr Alloys: Experimental Study at the Atomic Level and Comparison with Computer Models - I. Introduction and Methodology,” *Acta metall. mater.*, vol. 43, no. 9, pp. 3385–3401, 1995.
[81] O. Soriano-Vargas, E. O. Avila-Davila, V. M. Lopez-Hirata, H. J. Dorantes-Rosales, and J. L. Gonzalez-Valazquez, “Spinodal decomposition in an Fe-29 at% Cr alloy

during isothermal aging," *Materials Transactions*, vol. 50, no. 7, pp. 1753–1757, 2009.
[82] S. Ankem and H. Margolin, "A Rationalization of Stress-Strain Behavior of 2-Ductile Phase Alloys," *Metallurgical Transactions A*, vol. 17, no. 12, pp. 2209–2226, 1986.
[83] T. S. Byun and I. S. Kim, "Stress and strain partition in elastic and plastic deformation of two phase alloys," *J Mater Sci*, vol. 26, no. 14, pp. 3917–3925, Jul. 1991.
[84] P. Hedström, T.-S. Han, U. Lienert, J. Almer, and M. Odén, "Load partitioning between single bulk grains in a two-phase duplex stainless steel during tensile loading," *Acta Materialia*, vol. 58, no. 2, pp. 734–744, Jan. 2010.
[85] C. A. Greene and S. Ankem, "Modelling of elastic interaction stresses in two-phase materials by FEM," *Materials Science and Engineering: A*, vol. 202, no. 1–2, pp. 103–111, Nov. 1995.
[86] S. Neti, M. N. Vijayshankar, and S. Ankem, "Finite-Element Method Modeling of Deformation-Behavior of 2-Phase Materials. 1. Stress-Strain Relations," *Materials Science & Engineering A*, vol. 145, no. 1, pp. 47–54, 1991.
[87] B. Guelorget and M. Francois, "Extracting the plastic properties of metal materials from microindentation tests: Experimental comparison of recently published methods," *J. Mater. Res.*, vol. 22, no. 6, pp. 1512–1518, 2007.
[88] D. A. Terentyev, G. Bonny, and L. Malerba, "Strengthening due to coherent Cr precipitates in Fe-Cr alloys: Atomistic simulations and theoretical models," *Acta Materialia*, vol. 56, pp. 3229–3235, 2008.
[89] W. C. Oliver and G. M. Pharr, "Measurement of hardness and elastic modulus by instrumented indentation: Advances in understanding and refinements to methodology," *Journal of Materials Research*, vol. 19, no. 1, pp. 3–20, Jan. 2004.
[90] D. Tabor, "The physical meaning of indentation and scratch hardness," *British Journal of Applied Physics*, vol. 7, pp. 159–166, 1956.
[91] W. C. Oliver and G. M. Pharr, "An improved technique for determining hardness and elastic modulus using load and displacement sensing indentation experiments," *J. Mater. Res.*, vol. 7, no. 6, pp. 1564–1583, 1992.
[92] "ASTM Standard E2546-07. Standard Practice for Instrumented Indentation Testing," ASTM International, West Conshohocken, PA, ASTM Standard E2546-07, 2007.
[93] M. Dao, N. Chollacoop, K. J. Van Vliet, T. A. Venkatesh, and S. Suresh, "Computational modeling of the forward and reverse problems in instrumented sharp indentation," *Acta Materialia*, vol. 49, pp. 3899–3918, 2001.
[94] N. Ogasawara, N. Chiba, and X. Chen, "Measuring the plastic properties of bulk materials by single indentation test," *Scripta Materialia*, vol. 54, pp. 65–70, 2006.
[95] T. Belytschko, R. Gracie, and G. Ventura, "A review of extended/generalized finite element methods for material modeling," *Modelling Simul. Mater. Sci. Eng.*, vol. 17, no. 4, p. 043001, 2009.
[96] J. G. Rao and S. Ankem, "The effect of volume percent and morphology of phases on the damping behavior of epoxy/aluminum composites," *MMTA*, vol. 27, no. 8, pp. 2366–2373, Aug. 1996.
[97] F. Roters, P. Eisenlohr, T. R. Bieler, and D. Raabe, *Crystal Plasticity Finite Element Methods in Materials Science and Engineering*. Singapore: Wiley-VCH, 2010.

[98] S. C. Schwarm, R. P. Kolli, E. Aydogan, S. Mburu, and S. Ankem, "Characterization of phase properties and deformation in ferritic-austenitic duplex stainless steels by nanoindentation and finite element method," *Materials Science and Engineering: A*, vol. 680, pp. 359–367, Jan. 2017.
[99] X. Sun, K. S. Choi, A. Soulami, W. N. Liu, and M. A. Khaleel, "On key factors influencing ductile fractures of dual phase (DP) steels," *Materials Science and Engineering: A*, vol. 526, no. 1–2, pp. 140–149, Nov. 2009.
[100] X. Sun, K. S. Choi, W. N. Liu, and M. A. Khaleel, "Predicting failure modes and ductility of dual phase steels using plastic strain localization," *International Journal of Plasticity*, vol. 25, no. 10, pp. 1888–1909, Oct. 2009.
[101] S. K. Paul, "Real microstructure based micromechanical model to simulate microstructural level deformation behavior and failure initiation in DP 590 steel," *Materials & Design*, vol. 44, pp. 397–406, Feb. 2013.
[102] S. K. Paul, "Micromechanics based modeling of Dual Phase steels: Prediction of ductility and failure modes," *Computational Materials Science*, vol. 56, pp. 34–42, Apr. 2012.
[103] "ASTM Standard A351/A351M-14. Standard Specification for Castings, Austenitic, for Pressure-Containing Parts," ASTM International, West Conshohocken, PA, ASTM Standard A351/A351M-14, 2014.
[104] Herrera Clara, Ponge Dirk, and Raabe Dierk, "Characterization of the Microstructure, Crystallographic Texture and Segregation of an As-cast Duplex Stainless Steel Slab," *steel research international*, vol. 79, no. 6, pp. 482–488, Dec. 2016.
[105] "ASTM Standard E8/E8M-13a. Standard Test Methods for Tension Testing of Metallic Materials," ASTM International, West Conshohocken, PA, ASTM Standard E8/E8M-13a, 2013.
[106] "ASTM Standard E23-16b. Standard Test Methods for Notched Bar Impact Testing for Metallic Materials," ASTM International, West Conshohocken, PA, ASTM Standard E23-16b, 2016.
[107] H. M. Ledbetter and M. W. Austin, "Effects of carbon and nitrogen on the elastic constants of AISI type 304 stainless steel," *Materials Science and Engineering*, vol. 70, no. Supplement C, pp. 143–149, Apr. 1985.
[108] A. J. Ardell, "Precipitation Hardening," *Metallurgical Transactions A*, vol. 16, no. A, pp. 2131–2165, 1985.
[109] Z. Jiang, Z. Guan, and J. Lian, "The relationship between ductility and material parameters for dual-phase steel," *J Mater Sci*, vol. 28, no. 7, pp. 1814–1818, Jan. 1993.
[110] A. C. Fischer-Cripps, "Critical review of analysis and interpretation of nanoindentation test data," *Surface and Coatings Technology*, vol. 200, no. 14, pp. 4153–4165, Apr. 2006.
[111] J. H. Lee, T. Kim, and H. Lee, "A study on robust indentation techniques to evaluate elastic-plastic properties of metals," *International Journal of Solids and Structures*, vol. 47, pp. 647–664, 2010.
[112] H. M. Ledbetter, "Stainless Steel Elastic Constants at Low Temperatures," *J. Appl. Phys.*, vol. 52, pp. 1587–1589, 1981.

[113] E. Harvey, L. Ladani, and M. Weaver, “Complete mechanical characterization of nanocrystalline Al-Mg alloy using nanoindentation,” *Mechanics of Materials*, vol. 52, pp. 1–11, 2012.
[114] S. Mburu *et al.*, “Atom Probe Tomography Analysis of the Local Chemical Environment at the Austenite/Ferrite Interfaces of Cast Duplex Stainless Steels,” presented at the 14 th LACCEI International Multi-Conference for Engineering, Education, and Technology: “Engineering Innovations for Global Sustainability,” San Jose, Costa Rica, 2016.
[115] “ASTM Standard E1245-03. Standard Practice for Determining the Inclusion or Second-Phase Constituent Content of Metals by Automatic Image Analysis,” ASTM International, West Conshohocken, PA, ASTM Standard E1245-03, 2008.
[116] S. I. Wright, M. M. Nowell, and D. P. Field, “A Review of Strain Analysis Using Electron Backscatter Diffraction,” *Microscopy and Microanalysis*, vol. 17, no. 3, pp. 316–329, Jun. 2011.
[117] M. Kamaya, A. J. Wilkinson, and J. M. Titchmarsh, “Measurement of plastic strain of polycrystalline material by electron backscatter diffraction,” *Nuclear Engineering and Design*, vol. 235, no. 6, pp. 713–725, Mar. 2005.
[118] A. Hirata, T. Fujita, Y. R. Wen, J. H. Schneibel, C. T. Liu, and M. W. Chen, “Atomic structure of nanoclusters in oxide-dispersion-strengthened steels,” *Nature Materials*, vol. 10, no. 12, pp. 922–926, Dec. 2011.
[119] T. F. Kelly and D. J. Larson, “Atom Probe Tomography 2012,” *Annu. Rev. Mater. Res.*, vol. 42, no. 1, pp. 1–31, Jul. 2012.
[120] A. Devaraj *et al.*, “Three-dimensional nanoscale characterisation of materials by atom probe tomography,” *International Materials Reviews*, vol. 0, no. 0, pp. 1–34, Jan. 2017.
[121] Y. H. Yao, J. F. Wei, and Z. P. Wang, “Effect of long-term thermal aging on the mechanical properties of casting duplex stainless steels,” *Materials Science and Engineering: A*, vol. 551, pp. 116–121, Aug. 2012.
[122] T. J. Marrow and C. Harris, “The Fracture Mechanism of 475°c Embrittlement in a Duplex Stainless Steel,” *Fatigue & Fracture of Engineering Materials & Structures*, vol. 19, no. 7, pp. 935–947, Jul. 1996.
[123] R. W. Hertzberg, *Deformation and Fracture Mechanics of Engineering Materials*, 3rd ed. USA: John Wiley & Sons, Inc., 1989.
[124] A. Redjaimia, “Decomposition of Delta Ferrite in a Fe-22Cr-5Ni-3Mo-0.03C Duplex Stainless Steel. A Morphological and Structural Study,” *Duplex Stainless Steels ’91*, pp. 119–126, 1992.
[125] J.-Y. Xie, L.-D. Teng, N.-X. Chen, and S. Seetharaman, “Atomistic simulation on the structural properties and phase stability for Cr23C6 and Mn23C6,” *Journal of Alloys and Compounds*, vol. 420, no. 1, pp. 269–272, Aug. 2006.
[126] J. J. Han, C. P. Wang, X. J. Liu, Y. Wang, and Z.-K. Liu, “First-principles calculation of structural, mechanical, magnetic and thermodynamic properties for γ-M 23 C 6 (M = Fe, Cr) compounds,” *J. Phys.: Condens. Matter*, vol. 24, no. 50, p. 505503, 2012.
[127] J. Y. Xie, N. X. Chen, L. D. Teng, and S. Seetharaman, “Atomistic study on the site preference and thermodynamic properties for Cr23−xFexC6,” *Acta Materialia*, vol. 53, no. 20, pp. 5305–5312, Dec. 2005.

[128] S. C. Schwarm, S. Mburu, R. P. Kolli, D. E. Perea, and S. Ankem, “Effects of long-term thermal aging on bulk and local mechanical behavior of ferritic-austenitic duplex stainless steels,” *Materials Science and Engineering: A*, vol. 720, pp. 130–139, Mar. 2018.
[129] K. S. Choi, W. N. Liu, X. Sun, and M. A. Khaleel, “Microstructure-based constitutive modeling of TRIP steel: Prediction of ductility and failure modes under different loading conditions,” *Acta Materialia*, vol. 57, no. 8, pp. 2592–2604, May 2009.
[130] C. U. Jeong, Y.-U. Heo, J. Y. Choi, W. Woo, and S.-H. Choi, “A study on the micromechanical behaviors of duplex stainless steel under uniaxial tension using ex-situ experimentation and the crystal plasticity finite element method,” *International Journal of Plasticity*, vol. 75, pp. 22–38, Dec. 2015.
[131] C. A. Schneider, W. S. Rasband, and K. W. Eliceiri, “NIH Image to ImageJ: 25 years of image analysis,” *Nature Methods*, 28-Jun-2012. [Online]. Available: https://www.nature.com/articles/nmeth.2089. [Accessed: 16-Mar-2018].
[132] J. Johansson, “Residual stresses and fatigue in a duplex stainless steel,” Licentiate Thesis, Linkoping University, Linkoping, Sweden, 1999.
[133] K. M. Knowles and P. R. Howie, “The Directional Dependence of Elastic Stiffness and Compliance Shear Coefficients and Shear Moduli in Cubic Materials,” *J Elast*, vol. 120, no. 1, pp. 87–108, Jun. 2015.
[134] J. T. Busby, M. C. Hash, and G. S. Was, “The relationship between hardness and yield stress in irradiated austenitic and ferritic steels,” *Journal of Nuclear Materials*, vol. 336, pp. 267–278, 2005.
[135] G. R. Speich, A. J. Schwoeble, and W. C. Leslie, “Elastic constants of binary iron-base alloys,” *MT*, vol. 3, no. 8, pp. 2031–2037.
[136] J. T. Lenkkeri, “The elastic moduli of some body-centred cubic titanium-vanadium, vanadium-chromium and chromium-iron alloys,” *J. Phys. F: Met. Phys.*, vol. 10, no. 4, p. 611, 1980.
[137] Y. Z. Xia, H. Bei, Y. F. Gao, D. Catoor, and E. P. George, “Synthesis, characterization, and nanoindentation response of single crystal Fe–Cr–Ni alloys with FCC and BCC structures,” *Materials Science and Engineering: A*, vol. 611, pp. 177–187, Aug. 2014.
[138] H. Yasuda, T. Takasugi, and M. Koiwa, “Elasticity of Ni-Based L12-Type Intermetallic Compounds,” *Acta Metallurgia et Materialia*, vol. 40, no. 2, pp. 381–387, 1992.
[139] Y. Tomota, K. Kuroki, T. Mori, and I. Tamura, “Tensile deformation of two-ductile-phase alloys: Flow curves of α-γ Fe-Cr-Ni alloys,” *Materials Science and Engineering*, vol. 24, no. 1, pp. 85–94, Jul. 1976.
[140] V. M. Farber, “Initial stages decomposition of supersaturated solid solutions,” *Met Sci Heat Treat*, vol. 37, no. 10, pp. 391–398, Oct. 1995.
[141] T. Sourmail, C. H. Too, and H. K. D. H. Bhadeshia, “Sensitisation and Evolution of Chromium-depleted Zones in Fe-Cr-Ni-C Systems,” *ISIJ International*, vol. 43, no. 11, pp. 1814–1820, 2003.
[142] L. M’Cirdi, J. L. Lebrun, K. Inal, and G. Barbier, “Experimental approach of a crystallographic cleavage criterion in a cast aged duplex stainless steel,” *Acta Materialia*, vol. 49, no. 18, pp. 3879–3887, Oct. 2001.

[143] M. Martins, S. M. Rossitti, M. Ritoni, and L. C. Casteletti, “Effect of stress relief at 350 °C and 550 °C on the impact properties of duplex stainless steels,” *Materials Characterization*, vol. 58, no. 10, pp. 909–916, Oct. 2007.
[144] J. W. Cahn, “Hardening by spinodal decomposition,” *Acta Metallurgica*, vol. 11, no. 12, pp. 1275–1282, 1963.
[145] D. Jenko, S. Mandziej, C. Toffolon-Masclet, B. Sustarsic, and M. Jenko, “TEM Study of Dislocations in Duplex Stainless Steel,” *Materials and Technology*, vol. 48, no. 1, pp. 131–135, 2014.
[146] Y.-C. Hsieh *et al.*, “In-situ transmission electron microscopy investigation of the deformation behavior of spinodal nanostructured δ-ferrite in a duplex stainless steel,” *Scripta Materialia*, vol. 125, pp. 44–48, Dec. 2016.
[147] S. Mburu, S. C. Schwarm, R. P. Kolli, D. E. Perea, and S. Ankem, “Ongoing Work,” *Unpublished Work*.
[148] A. Mateo, L. Llanes, M. Anglada, A. Redjaimia, and G. Metauer, “Characterization of the intermetallic G-phase in an AISI 329 duplex stainless steel,” *Journal of Materials Science*, vol. 32, no. 17, pp. 4533–4540, Sep. 1997.